GOETHE
UNIVERSITÄT
FRANKFURT AM MAIN

DISSERTATION

Rydberg-dressed bosonic quantum gases trapped in optical lattices

Mathieu Julien Gérard Barbier

Frankfurt am Main, 2022
(D30)

RYDBERG-DRESSED BOSONIC QUANTUM GASES TRAPPED IN OPTICAL LATTICES

DISSERTATION
zur Erlangung des Doktorgrades
der Naturwissenschaften

vorgelegt beim Fachbereich Physik
Johann Wolfgang Goethe-Universität
in Frankfurt am Main

von
Mathieu Julien Gérard Barbier
geboren in Amiens, Frankreich

Frankfurt am Main, 2022
(D30)

vom Fachbereich Physik der Johann Wolfgang Goethe-Universität als Dissertation angenommen.

Dekan:	Prof. Dr. Harald Appelshäuser
Gutachter:	Prof. Dr. Walter Hofstetter
	Prof. Dr. Roser Valentí
Datum der Disputation:	11.07.2022

dédié à Souad Kabir, épouse Barbier

مهداة لسعاد كبير ، زوجة باربييه

Zusammenfassung

"*Kann ein Festkörper suprafluid sein?*," (orig.: "*Can a solid be superfluid?*") lautet der Titel einer von A.J. Leggett 1970 publizierten Arbeit und eine Frage, der sich diese Arbeit widmet. Intuitiv scheint diese Fragestellung eine klare Antwort zu besitzen, da in der klassischen Physik ein Festkörper und eine Flüssigkeit einer entgegengesetzter Natur sind und sich dementsprechend gegenseitig ausschließen. Doch im Rahmen der Quantenmechanik mag es für diese Frage keine offensichtliche Antwort geben. Deshalb kam es um 1970 zu einer Welle von Publikationen, die sich mit der Theorie von Quantenphasen beschäftigte, ein Zustand der sowohl Eigenschaften von Festkörpern und Suprafluiden besitzt. Die Existenz dieser quantenmechanischen Phase, die als Suprasolidität getauft wurde, schien jahrzentelang ein Rätsel zu sein.
Die Suche nach einem experimentell realisierbarem System eröffnete viele weitere Forschungszweige, doch im Grunde vereint sie ein Grundgedanke: Kondensierte System aus langreichweitig wechselwirkenden Teilchen. Trotz dieser recht simplen Idee ergaben sich eine Vielfalt von Kandidaten, mit denen eines Tages Suprasolidität experimentell nachgewiesen werden soll. Eines dieser vielversprechenden Systeme, welches das zentrale Thema dieser Arbeit bildet, sind Bose-Einstein Kondensate, dessen Atome an Rydberg-Zuständen gekoppelt sind.
Bose-Einstein Kondensation ist ein Phänomen, welches um 1924 von Albert Einstein vorhergesagt wurde, der die Arbeiten von Satyendranath Bose über die Quantenstatistik von Photonen auf den Fall von Atomen verallgemeinerte. Im Prinzip lässt sich der dazugehörige Aggregatzustand durch eine makroskopische Besetzung eines quantenmechanischen Zustandes charakterisieren, weshalb sich ein solches System aus ununterscheidbaren Atomen durch eine einzige Wellenfunktion beschreiben lässt. Da meist der besetzte Quantenzustand der energetisch geringste ist, wird mit der Kondensation von Gasen meist ultrakalte Temperaturen im Nanokelvin-Bereich assoziert. Die ersten experimentellen Realisierungen von einem Bose-Einstein Kondensat fanden erst 1995 statt und die dafür verantwortlichen Physiker wurden 2001 mit dem Nobelpreis ausgezeichnet. Doch lang bevor wurde vermutet, dass die Bose-Einstein Kondensation teilweise hinter dem Phänomen der Suprafluidität steckt, welches 1938 durch ultrakaltes Helium gefunden wurde. Darauffolgende theoretische und experimentelle Arbeiten fanden heraus, dass in Helium die Suprafluidität aus der Wechselwirkung zwischen den kondensierten Teilchen stammt und somit entstand die Beziehung zwischen Bose-Einstein Kondensation und Suprafluidität.

Folgend auf den ersten Realisierungen von Bose-Einstein Kondensaten erschienen weitere innovative Experimente, die sich in den optischen Gittern gefangenen Quantengasen widmeten. In diesen zahlreichen, wissenschaftlichen Untersuchungen konnten die Eigenschaften von Bose-Einstein Kondensaten besser verstanden werden. Das Prinzip von Vielteilchensystemen, gefangen in einem periodischen Potential, bot eine Plattform zur Untersuchung weiterer Quantenphasen.
Eine konzeptionell einfache Modifikation von solchen Systemen erhält man durch die Kopplung der Grundzustände der gefangenen Teilchen an hoch angeregten Zuständen mithilfe einer externen Lichtquelle. Im Falle dessen, dass diese Zustände nahe der Ionisationsgrenze des Atoms liegen, spricht man von Rydberg-Zuständen und Atome, welche zu diesen Zuständen angeregt werden, bezeichnet man als Rydberg-Atome. Eines der vielen charakteristischen Eigenschaften von Rydberg-Atomen ist die Fähigkeit über große Entfernungen jenseits der atomaren Längenskalen zu wechselwirken. Im Rahmen von Vielteilchensystemen wurden dementsprechend Kristallstrukturen aus gefangenen Rydberg-Atomen experimentell beobachtet.

Nun stellt sich die Frage, was mit einem gefangenen Bose-Einstein Kondensat passiert, dessen Teilchen an langreichweitig wechselwirkenden Zuständen gekoppelt sind. Gibt es ein Parameterregime, in dem sowohl Kristallstruktur als auch Suprafluidität in solchen Systemen koexistieren können? Dies ist die zentrale Frage dieser Arbeit, die sich mit der Theorie von gefangenen Quantengasen gekoppelt an Rydberg-Zuständen auseinandersetzt. Die Arbeit ist in vier Teile gegliedert:
Kapitel 1 erörtert die allgemeinen Konzepte hinter bosonischen Vielteilchensystemen gefangen in optischen Gittern. Zunächst werden in Abschnitt 1.2 die Kühlungsmethoden vorgestellt, mit denen Quantengase ultrakalte Temperaturen erreichen können. Im Anschluss wird der physikalische Hintergrund von optischen Gittern diskutiert, in denen diese gekühlten Gase gefangen werden. Dabei wird das periodische Potential, welches aus stehenden Wellen von Laserlicht resultiert, aus einer quantenmechanischen und semiklassischen Sicht erläutert. Abhängig von den Parametern des Laserlichts werden die Teilchen entweder von den Knoten oder Bäuchen angezogen. Diese periodisch angeorgneten Potentialminima werden als Gitterplätze bezeichnet. Aufgrund der Relevanz in weiteren, wichtigen Herleitungen wird das Konzept des reziproken Gitters ebenfalls vorgestellt. Ausgangspunkt bilden dabei die optischen Gitter für die Auseinandersetzung mit der Theorie von Teilchen gefangen in periodischen Potentialen. Dabei wird das in dem Kontext bekannte Bloch-Theorem eingeführt und die Bandstruktur des Systems in Abhängigkeit der Potentialparameter bestimmt,um Einblick in das Verhalten der Teilchen zu gewinnen und mit der Wannier-Darstellung abgeschlossen, die als Ortsraum-Wellenfunktion der Teilchen verstanden werden kann. Nachdem die Eigenschaften einzelner, gefangener Atome diskutiert wurden, widmet sich dieser Abschnitt den Vielteilchensystemen. Zuerst wird das sogenannte Bose-Hubbard Modell vorgestellt, mit dem sich bosonische Vielteilchensystem in der Zweiten Quantisierung beschreiben lassen. Dieses Modell beinhaltet Tunnelprozesse und Kontaktwechselwirkung, d.h. Wechselwirkung zwischen zwei Teilchen am selben Gitterplatz. Zusätzlich besitzt das Modell

einen theoretischen Parameter, das chemische Potential, mit denen sich in Berechnungen von Grundzuständen die Teilchenanzahl im System regulieren lässt. Da im Rahmen dieser Arbeit langreichweitige Wechselwirkung auch eine wichtige Rolle spielt, wird eine Erweiterung des Bose-Hubbard Modells mit Wechselwirkung zwischen Teilchen in benachbarten Gitterplätzen diskutiert. Durch das komplexe Zusammenspiel der Tunnelamplitude, der beiden Wechselwirkungsstärken und des chemischen Potentials ergeben sich in dem System die möglichen Quantenphasen, die im darauffolgenden Abschnitt diskutiert werden. Zuerst werden die möglichen Quantenphasen besprochen, die in einem solchen System erwartet werden, nämlich der Mott-Isolator, das Suprafluid, die Ladungsdichtewelle und das Suprasolid. Im Falle, dass solche Zustände in bestimmten Grenzfällen erhalten werden können, werden diese erörtert und die dazugehörigen analytischen Wellenfunktionen diskutiert. Um die Quantenphase des Systems jenseits dieser Grenzfälle zu erhalten, werden die Phasendiagramme des Systems anhand numerischer Rechnungen mit dem erweiterten Bose-Hubbard Modell bestimmt. Mithilfe von Ordnungsparametern lassen sich dann die Vielteilchengrundzustände charakterisieren und die Quantenphase identifizieren, womit Information über das Wechselspiel der Parameter des Modells gewonnen werden Diesem Abschnitt folgend werden letzendlich experimentelle Methoden diskutiert, mit denen diese Quantenphasen nachgewiesen werden können. Eine dieser Methoden ist die Flugzeitmessung, bei der das Potential ausgeschaltet wird und die Teilchenwolke aufgrund der Schwerkraft fällt. Während der Expansion des Gases kommt es möglicherweise zu Interferenzen zwischen den Teilchen, abhängig von der Quantenphase des Systems vor der Expansion. Nach einiger Zeit wird ein Bild der Wolke geschossen, welches die Impulsverteilung des vorher gefangenen Systems offenbart, woraus die Quantenphase erschlossen werden kann. Eine weitere Methode bietet das Quantengasmikroskop, mit welchem einzelne Teilchen abgebildet werden können und wodurch sich die genaue Ortsraumverteilung der Teilchen im System darstellen lässt. Damit wurden die für diese Arbeit wichtigsten theoretischen und experimentellen Aspekte von bosonischen Systemen gefangen in optischen Gittern besprochen.
In Kapitel 2 führen wir den zweiten, essenziellen Aspekt dieser Arbeit ein, nämlich Rydberg-Zustände und Systeme aus Rydberg-Atome. Begonnen wird mit der Herleitung der Wellenfunktion der Valenzelektronen, mit der sich die herausgehobenen Eigenschaften von Rydberg-Atomen besser verstehen lässt. In diesem Kontext wird die Hauptquantenzahl eingeführt, mit der sich die Skalierung relevanter Eigenschaften beschreiben lässt. Da der Rydberg-Zustand ein angeregter Zustand ist, besitzt dieser eine endliche Lebensdauer, welche auf spontane Emission und Schwarzkörperstrahlung zurückgeführt werden kann. Hierbei wird deren physikalischen Hintergründe dargestellt und deren Strahlungsraten in Abhängigkeit der Hauptquantenzahl quantifizieren. Im Anschluss wird die langreichweitige Wechselwirkung zwischen zwei Atomen im Rydberg-Zustand erläutert, die aus der Dipol-Dipol-Wechselwirkung zwischen den Atomenkernen und den entfernten Valenzelektronen stammt. Für zwei Atome im selben Rydberg-Zustand erhält man aus der Störungstheorie die charakteristische van-der-Waals Wechselwirkung, die sowohl isotrop als auch anisotrop sein kann und als langreichweitige Wechselwirkung im ersten Abschnitt von Kapitel 4 fungiert. Jedoch jenseits der Störungstheorie liefert die

Dipol-Dipol-Wechselwirkung sogenannte Spagetthi-Potentiale, in denen nicht nur die Wechselwirkung zwischen zwei Rydberg-Atomen ersichtlich werden, sondern auch die Existenz von Molekülen bestehend aus Rydberg-Atomen hervorgeht. Solche Moleküle werden im Kontext der Rydberg-Physik auch Macrodimere genannt und bilden die Basis für die langreichweitige Wechselwirkung im zweiten Abschnitt von Kapitel 4. Da sich die Diskussion der Wechselwirkung auf Atome im Rydberg-Zustand einschränkt, wird die Rolle der Wechselwirkung in Systemen aus wenigen Atomen, deren elektronischer Grundzustand an einem Rydberg-Zustand gekoppelt ist, diskutiert. Dabei wird der Vielteilchengrundzustand für verschiedene interatomare Distanzen im Bezug auf Kopplungsparameter und Wechselwirkungsstärke besprochen. Aus diesen Rechnungen wird das Phänomen der Rydberg-Blockade ersichtlich, in dem die Anregung aller Atome energetisch ungünstig ist, wenn die Atome nah genug beieinander sind. Für dichte Systeme aus vielen, ununterscheidbaren Atomen bildet sich ein sogenanntes Superatom und das System verhält sich wie ein einziges Rydberg-Atom mit modifizierten Kopplungsparametern. Dieses Kapitel schließt ab mit dem jetzigen Stand der Rydberg-Physik in Bezug auf Vielteilchensysteme. Dabei wird die experimentelle Realisierung von Kristallstrukturen aus lokalisierten Atomen erwähnt, die in einem tiefen optischen Gitter gefangen sind und dementsprechend nicht tunneln. Zusätzlich wird das sogenannte avalanche dephasing diskutiert, ein kollektiver Effekt in dem durch Schwarzkörperstrahlung unerwünschte Rydberg-Zustände in einem System besetzt werden, was zu störenden Wechselwirkungen und dem Verlust von Koheränz führen kann.
Vor den Hauptergebnissen dieser Arbeit werden in Kapitel 3 essenzielle numerische Aspekte und Methoden zur Berechnung von Vielteilchensysteme und deren Zeitentwicklungen besprochen. Da der Hilbertraum von Vielteilchensysteme und damit der dazugehörige numerische Rechenaufwand einfacher Operationen stark mit der Anzahl der Teilchen und berücksichtigen Einteilchenzustände wächst, wird eine Methode zur Vereinfachung der Rechnungen unentbehrlich. In dieser Arbeit wird die Gutzwiller-Theorie gewählt, in der sich mithilfe der Gutzwiller-Näherung das System in Untersysteme aufteilen lässt. Der Rechenaufwand, der mit der numerischen Berechnung Vielteilchengrundzustände assoziert wird, ist in diesen Untersystemen stark verringert und ermöglicht durch eine gescheite Wahl der Methodenparameter den Vielteilchengrundzustand des gesamten Systems approximativ zu erhalten. In diesem Kapitel wird ebenfalls die Mastergleichung in Lindblad-Form hergeleitet, mit der sich Dissipation und Dekohärenz im System beschreiben lässt. Der Einfluss dieser Prozesse wird aus nicht-unitäre Zeitentwicklungssimulationen ersichtlich.
In Kapitel 4 werden dann die Ergebnisse der zentralen Fragestellung dieser Arbeit vorgestellt. Im ersten Abschnitt wird ein bosonisches Quantengas gefangen in einem optischen Gitter gekoppelt an Rydberg-Zuständen untersucht. Das dazugehörige Modell beschreibt ein zweikomponentiges System bestehend aus Atomen im elektronischen Grundzustand und im Rydberg-Zustand. Das Modell beinhaltet zudem einen Kopplungsterm zwischen beiden Komponenten und der van-der-Waals Wechselwirkung zwischen den Rydberg-Atomen. Um möglichst viel Erkenntnis diesem Modell zu gewinnen werden die Vielteilchengrundzustände sowohl für isotrope als auch für anisotrope van-der-Waals

Wechselwirkung berechnet. Die Rechnungen werden für quadratische optische Gitter ebenso wie für dreieckige optische Gitter durchgeführt. Unabhängig der Geometrie der langreichweitigen Wechselwirkung und des optischen Gitters werden Phasendiagramme bestehend Ladungsdichtewellen, suprafluide und suprasolide Phasen entdeckt, wobei deren Parameterbereiche von den Geometrien abhängen. Die Kristallstrukturen, die in den Ladungsdichtewellen und suprasoliden Phasen auftauchen, weisen unterschiedlichste interatomare Abstände zwischen den Rydberg-Atomen. Dementsprechend kann festegestellt werden, dass anisotrope Wechselwirkung zu streifenförmige Dichtemodulation führt, die für die Koexistenz von Kristallstruktur und endliche Kondensation besonders vorteilhaft ist. Der Unterschied zwischen einem quadratischen und einem dreieckigen optischen Gitter ist nur im Bereich des Phasendiagramms bemerkbar, in dem das System eine dichte Dichtemodulation aufweist, dessen Längenskala vergleichbar mit den Abständen zwischen benachbarten Gitterplätzen ist. Für Parameterbereiche, in denen die Phasen aus Rydberg-Atomen mit großer interatomarer Distanz bestehen, ist der Unterschied zwischen den Gitter-Geometrien kaum bemerkbar. Da diese Ergebnisse vielversprechend für die experimentelle Realisierung sind, wird die Untersuchung durch das Einbeziehen von dissipative und dekohärente Prozessen vervollständigt. Da suprasolide Phasen durch eine Kristallstruktur aus Rydberg-Atome und einem endlichen Kondensat, welches aus der Phasenkohärenz der Atome hervorkommt, auszeichnet, ist es möglich, dass die endliche Lebenszeit der Rydberg-Zustände und Dephasierungsprozesse diesen beiden Charakteristika so sehr schadet, sodass suprasolide Phasen nur theoretisch existieren und experimentell in solchen Systemen nicht nachgewiesen werden können. Mithilfe der Mastergleichung in Lindblad-Form wird die Stärke der Dissipation und Dekohärenz im Kontext von Zeitentwicklungen überprüft. Dabei wird als Anfangszustand sowohl eine Ladungsdichtewelle als auch eine suprasolide Phase genommen, welche im Rahmen der vorherigen Rechnungen erhalten wurden, und in Anwesenheit der beiden genannten Prozesse in der Zeit entwicklen lassen. Hierdurch wird festgestellt, dass in der Tat Dissipation und Dekohärenz mit wachsenden Raten der spontanen Emission und Dephasierung zunimmt, jedoch selbst für hohe Raten das System langlebig ist. Zudem wird beobachtet, dass die suprasolide Phase von dem endlichen Kondensat profitiert, da die erlaubte Umverteilung der Atome in dieser Phase dazu führt, dass das System weniger Dissipation und Dekohärenz erfährt. Der erreichte langlebige Zustand besitzt zwar einen mit der Zeit verschwindendes Kondensat, welches jedoch für typische Lebenszeiten und Dephasierungs-Raten erst nach langer Zeit komplett verschwindet, sodass dieser Zustand experimentell beobachtet werden könnte. Wir kommen deshalb zum Schluss, dass bosonische Quantengase gefangen in optischen Gittern und gekoppelt an Rydberg-Zuständen ein vielversprechendes System für die Realisierung suprasolider Phasen ist.
Da jedoch kollektive Phänomene und weitere experimentelle Hürden, wie zum Beispiel die maximal realisierbare Tunnelamplitude und Kopplungsstärke, potentiell Schwierigkeiten bereiten könnten, wird ein weiteres System vorgestellt, mit dem suprasolide Phasen realisiert werden können. Im Gegensatz zum vorherigen System werden nun die Atome im elektronischen Grundzustand jeweils paarweise schwach an Macrodimer-Zustände gekoppelt. Dadurch erlangen die Atome im Grundzustand die Fähigkeit langreichweitig

zu wechselwirken, jedoch nur wenn der Abstand zwischen zwei Atomen der molekularen Bindungslänge entspricht. Zuerst werden die Eigenschaften der dazugehörigen Kopplung erläutert, die realisierbaren Wechselwirkungsstärken untersucht und den Einfluss von Dekohärenz bestimmt. Es stellt sich heraus, dass der Quotient zwischen resultierende Wechselwirkungsstärke und Dekohärenz besonders groß ist, welches vorteilhaft für Experimente wäre. Um herauszufinden, ob suprasolide Phasen überhaupt in einem solchen System möglich ist, wird das Phasendiagramm des dazugehörigen erweiterten Bose-Hubbard Modell berechnet. Da die Wechselwirkung anhand der Auswahl des gekoppelten Macrodimer-Zustandes verändert werden kann, werden die Phasendiagramme für Wechselwirkungen zwischen sowohl benachbarte als auch nächstnächste benachbarte Gitterplätze berechnet und verglichen. Für die vorher bestimmten, realistischen Wechselwirkungsstärken werden Ladungsdichtewellen, suprafluide und suprasolide Phasen gefunden. Es wird festgestellt, dass die Wechselwirkung zwischen nächstnächste Nachbarn zu streifenförmige Kristallstrukturen führt, welche vorteilhaft für suprasolide Phasen ist. Da diese Ergebnisse besonders positiv sind, wird dieser Abschnitt mit einem Vorschlag abgeschlossen, mit der in einem solchen System suprasolide Phasen realisiert werden können. Dabei wird experimentell relevante Prozesse wie das Anschalten des Kopplungslasers mithilfe Zeitentwicklungsrechnungen simuliert. Durch Bestimmung der nötigen Wechselwirkungsstärke um aus einem anfänglichen suprafluiden System eine suprasolide Phase zu erreichen und bilden eine Zeitentwicklung exemplarisch abgebildet. Zusammenfassend wird festegestellt, dass bosonische Quantengase gekoppelt an Rydberg-Zuständen vielversprechende Systeme für die experimentelle Realisierung suprasolider Phasen sind. Erhofft wird, dass in Zukunft relevante, kollektive Phänomene besser ergründet und neue Apparaturen entwickelt sein werden, um Experimente jenseits der jetzigen Einschränkungen durchführen zu können.

Publications

The following is a list of peer-reviewed journal articles and preprints which were published in the context of this work:

- "Decay-dephasing-induced steady states in bosonic Rydberg-excited quantum gases in an optical lattice"
  by Mathieu Barbier, Andreas Geißler, and Walter Hofstetter
  in *Phys. Rev. A.* **99**, 033602 (2019)

- "Supersolid phases of Rydberg-excited bosons on a triangular lattice"
  by Jaromir Panas, Mathieu Barbier, and Walter Hofstetter
  in *Phys. Rev. A* **99**, 063625 (2019)

- "Extended Bose-Hubbard models with Rydberg macrodimer dressing"
  by Mathieu Barbier, Simon Hollerith, and Walter Hofstetter
  in *Phys. Rev. A* **104**, 053304 (2021)

- "Supersolid phases of ultracold bosons trapped in optical lattices dressed with Rydberg p-states"
  by Mathieu Barbier, Henrik Lütjeharms, and Walter Hofstetter
  in *Phys. Rev. A* **105**, 013326 (2022)

Contents

Introduction

"*Can a solid be superfluid*" is the title of a paper published by A.J. Leggett in 1970 and a question to which this thesis is devoted. Intuitively, this question seems to have an obvious answer, since in classical physics a solid and a liquid are opposite in nature and accordingly mutually exclusive. But in the framework of quantum mechanics, there may be no obvious answer to this question. Therefore, around 1970 rose a wave of publications dealing with the theory of quantum phases possessing properties of both solids and superfluids. This quantum mechanical state was coined supersolids and its existence seemed to be a mystery for decades.

The search for an experimentally realizable system opened many branches of research, but they are basically united by one basic idea: Condensed systems of interacting particles. Despite this rather simple idea, a variety of candidates emerged through which supersolidity were hoped to be experimentally realized. One of these promising candidates, which forms the central theme of this thesis, are Bose-Einstein condensates whose atoms are coupled to Rydberg states.

Bose-Einstein condensation is a phenomenon predicted around 1924 by Albert Einstein, who generalized the work of Satyendranath Bose on the quantum statistics of photons to the case of atoms. In principle, the associated state of matter can be characterized by a macroscopic occupation of a quantum mechanical state, which is why such a system of indistinguishable atoms can be described by a single wave function. Since usually the occupied quantum state is the energetically lowest, ultracold temperatures in the nanokelvin range are usually associated with the condensation of gases. The first experimental realizations of a Bose-Einstein condensate took place only in 1995 and the physicists responsible for it were awarded the Nobel Prize in 2001. But long before that, it was suspected that Bose-Einstein condensation was partly behind the phenomenon of superfluidity, which was found for ultracold helium in 1938. Subsequent theoretical and experimental work found that in helium the superfluidity arose from the interaction between condensed particles, and thus the link between Bose-Einstein condensation and superfluidity was established.

Following the first realizations of Bose-Einstein condensates, other innovative experiments appeared dedicated to quantum gases trapped in optical lattices. In these numerous, scientific investigations, the properties of Bose-Einstein condensates could be better understood and many-particle systems trapped in a periodic potential provided a platform for the investigation of many further quantum phases. A conceptually simple modification of

such systems is obtained by coupling the ground states of trapped particles to highly excited states using an external light source. Such states, energetically close to the energy associated with the ionization of the atom, are called Rydberg states and atoms excited to these states are called Rydberg atoms. One of the many characteristic properties of Rydberg atoms is their ability to interact over large distances beyond the typical atomic length scales. Accordingly, in the context of many-body systems, crystalline structures of trapped Rydberg atoms have been observed experimentally.
The crucial question now arises as to what happens to a trapped Bose-Einstein condensate whose particles are coupled to strongly, long-range interacting states. Is there a parameter regime in which both crystalline structure and superfluidity can coexist in such systems? This is the central issue of this thesis, which studies the theory of trapped bosonic quantum gases coupled to Rydberg states. The work is divided into four chapters as follows:

- In Chapter 1 we discuss bosonic quantum gases trapped in optical lattices. We first elaborate on the various cooling methods, followed by a derivation of the optical lattice arising from the interference pattern of laser light. We then introduce the Bloch theorem commonly used for particles trapped in periodical potentials and examine the resulting Band structure. After the Wannier representation is presented, we go from the single particle picture to many-body systems. In the context of second quantization we derive the Bose-Hubbard model and an extension, through which the quantum phases relevant in the scope of this thesis can be introduced and discussed. We then conclude with experimental methods, by which these quantum phases can be detected and observed.

- Chapter 2 focuses on properties of the Rydberg states, interaction between Rydberg atoms and many-body ground states of atoms coupled to Rydberg states. We investigate the processes limiting the lifetime of such Rydberg states and the scaling of their magnitudes with the principal quantum number. We then derive the van-der-Waals interaction resulting from the dipole-dipole interaction between two identical Rydberg states through second-order perturbation theory and discuss the potential landscape obtained beyond perturbation theory. In the context of these potential landscapes we introduce macrodimer states, molecular bound states arising from such potential landscapes. This chapter is wrapped up with the study of few atom systems coupled to Rydberg states. We investigate the coupling scheme of such systems, introduce the concept of Rydberg-dressing and discuss the many-body phenomena of such systems, such as the Rydberg blockade and the superatom. We finalize this section with a recap of important many-body experiments, especially with respect to the emergence of crystalline structures and the avalanche dephasing.

- As an integral part of the numerical calculations performed in the scope of this thesis we devote the first part of Chapter 3 to Gutzwiller mean-field theory, through which the computational cost of the studied problems are reduced and the computation thus rendered feasible. We elaborate on the associated mean-field decoupling, and discuss the difference between the single-site and Cluster Gutzwiller approximations with respect to validity and computational effort. In the second part of the chapter

we derive the Lindblad master equation, which allows us to include dissipative and decoherent processes in the system through time evolution simulations.

- Chapter 4 contains the main results of this thesis. We first study a bosonic quantum gas dressed with Rydberg states, which yields van-der-Waals interaction. We investigate the phase diagrams, analyze the importance of the lattice and interaction geometry and conclude with time evolution simulations to assess the strength of the dissipation and decoherence arising from the finite lifetime of the Rydberg state and blackbody induced transitions. We then focus on a bosonic quantum gas dressed with macrodimer states. With respect to the associated coupling scheme we determine experimentally realizable dressed interaction strengths for macrodimer states emerging from the potential landscape obtained for two chemical elements. After the thorough investigation of more experimental aspects linked to the coupling scheme, we compute the corresponding phase diagrams given the previously determined dressed interaction strengths. We finally propose an adiabatic preparation of the system in order to obtain phases with spontaneously broken lattice translational symmetry.

Chapter 1

Ultracold quantum gases trapped in optical lattices

In this chapter we discuss the fundamental aspects of bosonic quantum gases trapped in optical lattices both from a theoretical as well as an experimental point of view. In Section 1.2 we elaborate on the various cooling techniques through which atoms are able to reach ultracold temperatures. We especially discuss the Doppler cooling and mention notable other techniques allowing the atoms to reach temperatures below the Doppler limit. In Section 1.3 the concept of optical lattices is reviewed. We examine the effect of an electromagnetic wave on an atom and derive the corresponding periodic potential arising through the light-atom interaction. As a useful notion we also introduce the reciprocal space and comment on its role in the context of atoms in a lattice. In Section 1.4 we study the properties of atoms in periodic potentials by means of the Bloch theorem. We furthermore introduce useful wave functions and examine their behavior with varying parameters of the periodic potential. In Section 1.5 we derive the plain and extended Bose-Hubbard model obtained withing the second quantization formalism and in section 1.6 we review the possible quantum phases of their corresponding many-body ground states. After establishing a way to classify these phases we compute their phase diagrams. Finally in Section 1.7 we review well-established methods to detect and distinguish between the various previously-discussed quantum phases. We derive the theoretical background behind time-of-flight measurements and explain the idea behind the quantum gas microscope.

1.1 Introduction

The field of condensed matter physics flourishes and keeps growing, as many versatile systems allow for the investigation of novel and exotic quantum phases. In the context of bosonic quantum gases a landmark has been provided by Albert Einstein which predicted, based on the work of Satyendranath Bose on quantum statistics [1], a quantum phase defined by the macroscopic occupation of the energetically lowest quantum state at

ultracold temperatures [2]. This state of matter, now known as *Bose-Einstein condensate*, was many years later experimentally achieved with Rubidium ^{87}Rb [3] and has since then been reproduced with other types of particles such as molecules [4] and photons [5].
The versatility of Bose-Einstein condensates is not limited to the type of particles involved in the state of matter. By using different types of external confinements it is possible to investigate different aspects of the quantum gas, further understand observed phenomena and even simulate other many-body systems. In this context Bose-Einstein condensates loaded in optical lattices became a strongly investigated field of research [6–9]. Thanks to their high tunability and versatility trapped quantum gases in optical lattices are expected to be an essential tool for the investigation of various phenomena [10–13] and a promising platform for quantum computation [14, 15].
As ultracold temperatures are a prerequisite for such systems we elaborate in what follows on the most prominent cooling method, i.e. the Doppler cooling, and techniques, by which the temperature can be subsequently cooled down even further.

1.2 Cooling atoms

The invention of laser cooling of atoms allowed for the investigation of many highly relevant systems and phenomena, and the various methods to reach ultracold temperatures have been studied both theoretically as well as experimentally. Among the most prominent methods is the *Doppler cooling*, which has been developed for free [16, 17] and trapped atoms [18]. It consists of the controlled absorption and spontaneous emission of photons, hereby reducing the kinetic energy and thus the velocity related temperature of the atom. Although widely used, the effectiveness is limited due to continuous heating induced by spontaneous emission. In order to reach temperatures below this limitation, various techniques such as the *Sisyphus cooling* [19–23], the *evaporative cooling* [24–27] and the *Raman sideband cooling* [28–31] have been established, by which temperatures close to the one associated with the motional ground state of an atom are obtained.
In the following, we briefly discuss the physics behind Doppler cooling and elaborate on the accessible range of temperatures. We then give an overview of the more popular cooling methods to go beyond the Doppler-cooling.

1.2.1 Doppler cooling

The idea behind laser cooling is the momentum exchange between a moving atom and a photon. The absorption of a photon with momentum k can be viewed as an inelastic collision and for a photon coming towards the atom, i.e. with opposite directions of their respective velocity, the momentum p' of the thus excited atom with initial momentum p is given by $p' = p - \hbar k$. Although the subsequent spontaneous emission of a photon affects the momentum of the atom, its contribution after many absorption-emission cycles is averaged to zero, because the atom radiates the photon in a random direction, but with a symmetric average distribution. The atom can thus theoretically be cooled down through quantizied deceleration.

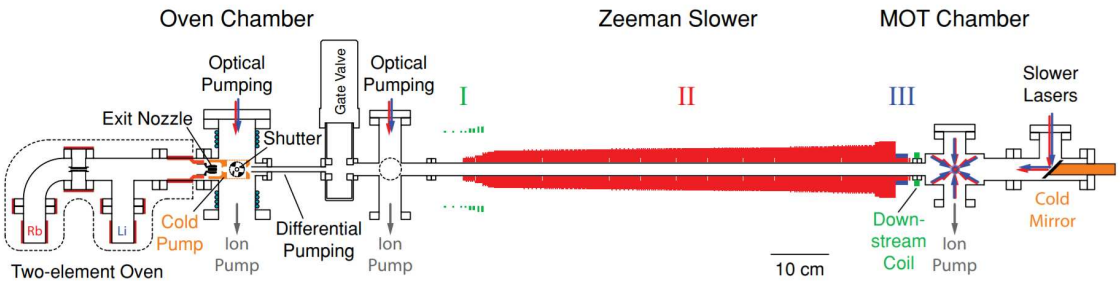

Figure 1.1: Schematic experimental setup for the Doppler cooling of atomic clouds. The atoms are prepared in the oven chamber and prepared into a beam. The beam is then directed into the Zeeman slower in which the atoms encounter the counterpropagating laser for the Doppler cooling. The Zeeman slower creates the magnetic field, which causes the fine splitting necessary for the photonic absorption of the atoms. After being cooled down the atoms are trapped in a magneto-optical trap (MOT), from where they can either be further cooled by subdoppler cooling techniques or transferred to an optical lattice. Reprinted figure with permission from [32]. © 2010 by the American Physical Society.

More realistically however, since the photonic absorption only happens if the energy of the photon is equivalent to the transition energy between the electronic ground and an excited state of the atom. Furthermore in an atomic cloud composed of identical atoms with random motion, the relative velocity of the photon depends on each individual atom and thus a single light source is not going to be able to cool down the atoms.
The latter issue can be partially solved by preparing the atoms in a directed beam (see Fig. 1.1). Through an opposing laser beam, we thus limit the description of the system to one spatial dimension. The direction of the motion is equal for all atoms, however a sharp distribution of velocities is not guaranteed and therefore only part of the atomic beam interacts with the incoming photons due to the persisting Doppler shift problem. Additionally atoms slowed down by several absorption-emission cycles are not able to absorb more photons beyond a certain point as relative energy the photon shifts out of resonance.
The solution to these issues is the *Zeeman slower*, which applies an inhomogeneous magnetic field along the propagation of the atomic beam in order to make use of the Zeeman effect [33–36] (see Fig. 1.2). The magnetic field splits degenerate states and shifts their energies such that the transition frequencies match the relative energy of the incoming atoms. As the atoms in the beam decelerate, the magnetic field is decreased to adapt to the continuously changing relative velocity of the photons. The atoms are thus experiencing a force opposite to their velocity and hereby cooled down. In order to guarantee that after many absorption-emission cycles no atoms propagating in the direction of the incoming photons are lost, a second laser beam with opposite direction to the first laser beam is used.

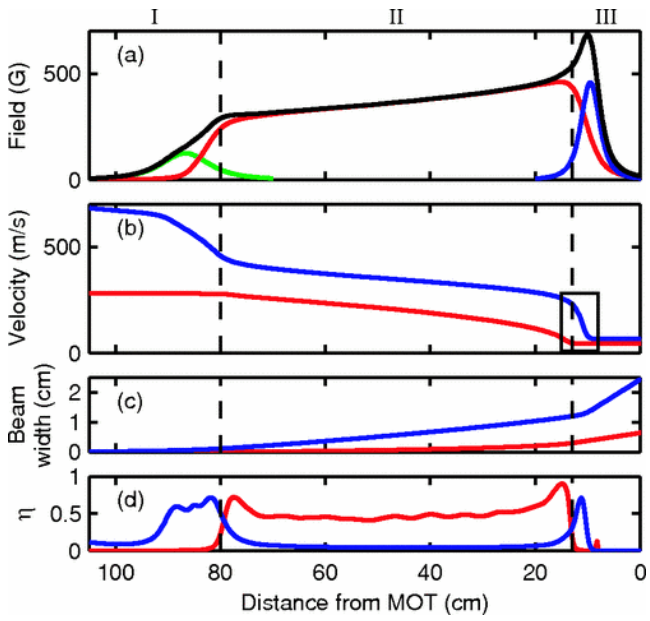

Figure 1.2: (a) Overall magnetic field generated within the experimental setup (black) in the oven chamber (green), the Zeeman slower (red) and the MOT chamber (blue). The continuously increasing magnetic field guarantees that the decelerated atoms are still in resonance with the optical transition frequency of the cooling laser. (b) The velocity of the cooled atoms. In this experiment, the atomic cloud consisted of Rubidium (red) and Lithium (blue) atoms. (c) The width of the atomic beam, which expands the further it travels. (d) Dimensionless acceleration of the atoms throughout the cooling process. Reprinted figure with permission from [32]. © 2010 by the American Physical Society.

Doppler limit

Due to the random nature of the spontaneous emission of a photon, the average velocity gain of the atoms is zero. The root mean squared velocity $\sqrt{\langle v^2 \rangle} = 2\sqrt{k_B T}/m$ however is non zero and implies that the atom is constantly heated during the emission part of the cycle. In the stationary state the cooling and heating rates of the atoms are equal, which means that the limit of the Doppler cooling is determined by the decay rate Γ of the excited state involved in the Doppler cooling. The Doppler limit is then defined through the lowest achievable temperature, the Doppler temperature $T_D = \hbar\Gamma/(2k_B)$. The validity of this limit has been experimentally demonstrated [37, 38]. The corresponding energy $E_D = m\langle v^2 \rangle/2$ is generally much larger than the energy gained through the momentum kick of a single, radiated photon, indicating that temperatures below the Doppler limit are in principle achievable given the appropriate technique. The Doppler cooling however can achieve temperatures of about several hundred mK.

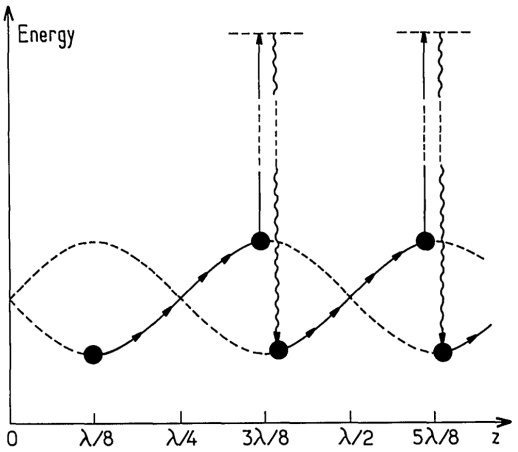

Figure 1.3: Sinusoidal polarization potential for the two degenerate ground states. An atom in one of the two ground states with residual velocity converts its kinetic energy into potential energy and upon reaching the maximum of the potential, the light field transfers the atom into the other ground state through optical pumping. The previously felt maximum of the potential becomes a potential minimum and the atom hereby loses the potential energy. This process is repeated until the kinetic energy is not sufficient to reach the potential maximum and the atom is thus cooled down. Reprinted figure with permission from [39]. © 1989 by the Optica Publishing Group.

1.2.2 Sub-Doppler cooling

Since the conception of Doppler cooling various techniques have been developed to go below its limit and approach the recoil temperature $k_B T_R = \hbar^2 k^2/(2m)$. In contrast to the Doppler cooling, which relies on a two-level system, several of these techniques utilize the hyperfine structure of the atoms to achieve ultracold temperatures. Among these are the Sisyphus, the evaporative and the Raman sideband cooling, which are apart from the above-mentioned common feature vastly different.

Sisyphus cooling

Starting point of the Sisyphus cooling is an experimental setup consisting of two counter-propagating laser beams with wavelength λ and orthogonal linear polarization. The resulting light field is then given by a polarization standing wave with period $\lambda/2$ [40]. It exhibits an overall linear polarization at the nodes of the standing wave, while the antinodes are characterized by alternating left-hand and right-hand circular polarized light.
Due to the periodic light field a multi-level atom experiences a spatially dependent shift of its energy level. For an atom with a twofold-degenerate electronic ground state a circular polarized light induces an optical pumping to the preferred ground state. The atom then experiences the light field with opposite circular polarization as repulsive, which

renders the standing light wave a periodic potential. An atom in the other ground state experiences a similar periodic potential, albeit shifted by $\lambda/4$.
An atom at rest is optically pumped in one of the ground states in dependence on its position in the light field and is then trapped due to the circular polarized light. A moving atom however is optically pumped into one ground state, depending on the handedness of circular polarization of the surrounding light field at that position, and then through its kinetic energy climbs up the potential hill 1.3. If the kinetic energy is large enough such that the atom reaches the top of the potential hill, it is optically pumped to the other ground state due to the light with opposite circular light and its kinetic energy is converted to potential energy, hereby losing velocity through the climb. This process is repeated until the atom is not able to further climb the potential hill.
With the Sisyphus cooling it is hereby possible to reach the recoil temperature, which is around a few mK and therefore much smaller than the Doppler cooling.

Evaporative cooling

We consider an atomic cloud trapped in an optical harmonic potential. As the atoms collide and exchange momentum they thermalize and hereby collectively reach a uniform temperature based on the principle of equilibration. By reducing the strength of the potential it is possible to let fast atoms escape through their higher kinetic energy. In magnetic traps however the lowering of the potential well is not as trivial and relies on the Zeeman effect. In a two-level atom with $F = 0$ and $F = 1$, where the Zeeman shift splits the threefold degenerate excited state into three states with $|m_F = -1, 0, 1\rangle$, the gradient of the magnetic field B leads to forces $\Delta E \propto -m_F B$ relative to the center of the harmonic potential. The force is attractive for one sublevel $(m_F = -1)$, while the other sublevels either do not feel the trap $(m_F = 0)$ or are expelled $(m_F = 1)$. The first state is referred to as the trapped state, while the last state as the anti-trapped state. Assuming all the trapped atoms in the trapped state, it is expected that faster atoms reside on the far edges of the potential. Through a radiofrequency source, which matches the energy difference between the trapped and anti-trapped state at the border of the potential, fast atoms are excited to the anti-trapped state and hereby lost. Although the procedure appears to be more complex than its optical trap counterpart, it is equivalent in its result as both method rely on the loss of fast particles. The slower atoms left in the potential rethermalize and reach a lower uniform temperature. The successive ramping down of the potential can be understood as a rescaling of the Maxwell-Boltzmann distribution. Instead of becoming more narrow, the peak of the distribution shifts to lower velocities and at the same time the atom number decreases such that its shape is not altered greatly. Finally, through evaporative cooling temperatures of a few nK can be achieved.

Raman sideband cooling

The basic idea of the Raman sideband cooling is the continuous optical pumping of particles into a low energy mode. For tightly-bound atoms theses energy modes are given by the vibrational levels ν, with the lowest energy mode $\nu = 0$, which results in unique states

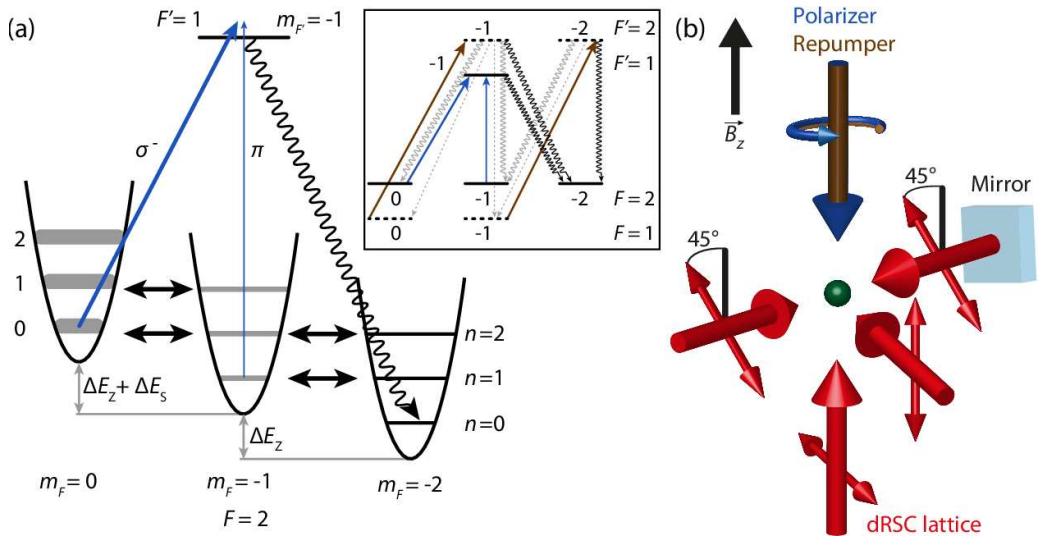

Figure 1.4: Left: Raman sideband cooling process, through which the kinetic energy of an atom is reduced by optical pumping it from a higher lying vibrational level to a lower lying level. Through an external magnetic field the different vibrational levels n of different states $|F, m_F\rangle$ are shifted such that they become degenerate, hereby allowing Raman transition between these two levels. After several Raman transitions the atom is optically pumped into an excited state, from which it decays to the initial state $|F, m_F\rangle$, albeit occupying a lower vibrational level. This repeated until a dark state is reached. Reprinted figure with permission from [31]. © 2017 by the American Physical Society.

$|F, m_F, \nu\rangle$ for the atom. Through an external magnetic field the Zeeman shift can lead to two states $|F, m_F, \nu\rangle$ and $|F, m_F - 1, \nu - 1\rangle$ being degenerate and additionally coupled through Raman transitions. Through several of these transitions the atom is transferred to the state with the lowest m_F, where it is optically pumped to an excited state. Subsequent decay leads to the population of the state $|F, m_F, \nu - n\rangle$, where n refers to the amount of Raman transitions involved in one cycle. After many cycles the atom is transferred to the lowest vibrational mode $|F, m_F, 0\rangle$ called the dark state, as it is only weakly coupled by the coupling lasers.
As Raman sideband cooling relies on tight confinement of atoms, it became a strong valuable asset in experiments with tunable optical traps. The limitation is only given by the spectral resolution of the Raman transitions and thus makes ultracold temperatures far below the Doppler limit of a few hundred nK accessible.

Atom cooling is an essential part of realizing degenerate quantum gases, as the phenomena we are interested in depend on reaching ultracold temperatures through which bosonic atoms are able to condense due to their enhanced de-Broglie wavelength. The subsequent step is the trapping of these cold down atomic clouds.

1.3 Optical lattices

Optical lattices belong to the category of optical dipole traps, which rely on the dipole force of a light field acting on atoms, hence the name. The elegant idea behind the trapping is based on the fact that neutral atoms immersed in a light field gain a finite, light-induced dipole moment. The thus polarized atom is then able to interact with the surrounding light field and feel a force, the strength of which depends on the intensity gradient of the field.
In the following, we discuss the origin of the light-particle interaction and illustrate how the dipole force can result in a periodic potential.

1.3.1 Light-atom interaction

The light-atom interaction is based on two properties: It couples the ground state of the atom to higher lying hyperfine states, hereby gaining a finite dipole moment, and simultaneously shifts the energy of these internal atomic states, such that the atom becomes sensitive to the light field intensity. The resulting potential landscape felt by the atoms can be obtained both through second-order perturbation theory and a classical oscillator picture. Since the derivations of the potential offer a different view on the origin of the interaction, we discuss both in the following.

Perturbation theory picture

A light field surrounding an atom induces transitions of its electronic ground state to other hyperfine states and additionally shifts its energy levels. For an atom at position $\boldsymbol{x}$ at time t, this shift, which is also known as the *AC Stark shift* [41–43], is determined through second-order perturbation theory given by

$$U_{\mathrm{AC}} = \sum_{j \neq i} \frac{|\langle i|\hat{\boldsymbol{d}}_\omega|j\rangle|^2}{E_i - E_j}, \tag{1.1}$$

where $\hat{\boldsymbol{d}}(\boldsymbol{x},t)_\omega = \boldsymbol{\mu}_\omega(\boldsymbol{x},t)\boldsymbol{E}_\omega(\boldsymbol{x},t)$ is the dipole operator, and $|i\rangle$ and $|j\rangle$ denote the electronic ground state and a hyperfine state respectively, with E_i and E_j being their respective energies. The dipole operator $\hat{\boldsymbol{d}}_\omega$ describes the dipole transition matrix element $\boldsymbol{\mu}_{ij}$ between the states $|i\rangle$ and $|j\rangle$ through the light field with amplitude $\boldsymbol{E}_\omega(\boldsymbol{x},t)$. If we set the internal energy of the atom in the electronic ground state to zero, only the light field consisting of n photons with energy ω contributes to the energy as $E_i = n\hbar\omega$. On the other hand, a transition to $|j\rangle$ implies the absorption of a photon from the surrounding field. The internal energy of the atom then is given by the optical transition frequency as $\hbar\omega_{ij}$, which yields $E_j = \hbar\omega_{ij} + (n-1)\hbar\omega$. The difference between both energies is then defined as the detuning $\Delta_{ij} = \hbar(\omega - \omega_{ij})$.
The higher lying hyperfine states have a finite lifetime and the corresponding decay rate

back to the electronic ground state is given by [44]

$$\Gamma_{ij} = \frac{\omega_{ij}^3}{3\pi\epsilon_0\hbar c^3}\mu_{ij}^2. \tag{1.2}$$

It is useful to reformulate the dipole transition matrix through a transition coefficient matrix c_{ij} as

$$\boldsymbol{\mu}_{ij} = c_{ij}|\boldsymbol{\mu}|, \tag{1.3}$$

since the squared value c_{ij}^2 also known as line strength is experimentally accessible and theoretically determined for a given atom and its hyperfine structure. We thus arrive at the most general form of the AC Stark shift

$$U_{\mathrm{AC}} = \frac{3\pi\epsilon_0 c^3\Gamma}{\omega_0^3}\sum_{j\neq i}\frac{c_{ij}}{\Delta_{ij}}|\boldsymbol{E}_\omega(x,t)|^2, \tag{1.4}$$

where Γ and ω_0 denote the decay rate and the transition frequency to the hyperfine state to which the ground state couples the strongest. Its strength not only depends on the properties of the atom, but more importantly on the intensity $|\boldsymbol{E}_\omega^2(x,t)|$ of the light field and the detunings Δ_{ij} given by the chosen light field through ω, which are experimentally tunable parameters. In dependence of the sign of Δ_{ij}, the atoms are either attracted ($\Delta_{ij} < 0$) or expelled ($\Delta_{ij} > 0$) by the maxima of the light field. If ω is chosen such that the signs of all detunings are not equal, further calculations are necessary to determine the potential minima induced by the light field.
In the case of a simple hyperfine structure consisting of only two levels or in the far off-resonant regime ($\Delta_{ij} \gg 0$), the sum drops out of the Eq. (1.4) and thus yields the simplified form

$$U_{\mathrm{AC}} = \frac{3\pi\epsilon_0 c^3\Gamma}{\omega_0^3\Delta}|\boldsymbol{E}_\omega(x,t)|^2, \tag{1.5}$$

where Δ is the detuning to the most relevant hyperfine state. Although being an approximation, Eq. (1.5) delivers qualitatively good result [44]. In subsection 1.3.1, we further discuss the difference between the approximated and the exact AC Stark shift based on an example.

Classical oscillator picture

Compared to the perturbation theory aspect of the light shift, the oscillator model offers a more classical view on the matter. Similar to the derivation of the AC Stark shift, the interaction between atom and light is based on the dipolar interaction through

$$V_{\mathrm{dip}}(x) = -\frac{1}{2}\langle \boldsymbol{d}_\omega(x,t)\boldsymbol{E}_\omega(x,t)\rangle_t \tag{1.6}$$

with the previously defined dipole operator $\boldsymbol{d}_\omega(x,t)$ and where $\langle\cdot\rangle_t$ signifies the time averaged expectation value. The goal now is to define the dipole moment $\boldsymbol{\mu}_\omega(x,t)$ based

on an oscillator model. Classically the electron of an atom in its electronic ground can be viewed as elastically bound to the nucleus and oscillating with undamped motion given by frequency ω_0 [45]. However in the presence of the additional light shift, the oscillation deviates from the unperturbed motion which thus results in a finite dipole moment. Given the deviation vector $r_{ij,\omega}(x,t)$, which describes the deviation of the electron from the unperturbed oscillation, we can define the dipole moment as

$$\boldsymbol{\mu}_\omega(x,t) = e\sum_{j\neq i}\boldsymbol{r}_{ij,\omega}(x,t) \tag{1.7}$$

We thus need to determine the light field dependence of the deviation. Since we are working in a classical picture, we can establish an equation of motion through the Lorentz's oscillator model, which yields

$$\ddot{\boldsymbol{r}}_{ij,\omega}(x,t) + \Gamma_\omega\dot{\boldsymbol{r}}_{ij,\omega}(x,t) + \omega_{ij}^2\boldsymbol{r}_{ij,\omega}(x,t) = -ec_{ij}^2\frac{\boldsymbol{E}_\omega(x,t)}{m_e}. \tag{1.8}$$

The damping $\Gamma_\omega = (\omega/\omega_{ij})^2\Gamma_{ij}$ results from the finite lifetimes of the hyperfine states. Through integration, the differential equation gives

$$\boldsymbol{r}_{ij,\omega}(x,t) = \frac{e}{m_e}\frac{1}{\omega_{ij}^2 - \omega^2 - i\omega\Gamma_\omega}\boldsymbol{E}_\omega(x,t) \tag{1.9}$$

Via substitution of the prefactor as

$$\frac{e^2}{m_e} = \frac{6\pi\epsilon_0 c^3\Gamma_\omega}{\omega^2} \tag{1.10}$$

and the decay rate Γ_{ij}, we obtain the potential obtained through the dipole interaction

$$V_{\mathrm{dip}}(x) = 3\pi\epsilon_0 c^3\sum_j\frac{1}{\omega_{ij}^3}\Big(\frac{\Gamma_{ij}}{\omega_{ij}+\omega} + \frac{\Gamma_{ij}}{\omega_{ij}-\omega}\Big)\langle\boldsymbol{E}_\omega^2(x,t)\rangle_t. \tag{1.11}$$

Although the previously defined detunings Δ_{ij} can be chosen to be large in the off-resonant regime, it is reasonable to assume the detunings to be all smaller than the actual transition frequencies $\omega_{ij} \gg \Delta_{ij}$. With this assumption, the potential reads

$$V_{\mathrm{dip}}(x) = \frac{3\pi\epsilon_0 c^3\Gamma}{\omega_0^3}\sum_j\frac{c_{ij}^2}{\Delta_{ij}}\langle\boldsymbol{E}_\omega^2(x,t)\rangle_t \tag{1.12}$$

resulting in the same potential as obtained with second-order perturbation theory, although both derivations are different and provide complementary aspects to the understanding of the light shift induced potential.

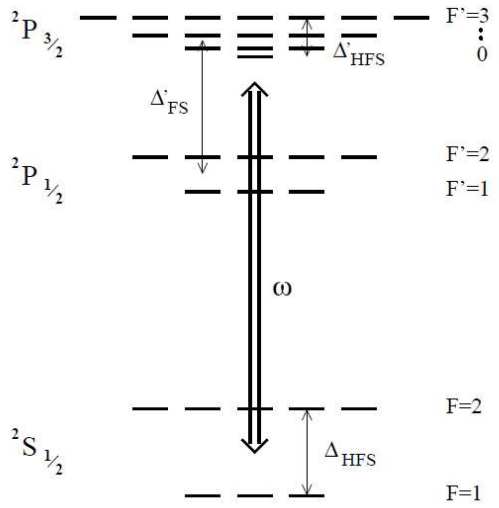

Figure 1.5: Fine and hyperfine states with fine state splitting Δ_{FS} and hyperfine state splittings Δ_{HFS} and Δ'_{HFS} coupled through the external light source with frequency ω resulting in the trapping of an alkali atom. Even though the full substructure of the alkali atom contributes to the trapping potential, the two-level approximation leads to an accurate description. Reprinted figure with permission from [44]. © 1999 by Elsevier.

Significance of the two-level approximation

The two-level description, from which (1.5) arises, appears to disregard potentially important hyperfine levels, which are also coupled to by the external light field. However alkali atoms typically used in optical lattice experiments, e.g. ^{7}Li, ^{41}Ka and ^{87}Rb, possess a number of hyperfine states, which are involved in the dipole interaction (see Fig. 1.5). The full substructure of such an alkali atom with nuclear spin $J = 3/2$ can be described by the hyperfine structure of the levels $\left|^2S_{1/2}\right\rangle$, $\left|^2S_{1/2}\right\rangle$ and $\left|^2S_{1/2}\right\rangle$. The associated energies of fine and hyperfine state are defined as $\hbar\Delta_{\mathrm{FS}}$, $\hbar\Delta_{\mathrm{HFS}}$ and $\hbar\Delta'_{\mathrm{HFS}}$. In such a system the interaction yields

$$V_{\mathrm{dip}}(x) = \frac{\pi\epsilon_0 c^3\Gamma}{\omega_0^3}\Big(\frac{2 + Pg_F m_F}{\Delta_{2,\mathrm{F}}} + \frac{1 - Pg_F m_F}{\Delta_{1,\mathrm{F}}}\Big)\langle \boldsymbol{E}^2_\omega(x,t)\rangle_t, \tag{1.13}$$

with the polarization P of the light-field ($P = 0$ for linear and $P = \pm 1$ for circular polarized light), the Landé factor g_F and the magnetic quantum number m_F [44]. $\Delta_{1,\mathrm{F}}$ and $\Delta_{2,\mathrm{F}}$ refer to the energetic difference between the lowest hyperfine state $\left|^2S_{1/2}, F\right\rangle$ and the center of the hyperfine splitting of $\left|^2P_{1/2}\right\rangle$ and $\left|^2P_{3/2}\right\rangle$ respectively. Since the splitting between the two levels are generally larger than the energies associated with the fine and hyperfine splitting, i.e. $|\Delta_{1,F}|, |\Delta_{2,F}| \gg |\Delta_{\mathrm{FS}}|, |\Delta_{\mathrm{HFS}}|, |\Delta_{\mathrm{HFS}}|$, we can define $|\Delta_{1,\mathrm{F}}| \approx |\Delta_{2,\mathrm{F}}| \equiv |\Delta|$ and thus obtain

$$V_{\mathrm{dip}}(x) = \frac{3\pi\epsilon_0 c^3\Gamma}{\omega_0^3\Delta}\Big(1 + \frac{1}{3}Pg_F m_F\frac{\Delta_{\mathrm{FS}}}{\Delta}\Big)\langle \boldsymbol{E}^2_\omega(x,t)\rangle_t. \tag{1.14}$$

The first term corresponds to the potential obtained within the two-level approximation, while the residual term reflects the contribution of other fine and hyperfine states, which is marginal due the considered limit $\Delta_{\mathrm{FS}}/\Delta \ll 1$. We thus conclude that for alkali atoms the two-level picture is a qualitatively good approximation for calculating the potential strength.

1.3.2 Atomic scattering

The interaction of the light field not only consists of the photon absorption of the atom, but also the subsequent radiative emission of photons through spontaneous decay. The power of the dipole radiation is given by

$$P_{\mathrm{rad}}(x) = \langle \dot{\boldsymbol{\mu}}_\omega(x,t)\boldsymbol{E}_\omega(x,t)\rangle_t. \tag{1.15}$$

Given the photonic energy $\hbar\omega$, the corresponding photonic scattering rate reads [44]

$$\Gamma_{\mathrm{sc}}(x) = \frac{P_{\mathrm{rad}}}{\hbar\omega} = \frac{3\pi\epsilon_0 c^3\Gamma^2}{2\hbar\omega_0^3}\sum_j \left(\frac{c_{ij}}{\Delta_{ij}}\right)^2 \langle \boldsymbol{E}_\omega^2(x,t)\rangle_t, \tag{1.16}$$

which possesses the same scaling of the light field intensity as the dipole interaction. In the two-level approximation, direct comparison of the scattering rate and the dipole interaction yields the relation

$$\hbar\Gamma_{\mathrm{sc}}(x) = -\frac{\Gamma}{\Delta}V_{\mathrm{dip}}(x). \tag{1.17}$$

Since strong dipole radiation could potentially hinder the trapping of the atoms, it is important to decrease the ratio between photonic scattering rate Γ_{sc} and dipole interaction V_{dip}, while maintaining a significant dipole interaction strength. Through the above-derived relation, we find that large detunings Δ allow us to achieve this goal. Thus optical dipole traps commonly work in the far off-resonant regime ($|\Delta| \gg 1$), in order to achieve low scattering rates and large enough interactions for the trapping.

1.3.3 Periodic lattices

Optical lattices are not only defined by their light-field induced trapping, but also through their periodic structure. The periodic nature of the potential arises from a set of counterpropagating laser beams, whose interference results in a standing wave with fixed nodes. These nodes represent the minima of the light-field intensity and thus either repel or attract the submerged atoms based on the detuning. The field of multiple lasers can be written as

$$\boldsymbol{E}_\omega(\boldsymbol{r},t) = \frac{1}{2}\sum_l \tilde{E}_l e^{i\boldsymbol{k}_L^l\boldsymbol{r}-i\omega t+i\phi_l}\hat{\boldsymbol{e}}_l \tag{1.18}$$

with the laser index l, their field amplitudes $\tilde{E}_l$ and phase shifts ϕ_l. The wave vector $\boldsymbol{k}_L^l = k_L^l\boldsymbol{n}_l$ are given by their wave number k_L^l and the normalized vectors $\boldsymbol{n}_l = (n_x^l, n_y^l, n_z^l)$,

which indicate their direction ($|\boldsymbol{n}_l| = 1$). Note that we omit the Gaussian shape of the laser perpendicular to the beam propagation for the sake of simplicity. Assuming that a set of counterpropagating lasers are identical in their properties, the potential resulting from their interference reads

$$V(\boldsymbol{r}) = \sum_m V_0^m \cos^2(k_L^m(\boldsymbol{r}\cdot\boldsymbol{n}_m) + \phi_m), \tag{1.19}$$

where m denotes the set of counterpropagating lasers. The dipole interaction strength $V_0^m = \frac{3\pi\epsilon_0 c^3}{\omega_0^3}\sum_j \frac{c_{ij}}{\Delta_{ij}}|\tilde{E}_m|^2$ is also known as the potential depth and is easily tunable by variation of the light-field intensity. On the other hand, the wave number $k_L^m = 2\pi/\lambda_m$ and thus the periodicity of the potential are directly related to the wavelength of the laser λ_m, which depend on the available lasers and can not be freely changed during an experiment. While changing the relative angle between both counterpropagating lasers might result in a standing wave with altered wave number, it can also lead to the loss of interference between the lasers due to its high sensitivity to the relative phase between both lasers. While several techniques to tune the periodicity of unloaded potentials in real-time have been established in recent years [46, 47], the continuous trapping of atoms during the periodicity tuning remains an important experimental challenge.
The resulting potential Eq. (1.19) is known as the optical lattice and the potential minima, in which the trapped atoms are most likely to be found, are called lattice sites. Through the chosen spatial configuration of several laser beams, optical lattices with vastly different geometries in one, two or three dimension are achievable. Since these optical lattices are theoretically infinite, they can be regarded as *Bravais lattices* and described by a lattice vector $\boldsymbol{R} = \sum_i n_i \boldsymbol{a}_i$, where $n_i \in \mathbb{Z}$ and $\boldsymbol{a}_i$ are the primitive translation vectors. Shifting the potential $V(\boldsymbol{r})$ by $\boldsymbol{R}$ would thus result in the same potential, i.e. $V(\boldsymbol{r}+\boldsymbol{R}) = V(\boldsymbol{r})$.

Examples

Unless mentioned otherwise, we choose the potential depth and the wave number of all lasers to be equal ($V_0^l \equiv V$ and $k_L^l \equiv k_L$) and set the lasers to be phase coherent($\phi_l = 0$). For a single standing wave with $\boldsymbol{n}_1 = (1,0,0)$, the resulting potential is simply given by

$$V_{1\mathrm{D}}(x) = V_0 \cos^2(k_L x). \tag{1.20}$$

While in this form the optical lattice resembles a one-dimensional chain, the full potential resembles stacked discs due to the Gaussian shape of the laser beams and thus reads

$$V_{1\mathrm{D}}(\boldsymbol{r}) = V_0 \cos^2(k_L x) e^{-\frac{(y+z)^2}{\sigma^2}}. \tag{1.21}$$

with the beam waist radius σ. The confinement along x-direction is usually sufficiently strong for trapping due to the large potential depths, whereas the confinement within the y,z-discs is weak and allows the atoms to be move more or less freely within the discs. For a tighter confinement an additional, external potential is necessary, which then restricts the movement within the discs and thus leads to a pure one-dimensional optical lattice [48].

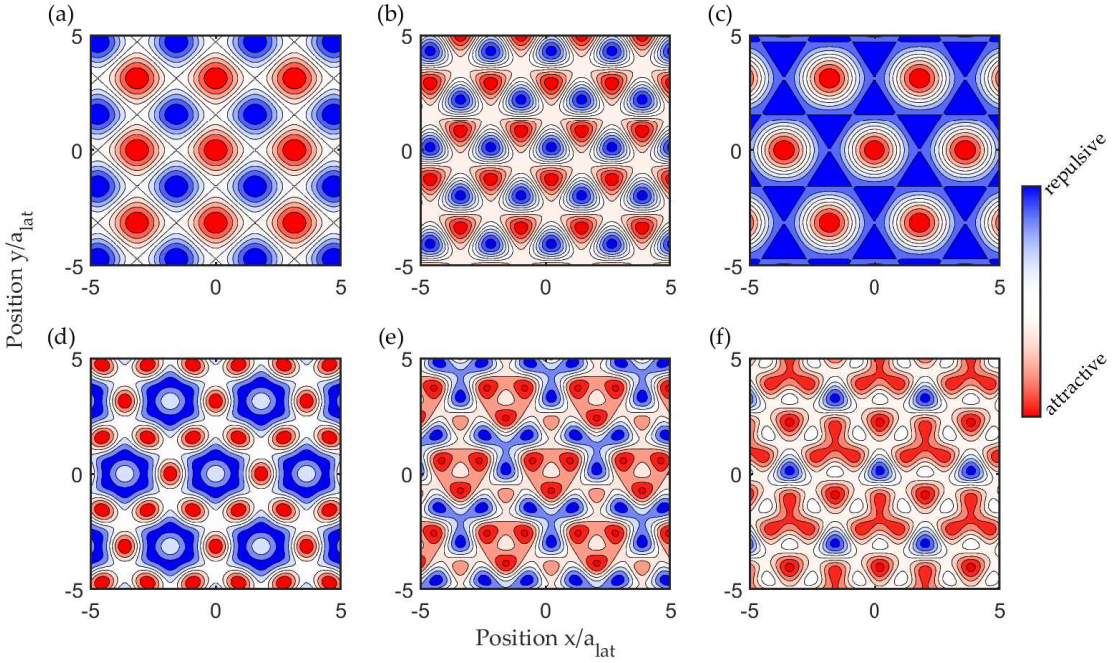

Figure 1.6: Set of exemplary two-dimensional optical lattices with different spatial geometries created by lasers with optical lattice constant $a_{\text{lat}} = \lambda/2 = 532$ nm. The most commonly used two-dimensional optical lattices are (a) square, (b) triangular, (c) honeycomb and (d) Kagome lattices. Through the inclusion of additional lasers and variation of their respective phases other configurations such as (e) and (f) can be obtained. The attractive and repulsive regions of the potential landscape of the lattice can be interchanged through variation of the detuning.

A two-dimensional square lattice can be realized through two perpendicular standing waves ($\boldsymbol{n}_1 = (1,0,0)$ and $\boldsymbol{n}_2 = (0,1,0)$) and reads

$$V_{\text{2D}}^{\text{square}}(\boldsymbol{r}) = V_0(\cos^2(k_L x) + \cos^2(k_L y))e^{-\frac{z^2}{\sigma^2}}, \tag{1.22}$$

which can be understood as two-dimensional square distribution of one-dimensional tubes, again due to the Gaussian beams involved in the creation of the potential. Although most cold atoms experimental setups involving two-dimensional square optical lattices also make use of an additional external confinement, the movement of the atoms within these tubes can be used to create and investigate so-called quantum wires [49–51].
Another two-dimensional optical lattice is the honeycomb lattice, which is created through the overlap of three standing waves with directions $\boldsymbol{n}_1 = (1,0,0)$ and $\boldsymbol{n}_2 = (\cos(\frac{2\pi}{3}), \sin(\frac{2\pi}{3}), 0)$ and $\boldsymbol{n}_3 = (\cos(\frac{4\pi}{3}), \sin(\frac{4\pi}{3}), 0)$, and is given by the potential

$$V_{\text{2D}}^{\text{hc}}(\boldsymbol{r}) = V_0\Big(\cos^2(k_L x) + \cos^2(\frac{k_L}{2}(x - \sqrt{3}y)) + \cos^2(\frac{k_L}{2}(x + \sqrt{3}y))\Big)e^{-\frac{z^2}{\sigma^2}}. \tag{1.23}$$

Superimposing two honeycomb lattices with two different wave numbers ($k_L^1 = 2k_L^2$) leads to an experimentally highly relevant lattice known as the Kagome lattice. While a configuration of twelve laser beams with two different wavelengths can be used to generate such a lattice [52], it is also possible to use three so-called superlaser beam with equal wavelength, but different polarizations [53–55].
Three perpendicular standing waves ($\boldsymbol{n}_1 = (1,0,0)$ and $\boldsymbol{n}_2 = (0,1,0)$ and $\boldsymbol{n}_3 = (0,0,1)$) generate a three-dimensional cubic optical lattice

$$V_{3D}^{\text{cube}}(\boldsymbol{r}) = V_0(\cos^2(k_L x) + \cos^2(k_L y) + \cos^2(k_L z)). \tag{1.24}$$

In three-dimensional optical lattices no additional confinement is necessary as the potential depth is larger than the weak Gaussian confinement. Note that for hypercubic lattices the distance between nearest neighboring potential minima is referred to as the *optical lattice constant* $a_{\text{lat}} = \lambda/2$.

1.3.4 Reciprocal space

Albeit difficult to visualize, momentum space offers an important physical insight on the trapped atoms. Within the plane wave description of the electromagnetic field (see Eq. (1.18)) lays the duality between space $\boldsymbol{r}$ and momentum $\boldsymbol{k}$. Although in the previous sections we considered the wave vector $\boldsymbol{k}$ to be fixed by the laser wavelength and the space as a variable $\boldsymbol{r}$, it is possible to view it the other way around. If we define $\boldsymbol{r} = \lambda\hat{\boldsymbol{e}}$ and choose the momentum $\boldsymbol{k}$ to be a variable, we see that the plane wave behaves equally in real and momentum space.
Similar to the plane wave, the optical lattice possesses a counterpart in momentum space, which is called the *reciprocal lattice*. The corresponding lattice vector in momentum space takes the form $\boldsymbol{K} = \sum_j m_j \boldsymbol{b}_j$ and is equivalent to the previously defined lattice vector $\boldsymbol{R}$ of a Bravais lattice. In order to find their relation, we perform a Fourier decomposition of the potential $V(\boldsymbol{r})$ as

$$V(\boldsymbol{r}+\boldsymbol{R}) = \sum_{\boldsymbol{K}} V_{\boldsymbol{K}} e^{i\boldsymbol{K}\boldsymbol{r}} = \sum_{\boldsymbol{K}} V_{\boldsymbol{K}} e^{i\boldsymbol{K}(\boldsymbol{r}+\boldsymbol{R})} = \sum_{\boldsymbol{K}} V_{\boldsymbol{K}} e^{i\boldsymbol{K}\boldsymbol{R}} e^{i\boldsymbol{K}\boldsymbol{r}} = V(\boldsymbol{r}). \tag{1.25}$$

For the equality to be true, the lattice vectors in real space and momentum space have to fulfill the relation

$$\boldsymbol{K}\boldsymbol{R} = 2\pi N \tag{1.26}$$

with $N \in \mathbb{Z}$. Since $\boldsymbol{R}$ is given by the configuration of laser beams, $\boldsymbol{K}$ is chosen such that $\boldsymbol{a}_i \boldsymbol{b}_j = 2\pi\delta_{ij}$. We hereby see that the reciprocal lattice spacing given by $2k_L$ is inversely proportional to the optical lattice constant a_{lat}. For a hypercubic lattice the wave number can be specified as $k_L = 2\pi/\lambda$.

1.4 Atoms in periodic potentials

In order to understand the behavior of the atoms trapped in the optical lattice, we determine the single-particle spectrum. The Hamiltonian of an atom reads

$$\hat{H} = -\frac{\hbar^2\nabla^2}{2m} + V(\boldsymbol{r}) \tag{1.27}$$

and simply describes an atom with kinetic energy in an arbitrary potential. Commonly used as a natural energy scale in an optical lattice, we introduce the so-called *recoil energy*, which reads

$$E_R = \frac{\hbar^2 k_L^2}{2m} \tag{1.28}$$

and describes the gain in kinetic energy of an atom initially at rest through spontaneous emission of a photon. In the following, we use the periodic nature of the potential in order to determine the eigenfunction of trapped atoms.

1.4.1 Bloch theorem

We define the action of the lattice translation operator $\hat{T}_{\boldsymbol{R}}$ on an arbitrary function $f(\boldsymbol{r})$ as

$$\hat{T}_{\boldsymbol{R}} f(\boldsymbol{r}) = f(\boldsymbol{r} + \boldsymbol{R}). \tag{1.29}$$

Through successive application of the operator

$$\hat{T}_{\boldsymbol{R}_2}\hat{T}_{\boldsymbol{R}_1} f(\boldsymbol{r}) = f(\boldsymbol{r} + \boldsymbol{R}_1 + \boldsymbol{R}_2) = \hat{T}_{\boldsymbol{R}_1+\boldsymbol{R}_2} f(\boldsymbol{r}) \tag{1.30}$$

we can show its commutative property

$$\hat{T}_{\boldsymbol{R}_1}\hat{T}_{\boldsymbol{R}_2} = \hat{T}_{\boldsymbol{R}_2}\hat{T}_{\boldsymbol{R}_1} = \hat{T}_{\boldsymbol{R}_1+\boldsymbol{R}_2}. \tag{1.31}$$

Since the periodic potential $V(\boldsymbol{r}) = V(\boldsymbol{r}+\boldsymbol{R})$ is invariant under translation $\hat{T}_{\boldsymbol{R}} V(\boldsymbol{r}) = V(\boldsymbol{r})$, the Hamiltonian Eq. (1.27) must also be invariant under translation and thus commutes with the operator

$$[\hat{T}_{\boldsymbol{R}}, \hat{H}] = 0. \tag{1.32}$$

Although it may seem trivial, the above commutation relation reveals that both operators share a set of common eigenfunctions

$$\begin{aligned} \hat{H}\Psi(\boldsymbol{r}) &= E\Psi(\boldsymbol{r}) \\ \hat{T}_{\boldsymbol{R}}\Psi(\boldsymbol{r}) &= c_{\boldsymbol{R}}\Psi(\boldsymbol{r}) \end{aligned} \tag{1.33}$$

with eigenvalues E and c_R. The commutative property of the translation operator implies

$$c_{\boldsymbol{R}_1} c_{\boldsymbol{R}_2} = c_{\boldsymbol{R}_1+\boldsymbol{R}_2} \tag{1.34}$$

and thus the eigenvalues of the translational operator can be rewritten with the wave vector $\boldsymbol{k}$ as

$$c_{\boldsymbol{R}} = e^{i\boldsymbol{k}\boldsymbol{R}}. \tag{1.35}$$

Finally, with the application of the translational operator and the definition of the eigenvalue c_R we find that the wave function fulfills

$$\Psi(\boldsymbol{r}+\boldsymbol{R}) = e^{i\boldsymbol{k}\boldsymbol{R}}\Psi(\boldsymbol{r}). \tag{1.36}$$

This is known as *Bloch's theorem* and it states, that the wave function of a single atom trapped in a periodic potential can be rewritten as

$$\Psi(\boldsymbol{r}) = e^{i\boldsymbol{k}\boldsymbol{r}}u(\boldsymbol{r}) \tag{1.37}$$

where $e^{i\boldsymbol{k}\boldsymbol{r}}$ describes a plane wave and $u(\boldsymbol{r})$ is a periodic function such that

$$u(\boldsymbol{r}) = u(\boldsymbol{r}+\boldsymbol{R}). \tag{1.38}$$

The wave function $\Psi(\boldsymbol{r})$ is commonly referred to as the *Bloch state* and can now be used in order to determine the single-particle spectrum.

1.4.2 Band theory

Before applying the newly defined eigenfunction on the Hamiltonian Eq. (1.27), it is useful to work in the momentum space and thus we perform a Fourier decomposition of the periodic function with momentum space lattice vector $\boldsymbol{K}$ as

$$u(\boldsymbol{r}) = \sum_{\boldsymbol{K}} u_{\boldsymbol{K}} e^{i\boldsymbol{K}\boldsymbol{r}}, \tag{1.39}$$

which leads to

$$\Psi(\boldsymbol{r}) = \sum_{\boldsymbol{K}} u_{\boldsymbol{K}} e^{i(\boldsymbol{K}+\boldsymbol{k})\boldsymbol{r}} = \sum_{\boldsymbol{p}} u_{\boldsymbol{p}} e^{i\boldsymbol{p}\boldsymbol{r}}. \tag{1.40}$$

The Fourier decomposition of the periodic potential yields

$$V(\boldsymbol{r}) = \sum_{\boldsymbol{K}} V_{\boldsymbol{K}} e^{i\boldsymbol{K}\boldsymbol{r}}. \tag{1.41}$$

Calculation of the eigenvalue equation of the Hamiltonian Eq. (1.27)

$$\nabla^2\Psi(\boldsymbol{r}) = \sum_{\boldsymbol{p}} u_{\boldsymbol{p}}(\nabla^2 e^{i\boldsymbol{p}\boldsymbol{r}}) = \sum_{\boldsymbol{p}} \boldsymbol{p}^2 u_{\boldsymbol{p}} e^{i\boldsymbol{p}\boldsymbol{r}} \tag{1.42}$$

$$V(\boldsymbol{r})\Psi(\boldsymbol{r}) = \sum_{\boldsymbol{K}\boldsymbol{p}} V_{\boldsymbol{K}} u_{\boldsymbol{p}} e^{i\boldsymbol{K}\boldsymbol{r}} e^{i\boldsymbol{p}\boldsymbol{r}} = \sum_{\boldsymbol{K}\boldsymbol{p}'} V_{\boldsymbol{K}} u_{\boldsymbol{p}'-\boldsymbol{K}} e^{i\boldsymbol{p}'\boldsymbol{r}} \tag{1.43}$$

results in

$$\sum_{\boldsymbol{p}} e^{i\boldsymbol{p}\boldsymbol{r}}\Big(\frac{\hbar^2}{2m}\boldsymbol{p}^2 u_{\boldsymbol{q}} + \sum_{\boldsymbol{p}} V_{\boldsymbol{p}} u_{\boldsymbol{p}-\boldsymbol{K}}\Big) = \sum_{\boldsymbol{p}} e^{i\boldsymbol{p}\boldsymbol{r}} E u_{\boldsymbol{q}} \tag{1.44}$$

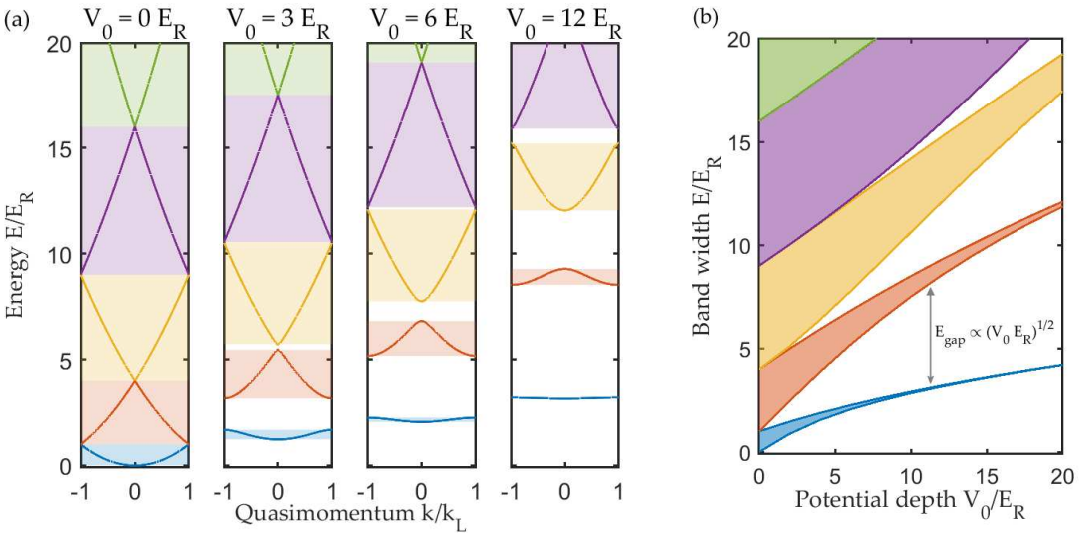

Figure 1.7: (a) Energy bands calculated in a one-dimensional lattice through Eq. (1.46). Each band corresponds to an energy level E_n, which varies with quasimomentum k. For no trapping potential $V_0 = 0$, the energy band result from the overlap of the quadratic dispersion relation of free electrons at different reciprocal lattice points given by $K_n = 2nk_L$ with $n \in \mathcal{Z}$. A finite potential depth $V_0/E_R > 0$ however leads to avoided crossings and shifts the bands to higher energies. At large potential depths, the lowest band becomes flat. (b) The width of the energy bands versus potential depth. The lowest band flattens fast and the gap E_{gap} between the lowest and second band becomes more important with increasing potential depth.

and by substituting back the wave vector $\boldsymbol{k}$ and the reciprocal lattice vector $\boldsymbol{K}$ in

$$\frac{\hbar^2}{2m}\left(\boldsymbol{k}-\boldsymbol{K}\right)^2 u_{\boldsymbol{k}-\boldsymbol{K}} + \sum_{\boldsymbol{K}'} V_{\boldsymbol{K}'-\boldsymbol{k}} u_{\boldsymbol{k}-\boldsymbol{K}'} = E(\boldsymbol{k}-\boldsymbol{K}) u_{\boldsymbol{k}-\boldsymbol{K}} \tag{1.45}$$

Although solving the equation in more than one dimension, we restrict the upcoming discussion on the one dimensional case as it reduces the complexity and still provides important insight on the physics at hand.

One dimensional optical lattice

By restricting the problem to one dimension, the Brillouin zone is simply given by $k \in (-k_L, k_L]$ with the center of the primitive cells separated by $K_n = 2nk_L$ with $n \in \mathbb{Z}$. For the one-dimensional optical lattice given by Eq. (1.20), the Fourier decomposition yields $V_{\boldsymbol{p}=0} = V_0$ and $V_{\boldsymbol{p}=\pm 1} = -V_0/4$, while all other components are zero, e.g. $V_{|\boldsymbol{p}|\geq 2} = 0$. We introduce the quasi-momentum $q_n = k - K_n$ and thus obtain the matrix representation of

the Hamiltonian

$$\begin{pmatrix} \ddots & \ddots & \ddots & \ddots & \ddots \\ \ddots & \frac{\hbar^2}{2m}q_{n-1}^2 & -\frac{V_0}{4} & 0 & \ddots \\ \ddots & -\frac{V_0}{4} & \frac{\hbar^2}{2m}q_n^2 & -\frac{V_0}{4} & \ddots \\ \ddots & 0 & -\frac{V_0}{4} & \frac{\hbar^2}{2m}q_{n+1}^2 & \ddots \\ \ddots & \ddots & \ddots & \ddots & \ddots \end{pmatrix} \begin{pmatrix} \vdots \\ u_{q_{n-1}} \\ u_{q_n} \\ u_{q_{n+1}} \\ \vdots \end{pmatrix} = E(k) \begin{pmatrix} \vdots \\ u_{q_{n-1}} \\ u_{q_n} \\ u_{q_{n+1}} \\ \vdots \end{pmatrix} \tag{1.46}$$

The spectrum obtained through this eigenvalue problem is composed of energy bands (see Fig. 1.7). In the case of no optical lattice ($V_0 = 0$), the lowest band corresponds to the parabolic dispersion relation $\varepsilon(q) = \hbar^2 q^2/2m$ of free particles with mass m. At the edges and the center of the Brillouin zone the energy band touch due to the degeneracy of the eigenstates at the corresponding values of q. A finite potential depth ($V_0 > 0$) however flattens the bands and thus opens a gap, hereby lifting the degeneracy. The parabolic shape of the lowest band still holds for small values of the quasi-momentum $|q| \ll k_L$ and reads

$$\varepsilon(q) = \varepsilon_0 + \frac{\hbar^2 q^2}{2m^*} \tag{1.47}$$

with an energy offset ε_0 and the effective mass m^*. Through the modified dispersion relation the trapped atom can be understood as a freely propagating particle with reduced mass $m^* < m$ as long as the quasi-momentum is small enough.

Single-band approximation

For deep enough lattices, it is reasonable to assume that only the lowest band $E_0(k)$ is filled. This is called the *single-band approximation* and its validity is related to the band gap width E_{gap} between the lowest and the second band. As the lattice depth increases, so does the energy difference between both bands, which is given by

$$E_{\text{gap}} = 2\sqrt{V_0 E_R} \tag{1.48}$$

Since interaction and kinetic processes could potentially excite atoms from the lowest to the second band, it is important that all corresponding energies are below the band gap width. In the upcoming sections, we use the single-band approximation to simplify expressions.

1.4.3 Wannier function

The Bloch functions are useful to determine the energy eigenspectrum, yet it does not provide a real space representation of the trapped atoms. To this end we make use of the *Wannier functions* $w_n(\boldsymbol{r} - \boldsymbol{R}_i)$, a set of orthogonal functions obtained through the Fourier transform of the Bloch functions as

$$w_n(\boldsymbol{r} - \boldsymbol{R}_i) = \frac{1}{V_{\text{BZ}}} \int_{\boldsymbol{k} \in \text{BZ}} \Psi_{n,\boldsymbol{k}}(\boldsymbol{r}) e^{-i\boldsymbol{k}\boldsymbol{R}_i} d\boldsymbol{k}. \tag{1.49}$$

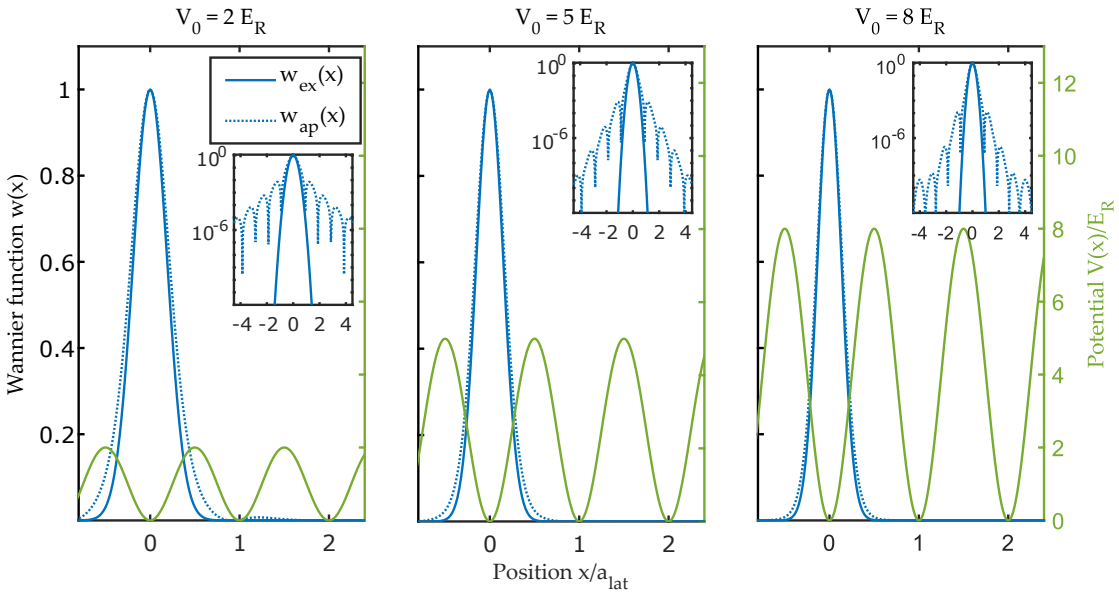

Figure 1.8: The exact Wannier function $\omega_{\mathrm{ex}}(x)$ and the approximated Wannier function $\omega_{\mathrm{ap}}(x)$ of the lowest band at site $\boldsymbol{R}_i = 0$ for different lattice depths. The Wannier function becomes more narrow as the depth increases, which indicates stronger localization of the atoms within the lattice. The Wannier functions within the deep lattice approximation give very reasonable results with larger deviation from the exact Wannier function for shallow lattices. The differences can be seen at through logarithmic depiction of the tails (see inset).

where $\boldsymbol{R}_i$ is the position of lattice site i in real space. On a given lattice site, each band n possesses its own Wannier function. We also define an inverse transformation

$$\Psi_{n,\boldsymbol{k}}(\boldsymbol{r}) = \left(\frac{1}{V_{\mathrm{BZ}}}\right)^{\frac{3}{2}} \sum_{\boldsymbol{R}_i} w_n(\boldsymbol{r} - \boldsymbol{R}_i) e^{i\boldsymbol{k}\boldsymbol{R}_i} \tag{1.50}$$

and given the orthogonality of the Bloch eigenfunctions, we derive the orthogonality relation for the Wannier functions

$$\int d\boldsymbol{r} w_m^*(\boldsymbol{r} - \boldsymbol{R}_j) w_n(\boldsymbol{r} - \boldsymbol{R}_i) = \delta_{m,n}\delta_{\boldsymbol{R}_j,\boldsymbol{R}_i} \tag{1.51}$$

Due to the translation symmetry of the lattice, we obtain all Wannier functions within the optical lattice after computation of the Wannier functions on one lattice site.
The Wannier functions are not invariant under global phase shifts of the Bloch functions, e.g. $\Psi_{n,\boldsymbol{k}} \to \Psi_{n,\boldsymbol{k}} e^{i\theta}$ with $\theta \in \mathbb{R}$. This global phase shift does not yield a different energy spectrum and therefore does not change the physics of the atom, but results in a vastly different Wannier function. Although this arbitrariness appears to be inconvenient, it provides us with an additional degree of freedom to shape the Wannier function to our

liking. For example, it is possible to choose a global phase shift of the Bloch functions such that the Wannier function is real, possesses a well defined parity and is highly localized around the position $\boldsymbol{R}_i$ with exponential decay away from the center.

Deep lattice

Usually the Wannier functions are numerically computed based on the Bloch functions obtained through the eigenvalue equation Eq. (1.46). For deep enough lattices $V_0/E_R \gg 1$ the complexity of the problem can be reduced by assuming that the potential $V(\boldsymbol{r})$ decouples into disconnected harmonic wells given by

$$V_{\text{dip}}(\boldsymbol{r}-\boldsymbol{R}_i) = \frac{1}{2}m\omega_{\text{trap}}^2(\boldsymbol{r}-\boldsymbol{R}_i)^2 \tag{1.52}$$

with the trapping frequency $\hbar\omega_{\text{trap}} = 2\sqrt{V_0 E_R}$. Within this limit the single-band approximation is valid as the resulting band gap in the energy eigenspectrum between the lowest and the second band is large enough. Then the atom in lattice site i is described by the Wannier function of the lowest band, which can be analytically calculated, and reads

$$w(\boldsymbol{r}-\boldsymbol{R}_i) = \frac{1}{\pi^{3/4}\sigma_{\text{lat}}^{3/2}} e^{-\frac{(\boldsymbol{r}-\boldsymbol{R}_i)^2}{2\sigma_{\text{lat}}^2}}. \tag{1.53}$$

In this limit the shape of the Wannier function is a Gaussian with width $\sigma = \sqrt{\hbar/m\omega_{\text{trap}}}$. As expected we find that for increasing lattice depths V_0 the width σ decreases, which implies a higher localization of the atom.
The numerically determined, exact Wannier function and the approximate analytical Wannier function Eq. (1.53) are in good agreement for deep lattices: Both are localized around the center of the lattice site and decay exponentially. The main difference is in the tail of the decay, which is finite but small. We conclude that although the disconnected well picture may not capture the full Wannier function, it is a simple and useful approximation.

1.5 Bose-Hubbard model

While the previous sections focused on the single-particle case, we are interested in the many-body eigenstates of the system. A useful formalism developed for describing systems consisting of many atoms through wave functions is the *second quantization*, in which many-body wave functions take the form

$$\Psi(\boldsymbol{r}_1, \boldsymbol{r}_2, ...) \tag{1.54}$$

with the position $\boldsymbol{r}_i$ of atom i. The underlying idea of these wave functions is the idea of indistinguishability of the quantum particles, through which these wave functions become invariant upon an exchange of the positions of two atoms up to a prefactor

$$\Psi(..., \boldsymbol{r}_i, ..., \boldsymbol{r}_j, ...) = \zeta\Psi(..., \boldsymbol{r}_j, ..., \boldsymbol{r}_i, ...) \tag{1.55}$$

The wave function is symmetric ($\zeta = 1$) or antisymmetric ($\zeta = -1$), if the atoms are bosonic or fermionic respectively. Since the relevant atoms in this work are bosonic, we omit the fermionic descriptions in the following derivations.
Within second quantization, the many-body Hamiltonian in the many-body wave function basis is given through

$$\begin{aligned}\hat{H} = &\int d\boldsymbol{r}\hat{\Psi}^\dagger(\boldsymbol{r})\Big(-\frac{\hbar^2\boldsymbol{\nabla}^2}{2m} + V(\boldsymbol{r})\Big)\hat{\Psi}(\boldsymbol{r}) \\ &+ \iint d\boldsymbol{r}d\boldsymbol{r}'\hat{\Psi}^\dagger(\boldsymbol{r})\hat{\Psi}^\dagger(\boldsymbol{r}')U(\boldsymbol{r},\boldsymbol{r}')\hat{\Psi}(\boldsymbol{r})\hat{\Psi}(\boldsymbol{r}')\end{aligned} \tag{1.56}$$

with the field operators $\hat{\Psi}^\dagger(\boldsymbol{r})$ ($\hat{\Psi}(\boldsymbol{r})$), which add (remove) an atom in position $\boldsymbol{r}$. The first term describes atoms trapped in a potential $V(\boldsymbol{r})$ and is known from the previous section. We introduce an interaction term through $U(\boldsymbol{r},\boldsymbol{r}')$ acting between two atoms at positions $\boldsymbol{r}$ and $\boldsymbol{r}'$. In order to deal with this Hamiltonian, we first need to specify the field operators.

An important algebraic construction of quantum states beyond the single-particle picture is the so-called *Fock space*, which contains all states composed of identical particles with variable particle number. Let us first consider an atom i in a state $\phi_i = \{\psi_1, ..., \psi_M\}$. The states ψ_j with $j \in M$ form the complete single-particle basis. The N-particle basis is then spanned by the states

$$|\Phi\rangle = |\phi_1\phi_2...\phi_N\rangle = \prod_k |\phi_k\rangle\,. \tag{1.57}$$

Due to their indistinguishability and therefore their common Hilbert space, it is useful to work in the occupancy number basis. For n_j atoms in state $|\psi_j\rangle$, we obtain

$$|\Phi\rangle = |\psi_1\rangle^{n_1}|\psi_2\rangle^{n_2}...|\psi_M\rangle^{n_M} \equiv |n_1, n_2, ..., n_M\rangle \tag{1.58}$$

with $\sum_i n_i = N$. These Fock states form a complete and orthogonal set of basis states such that

$$\langle\Phi'|\,\Phi\rangle = \langle n_1', n_2', ..., n_M'|\,n_1, n_2, ..., n_M\rangle = \prod_i \delta_{n_i,n_i'} \tag{1.59}$$

$$\sum_{\sum_i n_i = N} |n_1, n_2, ..., n_M\rangle\langle n_1, n_2, ..., n_M| = \mathbb{1} \tag{1.60}$$

Within the Fock space two operators of great importance are the *creation operator* $\hat{b}_i^\dagger$ and the *annihilation operator* $\hat{b}_i$. As the name suggests these operator create or remove one atom in state ψ_i as

$$\hat{b}_i\,|n_1, n_2, ..., n_i, ..., n_M\rangle = \sqrt{n_i}\,|n_1, n_2, ..., n_i - 1, ..., n_M\rangle \tag{1.61}$$

$$\hat{b}_i^\dagger\,|n_1, n_2, ..., n_i, ..., n_M\rangle = \sqrt{n_i + 1}\,|n_1, n_2, ..., n_i + 1, ..., n_M\rangle \tag{1.62}$$

These operators follow the commutation relation

$$[\hat{b}_i, \hat{b}_j^\dagger] = \delta_{ij} \tag{1.63}$$

meaning that the result of the successive application of both operators on a state depends on their order. In this context we introduce the *number operator* $\hat{n}_i$, which is an eigenoperator of the Fock states

$$\hat{n}_i \left| n_1, n_2, ..., n_i, ..., n_M \right\rangle = n_i \left| n_1, n_2, ..., n_i, ..., n_M \right\rangle \tag{1.64}$$

and through the above-defined creation and annihilation operator can be written as

$$\hat{n}_i = \hat{b}_i^\dagger \hat{b}_i \tag{1.65}$$

While these operators appear to be very basic, they can be used to define the field operators. In the context of optical lattices occupancy of a state represents the number of atoms on a lattice site. Thus the field operators are rewritten through the creation and annihilation operators as

$$\hat{\Psi}^\dagger(\boldsymbol{r}) = \sum_{i,n} w_n(\boldsymbol{r} - \boldsymbol{R}_i)\hat{b}_i^\dagger. \tag{1.66}$$

The application of field operators thus can be seen as adding or removing at an atom on lattice site i for $\boldsymbol{r} \approx \boldsymbol{R}_i$. For positions $\boldsymbol{r}$ not close to the center of any lattice site the field operator has no effect due to the exponential decay of the highly localized Wannier function. We thus rewrite the Hamiltonian with the newly defined field operators

$$\begin{aligned} \hat{H} = &\sum_{mn}\sum_{ij} \int d\boldsymbol{r} w_m^*(\boldsymbol{r} - \boldsymbol{R}_i)\Big(-\frac{\hbar^2 \boldsymbol{\nabla}^2}{2m} + V(\boldsymbol{r})\Big) w_n(\boldsymbol{r} - \boldsymbol{R}_j)\hat{b}_i^\dagger \hat{b}_j \\ + &\sum_{mnpq}\sum_{ijkl} \iint d\boldsymbol{r} d\boldsymbol{r}' w_m^*(\boldsymbol{r} - \boldsymbol{R}_i) w_n^*(\boldsymbol{r}' - \boldsymbol{R}_j) U(\boldsymbol{r}, \boldsymbol{r}') w_o(\boldsymbol{r} - \boldsymbol{R}_k) w_p(\boldsymbol{r}' - \boldsymbol{R}_l)\hat{b}_i^\dagger \hat{b}_j^\dagger \hat{b}_k \hat{b}_l \end{aligned} \tag{1.67}$$

The Hamiltonian can be split into the non-interacting, single-particle Hamiltonian $\hat{H}_0$ and the interaction Hamiltonian $\hat{H}_{\text{int}}$. The first part reads

$$\hat{H}_0 = \sum_i \epsilon_i \hat{n}_i + \sum_{i \neq j} J_{ij} \hat{b}_i^\dagger \hat{b}_j \tag{1.68}$$

and consists of an on-site term with energy

$$\epsilon_i = \sum_{mn} \int d\boldsymbol{r} w_m^*(\boldsymbol{r} - \boldsymbol{R}_i)\Big(-\frac{\hbar^2 \boldsymbol{\nabla}^2}{2m} + V(\boldsymbol{r})\Big) w_n(\boldsymbol{r} - \boldsymbol{R}_i), \tag{1.69}$$

which in case of no external potential is equal for all lattice sites due to the periodicity of the optical lattice, e.g. $\epsilon_i \equiv \epsilon$. As it merely changes the energy of each atom, it does not contribute to the overall physics and can be set $\epsilon = 0$. The latter term removes an atom from site j and creates it in site i with amplitude

$$J_{ij} = \sum_{mn} \int d\boldsymbol{r} w_m^*(\boldsymbol{r} - \boldsymbol{R}_i)\Big(-\frac{\hbar^2 \boldsymbol{\nabla}^2}{2m} + V(\boldsymbol{r})\Big) w_n(\boldsymbol{r} - \boldsymbol{R}_j), \tag{1.70}$$

which effectively describes tunneling of an atom from site i to site j. The amplitude J_{ij} gives the likeliness of this process. J_{ij} is therefore referred to as *tunneling* or *hopping amplitude* and can be calculated through

$$\begin{aligned} J_{ij} &= \frac{1}{V_{\mathrm{BZ}}} \sum_{mn} \sum_{k,k' \in \mathrm{BZ}} e^{-i(\boldsymbol{k}\boldsymbol{R}_i - \boldsymbol{k}'\boldsymbol{R}_j)} \int d\boldsymbol{x} \Psi^*_{m,\boldsymbol{k}}(\boldsymbol{r}) \Big(-\frac{\hbar^2 \boldsymbol{\nabla}^2}{2m} + V(\boldsymbol{r}) \Big) \Psi_{n,\boldsymbol{k}'}(\boldsymbol{r}) \\ &= \frac{1}{V_{\mathrm{BZ}}} \sum_{mn} \sum_{k,k' \in \mathrm{BZ}} E(\boldsymbol{k}) e^{-i(\boldsymbol{k}\boldsymbol{R}_i - \boldsymbol{k}'\boldsymbol{R}_j)} \int d\boldsymbol{x} \Psi^*_{m,\boldsymbol{k}}(\boldsymbol{r}) \Psi_{n,\boldsymbol{k}'}(\boldsymbol{r}) \\ &= \frac{1}{V_{\mathrm{BZ}}} \sum_{n} \sum_{k \in \mathrm{BZ}} E_n(\boldsymbol{k}) e^{-i\boldsymbol{k}(\boldsymbol{R}_i - \boldsymbol{R}_j)} \end{aligned} \tag{1.71}$$

with the energy bands $E_n(\boldsymbol{k})$ determined in section 1.4.2. Within the single-band approximation, calculation of J_{ij} for various lattice depths reveals a decaying behavior. This can be traced back to the narrowing of the Wannier functions, since J_{ij} essentially describes overlap of Wannier functions at two different sites i and j. Quantum mechanically speaking, a larger potential depth result in higher potential walls between atoms, which decreases the tunneling probability. Additionally the amplitude greatly decreases for increasing distances between these two sites as the overlap between the exponential tails of the Wannier functions vanishes.
In a hypercubic lattice the so-called *Mathieu equation* [56–58] yields an analytic formula for the hopping amplitude between neighboring sites

$$J_{01} \equiv J \approx \frac{4}{\sqrt{\pi}} \Big(\frac{V_0}{E_R} \Big)^{\frac{3}{4}} e^{-2\sqrt{\frac{V_0}{E_R}}} E_R \tag{1.72}$$

with the recoil energy Eq. (1.28), which is in good agreement with the numerically computed values of J_{ij}, even for more shallow lattices (see Fig. 1.9).

While long-range interactions can be incorporated into the many-body system, the interaction $U(\boldsymbol{r}, \boldsymbol{r}')$ usually describe s-wave scattering between two atoms and is given by

$$U(\boldsymbol{r}, \boldsymbol{r}') = \frac{4\pi\hbar^2 a}{m} \delta(\boldsymbol{r} - \boldsymbol{r}') \frac{\partial}{\partial(\boldsymbol{r} - \boldsymbol{r}')} |\boldsymbol{r} - \boldsymbol{r}'| \tag{1.73}$$

with the scattering length a. The interaction Hamiltonian can thus be rewritten as

$$\hat{H}_{\mathrm{int}} = \sum_{ij} U_{ij} \hat{b}_i^\dagger \hat{b}_j^\dagger \hat{b}_j \hat{b}_i \tag{1.74}$$

with the interaction strength

$$U_{ij} = \frac{4\pi\hbar^2 a}{m} \sum_{mn} \int d\boldsymbol{r} |w_m(\boldsymbol{r} - \boldsymbol{R}_i)|^2 |w_n(\boldsymbol{r} - \boldsymbol{R}_j)|^2. \tag{1.75}$$

Through calculation of the Wannier functions for various lattice depths, we are able to compute U_{ij} (see Fig. 1.9). While we find that the interaction strength between two atoms

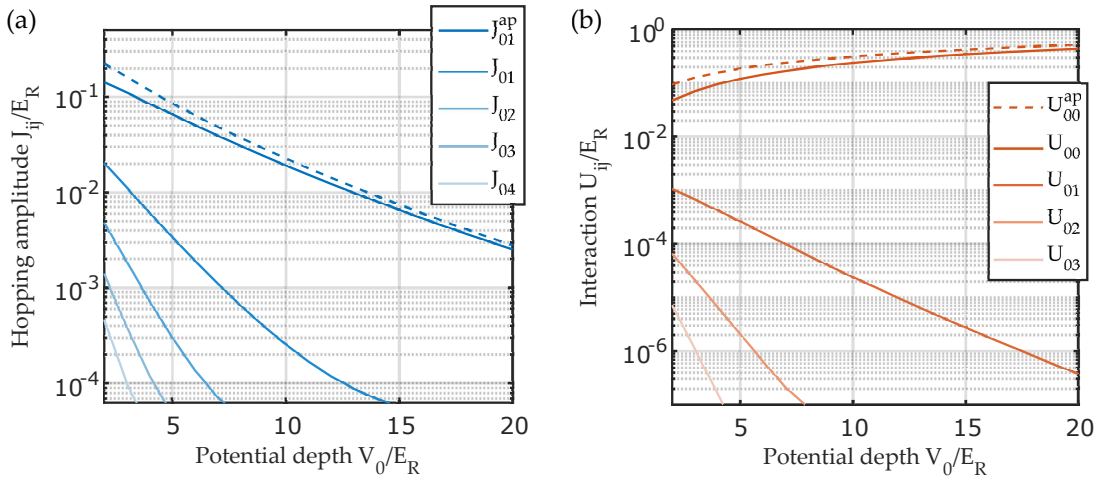

Figure 1.9: (a) The hopping amplitude J_{0i} between lattice sites $\boldsymbol{R}_0$ and $\boldsymbol{R}_i$ (solid lines). The hopping amplitude decreases with increasing lattice depth, which is consistent with the narrowing of the Wannier functions and the hereby resulting smaller overlap between neighboring and far apart Wannier functions. Furthermore, the hopping amplitude is considerably smaller between non-nearest neighboring lattice sites. The solution of the Mathieu equation yields a qualitatively reasonable approximation of the nearest-neighbor hopping amplitude through Eq. (1.72) (dashed line). (b) The on-site interaction between to atoms either on the same site U_{00} or on different sites U_{0i} for various lattice depths (solid lines). The on-site interaction between two atoms on the same site increases for larger lattice depths due to higher localization of the atoms, while the initially already weak interactions between distant atoms decay. The deep lattice approximated on-site interaction given by Eq. (1.76) gives good results (dashed lines).

decreases rapidly with increasing distance, which is similar to the result obtained for J_{ij}, we observe that the interaction strength between two atoms on the same site increases with increasing potential depth. This is due to the higher localization of the Wannier function, which is reflected in the overlap integral of U_{ij}. The interaction between two atoms on the same site is known as the *on-site interaction*.

Within the deep lattice approximation we obtain the analytical expression of the on-site interaction

$$U \approx \sqrt{\frac{8}{\pi}} k_L a \left(\frac{V_0}{E_R}\right)^{\frac{3}{4}} E_R, \tag{1.76}$$

which is also in good agreement with the on-site interaction obtained through calculation of the exact Wannier functions.
The resulting Hamiltonian is known as the *Bose-Hubbard model*

$$\hat{H} = -\mu \sum_i \hat{n}_i - J \sum_{\langle ij \rangle} (\hat{b}_i^\dagger \hat{b}_j + \hat{b}_j^\dagger \hat{b}_i) + \frac{U}{2} \sum_i \hat{n}_i (\hat{n}_i - 1) \tag{1.77}$$

and describes a bosonic many-body system trapped in an optical lattice, where atoms tunnel between nearest neighboring sites with hopping amplitude J and interact with other atoms on the same site with strength U [59]. Here $\langle ij \rangle$ denotes a pair of nearest neighbors. Rather than an experimental parameter, the chemical potential μ is a theoretical tool to adjust the number of trapped atoms. Note that this Hamiltonian is obtained within the single-band approximation. The inclusion of higher Bloch bands leads to a multiband version of the model, which in some situations can be mapped back to an effective single-band Hamiltonian [60–62]. The single-band approximation however is reasonable for the range of parameters considered in this work as the band gap between the lowest and the second band is sufficiently large compared to the parameters of the model, thus leaving higher Bloch bands mostly unoccupied.
The Bose-Hubbard model possesses a high tunability of its parameters in cold atom realizations. The hopping amplitude is usually controlled through variation of the lattice depth, while the on-site interaction can be tuned through Feshbach resonances, with which the scattering length can be adjusted and the on-site interaction made attractive ($U < 0$) or repulsive ($U > 0$) [63–65].
The Bose-Hubbard model with repulsive on-site interaction has been investigated in many studies. Since the on-site interaction favors localized atoms in the lattice, while a large hopping amplitude implies that the atoms are delocalized, the interplay between both processes at various fillings of the lattice is a non-trivial problem.
Due to the intuitive nature of the Hamiltonian, it is easy to describe additional processes present in the system through inclusion of appropriate expressions and simple modification of already existing terms without tedious derivation. These variations of the model are referred to as *extended Bose-Hubbard model* and allow to investigate novel quantum phases not captured by the plain Bose-Hubbard model.

1.6 Phases of bosonic quantum gases

In this section, we discuss and understand the physics behind each of the quantum phases arising due to the competition between the different processes in bosonic gases trapped in hypercubic optical lattices. Some of these phases possess an exact analytical description in limiting cases, while the many-body ground state of others can only be retrieved from numerical computation with the corresponding Hamiltonian.
For the sake of introducing all quantum phases relevant for this work, we introduce a simple extended Bose-Hubbard model. Since the Bose-Hubbard model does not break lattice translation symmetry, i.e. translation of the system by a lattice vector does not change the Hamiltonian, we include an additional repulsive, long-range interaction term. The extended Bose-Hubbard model reads

$$\hat{H} = -\mu \sum_i \hat{n}_i - J \sum_{\langle ij \rangle} (\hat{b}_i^\dagger \hat{b}_j + \hat{b}_j^\dagger \hat{b}_i) + \frac{U}{2} \sum_i \hat{n}_i (\hat{n}_i - 1) + V \sum_{\langle ij \rangle} \hat{n}_i \hat{n}_j \tag{1.78}$$

with the additional nearest neighbor interaction term with strength $V > 0$. Note that $V = 0$ yields the plain Bose-Hubbard model. For a given set of parameters μ, J, U and V

we are able to compute the ground state, i.e. the eigenstate with the lowest energy, of the system.

1.6.1 Mott insulator

In the limiting case $J/U \to 0$, which is known as the atomic limit, and no long-range interaction $V = 0$, the system is best described by a homogeneous distribution of highly localized atoms. These states are known as the *Mott insulators* (MI) and further described by their filling n, i.e. the amount of atoms per site, and for N lattice sites thus read

$$|\Psi_{\mathrm{MI}}(n)\rangle = \prod_{i=1}^{N} |n_i = n\rangle = \prod_{i=1}^{N} \frac{(\hat{b}_i^\dagger)^n}{\sqrt{n!}} |0\rangle \tag{1.79}$$

Due to the localization of the atoms, the filling only takes integer values $n \in \mathbb{Z}$. The energy of a MI can be calculated through the Hamiltonian Eq. (1.78)

$$E_{\mathrm{MI}}(n) = \langle \Psi_{\mathrm{MI}}(n)| \hat{H} |\Psi_{\mathrm{MI}}(n)\rangle = -N(\mu n - \frac{U}{2} n(n-1)) \tag{1.80}$$

and through comparison of the energies for different fillings, we find the parameter regime for which a MI with filling n represents the ground state of the system

$$|\Psi_{\mathrm{MI}}(n)\rangle \to n - 1 < \frac{\mu}{U} < n \tag{1.81}$$

The MI is phase incoherent, i.e. the state is invariant under a global phase shift. This is not too surprising as the original Hamiltonian itself possesses a $U(1)$ symmetry meaning that the transformation $\hat{b}_i \to \hat{b}_i e^{i\theta_j}$ and $\hat{b}_j^\dagger \to \hat{b}_j^\dagger e^{-i\theta_j}$ does not change the Hamiltonian.
As a way to further understand and classify the quantum phases, we introduce the single-particle density matrix

$$\rho_{ij} = \langle \Psi| \hat{b}_i^\dagger \hat{b}_j |\Psi\rangle \tag{1.82}$$

for a general many-body state $|\Psi\rangle$, which gives a measure of the correlation between two lattice sites i and j in the system. For the MI the density matrix becomes

$$\begin{aligned} \rho_{kl} &= \langle \Psi_{\mathrm{MI}}| \hat{b}_k^\dagger \hat{b}_l |\Psi_{\mathrm{MI}}\rangle = \prod_{ij} {}_j\langle m|\hat{b}_k^\dagger \hat{b}_l |n\rangle_i \\ &= \prod_{ij} \sqrt{m}\sqrt{n}\, {}_j\langle m-1|n-1\rangle_i \delta_{il}\delta_{jk} \\ &= \prod_{ij} \sqrt{m}\sqrt{n}\delta_{mn}\delta_{ij}\delta_{il}\delta_{jk} \\ &= n\delta_{kl} \end{aligned} \tag{1.83}$$

The density matrix becomes diagonal with n as its only elements. This alludes to the fact that the atoms are highly localized and thus do not influence lattice sites away from their own.

1.6.2 Superfluid

In the opposite limiting case $U/J \to 0$, the atoms are delocalized and condensed into the lowest single-particle state, forming a Bose-Einstein condensate. The exact wave-function reads in this limit

$$|\Psi_{\mathrm{SF}}\rangle = \frac{1}{\sqrt{n!}}\Big(\frac{1}{\sqrt{N}}\sum_{i=1}^{N}\hat{b}_i^\dagger\Big)^n|0\rangle \tag{1.84}$$

where the filling can take non-integer values $n \in \mathbb{R}$. These phases are called *superfluid* (SF) and the state of each site is given by a superposition of Fock states. Compared to the MI for which the filling represents the amount of atoms on a lattice site, SF phases do not possess well-defined atom numbers on each site and thus only the probability distribution of atom numbers can be determined. The probability $p(n_i)$ of finding n_i atoms on a lattice site for a SF phase is given by

$$p(n_i) = |\langle n_i|\Psi_{\mathrm{SF}}\rangle|^2 \tag{1.85}$$

By using the multinomial formula

$$\Big(\sum_{i=1}^{N}\hat{b}_i^\dagger\Big)^n = \sum_{\sum_i n_i = N}\frac{N!}{\prod_i n_i}\prod_k(\hat{b}_k^\dagger)^{n_i} \tag{1.86}$$

we rewrite the wave function of the SF phase as

$$|\Psi_{\mathrm{SF}}\rangle = \sum_{\sum_i n_i = N}\sqrt{\frac{n!}{N^n\prod_i n_i}}\,|n_i\rangle \tag{1.87}$$

Using the rewritten wave function for the probability distribution

$$p(n_i) = |\langle n_i|\Psi_{\mathrm{SF}}\rangle|^2 = \frac{n!}{(n-n_i)!}\frac{(N-1)^{n-n_i}}{N^n}\frac{1}{n_i!} \tag{1.88}$$

and applying the Stirling formula $n! \approx \sqrt{2\pi n}n^n e^{-n}$ leads us to

$$p(n_i) = e^{-\bar{n}}\frac{\bar{n}^{n_i}}{n_i!} \tag{1.89}$$

We see that the probability distribution of the atom number is given by a Poisson distribution in the limiting case. Other quantum states with the same distribution are *coherent states* and using their definition, we obtain an alternative form of the condensate wave function

$$|\Psi_{\mathrm{SF}}\rangle = \prod_i e^{-\frac{\bar{n}}{2}}\sum_{n_i=0}^{\infty}\frac{\alpha^{n_i}}{\sqrt{n_i!}}|n_i\rangle = \prod_i|\alpha_i\rangle \tag{1.90}$$

with the coefficient $\alpha = \sqrt{n}e^{i\phi}$, which is the eigenvalue of the eigenvalue equation $\hat{b}_i|\alpha_i\rangle = \alpha|\alpha_i\rangle$. The single-particle density matrix can now be easily determined through the

coherent state description and

$$\begin{aligned}\rho_{kl} &= \langle \Psi_{\mathrm{SF}} | \, \hat{b}_k^\dagger \hat{b}_l \, | \Psi_{\mathrm{SF}} \rangle \\ &= \prod_{ij} \langle \alpha_i | \, \hat{b}_k^\dagger \hat{b}_l \, | \alpha_j \rangle \\ &= \prod_{ij} \langle \alpha_i | \, \alpha_i^* \alpha_j \, | \alpha_j \rangle \\ &= n\end{aligned} \tag{1.91}$$

Through the derivation we gain several important insights on SF phases. First, since the wave function can be written as a coherent state, the delocalized atoms are phase-coherent and each SF phase can be uniquely identified by the common phase of each boson. Furthermore, SF phases do not have a $U(1)$ symmetry and hence are not invariant under a global phase shift. This is unexpected as the Hamiltonian itself is $U(1)$-symmetric. The broken symmetry of the SF phase can also be understood in the context of particle number conservation [66]. As a conserved atom number in a system is a consequence of $U(1)$ symmetry and the coherent state violates this conservation law, since it is invariant to adding or removing a particle, the $U(1)$ symmetry has to be broken. As the SF phase breaks a symmetry otherwise present in the Hamiltonian, we refer to this as *spontaneous symmetry breaking*.
Another intriguing aspect of SF phases is the single-particle density matrix, which has non-vanishing off-diagonal terms. The density matrix element ρ_{ij} can be understood as a measure of phase coherence between two atoms on lattice site i and j and in SF systems does not diminish with distance between these two lattice sites. The presence of non-zero off-diagonal terms is called *off-diagonal long-range order* (ODLRO) and is related to the single-particle wave functions of each atom: At the temperatures typical for optical lattice experiments their de-Broglie wavelength increases and the atoms hereby delocalize over many lattice sites. Through the overlap of all waves the atom become phase coherent over long distances, which reflects in ODLRO.
Note that while in the limiting case the condensate wave function Eq. (1.90) represents the SF phase well, condensation and superfluidity imply different properties of a system. While a BEC is characterized by the macroscopic occupation of the energetically lowest quantum state at vanishing temperatures $T \approx 0$, superfluidity refers to the frictionless flow of particles. Thus they are generally not directly related to one another and therefore neither mutually exclusive nor inclusive [67]. In the context of bosonic quantum gases however the *Landau criterion* establishes a link between both physical phenomena [68–70]. To this end we consider an impurity in a BEC moving with a certain velocity. In order for the movement of the impurity to be frictionless its velocity has to be below the *Landau critical velocity* given by the energy of a single elementary excitation ϵ_p with BEC momentum p as $v_c = \min_p(\epsilon_p / p)$ [71, 72]. In layman's terms it means that flow of an impurity without any loss of kinetic energy is only achievable if the velocity does not excite the underlying BEC and thus depends on the energy of these elementary excitations. For an interacting BEC with small momentum the dispersion relation of these elementary excitations can be approximately given by the Bogoliubov phonons and thus scales as

$\epsilon_p \propto U^{1/2}$. This implies that in the limit of a non-interacting BEC $U \to 0$ the critical velocity vanishes and hereby the system does not possess any superfluidity. Therefore even though we consider the limit $U/J \to 0$ we always require a finite interaction strength in order to call the obtained phase a SF. Experimentally the critical velocity was observed by moving a laser through a BEC and measurement of heating in dependence on the velocity [73]. We thus conclude that while ODLRO is a characteristic feature of a condensate it serves also as a property of the SF phase in combination with a finite interaction strength.
Note that the above-defined many-body wave function Eq. (1.90) is only exact in the limiting case $U/J \to 0$ and therefore the experimentally accessible single-particle density matrix may exhibit features of the MI.

1.6.3 Density wave

We consider the previously discussed atomic limit $J/U \to 0$, but with finite long-range interaction $J/V \to 0$. Similar to the MI, the ground state is given by highly localized atoms, although the repulsive long-range interaction leads to an inhomogeneous distribution of the atoms within the optical lattice. The corresponding wave function reads

$$|\Psi_{\mathrm{DW}}\rangle = \prod_{i=1}^{N} |n_i\rangle_i = \prod_{i=1}^{N} \frac{(\hat{b}_i^\dagger)^{n_i}}{\sqrt{n_i!}} |0\rangle \tag{1.92}$$

and the quantum phase is referred to as a *density wave* (DW). These DW phases exhibit unique crystalline order given by the type of long-range interaction and have thus to be characterized their spatial modulation. In the case of nearest neighbor interaction, the long-range interaction leads to a checkerboard-type distribution of two integer atom numbers [74,75].
The single-particle density matrix is obtained through

$$\begin{aligned}
\rho_{kl} &= \langle \Psi_{\mathrm{DW}}| \hat{b}_k^\dagger \hat{b}_l |\Psi_{\mathrm{DW}}\rangle = \prod_{ij} {}_j\langle m_j| \hat{b}_k^\dagger \hat{b}_l |n_i\rangle_i \\
&= \prod_{ij} \sqrt{m_k}\sqrt{n_l}\, {}_j\langle m-1|n-1\rangle_i \delta_{il}\delta_{jk} \\
&= \prod_{ij} \sqrt{m_k}\sqrt{n_l}\delta_{mn}\delta_{ij}\delta_{il}\delta_{jk} \\
&= n_l \delta_{kl}
\end{aligned} \tag{1.93}$$

and reflects the inhomogeneous distribution of localized atoms. Since the Hamiltonian itself is invariant under translation by a lattice vector, the DW phase has so-called *spontaneously broken lattice translational symmetry*. Due to the periodic density modulation of DW phases they are often defined by a finite (diagonal) *long-range order* (LRO) [76,77].

1.6.4 Supersolids

The most peculiar quantum phase discussed in this work is not obtained by any if the above-mentioned limiting case. The *supersolid* (SS) combines the crystalline properties of

the DW phase and the finite condensation of the SF, and intuitively is given when the long-range interaction strength and hopping amplitude are in the same order of magnitude. Although no exact wave function has been formulated yet, these phases are characterized by a spontaneously broken $U(1)$-symmetry as well as a translational symmetry.
Whether SS phases exist or not has been an intensively researched field in the last decades. After the initial theoretical speculations and descriptions of phases exhibiting both LRO and ODLRO [78–81], a long time passed until SS phases were finally experimentally observed. In recent years SS phases have finally been appeared in first experiments involving either quantum gases with cavity-mediated long-range interaction in the continuum [82] and on the lattice [83,84], and with dipolar BECs [85–87] and therefore definite proof of their existence. Subsequently the study of SS phases became popular and lead to many further research on their properties such as the ability to form quantized vortices [88] and their phase rigidity [89,90].
Note that in the scope of this thesis all subsequent discussions about and mentions of SS phases refer to many-body states, which spontaneously break the lattice translational symmetry, and are therefore called *lattice supersolids* [91]. This specification is important, since lattice supersolids may not exhibit spontaneously broken translational symmetry in a continuous system and benefits from the discretization of real-space through the trapping an optical lattices.

Classification of phases

These quantum phases are unique in their physics and can thus be provided with distinct quantities, through which their identification becomes possible. We first define a set of local order parameters, namely the *condensate order parameter* $\phi_i = |\langle \hat{b}_i \rangle|$ and the *occupation number* $n_i = \langle \hat{b}_i \rangle$. Since we are also expecting inhomogeneous phases to be many-body ground states, it is necessary to introduce the corresponding spatially averaged order parameters $\bar{\phi} = 1/N \sum_{i=1}^{N} \phi_i$ and $\bar{n} = 1/N \sum_{i=1}^{N} n_i$ for a system with N sites. Another important quantities in the context of inhomogeneous phases are staggered order parameters ϕ_{stag} and n_{stag}. However no general expression for these order parameters exist, since they are individually defined by the expected density modulation in the system.
Through the average condensate order parameter we identify whether a many-body state exhibits insulating or SF properties. We can further differentiate between the homogeneous and inhomogeneous phases through the staggered occupation number, as it becomes finite if a crystalline structure is present. The culmination of these properties, with which a many-body state can be classified, are written in Tab. 1.1.

Note that for homogeneous systems the local order parameters are equal to their averaged counterparts. Although the staggered order parameters are in theory very useful, the expected superlattice unit cell of the crystalline structure has to be known beforehand. For example, a checkerboard-type ordering of local order parameters can be determined through a finite staggered occupation number defined as $O_{\text{stag}}^{\text{ch}} = 1/N \sum_{i=1}^{N} (-1)^{x(i)+y(i)} O_i$,

Phase	$\bar{n}$	$\bar{\phi}$	n_{stag}	ϕ_{stag}
MI	$\mathbb{N}$	0	0	0
SF	$\mathbb{R}$	$\mathbb{R}$	0	0
DW	$\mathbb{Q}$	0	$\mathbb{Q}$	0
SS	$\mathbb{R}$	$\mathbb{R}$	$\mathbb{R}$	$\mathbb{R}$

Table 1.1: Classification table for the identification of quantum phases in the plain and extended Bose-Hubbard model. These phases Mott-insulating (MI), superfluid (SF), density wave (DW) and supersolid (SS) phases.

while striped configurations would be identified through $O_{\text{stag}}^{\text{str}} = 1/N \sum_{i=1}^{N} (-1)^{x(i)} O_i$ with $O \in \{\phi, n\}$. For the computation of phase diagrams, which can possibly exhibit many unique crystalline structures, it becomes necessary to check the spatial distribution of the local order parameters.

1.6.5 Phase diagrams

The phase diagrams of the plain and extended Bose-Hubbard model are obtained through computation of the ground state wave function (see Appendix A.1) and subsequent identification of the quantum phase based on order parameters (see Appendix B.1). This allows to investigate the interplay between the different terms contained in the Hamiltonian beyond the limiting cases. In the following, we introduce the coordination number z through which we are able to depict the phase diagrams independently on the dimension of the optical lattice. The coordination number refers to the number of neighbors and in a hypercubic lattice simplifies to $z = 2d$, where d is the dimension of the lattice (see Section 3.2).
For $V = 0$, we obtain the well-known phase diagram of the Bose-Hubbard model (see Fig. 1.10). The domains of MI phases of different fillings are called *Mott lobes*. Their shape can be understood through the degeneracy of two MI phases at integer values of $\mu/U \in \mathbb{N}$ and vanishing hopping: In the atomic limit an excitation of a MI with filling n is gapped due to the energy cost of adding a particle $E_+ = Un - \mu$ or removing a particle $E_- = U(n-1) + \mu$. This also implies that the energy associated with adding a particle in a MI phase with filling n is equal to the energy of removing a particle in a MI with filling $n+1$. Beyond the atomic limit however the energy gap can be bridged through a finite hopping, which the results in condensation of the system. Since the gap is marginally small around integer values of μ/U, only a small hopping amplitude J is necessary. Larger hopping amplitudes are necessary between two integer values of μ/U, where the energy gap reaches its largest values. We therefore obtain the lobe shaped phase transitions between the MI and SF regimes.

While the phase diagram was determined without any external potential, most optical lattice experiments work with an additional harmonic confinement. In our numerical

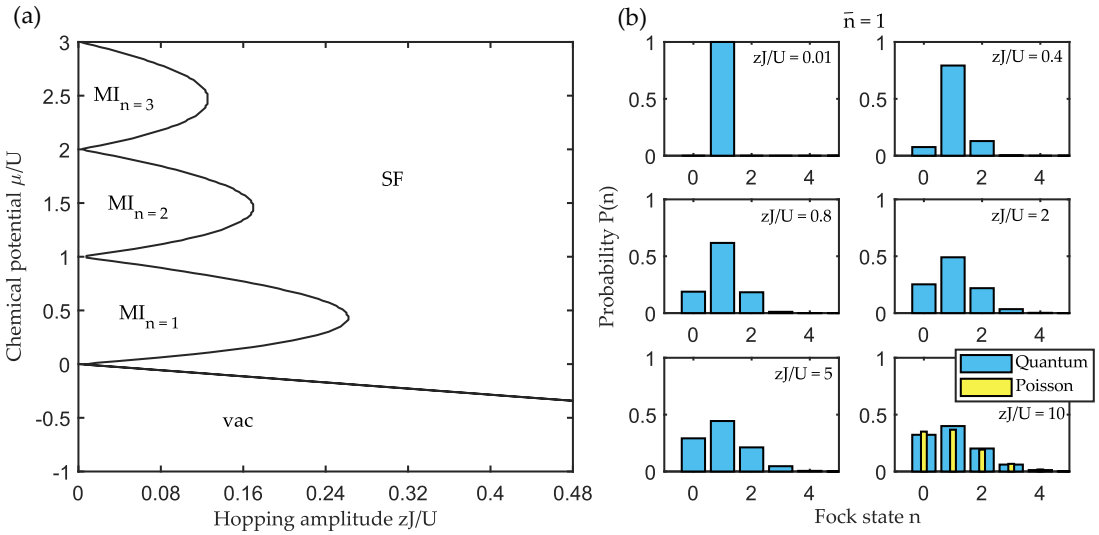

Figure 1.10: (a) Phase diagram of the Bose-Hubbard model for various hopping amplitudes zJ/U and chemical potentials μ/U. The phase diagram consists of integer-filling MI phases, a SF regime and a vacuum regime. The boundary between the Mott-insulator phases and the SF regime is lobe-shaped. (b) The occupation probability $P(n) = |\langle n|\Psi\rangle|^2$ of a Fock state n for different ratios zJ/U for fixed filling $\bar{n} = 1$. For on-site interactions larger than the hopping amplitude the probability $P(n = \bar{n}) = 1$ hints at the integer-filling of the system, which indicates a Mott-insulating phase. Increasing the hopping amplitude leads to a more spread distribution of the propabilities $P(n)$. For very large hopping amplitudes the probability distribution is close to the Poisson distribution, consistent with a SF phase.

calculations, we take the harmonic potential into account by making the chemical potential site dependent, i.e. $\mu \to \mu_i$. The chemical potential of a given site decreases in dependence on the distance to the center of the harmonic confinement, which ultimately leads to a vanishing population of the sites far away from the center. For given parameters we determine the ground state inside the potential and visualize the results through the expectation values $\langle \hat{n}_i \rangle$ and $\langle \hat{b}_i \rangle$. We observe ring-like shells with either constant filling and no condensation or decreasing filling and finite condensation, implying that the shell-structure is given by alternating MI and SF phases. This result is reflected in the phase diagram, since for a finite hopping amplitude a variation of the chemical potential leads to various quantum phase transitions between both types of phases. Due to its shape this result is known as the *wedding cake* (see Fig. 1.11) and has been observed in many experiments.

Now we consider the extended Bose-Hubbard model with finite long-range interaction strength $V > 0$. Through computation of the phase diagram at different values of zV/U, we investigate the additional competition in the system (see Figure 1.12). At $zV/U = 1$

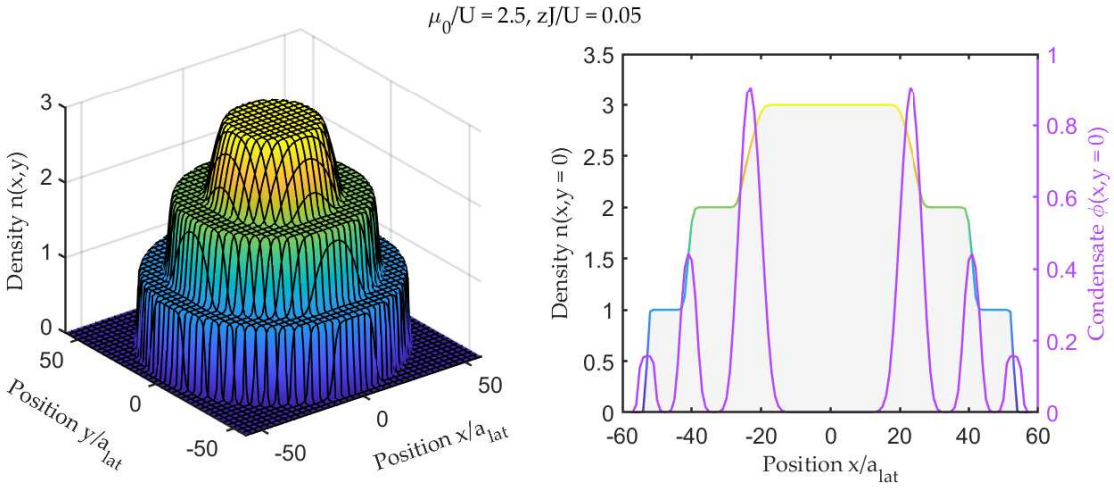

Figure 1.11: The well-known wedding cake shape of the density $n(x, y)$ for a system with external harmonic confinement given by $\mu_i = \mu_0 + \tilde{\mu}(x^2 + y^2)$. Each plateau of the wedding cake distribution corresponds to a Mott-insulator. These are commonly referred to as Mott-insulator shells due to their ring-shape. Calculation of the condensate order parameter ϕ hints at the presence of SF regions between various Mott-insulating shells. The width of these regions depends on the hopping amplitude zJ/U and vanishes in the atomic limit. The alternating shells of Mott-insulating and SF phases reflect the shape of the phase boundaries (see Fig. 1.10).

the on-site and the long-range interaction are of equal strength, which is reflected in the phase diagram through the lobes alternating between MI and checkerboard DW phase. The occupation numbers of the two different sublattices are n and $n-1$, which results in DW phases of average filling $\bar{n} = n - 1/2$ between a MI with filling n and one with filling $n-1$. Furthermore checkerboard supersolid regimes emerge at the tip of the DW lobes. Although these supersolid phases exhibit an occupation number distribution similar to their insulating counterpart of the adjacent DW lobe, the atoms are delocalized and therefore finite condensation emerges. For large enough hopping amplitudes, the crystalline order breaks down and the system exhibits a SF phase.

For large $zV/U = 1.5$, the long-range interaction dictates the phase diagram and regimes of checkerboard phases dominate. The Mott-insulator lobes are suppressed due to the strong nearest neighbor repulsion and the checkerboard DW phase are characterized by one site with filling n and an empty site, which leads to the same average filling obtained for smaller zV/U. Furthermore, due to the larger long-range interaction the regime of coexistence between condensation and crystalline order increases and thus the supersolid regime extends. Its boundary to the SF phase is shifted to much larger hopping amplitudes, which increase with increasing filling, i.e. increasing chemical potential.
These phase diagrams are helpful to get an intuition on the origin of the different quantum

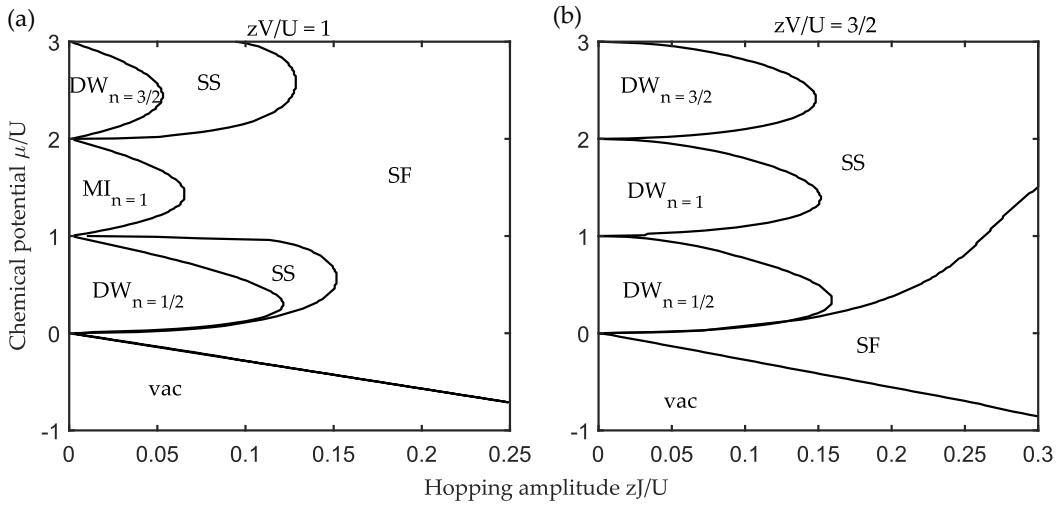

Figure 1.12: Phase diagrams of the extended Bose-Hubbard model with (a) moderate long-range interaction $zV/U = 1$ and (b) larger long-range interaction $zV/U = 1.5$. In addition to the Mott-insulating and SF phases, the phase diagram exhibits inhomogeneous DW and supersolid phases. For moderate long-range interaction the lobe-shaped phase boundaries are still present to a certain extent, although Mott-lobes of integer filling are now seperated by DW regimes, which are surrounded by supersolid regimes. Larger long-range interaction however renders the Mott-insulator energetically unfavorable and thus all lobes arising consist of DW phases. The supersolid regime extends to higher hopping amplitudes with increasing chemical potential. At a critical hopping amplitude there is a transition from the supersolid regime to a SF regime.

phases and the corresponding models have been well studied in many works. Although theoretically we are able to identify these phases from calculation of expectation values through the wave function, experimental observation is no trivial task. In the following, we discuss the experimental techniques and apparatus for probing quantum gases and detecting phases.

1.7 Detection of quantum phases

The two most commonly used and efficient techniques to experimentally detect the various quantum phases are the *time-of-flight measurements* (TOF) [92, 93] and the *quantum gas microscope* [94–96]. Both techniques probe the real-space atomic distribution of the bosonic quantum gas, however rely on different types of imaging and possess different ranges of applicability.
We first introduce the notion of time-dependence, since until now the description of the Hamiltonian and its ground states has been purely stationary. We first define the

time-dependent field operator at time t

$$\hat{\Psi}(\boldsymbol{r},t) = \sum_i w_0(\boldsymbol{r}-\boldsymbol{R}_i,t)\hat{b}_i \tag{1.94}$$

with the time-dependent Wannier function $w_n(\boldsymbol{r}-\boldsymbol{R}_i,t) = \hat{U}^\dagger(t)w_n(\boldsymbol{r}-\boldsymbol{R}_i,0)\hat{U}(t)$ obtained through unitary time evolution given by the operator $\hat{U}(t)$. Its momentum-space counterpart can be obtained through the Fourier transform and reads

$$\hat{\Psi}(\boldsymbol{k},t) = \int d\boldsymbol{r} e^{-i\boldsymbol{k}\boldsymbol{r}}\hat{\Psi}(\boldsymbol{r},t) \tag{1.95}$$

We now are able to define the time-dependent real-space distribution of atoms

$$\begin{aligned} n(\boldsymbol{r},t) &= \langle\hat{\Psi}^\dagger(\boldsymbol{r},t)\hat{\Psi}(\boldsymbol{r},t)\rangle \\ &= \sum_{ij} w_0^*(\boldsymbol{r}-\boldsymbol{R}_j,t)w_0(\boldsymbol{r}-\boldsymbol{R}_i,t)\langle\hat{b}_j^\dagger\hat{b}_i\rangle \end{aligned} \tag{1.96}$$

and the time-dependent momentum-space distribution

$$\begin{aligned} n(\boldsymbol{k},t) &= \langle\hat{\Psi}^\dagger(\boldsymbol{k},t)\hat{\Psi}(\boldsymbol{k},t)\rangle \\ &= \iint d\boldsymbol{r}d\boldsymbol{r}' e^{-i\boldsymbol{k}(\boldsymbol{r}-\boldsymbol{r}')}\langle\hat{\Psi}^\dagger(\boldsymbol{r}',t)\hat{\Psi}(\boldsymbol{r},t)\rangle \\ &= |w_0(\boldsymbol{k},t)|^2\sum_{ij} e^{i\boldsymbol{k}(\boldsymbol{r}_i-\boldsymbol{r}_j)}\langle\hat{b}_j^\dagger\hat{b}_i\rangle \end{aligned} \tag{1.97}$$

where the time-dependent momentum-space Wannier function is given by

$$w_0(\boldsymbol{k},t) = \frac{1}{(2\pi)^3}\int d\boldsymbol{r} e^{-i\boldsymbol{k}\boldsymbol{r}}w_0(\boldsymbol{r},t) \tag{1.98}$$

Both distributions are given by Wannier functions in their respective spaces and the single-particle density matrix $\rho_{ij} = \langle\hat{b}_j^\dagger\hat{b}_i\rangle$, and are thus related.

1.7.1 Time-of-flight measurement

The basic idea behind time-of-flight (TOF) measurements is simple: Through Feshbach resonances the interactions are initially switched off and the trapping potential of a quantum gas is turned off, which leads the released atomic cloud to fall due to gravity and freely expand. During this expansion the atoms are able to interfere with each other. After some time, an absorption image of the cloud is taken, which reveals their interference pattern and thus the quantum phase of the cloud before its release.
The quench-type time evolution of the atoms after turning off the interaction and the trap is only given by the kinetic term through the operator $\hat{U}(t) = e^{-i\hat{H}_{\text{kin}}t/\hbar}$ at $t > 0$. As the kinetic Hamiltonian $\hat{H}_{\text{kin}} = \hbar^2\boldsymbol{k}^2/(2m)$ is diagonal in momentum space, it is useful to define the time-dependent real-space Wannier function

$$w_0(\boldsymbol{r},t) = \frac{1}{(\sqrt{2\pi})^3}\int d\boldsymbol{k} e^{i(\boldsymbol{k}\boldsymbol{r}-\frac{\hbar k^2}{2m}t)}w_0(\boldsymbol{k},t=0) \tag{1.99}$$

through their Fourier transform. Within the stationary phase approximation [97], the integral reveals

$$w_0(\boldsymbol{r},t) \approx \left(\frac{m}{i\hbar t}\right)^{3/2} w_0(\boldsymbol{k},t) e^{i\frac{m}{2\hbar t}\boldsymbol{r}^2} \tag{1.100}$$

with which we rewrite the real-space distribution

$$n(\boldsymbol{r},t) = \left(\frac{m}{\hbar t}\right)^3 |w_0(\boldsymbol{k},t)|^2 S(\boldsymbol{k},t) \tag{1.101}$$

with the structure factor

$$S(\boldsymbol{k},t) = \sum_{ij} e^{i\boldsymbol{k}(\boldsymbol{R}_i-\boldsymbol{R}_j)} e^{-i\frac{m}{2\hbar t}(\boldsymbol{R}_i^2-\boldsymbol{R}_j^2)} \langle \hat{b}_j^\dagger \hat{b}_i \rangle \tag{1.102}$$

While the first exponential function in the structure factor is a discrete Fourier transform, we also obtain an additional phase shift given by the phase factor $\approx \boldsymbol{R}_i^2 - \boldsymbol{R}_j^2$, which bears strong resemblance to the Fresnel distance [92]. If the latter vanishes the structure factor would allow us to rewrite the real-space distribution through its Fourier transform. Unfortunately the phase factor can not be engineered to be zero, however, since its amplitude decreases with time, it is possible to define a time t_c for which the phase factor is negligible. We therefore differentiate between the near-field ($t \ll t_c$) and far-field ($t_c \gg t$) regimes.

Near-field and far-field approximation

Within the near-field regime the interference pattern is not purely given by the momentum-space distribution and features a more complex pattern, while in the far-field regime the atomic cloud has expanded enough for the additional phase factor to be vanishing and thus allows for detection of the quantum phase through absorption imaging. The threshold time t_c can be quantitatively determined through estimation of the magnitude of the phase factor. Since the single-particle density matrix elements $\langle \hat{b}_j^\dagger \hat{b}_i \rangle$ limit the sum in dependence on the coherence length ζ_0 of the initial quantum states, the largest contributions are given by the coherence length itself through

$$\frac{m}{2\hbar t}(\boldsymbol{R}_i^2 - \boldsymbol{R}_j^2) \sim \frac{m\zeta_0 L}{\hbar t} \tag{1.103}$$

with the characteristic size L of the atomic cloud before turning off the trap. We thus identify the threshold value for the distinction between near-field and far-field regime through

$$t_c = \frac{m\zeta_0 L}{\hbar} \tag{1.104}$$

Note that t_c therefore depends on the quantum phase of the bosonic gas before its release. While localized phases such as MI or DW phases have short coherence lengths and can thus enter the far-field regime fast, phase coherent states like SF or supersolid phases require longer expansions as the coherence length is typically of the same order of magnitude as

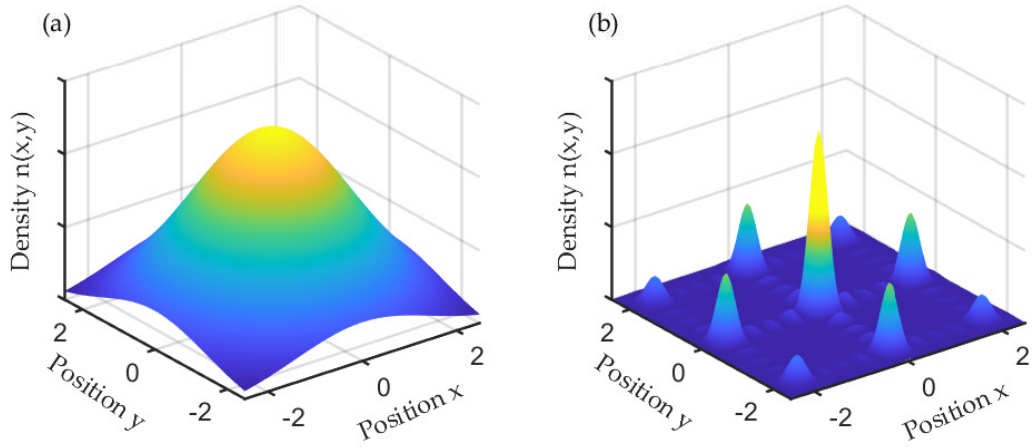

Figure 1.13: The density distribution of (a) a Mott-insulator and (b) a SF phase expected in a TOF measurement. The Gaussian shape distribution of the initial Mott-insulator originates from the diffusion of the decoherent atoms after turning off the trap. A SF however displays an interference pattern due to the free falling phase-coherent atoms. The sharp peak at the center indicates a high collective occupation of the lowest energy mode and the spacing of the emerging peaks can be traced back to the lattice vector $\boldsymbol{K}$ of the reciprocal space.

the characteristic system size, i.e. $\zeta_0 \approx L$.
In the far-field regime the additional phase factor vanishes and the real-space density distribution after TOF is thus given by

$$n(\boldsymbol{r}, t) = \left(\frac{m}{\hbar t}\right)^3 n(\boldsymbol{k}, t) \tag{1.105}$$

from which we see that the free time evolution of the quantum gas reveals its momentum-space distribution directly before being released from the trap.

Measurements

With the previously defined single-particle density matrix we are able to theoretically predict the expected absorption images based on the initial quantum phase. The most

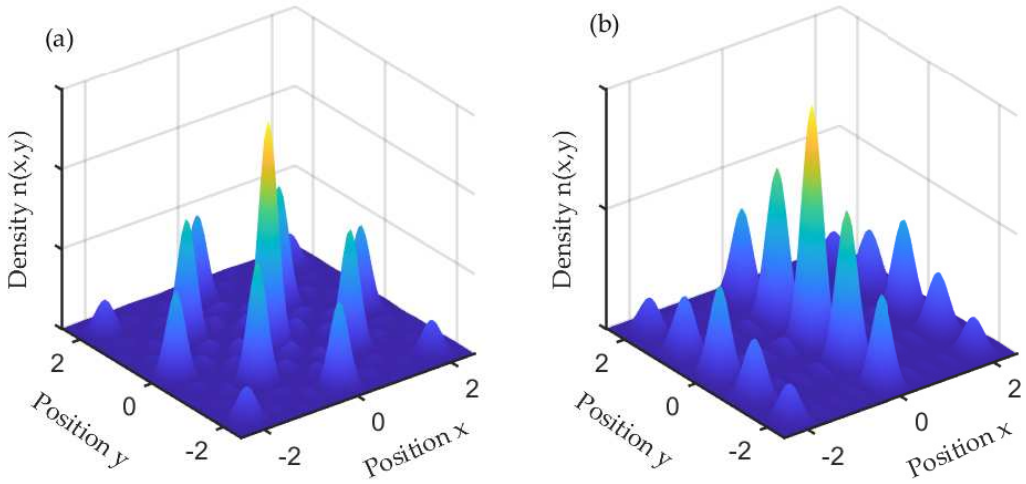

Figure 1.14: Density distribution of (a) checkerboard and (b) a striped supersolid phase appearing through TOF measurements. Similar to the density distribution of the SF, we obtain peaks given by the lattice vector of the reciprocal lattice due to the coherent nature of the atoms. Furthermore, additional peaks emerge due to the phase being inhomogeneous. The peaks not only distinct the SF from the supersolid, but their distributions also characterizes the superlattice unit cell of the crystalline phase, since the distribution is defined through the reciprocal lattice vector $\boldsymbol{G}$ of the superlattice.

simple case, namely the MI, yields

$$\begin{aligned} n_{\mathrm{MI}}(\boldsymbol{r}, t \gg t_c) &= \left(\frac{m}{\hbar t}\right)^3 |w_0(\boldsymbol{k}, t)|^2 \sum_{ij} e^{i\boldsymbol{k}(\boldsymbol{R}_i - \boldsymbol{R}_j)} n\delta_{ij} \\ &= \left(\frac{m}{\hbar t}\right)^3 |w_0(\boldsymbol{k}, t)|^2 \sum_{i} n \\ &= \left(\frac{m}{\hbar t}\right)^3 |w_0(\boldsymbol{k}, t)|^2 nN \end{aligned} \tag{1.106}$$

which is merely a rescaled Wannier function. This is not surprising, since the atoms are not phase coherent and their wave packets therefore just expand with time. The shape of the distribution broadens as time increases, which further validates the diffusive expansion of the atoms (see Fig. 1.13 (a)). The quasi momentum-distribution corresponding to this absorption image is flat, i.e. $n(\boldsymbol{k}, t) = N$, which can be traced back to the atomic limit considered for the MI: The atoms due to the large on-site interaction are highly localized, which implies due to the uncertainty relation a strong momentum-space delocalization. Furthermore, the on-site interaction induces the population of higher momentum modes $|\boldsymbol{k}| > 0$.

On the other hand, the condensate wave function given by Eq. (1.90) leads to

$$\begin{aligned} n_{\mathrm{SF}}(\boldsymbol{r}, t \gg t_c) &= \left(\frac{m}{\hbar t}\right)^3 |w_0(\boldsymbol{k}, t)|^2 \sum_{ij} e^{i\boldsymbol{k}(\boldsymbol{R}_i - \boldsymbol{R}_j)} n \\ &= \left(\frac{m}{\hbar t}\right)^3 |w_0(\boldsymbol{k}, t)|^2 n \sum_{ij} e^{i\boldsymbol{k}(\boldsymbol{R}_i - \boldsymbol{R}_j)} \\ &= \left(\frac{m}{\hbar t}\right)^3 |w_0(\boldsymbol{k}, t)|^2 n \delta(\boldsymbol{k} = \boldsymbol{K}) \end{aligned} \tag{1.107}$$

The density distribution is characterized by peaks with an enveloping Wannier function (see Fig. 1.13 (b)). The constructive interference at $\boldsymbol{k}$ not only reflects the phase coherent overlap of the atoms, but also hints at the fact that all atoms populate the energetically lowest single-particle mode, i.e. form a BEC, which is possible due to their bosonic nature. The other peaks arise from the periodicity of the reciprocal lattice.
Although DW phases exhibit an unique crystalline order, their TOF absorption image does not differ from the one obtained for MI phases, i.e. $n_{\mathrm{MI}}(\boldsymbol{r}, t \gg t_c) = n_{\mathrm{DW}}(\boldsymbol{r}, t \gg t_c)$, since the evolution of both is given by a diffusive expansion and thus it is not possible to distinguish these phases within TOF. While for systems with no spontaneously broken lattice translational symmetry, such as the plain Bose-Hubbard model, it is safe to associate these absorption images to MI states. The distinction only becomes relevant in the addition of long-range interacting processes.
Finally for supersolid phases, the structure of the real-space distribution is given by

$$n_{\mathrm{SS}}(\boldsymbol{r}, t \gg t_c) \propto \left(\frac{m}{\hbar t}\right)^3 |w_0(\boldsymbol{k}, t)|^2 (\delta(\boldsymbol{k} = \boldsymbol{K}) + \lambda \delta(\boldsymbol{k} = \boldsymbol{G})) \tag{1.108}$$

where $\boldsymbol{G}$ is the reciprocal lattice vector of the superlattice unit cell, which describes the crystalline order of the supersolid phase. The density distribution is similar to the one of a SF, although with peaks at $\boldsymbol{k} = \boldsymbol{G}$ with modified amplitude λ. These additional features emphasize the spatially dependent phase coherence and are unique to each spatial modulation of the condensate wave function (see Fig. 1.14).

Through TOF experiments, it was possible to experimentally investigate the phase diagram of the Bose-Hubbard model and determine the Mott-SF transition [98] (see Fig. 1.15). TOF measurements are to this day an important experimental tool to monitor phase transitions and detect physical phenomena. Unfortunately the inability to distinguish between MI and DW phases renders this measurement method insufficient for the determination of phase diagrams of systems, which can potentially break lattice translational symmetry. Furthermore the absorption imaging does not allow for high real-space resolution and thus only relies on the interference pattern. Finally, it is worth mentioning that in the time-evolution considered for the theoretical derivation of the real-space density distributions we disregarded possible interactions between the atoms during the expansion. While several studies have found that, for experimentally relevant on-site interaction strengths, the incorporation of interaction in the time evolution does not affect the real-space distribution too importantly, it is possible that at the scattering resonance higher Bloch bands

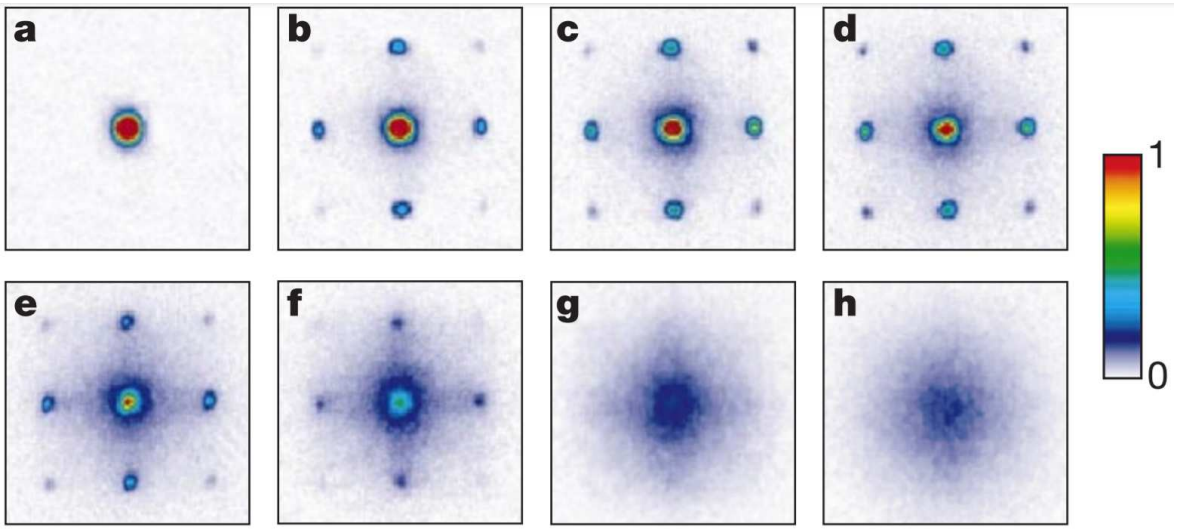

Figure 1.15: TOF measurements obtained for a bosonic quantum gas trapped in a lattice with depth **a** $V_0/E_R = 0$, **b** $V_0/E_R = 3$ **c** $V_0/E_R = 7$ **d** $V_0/E_R = 10$ **e** $V_0/E_R = 13$ **f** $V_0/E_R = 14$ **g** $V_0/E_R = 16$ and **h** $V_0/E_R = 20$. The interference pattern obtained for shallow lattices is obtained due to the interference of the coherent atoms of a SF. For deep enough lattices a MI phase arises, which can be identified through the image of an expanding atomic cloud of incoherent bosons. Reprinted figure with permission from [98].

become populated and the single-band approximation does not hold anymore, leading to a reduced visibility of the interference pattern [99].

1.7.2 Quantum gas microscope

Although various experimental techniques have been able to generate single-site resolved images for systems with large periodicity, achieving resolutions necessary for the single-site imaging in optical lattice experiment with typical lattice spacing proved to be a challenging task. While the absorption imaging allowed for a resolution of several microns in two-dimensional systems [100, 101], the fluorescence images were realized in three-dimensional lattices with similar spacing [102]. The peak resolution of fluorescence techniques has been reached in a one-dimensional lattice with a spacing of 433 nm, although the image was only obtained thanks to a dilute filling of the system.
Single-site resolved images became accessible through a recently developed experimental apparatus called quantum gas microscope, which combines fluorescence imaging with a hemispherical lens. Within the quantum gas microscope the atoms are loaded in two-dimensional optical lattices by creation of a three-dimensional lattice and ramp up of the lattice depth in one dimension, hereby disconnecting two-dimensional layers. The atoms are then illuminated from the side and the scattered fluorescence photons are detected

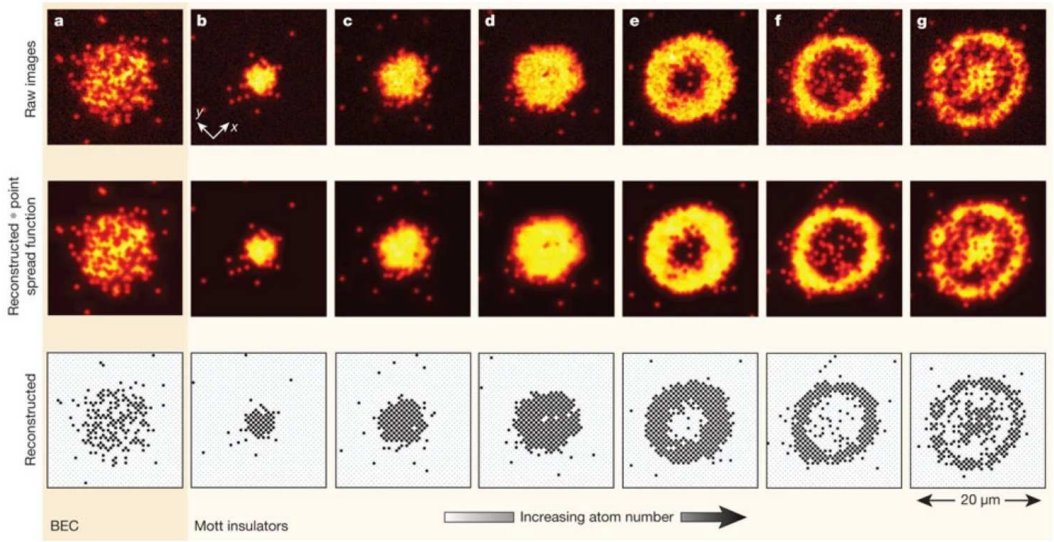

Figure 1.16: Single-site resolved images of atoms trapped in an optical lattice with external harmonic confinement obtained through a quantum gas microscope. While a BEC exhibits a seemingly random distribution within the external trap, the atoms of MI phases prefer to localize in the center of the harmonic potential after preparation. Increasing the number of atoms leads to more occupied sites. Beyond a certain filling the sites in the center start to be doubly occupied, which leads to empty circles in the single-site fluorescence images due to two-body loss processes. Further increasing hints at sites occupied with three atoms at the center, while two Mott shells with single and double filling appear. Reprinted figure with permission from [105]. © 2010 by Springer Nature.

by objective lenses [94, 95]. Through a deconvolution algorithm the original density distribution of the atom configuration is reconstructed with very high fidelity [103]. The resolution obtained is about 600 nm, which matches the lattice spacings relevant in optical lattice experiments and thus allow for single-site resolved imaging. Note that although the first quantum gas microscopes were conceived for probing two-dimensional layers, an extension of the microscope through which fluorescence imaging of single atoms in three-dimensional optical lattices has been established [104].
The fluorescence imaging however leads to dissipative, light-assisted collisions. The fluorescence light induces photoassociation, which leads to the pairwise loss of atoms. Since the time scale of the dissipation is far shorter than the necessary illumination time of the microscope, the system is left with zero or one atom per site. The quantum gas microscope thus not only allows for single-site resolution, but also possesses single-atom sensitivity.
With the quantum gas microscope single-site-resolved imaging of MI phases have been recently accessible. While the insulating phases with filling n can be determined from a single fluorescence image, condensed phases are reconstructed through many images, since

the corresponding occupation of a site follows the Poisson distribution. Then through number statistics using a Poisson distribution modified according to the single-atom sensitivity, it is possible to determine their filling.
Since all discussed quantum phases can be determined through the quantum gas microscope, it is even possible to image the wedding cake density distribution [105,106] (see Fig. 1.16). In the atomic limit, the image exhibits a ring-shaped shell structure of MI phases with decreasing filling up to the edge of the system. Due to the single-atom sensitivity, the MI phase with odd filling result in a bright shell while even filling is detected through an empty shell. Thus we are able to visualize the wedding cake through rings with filling alternating between zero and one. Beyond the atomic limit, the image additional displays non-integer filling due to the emerging SF phases.
Since then the quantum gas microscope was used for many purposes, such monitoring dynamics and losses [107], investigation of quantum of spin system [108] and study blocking mechanism in many-body systems [109], and has thus proven to be a powerful apparatus.

Chapter 2

Rydberg atoms

The goal of this chapter is to discuss all properties of Rydberg states, atoms and ensembles relevant in the scope of this thesis. We start in Section 2.2 with the important properties of the Rydberg state. We establish the valence electron wave function and examine the energy levels of an excited atom. We then discuss the dipole transitions between different Rydberg state and the hereby obtained selection rules. Additionally we examine the main mechanisms behind the finite lifetime of Rydberg states, namely the spontaneous emission and the blackbody radiation. In Section 2.3 we analyze the different types of interactions between Rydberg atoms. We complete the description through the full potential landscape of pair states composed of Rydberg atoms and elaborate on molecular bound state arising due to avoided crossings within these potentials. In Section 2.4 we explain the coherent coupling of atoms in their electronic ground state to Rydberg states and the idea behind the Rydberg-dressing. We examine the phases of few Rydberg-dressed atoms to further understand the effect of the interatomic interaction and conclude with the characteristic physical phenomena observed in Rydberg ensembles, namely the emergence of crystalline structures and the avalanche dephasing mechanism.

2.1 Introduction

Rydberg atoms are to be found in many different fields of research thanks to their exaggerated properties and unique applicability. For example in the context of quantum simulation, ensembles of Rydberg atoms offer a platform for the investigation of solid state physics [110,111] and spin lattices [112,113], since the energy scales of Rydberg states are orders on magnitude larger than the typical energies of such systems, beneficial for experimentally probing diverse many-body phenomena. Furthermore quantum gates for the sake of quantum computation have already been realized with Rydberg atoms trapped in optical lattices and optical tweezers [114–117]. Despite already possessing many applicabilities, Rydberg ensembles are not yet fully understood, as collective phenomena and universal scaling behavior are still in the focus of current research. The properties of Rydberg states and a single atom coupled to those such states however have been

thoroughly studied for many years and provide a perfect starting point on the way to understand many-body physics involving Rydberg atoms.

2.2 Properties of Rydberg atoms

Rydberg states are high-lying electronic states energetically close to the ionization threshold. The excitation of an atom to such states greatly increases the distance of an electron to the nuclei and thus drastically enhances its properties. The potential of the nuclei surrounded by the core electrons resembles at great distances the potential of an hydrogen atom, which is why they are commonly referred to as hydrogen-like. The large distance of the electron induces a high dipole moment, through which the atoms gain high sensitivity and exaggerated response to external electromagnetic fields. Although the properties of the different Rydberg states are not directly tunable the desired magnitude of these properties can be chosen via selection of the chemical element and energy level. Further tunability exists in the context of coherent coupling between the electronic ground state and a Rydberg state of an atom.
In the following section, we discuss the elementary properties of Rydberg levels such as the wave function, the orbital radius of the distant electron and the associated lifetimes.

2.2.1 Valence electron wave function and energy levels

Due to its increased size and hydrogen-like character, it is possible to derive a few quantities either quantum mechanically or within a classical picture. Although the latter provides qualitatively good values through simpler calculations, it is important to understand the quantum mechanical nature of the Rydberg atom. Starting point is the wave function of the Rydberg atom valence electron, which can be determined through the time-independent Schrödinger equation

$$-\frac{\hbar^2\nabla^2}{2m}\Psi(\boldsymbol{r}) + V(\boldsymbol{r})\Psi(\boldsymbol{r}) = E\Psi(\boldsymbol{r}), \tag{2.1}$$

where E is the energy and $V(\boldsymbol{r})$ is the Coulomb potential felt by the valence electron in the orbit far from the nucleus

$$V(\boldsymbol{r}) = -\frac{1}{4\pi\varepsilon_0}\frac{e^2}{r}. \tag{2.2}$$

Due to the radial symmetry of the atom, the wave function in spherical coordinates can be seperated as

$$\Psi_{n,\ell,m}(\boldsymbol{r}) = R_{n,\ell}(r)Y_\ell^m(\theta,\phi) \tag{2.3}$$

with the position $\boldsymbol{r} = (r,\theta,\phi)$ in spherical coordinates, the radial wave function $R_{n,\ell}(r)$ and the spherical harmonics $Y_\ell^m(\theta,\phi)$, which are the solutions of the angular Schrödinger equation. Here we introduce quantum numbers with which we can define the individual Rydberg states, namely the principal quantum number n, the orbital quantum number ℓ and the magnetic quantum number m. The orbital quantum number $\ell = 0,1,2,...$ defines the $S,P,D,...$-orbitals. The last two quantum numbers appear in the Schrödinger equation

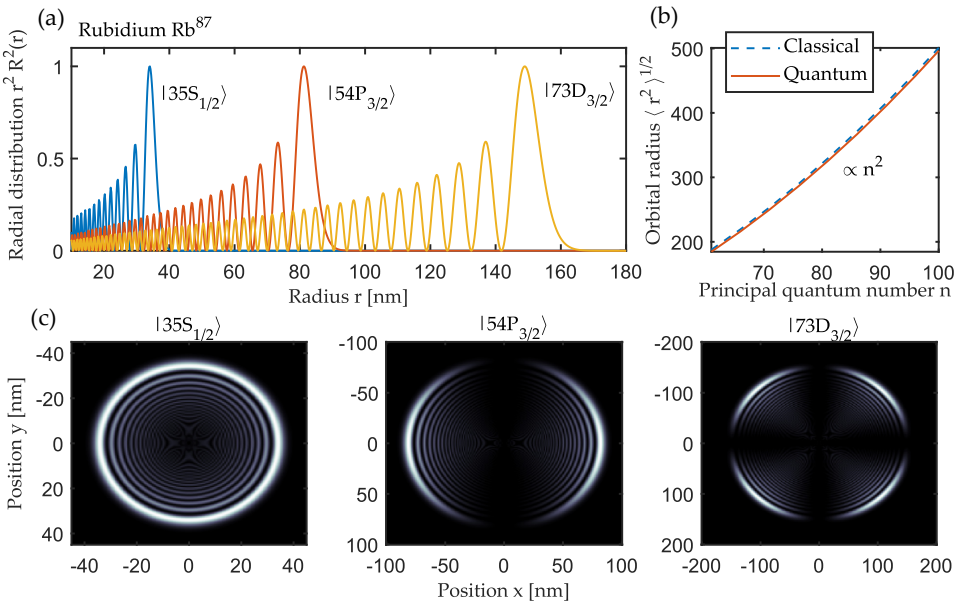

Figure 2.1: (a) Radial distribution $\langle rR(r)\rangle^2$ given by the radial wave function $R_{n,\ell}(r)$ for various states with different principal quantum number n and orbital quantum number ℓ. The overall shape of the radial wave function does not seem to be dependent on the orbital quantum number. (b) The characteristic radius of the electron orbital determined through the radial wave function (solid line) and the Bohr model (dashed lines), which grows quadratic with increasing principal quantum number. Both lines are in excellent agreement despite the difference in their nature. (c) Probability distribution of the electron given by $\Psi^2(x, y, z = 0)$ for various principal quantum numbers and orbital quantum numbers. Additionally to the larger sizes of the atom due to the increasing principal quantum number, we find characteristic shapes of the probability distribution dependent on the orbital quantum number. Although not mentioned, these shapes also depend on the magnetic quantum number m.

through the kinetic term in spherical coordinates and each set of these numbers represents a solution of the equation.
The radial Schrödinger equation

$$-\frac{\hbar^2}{2\mu}\left[\frac{1}{r^2}\frac{\partial}{\partial r}\left(r^2\frac{\partial R_{n,\ell}(r)}{\partial r}\right)-\frac{\ell(\ell+1)R_{n,\ell}(r)}{r^2}\right]+V(r)R_{n,\ell}(r)=E_nR_{n,\ell}(r) \tag{2.4}$$

contains the term $\ell(\ell+1)/r^2$, which reflects the kinetic energy of the different angular degrees of freedom. As an effective potential it wards off electrons with non-zero angular momentum $\ell \neq 0$ from collapsing into the nuclei [118]. The solutions of the radial Schrödinger equation are thus also dependent on the orbital quantum number and the

radial wave functions are given by

$$R_{n,\ell}(r) = -\sqrt{\left(\frac{2Z}{na_\mu}\right)^3 \frac{(n-\ell-1)!}{2n(n+\ell)!}} e^{\frac{-Zr}{na_\mu}} \left(\frac{2Zr}{na_\mu}\right)^\ell L_{n-\ell-1}^{(2\ell+1)}\left(\frac{2Zr}{na_\mu}\right) \tag{2.5}$$

with the generalized Laguerre polynomials $L_{n-\ell-1}^{(2\ell+1)}$. The corresponding energies are

$$E_n = -\left(\frac{Z^2\mu e^4}{8\epsilon_0^2 h^2}\right)\frac{1}{n^2} = -\frac{Rhc}{n^2} \tag{2.6}$$

where we define the *Rydberg constant* $R = \frac{Z^2\mu e^4}{8\epsilon_0^2 h^3 c}$. The corresponding unit of energy is $1Ry \equiv Rhc \approx 13.6$ eV, which is the characteristic value associated with the binding energy of an electron to the nuclei in a hydrogen atom. The binding energies E_n become smaller as the principal quantum number increases and become vanishing for very large quantum numbers, which makes atoms excited to high Rydberg states highly susceptible to ionization. Despite the strong similarity between the Coulomb potentials of the hydrogen atom and the Rydberg atom, it is important to add a correction to the binding energy to take the shielding effect of the core electrons into account through

$$E_{n,\ell} = -\frac{Rhc}{(n-\delta_{n,\ell})^2} = \frac{Rhc}{(n^*)^2}. \tag{2.7}$$

Here we introduced the *effective principal quantum number*, which is simply a modification of the principal quantum number by the *quantum defect* $\delta_{n,\ell}$ [119,120] (see Fig. 2.2). Since the binding energy decreases with increasing effective principal quantum number, the density of Rydberg states increases close to the ionization boundary and the transition frequency between the Rydberg states of principal quantum number n and $n \pm 1$ decreases as

$$\omega_{n\ell,n'\ell'} \propto \frac{1}{(n^* \pm 1)^2} - \frac{1}{(n^*)^2} \propto \frac{1}{(n^*)^3} \tag{2.8}$$

The distance of the electron to the nuclei can be obtained through the radial wave function $R_{n,\ell}(r)$. Calculation of the radial probability density $r^2 R_{n,\ell}(r)$ yields a wide probability distribution, which maximizes at the outer edge and becomes wider with growing principal quantum numbers. The dependence of the average distance on the principal quantum number can be determined through computation of the average of the radial probability distribution and gives $\sqrt{\langle r^2 R_{n,\ell}^2(r)\rangle} \propto n^2$. This result can be understood within the Bohr model, in which the electron orbitals are defined by the equilibrium of forces [122]. For an electron on a circular orbit with radius r, the attractive Coulomb force of the nuclei and the centrifugal force are equal

$$\frac{1}{4\pi\varepsilon_0}\frac{e^2}{r^2} = \frac{mv^2}{r} \tag{2.9}$$

The orbital momentum of the electrons is quantized, i.e. $mvr = n\hbar$, and thus the solutions of the equations are given through

$$r_n = a_0 n^2 \tag{2.10}$$

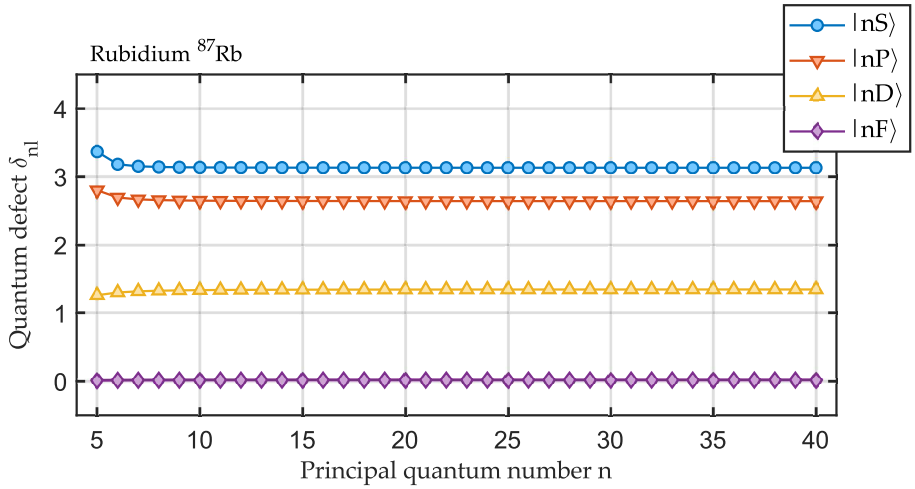

Figure 2.2: Quantum defects δ_{nl} for various principal quantum numbers n and orbital quantum number ℓ. As the principal quantum number increases the quantum defects saturate towards constant values. Calculations for these results were performed with the help of the package `Alkali Rydberg Calculator` [121].

with the Bohr radius $a_0 = \frac{4\pi\varepsilon_0\hbar^2}{e^2 m_e}$, which is the distance between the nuclei and electron of a hydrogen atom in its ground state. The obtained relation matches the one obtained with the radial probability distribution. Furthermore, calculation of r and $\sqrt{\langle r^2 R_{n,\ell}^2(r)\rangle}$ yield strikingly equal results despite being derived in completely different pictures, which can be attributed to the strong resemblance to the hydrogen atom and the typical large length scales associated to Rydberg atoms (see Fig. 2.1).

2.2.2 Dipole transitions

Optical transitions between two Rydberg states can be induced through an external electromagnetic field given by $\boldsymbol{E}(t) = E_0 e^{-i(\omega t - \boldsymbol{k}\boldsymbol{r})}\hat{\boldsymbol{e}}_{\boldsymbol{r}}$, where $\boldsymbol{k} = 2\pi/\lambda$. Given a frequency ω close to the transition frequency between two Rydberg states, the electromagnetic field induces an oscillating drive between these two states. The corresponding time-dependent Hamiltonian $\hat{H} = \hat{\boldsymbol{d}}\boldsymbol{E}(t)$, where $\boldsymbol{d} = e\boldsymbol{r}$ is the dipole operator, can be simplified through the *dipole approximation*, where we assume that the wavelength $\boldsymbol{k}$ is much larger then the size of the atom, i.e. $\boldsymbol{k}\boldsymbol{r} \ll 1$ [118, 123]. The transition rate between two states $\Psi_{n,\ell,m}(\boldsymbol{r})$ and $\Psi_{n',\ell',m'}(\boldsymbol{r})$, the rate with which a photon of energy $\hbar\omega$ is absorbed by the atom and hereby transitions from one state to another, is given by

$$W_{n\ell m}^{n'\ell'm'} = \frac{\pi e^2}{2\hbar}|E_0|^2\left|\int \mathrm{d}^3\boldsymbol{r}\Psi_{n',\ell',m'}^*(\boldsymbol{r})\boldsymbol{r}\Psi_{n,\ell,m}(\boldsymbol{r})\right|^2 \equiv \frac{\pi e^2}{2\hbar}|E_0|^2|\langle n'\ell'm'|\boldsymbol{r}|n\ell m\rangle|^2, \quad (2.11)$$

where we adopt the ket-notation of the wave function $|n\ell m\rangle$. The first integral is known as the transition moment integral and its braket-version is the so-called *dipole matrix element*,

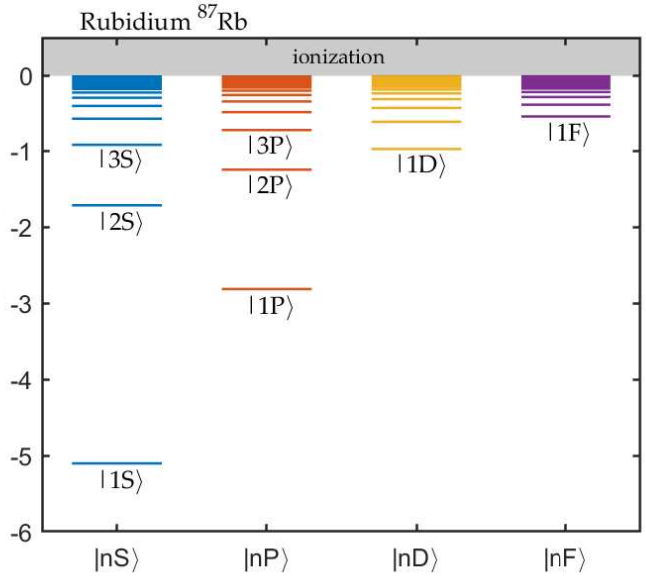

Figure 2.3: Energy levels of the different orbitals ℓ for various principal quantum numbers n for Rubidium ^{87}Rb. The higher lying levels are densely distributed and their binding energy are vanishingly small, which renders highly excited atoms susceptible to ionization. Calculations for these results were performed with the help of the package `Alkali Rydberg Calculator` [121].

which is written as a product

$$\langle n'\ell'm'|\boldsymbol{r}|n\ell m\rangle = \mathcal{R}^{n'\ell'}_{n'\ell'}\mathcal{I}_{\text{ang}} \tag{2.12}$$

with the radial integral

$$\mathcal{R}^{n'\ell'}_{n'\ell'} = \int_0^\infty R_{n',\ell'}(r) r R_{n,\ell}(r) r^2 \mathrm{d}r \tag{2.13}$$

and the angular integral

$$\mathcal{I}_{\text{ang}} = \int_0^{2\pi}\int_0^{\pi} (Y^{m'}_{\ell'}(\theta,\phi))^* \hat{\boldsymbol{r}} Y^m_\ell(\theta,\phi)\sin(\theta)\mathrm{d}\theta\mathrm{d}\phi \tag{2.14}$$

Both integrals offer a valuable information about the dipole matrix element: Due to the previously determined proportionality of the radial wave function and the independent angular wave function, we obtain an overall scaling of the dipole matrix element $\langle n'\ell'm'|\boldsymbol{r}|n\ell m\rangle \propto (n^*)^2$. This is intuitive, since the orbital radius of the electron assumes the same scaling and the dipole moment is defined through the distance between two charges. Furthermore, the radial integral is always finite, albeit small if the two radial wave functions of different quantum numbers have an inconsiderable overlap, e.g. for very different principal quantum numbers $n' \gg n$. On the other hand, the angular integral

is only finite for certain pair of quantum numbers, which follow strict criteria. Unless these criteria are met the angular integral vanishes and the transition rate becomes zero, hereby making the transition forbidden.
The criteria for a finite angular integral are known as the *selection rules*. They describe conditions for the allowed transitions, which can be derived by computation of the angular integral.

Selection rules

We restrict the discussion to the orbital quantum number ℓ and the magnetic quantum number m, although selection rules for other quantum numbers such as the total angular momentum quantum number or the spin quantum number exist [118, 124].
The orbital quantum number ℓ has to change upon transition. Since the Coulomb potential used to determine the wave function does not change upon rotation or reflection, the wave function can be chosen to have well-defined parities and thus invariant under parity transformation. By application of the parity operator on the angular wave function, more specifically the dipole operator, one finds that the invariance is only guaranteed for $\Delta\ell = \ell - \ell' = \pm 1$ [118, 124].
For the magnetic quantum number m the selection rule depends on the polarization of the electromagnetic field. Calculation of the angular integral with linear polarized light leads to the constraint $\Delta m = m - m' = 0$, while for circular polarized light we obtain the criteria $\Delta m = \pm 1$, where the sign depends on the kind of circular polarized light. For unpolarized light none of these constraints apply.
Although these selection rules inhibit certain experimentally valuable coupling schemes, the existence of forbidden and allowed transitions is a vital part of many cooling methods as these can be exploited to optically pump an atom in desired hyperfine states (see Section 1.2).

2.2.3 Lifetimes

Another characteristic property of Rydberg atoms is their lifetime, which is determined through spontaneous decay and blackbody-induced transitions. The latter is surprising, since we do not expect Rydberg states to be thermally populated in a gas of atoms in their electronic ground states and thus assume thermal effects to be negligible. But at high principal quantum numbers the transition frequency between energetically neighboring Rydberg states becomes marginal such that transitions are enabled, i.e. $\hbar\omega_{n\ell,n'\ell'} < k_B T$ even at room temperature. Furthermore the dipole matrix element is particularly large for neighboring Rydberg states due to the large overlap between the radial wave functions. Thus we define the effective lifetime of a Rydberg state through the rate of the spontaneous emission $\Gamma_0 = 1/\tau_0$ and the blackbody-induced transition rate $\Gamma_{\mathrm{BBR}} = \tau_{\mathrm{BBR}}$, which we write as

$$\frac{1}{\tau} = \Gamma_0 + \Gamma_{\mathrm{BBR}} = \frac{1}{\tau_0} + \frac{1}{\tau_{\mathrm{BBR}}} \tag{2.15}$$

In order to understand the overall scaling of the lifetime with principal quantum number we investigate both the decay rates associated with spontaneous emission and the black-body radiation by themselves, and finally discuss the regimes in which either of these processes dominates.

Spontaneous emission

An important quantity appearing in the context of photo-absorption and -emission are the *Einstein A coefficients* $A_{n\ell}^{n'\ell'}$, which describe the transition rates between the states $|n\ell\rangle$ and $|n'\ell'\rangle$ due to spontaneous emission [125]. The coefficients are related to the dipole matrix elements and read

$$A_{n\ell}^{n'\ell'} = \frac{4e^2\omega_{n\ell n'\ell'}^3}{3\hbar c^3}\frac{\ell_{\max}}{2\ell+1}|\left\langle n'\ell'm\right|\hat{r}\left|n\ell m\right\rangle|^2 \tag{2.16}$$

with $\ell_{\max}$ being the larger of the two involved quantum numbers ℓ and ℓ'. Note, that we drop the quantum number m in the description of the coefficient since we expect spontaneous decay to be independent of m. The spontaneous decay rate of a state $|n\ell\rangle$ is then simply given by the sum of all coefficients with lower lying $|n'\ell'\rangle$ states

$$\frac{1}{\tau_0} = \sum_{E_{n,\ell}>E_{n',\ell'}} A_{n\ell}^{n'\ell'}. \tag{2.17}$$

It is usual to introduce the *average oscillator strength* $\bar{f}_{n\ell}^{n'\ell'}$ at this point as

$$\bar{f}_{n\ell}^{n'\ell'} = \frac{2}{3}\omega_{n\ell n'\ell'}\frac{\ell_{\max}}{2\ell+1}|\left\langle n'\ell'm\right|\hat{r}\left|n\ell m\right\rangle|^2. \tag{2.18}$$

The average oscillator strengths are dimensionless and follow the sum rule $\sum_{n'\ell'}\bar{f}_{n\ell}^{n'\ell'} = 1$ for $\ell' \in \{\ell \pm 1\}$. It is therefore possible to get quantitatively good results on the distribution of transitions rates through the calculation of just a few oscillator strengths.
We thus rewrite the Einstein A coefficient as

$$A_{n\ell}^{n'\ell'} = \frac{2e^2\omega_{n\ell n'\ell'}^2}{\hbar c^3}\bar{f}_{n\ell}^{n'\ell'} \tag{2.19}$$

The overall scaling of the coefficient with the principal quantum number depends on whether the transition occurs between energetically close ($n \approx n'$) or distant ($n \gg n'$) Rydberg levels. In the first case, we can just use the previously obtained scalings of the transition frequency $\propto (n^*)^{-3}$ and the dipole matrix element $\propto (n^*)^2$ to obtain an overall scaling of

$$\tau_0^{n\gg n'} \propto (n^*)^5 \tag{2.20}$$

However, these are not the dominant transitions, since the transition rate increases with increasing transition frequency. Thus we consider the second case, where the spontaneous emission leads to a transition from a high-lying to a low-lying state (see Fig. 2.4 (a)). The previously obtained scaling of $\omega_{n\ell n'\ell'}$ is not valid anymore and its value approaches

the ionization energy. Furthermore the dipole matrix element for Rydberg states with differing wave function yields an $\propto (n^*)^{-3}$ scaling, which results in

$$\tau_0^{n\approx n'} \propto (n^*)^3 \tag{2.21}$$

As the second case gives a lower limit, it is commonly used as the scaling of the lifetime τ_0. Analytic calculation of the spontaneous decay rates only exist for hydrogen, while for other atoms, such as alkali-atoms, various numerical approaches have been established [126, 127].

Blackbody radiation

For the definition of the blackbody-induced transition rates we first introduce the Planck distribution

$$\bar{n}(\omega) = (\exp(\omega/k_B T) - 1)^{-1}, \tag{2.22}$$

which describe the average photon occupation number $\bar{n}(\omega)$ of each mode ω. The stimulated absorption and emission rate is related to the *Einstein B coefficient*

$$B_{n\ell}^{n'\ell'} = \bar{n}(\omega_{n\ell,n'\ell'}) A_{n\ell}^{n'\ell'}, \tag{2.23}$$

which is defined as the A coefficient rescaled with the photonic distribution. The blackbody-induced transition rate thus reads

$$\begin{aligned} \frac{1}{\tau_{\mathrm{BBR}}} &= \sum_{n'\ell'} B_{n\ell}^{n'\ell'} \\ &= \frac{2}{c^3} \sum_{n'\ell'} \omega_{n\ell,n'\ell'} \bar{f}_{n\ell}^{n'\ell'} \frac{\omega_{n\ell,n'\ell'}}{\exp(\omega_{n\ell,n'\ell'}/k_B T) - 1)} \end{aligned} \tag{2.24}$$

Note, that we are not limited to lower lying Rydberg levels and transitions to higher Rydberg levels are also allowed (see Fig. 2.4 (a)). Since these transitions are only relevant between neighboring, higher lying levels we solely consider the case $n \approx n'$. We can furthermore use the above-mentioned sum rule of the average oscillator strengths, which yields

$$\sum_{n'\ell'} \omega_{n\ell,n'\ell'} \bar{f}_{n\ell}^{n'\ell'} = \frac{2}{3(n^*)^2}. \tag{2.25}$$

We obtain an analytic expression of the blackbody transition rate

$$\frac{1}{\tau_{\mathrm{BBR}}} = \frac{4}{3(n^*)^5 c^3} \frac{1}{\exp(1/(n^*)^3 k_B T) - 1}, \tag{2.26}$$

which is in good agreement with experimentally observed transition rates [128, 129]. In the case of large $n^* \gg 1$ we approximate the the expression and obtain the simplified proportionality

$$\frac{1}{\tau_{\mathrm{BBR}}} \approx \frac{4 k_B T}{3(n^*)^2 c^3} \propto (n^*)^{-2}. \tag{2.27}$$

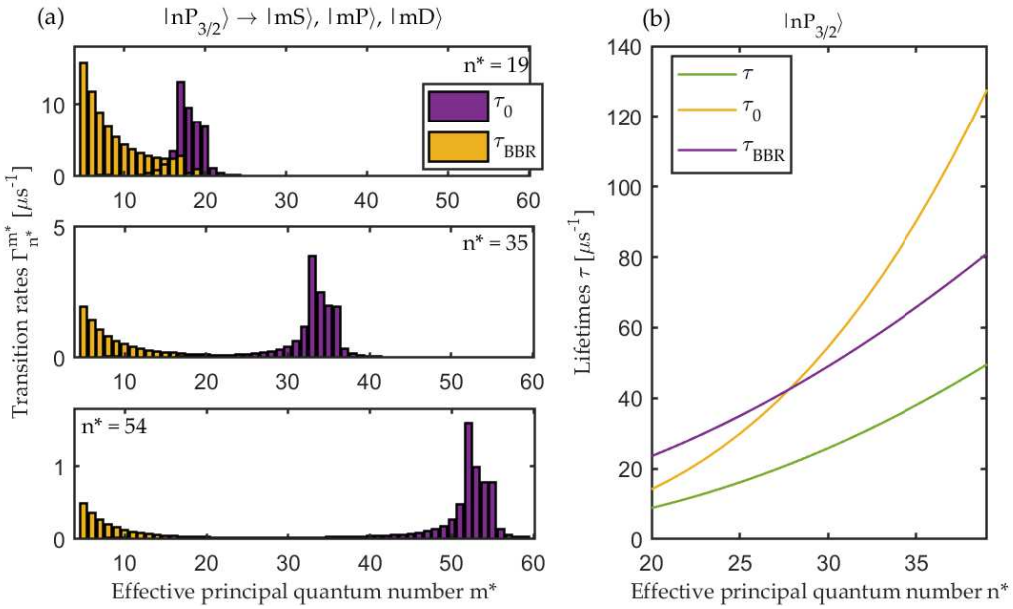

Figure 2.4: (a) Transition rates $\Gamma_{n^*}^{m^*}$ of a Rubidium ^{87}Rb in the $|nP_{3/2}\rangle$ state to $|mS\rangle$, $|mP\rangle$ and $|mD\rangle$ versus the effective principal quantum number m^* of the target state for different n^*. The radiative through spontaneous emission governs the transitions to lower lying states, while the blackbody radiation induces transitions to states with effective principal quantum number close to the original one. (b) Lifetimes given by the radiative decay τ_0 and by the blackbody radiation τ_{BBR}. The overall lifetime of an atom increases with the effective principal quantum number. Furthermore, radiative decay dominates the lifetimes for lower quantum numbers, while blackbody radiation governs the higher quantum number regime. Calculations for these results were performed with the help of the package `Alkali Rydberg Calculator` [121].

This approximation is valid for $n^* > 30$, but overestimates the transition rates below this value. Numerical methods also exist to determine the rates of the blackbody-induced transition, although these methods require high computational effort [130, 131].

Due to the two different scalings it is possible to define two regimes for n^* in which either the spontaneous decay or the blackbody-induced transitions dominate the effective lifetime (see Fig. 2.4 (b)), although the threshold value n_c^* depends on the numerous intrinsic properties of the atom and the temperature T. For smaller effective principal quantum numbers the spontaneous emission governs the overall lifetime of the Rydberg atom, i.e. $\tau \propto (n^*)^3$ for $n^* \ll n_c^*$, while large effective principal quantum number yield large blackbody induced transition rates, i.e. $\tau \propto (n^*)^2$ for $n^* \gg n_c^*$. Independently of the exact scaling, we find an increasing effective lifetime, which implies that Rydberg atoms are generally long-lived. Experimentally determined power laws of both types of lifetimes are in good agreement with the derived relations [132–134].

2.3 Interactions between Rydberg atoms

The ability of two highly-excited atoms to interact on large spatial scales arises through their vastly increased size and thus induced sensitivity to external electromagnetic fields. For two independent atoms, whose energy eigenstates are defined through the Hamiltonian $\hat{H}_0$, the long-range interaction acts as a perturbation in the complete Hamiltonian

$$\hat{H} = \hat{H}_0 + \hat{V} \tag{2.28}$$

The interaction Hamiltonian $\hat{V}$ modifies the energy levels E_0 of the unperturbed atoms and the shift can be determined through second-order perturbation theory

$$E = E_0 + \langle i,j|\,\hat{V}\,|i,j\rangle + \sum_{\substack{k\neq i\\ l\neq j}} \frac{|\,\langle i,j|\,\hat{V}\,|k,l\rangle\,|^2}{E_i + E_j - E_k - E_l} \tag{2.29}$$

for two atoms in the Rydberg states $|i\rangle$ and $|j\rangle$. Note, that we now simplify the ket-notation of the wave function and define for each state i a unique set of quantum numbers, i.e. $|i\rangle \equiv |n\ell m\rangle$. Here $|i,j\rangle$ denotes two atoms in states i and j.
In order to compute the induced shifts, it is important to specify the interaction. In a slightly simplified picture, both atoms can described by two point charges $+q$ and $-q$, representing the nuclei and the outer electron respectively, separated by distance $\boldsymbol{r}_1$ ($\boldsymbol{r}_2$) for the first (second) atom. While the Hamiltonian $\hat{H}_0$ takes into account the interaction between nuclei and electron of each atom individually, the interaction $\hat{V}$ describes the Coulomb interaction between all nuclei and electrons of both atoms

$$\hat{V} = \frac{e^2}{4\pi\epsilon_0}\Big(\frac{1}{|\boldsymbol{R}|} + \frac{1}{|\boldsymbol{R} - \hat{\boldsymbol{r}}_1 + \hat{\boldsymbol{r}}_2|} - \frac{1}{|\boldsymbol{R} - \hat{\boldsymbol{r}}_1|} - \frac{1}{|\boldsymbol{R} + \hat{\boldsymbol{r}}_2|}\Big) \tag{2.30}$$

Within the dipole approximation $|\boldsymbol{R}| \gg |\boldsymbol{r}_1|, |\boldsymbol{r}_2|$, it is possible to only consider the dipole moment of the field, which reduces the Coulomb interaction to the dipole-dipole contributions as

$$\hat{V}_{\text{dip}} = \frac{1}{4\pi\epsilon_0 R^3}\Big(\hat{\boldsymbol{d}}_1\hat{\boldsymbol{d}}_2 - 3(\hat{\boldsymbol{d}}_1\cdot\boldsymbol{e}_r)(\hat{\boldsymbol{d}}_2\cdot\boldsymbol{e}_r)\Big), \tag{2.31}$$

where $\hat{\boldsymbol{d}}_1$ ($\hat{\boldsymbol{d}}_2$) is the dipole operator of the first (second) atom.

2.3.1 Dipole-dipole interaction

The most general form of the dipole-dipole interaction is given by

$$\langle i,j|\,\hat{V}_{\text{dip}}\,|k,l\rangle = \frac{1}{4\pi\epsilon_0 R^3}\Big(\boldsymbol{d}_{ik}\boldsymbol{d}_{jl} - 3(\boldsymbol{d}_{ik}\cdot\boldsymbol{e}_r)(\boldsymbol{d}_{jl}\cdot\boldsymbol{e}_r)\Big) \tag{2.32}$$

with the dipole moment $\boldsymbol{d}_{mn} = \langle m|\,\hat{\boldsymbol{d}}_{1(2)}\,|n\rangle$ [135–138]. As we know from the previously discussed dipole matrix elements, only certain transitions are allowed by the selection rules. In order to describe the interaction between two atoms in state i and j we require

that the atoms after the interaction are in the same state, i.e. $i = k$ and $j = l$. Thus the dipole-dipole interaction is given by $\langle i(j)|\,\hat{r}\,|i(j)\rangle \equiv \langle n\ell m|\,\hat{r}\,|n\ell m\rangle$. However this is a forbidden transition, which implies a vanishing dipole moment $\boldsymbol{d}_{ii} = 0$ and thus no dipole-dipole interaction between two atoms in the same state.
The dipole-dipole interaction is finite, if the interaction induces a transition in both atoms, i.e. $i \neq k$ and $j \neq l$. In the presence of an external electric field, the special case $i = l$ and $k = j$ yields

$$\langle i,j|\,\hat{V}_{\text{dip}}\,|j,i\rangle = \frac{|\hat{\boldsymbol{d}}|^2}{4\pi\epsilon_0 R^3}(1 - 3\cos^2(\theta)). \tag{2.33}$$

Due to the electromagnetic field both atom align and thus $\boldsymbol{d} = \boldsymbol{d}_{ij} = \boldsymbol{d}_{ji}$ holds. Here we used $\hat{\boldsymbol{d}} \cdot \boldsymbol{e}_r = \cos(\theta)$ with $\cos(\theta)$ being the direction of the field. We see from the interaction in this form that the dipole-dipole interaction leads to an exchange of the Rydberg levels, which corresponds to energy transfer from one atom to another. This process is referred to as *dipolar exchange* [139–143].
With the known proportionality of the dipole moment $\boldsymbol{d} \propto (n^*)^2$, we obtain a scaling law of the dipole-dipole interaction term

$$V_{\text{dip}} \equiv \frac{C_3}{R^3} \propto \frac{(n^*)^4}{R^3}. \tag{2.34}$$

In the end, we find that the dipole-dipole interaction term is only finite in the case of energy transfer and thus the interaction between two atoms in the same state is only given in second-order by the perturbation theory.

2.3.2 Van-der-Waals interaction

The second-order shift of the energy eigenstates is given by

$$\sum_{\substack{j\neq i\\ k\neq i}} \frac{|\,\langle i,j|\,\hat{V}\,|k,l\rangle\,|^2}{\hbar(\omega_{ik} + \omega_{jl})}, \tag{2.35}$$

with the transition frequencies $\omega_{mn} = (E_m - E_n)/\hbar$. The interaction as a second-order process can be understood in the following way: Due to potential coupling obtained through finite dipole matrix elements, the overall energy shift of the unperturbed state i arises through the instantaneous transition from said state j or k and back. The atom stays in the same state i, but the virtual transition leads to an energy shift, which depend on the energy difference between i and j or k and the coupling strength. This transition process can also be formulated with the corresponding Hamiltonian

$$\hat{H}_{\text{vdW}} = \begin{pmatrix} 0 & \langle i,j|\,\hat{V}_{\text{dip}}\,|k,l\rangle \\ \langle k,l|\,\hat{V}_{\text{dip}}\,|i,j\rangle & \hbar(\omega_{ik} + \omega_{jl}). \end{pmatrix} \tag{2.36}$$

Assuming $|\hbar\omega_{mn}| \gg |V_{\text{dip}}|$, we determine the lower eigenenergy and hereby obtain the interaction strength between two atoms in state i and j separated by distance R

$$V_{\text{vdW}} \approx -\frac{|\boldsymbol{d}|^4}{32\pi^2\epsilon^2\hbar(\omega_{ik} + \omega_{jl})R^6}. \tag{2.37}$$

The second-order interaction is known as the *van-der-Waals interaction* and its scaling with the effective principal quantum number

$$V_{\mathrm{vdW}} \equiv \frac{C_6}{R^6} \propto \frac{(n^*)^{11}}{R^6} \tag{2.38}$$

hints at the magnitude of the interaction strength. Although the van-der-Waals interaction decays rapidly with increasing distance between two atoms, the C_6-coefficient is generally very large thanks to its scaling even for moderate values of the effective principal quantum number. Furthermore, its sign indicates whether the van-der-Waals interaction is attractive or repulsive. For an atom in its ground state the transition frequencies are all positive, i.e. $\omega_{mn} > 0$, which yields the characteristic attractive van-der-Waals interaction. However for Rydberg atoms the transition frequencies can be positive or negative and their sum weighted by the coupling strength given by the dipole-dipole interaction leads to either repulsive or attractive interactions.
Note that while the long-range interaction is only given by V_{vdW}, both the first- and the second-order term contribute to the dipolar-exchange. An useful quantity to define is the *Förster defect* $\Delta = \omega_{ik} + \omega_{jl}$, which is simply the sum of both involved transition frequencies in the exchange. For large defects $|\Delta| \gg |V_{\mathrm{dip}}|$, the energy eigenstates of the system are predominantly given by the van-der-Waals interaction, however a vanishing defect $|\Delta| \ll |V_{\mathrm{dip}}|$ enhances the dipolar-exchange. The case $|\Delta| \to 0$ is known as the *Förster resonance* and implies that the transition frequencies $\omega_{ik} = -\omega_{jl}$ are equal in magnitude, but opposite in sign. The boundary between the dipole-dipole and van-der-Waals regime is defined by the crossover distance

$$R_c = \frac{C_6}{(\hbar\Delta)^2} \tag{2.39}$$

At the Förster resonance, the improved dipolar-exchange is also referred to as Förster Resonance Energy Transfer [citation missing, more explanations required].

Isotropic and anisotropic interaction

Although important to understand the characteristic features of the Rydberg atom, the principal quantum number alone does not define all relevant properties. The orbital quantum number ℓ appears in the angular wave function and defines its spatial properties. Since the dipole matrix element also depends on ℓ, we have to differentiate the van-der-Waals interaction based on different values of the orbital quantum number. The simplest case $\ell = 0$ defines the S-orbital and corresponds to an isotropic wave function. The dipole-dipole interaction between two Rydberg atoms is thereby also isotropic. The associated van-der-Waals interaction can be written as

$$V_{\mathrm{vdW}} = \frac{C_6^S}{R^6}, \tag{2.40}$$

where the isotropic C_6^S-coefficient is fixed by choice of Rydberg level and chemical element and does not depend on the direction. On the other hand, $\ell = 1$ represents the P-orbital

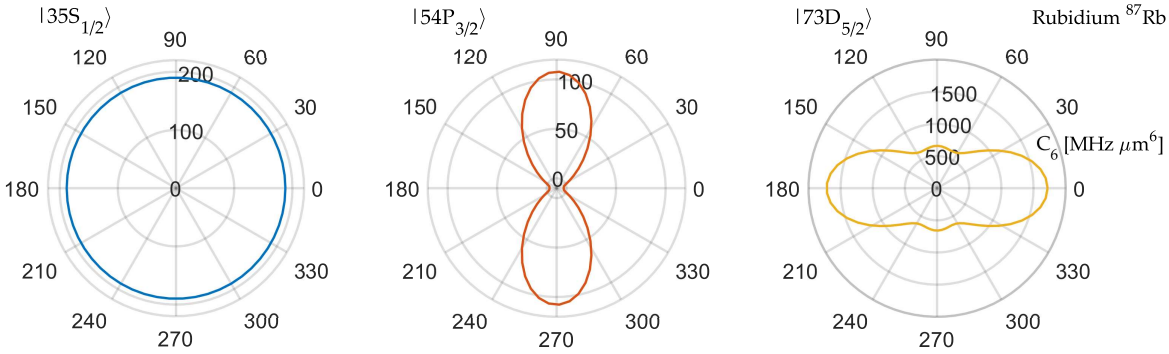

Figure 2.5: C_6-coefficient between pairs of atoms both in the state $|n\ell, n\ell\rangle$ with $|n\ell\rangle \in \{|35S_{1/2}\rangle, |54P_{3/2}\rangle, |73D_{3/2}\rangle\}$. Contrary to intuition, the interaction geometry is a property of a pair state rather than each atom individually. For two atoms in the S-orbital ($\ell = 0$) the inter-atomic long-range resulting interaction is isotropic. Going to higher orbitals such as P- or D-orbitals results in anisotropic interactions, which is sensitive to the orientation of both atoms. The strength is predominantly given by the principal quantum numbers of both atoms. Calculations for these results were performed with the help of the package `Alkali Rydberg Calculator` [121].

and the shape of the wave function is strongly anisotropic [144, 145]. The interaction between two atoms excited to Rydberg P-states then strongly depends on the orientation of both atoms

$$V_{\mathrm{vdW}} = \frac{C_6^P(\vartheta, \vartheta', \varphi, \varphi')}{R^6} \tag{2.41}$$

with the angles ϑ (ϑ') and φ (φ') of the first (second) atom. The complexity of the interaction can be reduced by introducing an external magnetic field $\boldsymbol{B} = B \cdot \hat{\boldsymbol{e}}_B$, which causes the atoms to align. The van-der-Waals interaction is then simplified to

$$V_{\mathrm{vdW}} = \frac{C_6^P(\vartheta)}{R^6}. \tag{2.42}$$

The exact shape of the $C_6^P(\vartheta)$-coefficient can be obtained through calculation of the angular integrals of the dipole matrix element. Based on the selection rules a state $|nP\rangle$ is allowed to transition to the states $|n'S\rangle$ and $|n'D\rangle$. The dipole matrix element is larger for $|n'S\rangle$ and thus presents the main channel of the virtual transition in the van-der-Waals interaction. The resulting angular dependence results in

$$V_{\mathrm{vdW}} \propto \frac{(n^*)^{11}}{R^6} \sin^4(\vartheta), \tag{2.43}$$

where $\vartheta = \boldsymbol{R} \cdot \hat{\boldsymbol{e}}_B$ denotes the angle between the two Rydberg P-state excited atoms separated by $\boldsymbol{R}$ [144, 145] (see Fig. 2.6). The interaction seems purely anisotropic and

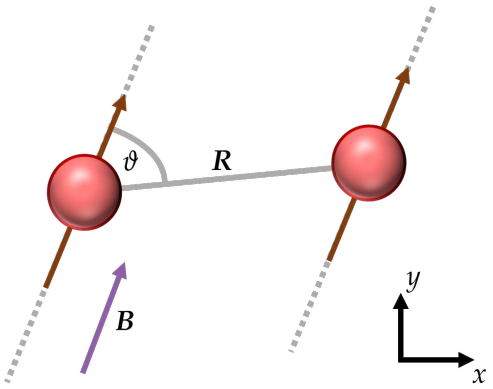

Figure 2.6: Visualization of the angle ϑ between two atoms separated by the distance vector $\boldsymbol{R}$ aligned in a magnetic field $\boldsymbol{B}$ simplified to the xy-plane.

appears to be vanishing for $\vartheta = 0$, however a small residual isotropic interaction appears due to finite coupling to a $|n'D\rangle$ state, although its magnitude is much smaller than its anisotropic counterpart.

The discussed interactions are the basis of the energy levels between two Rydberg atoms. While the energy eigenstates for infinitely large distances $R \to \infty$ is solely given by the unperturbed energies of the individual atoms, it is now possible to determine the shift of the energies and the modification of the eigenstates in dependence of the distance R. Numerical computation of these energies however gives rise to a complex potential landscape due to the avoided crossing of many different pair states $|n\ell, n'\ell'\rangle$ at shorter distances.

2.3.3 Pair potential landscape

In order to determine the correct energy of a pair state $|n\ell, n'\ell'\rangle$, the dipole interaction has to be treated beyond perturbation theory [147–150]. Calculation with the exact Hamiltonian Eq. (2.28) in the basis spanned by all possible pair states gives rise to the so-called *spaghetti curves*, which arise through the overlap of strongly varying pair state energy at short distances (see Fig. 2.7).
At far distances the pair state energy converges to the summation of both unperturbed energies. These asymptotic pair state energies shift by decreasing the distance initially according to the van-der-Waals interaction. At short distances however various pair state energies grow closer and can potentially exhibit avoided crossings if the dipole transition matrix for the set of crossing pair states is finite. Along the avoided crossing a pair state admixes with the other involved pair state through to the dipolar exchange. In most cases however the distance-dependent admixing of an adressed pair state with other pair states is not problematic, as the energy of the superposition of all pair states with finite admixture yields the characteristic van-der-Waals curve (see Fig. 2.7 (b) and (c)) and thus the desired long-range interaction is retrieved.

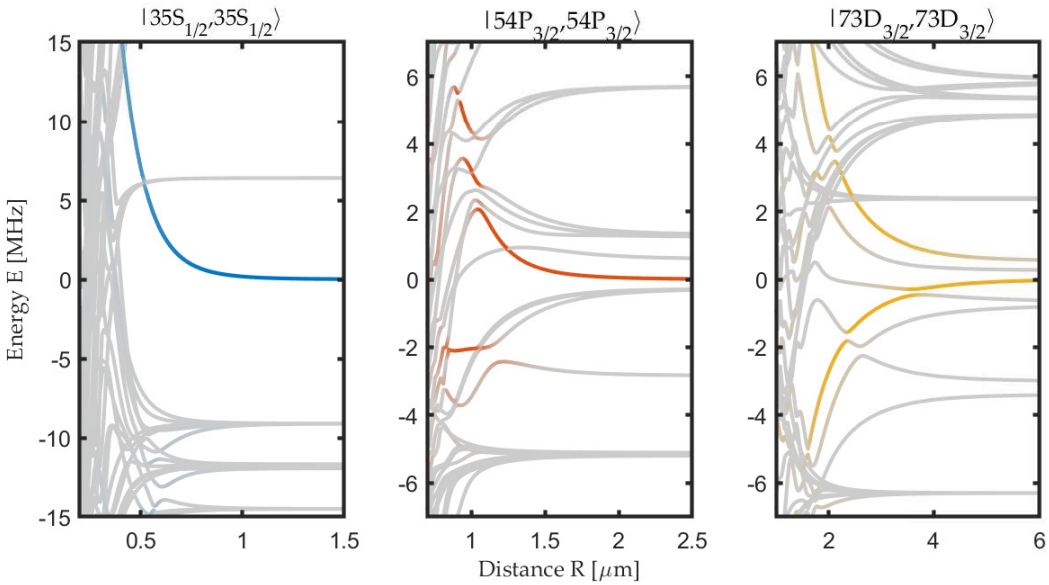

Figure 2.7: Energy of the pair states $|n\ell, n\ell\rangle$ with $|n\ell\rangle \in \{|35S_{1/2}\rangle, |54P_{3/2}\rangle, |73D_{3/2}\rangle\}$ centered around the summed energy of two unperturbed atoms in their respective state $|n\ell\rangle$. All gray lines correspond to the energies of other pair states $|n\ell, n'\ell'\rangle$. At close inter-atomic distances the energetic shift of all pair states lead to many crossing and avoided crossings. For $|n\ell\rangle = |35S_{1/2}\rangle$ the energy shifts towards larger values as the distance between both atoms grows closer. For $|n\ell\rangle = |54P_{3/2}\rangle$ a similar curve can be found, although the pair state admixes with other pair states due to being energetically close. For $|n\ell\rangle = |73P_{3/2}\rangle$ we again obtain position-dependent admixing of the pair state with other pair states. Additionally we observe the energy going to both higher and lower values through branching of the admixed state. We conclude that the long-range interaction is not just given by a shift of the energy to larger values, but can rather be defined as an out-of-resonance shift of the unperturbed pair state. Calculations for these results were performed with the help of the package `Pair Interaction` [146].

On the other hand the energy of the admixed pair state does not necessarily monotonically increase or decrease (see Fig. 2.8). In these cases the admixing gives rise to potential wells through the avoided crossings. By addressing these wells it is possible to excite two atoms, whose interatomic distance matches the distance of the corresponding avoided crossing, to a molecular bound state. These molecules are referred to as *macrodimers* [151–156]. Ultimately the desired long-range interaction heavily depends on the Rydberg levels and always requires a full calculation of the pair potential spectrum.

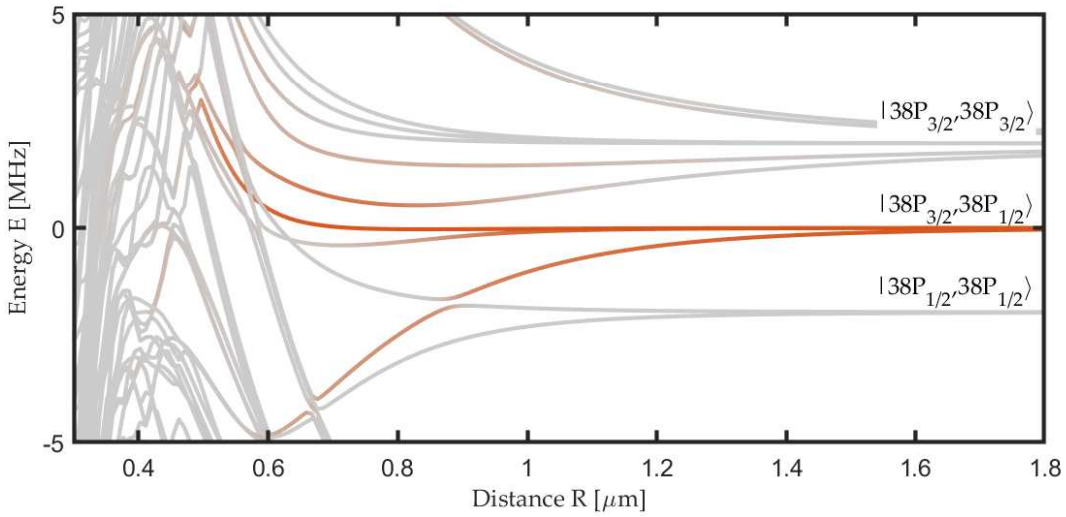

Figure 2.8: Energy of the pair states $|38P_{1/2}, 38P_{3/2}\rangle$ centered around the summed energy of two unperturbed atoms in their respective state $|38P_{1/2}\rangle$ and $|38P_{3/2}\rangle$. We observe avoided crossings of the pair states, which lead to effective potential wells. For a pair state, which exhibits a large admixture of pair states giving rise to such avoided crossings, it is possible to address these potential wells and thus create molecular states in different vibrational modes. Calculations for these results were performed with the help of the package `Pair Interaction` [146].

2.4 Coherent coupling to Rydberg states

In this section we discuss systems of atoms in an electronic ground state coherently coupled to a Rydberg state. We study the important properties of the coupling scheme, introduce the concept of dressing and discuss the role of the van-der-Waals interaction in systems composed of few atoms. We furthermore elaborate previously observed phenomenon in many-body Rydberg ensembles.

2.4.1 Coupling schemes and Rydberg-dressing

We consider the simplest coupling scheme, which involves a two-level system coherently coupled through an external light field $\boldsymbol{E}(t)$. We denote the ground state $|g\rangle$ and the excited state $|e\rangle$, whose energy difference is given by the optical transition frequency ω_0. The corresponding Hamiltonian of the two-level system in the $\{|g\rangle, |e\rangle\}$ basis is written as

$$\hat{H}(t) = \hat{H}_0 + \hat{H}_{\text{cpl}}(t) \tag{2.44}$$

where $\hat{H}_0$ gives the unperturbed ground and excited state, while $\hat{H}_{\text{cpl}}(t)$ represents the time-dependent coupling between both states. It reads

$$\hat{H}_{\text{cpl}}(t) = -\hat{\boldsymbol{d}}\boldsymbol{E}(t) \tag{2.45}$$

with the dipole operator $\hat{\boldsymbol{d}}$. The driving within the two-level scheme occurs through dipole transitions

$$\hat{\boldsymbol{d}} = \sum_{i,j\in\{e,g\}} \boldsymbol{d}_{ij} \left|i\right\rangle \left\langle j\right| \tag{2.46}$$

with the dipole moment d_{ij}. Given the laser frequency ω_L, we rewrite the external light field as

$$\boldsymbol{E} = \boldsymbol{E}_0 e^{-i\omega_L t} + \boldsymbol{E}_0^* e^{i\omega_L t} \tag{2.47}$$

which yields the coupling Hamiltonian

$$\hat{H}_{\text{cpl}}(t) = -\frac{1}{2}(\Omega e^{-i\omega_L t} + \Omega^* e^{i\omega_L t})\hat{b}_e^\dagger \hat{b}_g - \frac{1}{2}(\Omega^* e^{-i\omega_L t} + \Omega e^{i\omega_L t})\hat{b}_g^\dagger \hat{b}_e. \tag{2.48}$$

Here we introduced the *Rabi frequency* $\Omega = 2\left\langle e\right| \hat{\boldsymbol{d}}\boldsymbol{E} \left|g\right\rangle$, which quantifies the coupling strength through the corresponding dipole matrix element of the transition between $|g\rangle$ and $|e\rangle$. Furthermore we use the creation and annihilation operator notation to describe the transition $(\hat{b}_g)^\dagger \hat{b}_e = \left|g\right\rangle \left\langle e\right|$. It is useful to perform a unitary transformation $U(t) = e^{-i\hat{H}_0 t/\hbar} = e^{i\phi}(\hat{n}_g + e^{-i\omega_0 t}\hat{n}_e)$ into the interaction picture, where ϕ is a complex number representing the general energy offset of the two-level system. We hereby access the so-called *rotating frame* and the coupling Hamiltonian within this representation yields,

$$\hat{H}_{\text{cpl}}^{\text{RF}}(t) = -\frac{1}{2}(\Omega e^{-i\Delta t} + \Omega^* e^{i(\omega_L+\omega_0)t})\hat{b}_e^\dagger \hat{b}_g - \frac{1}{2}(\Omega^* e^{-i(\omega_L+\omega_0)t} + \Omega e^{i\Delta t})\hat{b}_g^\dagger \hat{b}_e \tag{2.49}$$

where we define the detuning $\Delta = \omega_L - \omega_0$. We identify two oscillating terms, the frequencies of which strongly. We expect the transition and laser frequency to be in the same order of magnitude, which yields the limit $\omega_L + \omega_0 \gg \Delta$. The terms with frequency $\omega_L + \omega_0$ oscillate much faster than the oscillation given by Δ and can therefore be neglected, as they average to zero on the relevant time scales of the system. This approximation is known as the *rotating wave approximation* (RWA) and yields the simplified Hamiltonian

$$\hat{H}_{\text{cpl}}^{\text{RF}}(t) \approx -\frac{\Omega}{2}(e^{-i\Delta t}\hat{b}_e^\dagger \hat{b}_g + e^{i\Delta t}\hat{b}_g^\dagger \hat{b}_e) \tag{2.50}$$

Another unitary transformation defined by $\hat{U}(t) = e^{-i\lambda}(\hat{n}_g + e^{-i\Delta t}\hat{n}_e)$ leads to the co-rotating frame and allows a time-independent description of the coupling

$$\hat{H}_{\text{cpl}}^{\text{RF}} = \frac{\Omega}{2}((\hat{b}_g)^\dagger \hat{b}_e + \text{h.c.}) - \Delta\hat{n}_e. \tag{2.51}$$

This Hamiltonian allows to describe the coupling of an atom in its electronic ground state $|g\rangle$ to the excited state $|e\rangle$. We compute the eigenstates and their corresponding energies and obtain an eigenstate, which can be written as

$$\left|\tilde{g}\right\rangle = \frac{1}{C}(\left|g\right\rangle + \beta \left|e\right\rangle) \tag{2.52}$$

with the normalization factor C. It describes an atom in its electronic ground state with admixture $\beta = (\sqrt{\Delta^2 + \Omega^2} - \Delta)/\Omega$ of the Rydberg state. This eigenstate defines the so-called

Rydberg-dressing, which is the idea that an electronic ground state atom weakly coupled to a Rydberg state can be effectively seen as a modified ground state adopting properties of Rydberg states [157–160]. Note, that this is not the eigenstate of the Hamiltonian with the lowest energy, but its relevance appears in a later subsection of this chapter.
In experiments the detuning is usually comparable to or larger than the Rabi frequency and we hereby approximate $\beta \approx \Omega/(2\Delta)$ through $|\Delta|/\Omega \gtrsim 1$ and define the squared admixture

$$P_{\mathrm{Ryd}} = \beta^2 = \frac{\Omega^2}{(2|\Delta|)^2} \tag{2.53}$$

as a measure for the population of the Rydberg state in $|\tilde{g}\rangle$. In the weakly-dressed limit $|\Delta|/\Omega \gg 1$, the admixture of the Rydberg state is small and it is common to drop the normalization factor. It is also worth mentioning that coupling the electronic ground to an excited state induces a non-trivial AC Stark shift

$$U_{\mathrm{AC}} = \frac{\Omega^2}{4\Delta}, \tag{2.54}$$

which even in the weakly-dressed limit is potentially large. As mentioned before the Rydberg-dressed ground state acquires properties of the Rydberg state such as a overall enhanced lifetime and the long-range van-der-Waals interaction, albeit modified in their amplitude. Due to the finite admixing, the lifetime $\tilde{\tau}$ of the dressed ground state is enhanced

$$\frac{1}{\tilde{\tau}} = \beta^2 \frac{1}{\tau} \tag{2.55}$$

and the long-range interaction strength rescaled

$$V_{\mathrm{vdW}} \propto \beta^4 \frac{C_6}{R^6}. \tag{2.56}$$

Experimentally both the detuning and the Rabi frequency are tunable, although the Rabi frequency inherits the scaling with the effective principal quantum number through the dipole matrix element and its magnitude thus relies on the addressed Rydberg state. This ability to tune the atoms and choose the resulting admixture is particularly useful, as longer lifetimes of long-range interacting atoms are experimentally important.

The choice of coupling scheme has to be in accordance to the selection rules. For example, for the commonly used ground state $|g\rangle = |5S_{1/2}\rangle$ we are able to use the convenient two-level scheme to couple to $|e\rangle = |nP_{3/2}\rangle$. However since the transition from $|g\rangle$ to the excited state $|e\rangle = |nS_{1/2}\rangle$ is forbidden, it is necessary to use an intermediate state $|i\rangle = |n'P_{3/2}\rangle$ (see Fig. 2.9). In the three-level coupling scheme, we thus require two lasers with respective Rabi frequencies Ω_1 and Ω_2, which couple $|g\rangle$ to $|i\rangle$ with detuning δ and $|i\rangle$ to $|e\rangle$ with detuning Δ. The corresponding three-level coupling Hamiltonian can be mapped back to an effective two-level Hamiltonian by computing the parameter regime in which the intermediate state possesses a vanishing population. This is called adiabatic elimination and yields the effective Rabi frequency $\Omega = \Omega_1\Omega_2/\delta$ [161–164].

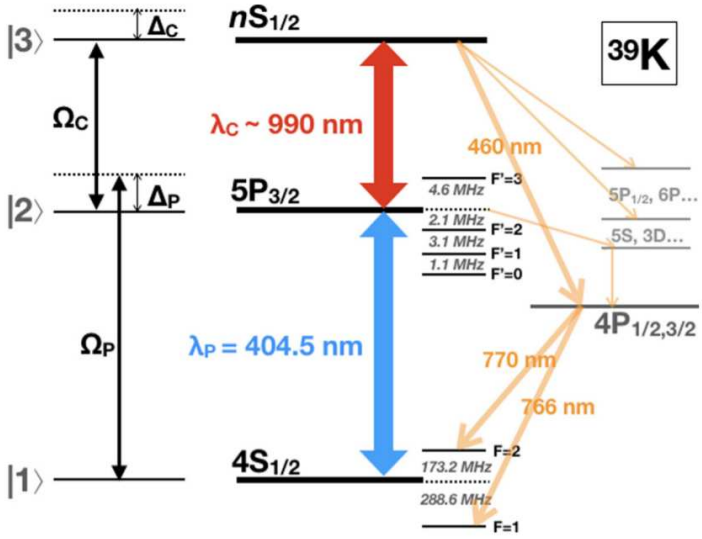

Figure 2.9: Schematic depiction of a three-level system involving a two-photon coupling scheme for Potassium ^{39}K. The electronic ground state $|4S_{1/2}\rangle$ is effectively coupled to a Rydberg $|nS_{1/2}\rangle$ state, however due to selection rules it requires an intermediate $|5P_{3/2}\rangle$. Through a large detuning of the intermediate state its population can be kept vanishingly small. Reprinted figure with permission from [161]. © 2020 by the American Physical Society.

Although the effective two-level system gives a good approximation of the three-level system, the results deviate for larger values of Ω_1/δ. Therefore several methods beyond adiabatic elimination have thus been established, which give a more accurate reflection of the three-level system [165–167]. In general these methods can be used to map various multi-photon processes to single-photon transitions and thus we rely on the coupling Hamiltonian Eq. (2.51) as an effective description of other coupling schemes.
The inclusion of intermediate states unfortunately yields several limitations. Since we require the intermediate state to be only weakly populated, it is important to use a large detuning to these states, i.e. $\delta/\Omega_1 \gg 1$, which consequently limits the effective Rabi frequency [168]. Additionally the overall lifetime of the excited state is modified to take into account the lifetime of the intermediate states, i.e. $\frac{1}{\tau} \to \frac{1}{\tau} + \sum_i \beta_i^2 \frac{1}{\tau_i}$, and thus generally yields smaller values even for weakly admixed intermediate states, i.e. $\beta_i \ll 1$ [169–171]. Finally the strength of the overall AC Stark shift increases with the number of single-photon transitions involved in the coupling scheme. Although all of these limitations can be controlled to a certain degree through the experimental parameters, it is often more beneficial to simply use a single-photon coupling scheme.
In order to understand the many-body physics of bosonic quantum gases dressed with Rydberg states, we determine in the following the spatially dependent energy eigenstates of only two atoms.

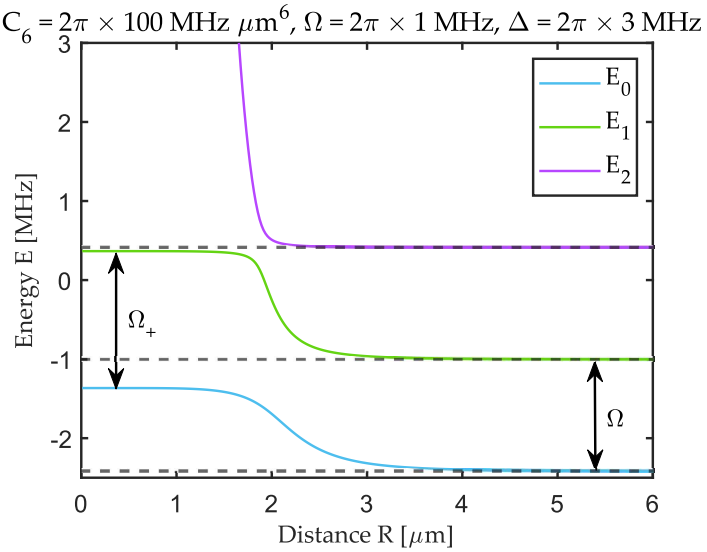

Figure 2.10: Energies of the eigenstate of Hamiltonian Eq. (2.60) in a two-atom system for $\Omega = 2\pi \times 1$ MHz, $\Delta = 2\pi \times 1$ MHz and $C_6 = 100$ MHz μm^6. At large distances, the eigenstate of the lowest energy is defined by two Rydberg atoms. Reducing the distance leads to a transition to a superatomic state, where the ground state of only one of the atoms is coupled to the Rydberg state.

2.4.2 Two-atom system and soft-core interaction

The Hamiltonian of a system consisting of N atoms coupled to Rydberg state within the two-level picture is given by

$$\begin{aligned}\hat{H} &= \hat{H}_{\text{cpl}} + \hat{H}_{\text{vdW}} \\ &= -\Delta \sum_{i=1}^{N} \hat{n}_i^e + \frac{\Omega}{2} \sum_{i=1}^{N} ((\hat{b}_i^g)^\dagger \hat{b}_i^e + \text{h.c.}) + C_6 \sum_{i=1}^{N} \sum_{j>i}^{N} \frac{\hat{n}_i^e \hat{n}_j^e}{R_{ij}^6}\end{aligned} \tag{2.57}$$

with the distance R_{ij} between atoms i and j. A general product state of the system is given by $|\Psi\rangle = |\psi_1, \psi_2, ..., \psi_N\rangle$ with $\psi_i \in \{g, e\}$ and the dimension of the corresponding Hilbert space is thus $\dim(\mathcal{H}) = 2^N$. For two atoms, i.e. $N = 2$, the matrix representation of the Hamiltonian reads

$$\hat{H} = \begin{pmatrix} 0 & \Omega/2 & \Omega/2 & 0 \\ \Omega/2 & -\Delta & 0 & \Omega/2 \\ \Omega/2 & 0 & -\Delta & \Omega/2 \\ 0 & \Omega/2 & \Omega/2 & -2\Delta + C_6/R^6 \end{pmatrix} \tag{2.58}$$

Since we consider indistinguishable atoms, the states $|g, e\rangle$ and $|e, g\rangle$ are identical with respect to their coupling to the two-atom ground state $|g, g\rangle$ and the two-atom excited

state $|e,e\rangle$. We thus define a symmetric and anti-symmetric superposition of both states as

$$|\pm\rangle = \frac{1}{\sqrt{2}}(|g,e\rangle \pm |e,g\rangle). \tag{2.59}$$

Through calculation of the corresponding adapted coupling strength Rabi frequency $\Omega_+ = \langle +| \hat{H}_{\text{cpl}} |g,g\rangle = \langle +| \hat{H}_{\text{cpl}} |e,e\rangle = \sqrt{2}\Omega$ and $\Omega_- = \langle -| \hat{H}_{\text{cpl}} |g,g\rangle = \langle -| \hat{H}_{\text{cpl}} |e,e\rangle = 0$, we see that the antisymmetric wave function is not coupled to any state. $|-\rangle$ can therefore be eliminated, which yields

$$\hat{H} = \begin{pmatrix} 0 & \Omega/\sqrt{2} & 0 \\ \Omega/\sqrt{2} & -\Delta & \Omega/\sqrt{2} \\ 0 & \Omega/\sqrt{2} & -2\Delta + C_6/R^6 \end{pmatrix} \tag{2.60}$$

We compute the eigenstates and plot the respective energies versus the distance R for a detuning $\Delta/\Omega = 2\pi \times 1$ MHz and an interaction strength given by $C_6 = 100$ MHz μm^6 (see Fig. 2.10). Several of the energies diverge as we decrease the distance. The corresponding eigenstates have a very large Rydberg admixture, which results in considerable long-range repulsion for small distances. The lowest energy also increases with distance, however saturates to a certain value in the limit $R \to 0$. For large interatomic distances, the eigenstate takes the form

$$|\Psi_0\rangle_{R\to\infty} = |e,e\rangle\,. \tag{2.61}$$

Since both atoms are very far apart, they do not interact with each other and the overall energy is given by the unperturbed energies of each atom. Decreasing the distance leads to increasingly strong long-range repulsion between the Rydberg atoms. On the other hand at small distances the eigenstate becomes

$$|\Psi_0\rangle_{R\to 0} = \frac{1}{\sqrt{2}}(|g,g\rangle + |+\rangle). \tag{2.62}$$

The eigenstate implies that only one of the two atoms is coupled to the Rydberg state, while the other rests in its electronic ground state. The symmetric wave function $|+\rangle$ appears due to the indistinguishability of both atoms. The eigenstate results from the substantial long-range interaction, which greatly shifts $|e,e\rangle$ to larger values and thus it is energetically more favorable to have only one atom coupled to the Rydberg state.
The suppressed excitation of an atom in its ground state to the Rydberg state in the vicinity of an already excited atom is known as the *Rydberg blockade* [172–175]. The characteristic blockade radius is given by

$$R_b = \left(\frac{C_6}{\Omega}\right)^{\frac{1}{6}}, \tag{2.63}$$

and defines the volume around the excited atom, in which excitation to the Rydberg state is inhibited. For N atoms, the wave function can be generalized to

$$\left|\Psi_0^N\right\rangle_{r\ll R_b} = |g_1,...,g_N\rangle + \frac{1}{\sqrt{N}}\sum_{i=1}^{N} |g_1,g_2,...,e_i,...,g_N\rangle \tag{2.64}$$

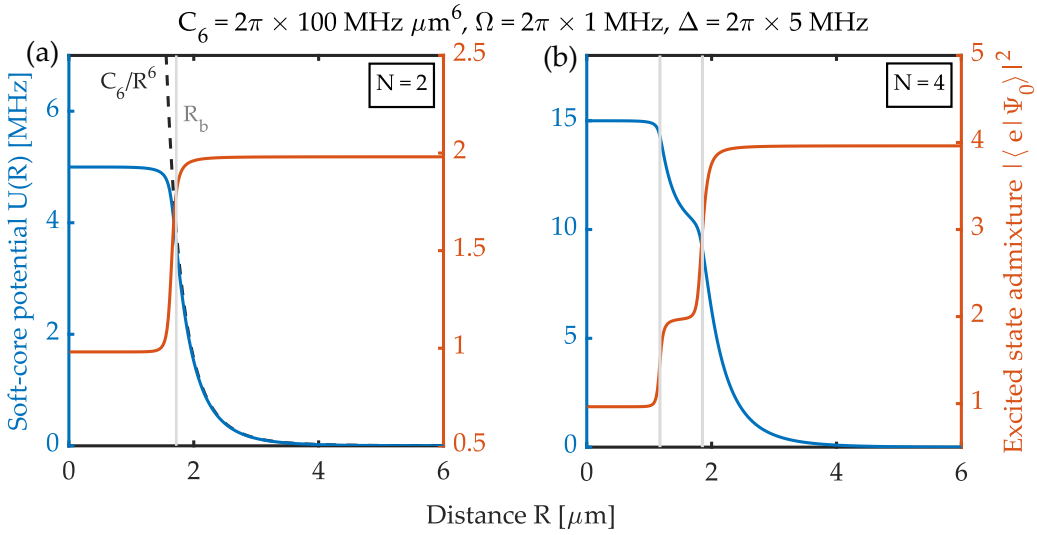

Figure 2.11: (a) Soft-core potential $U(R)$ of two atoms coupled to the Rydberg state (blue line) and total excited-state admixture of both atoms (orange line) obtained at $\Omega = 2\pi \times 1$ MHz, $\Delta = 2\pi \times 5$ MHz and $C_6 = 100$ MHz μm^6. Reducing the distance between two excited atoms leads to the characteristic van-der-Waals interaction. The transition from the unperturbed pair state to the superatom regime occurs when the energy cost of the interaction becomes larger than the energy loss of suppressing the coupling of one atom to the Rydberg state. (b) For four atoms the transition from the unperturbed for large interatomic distances to the superatom regime happens through an intermediate regime, in which the four atoms collectively share two excitations. For larger system sizes of N atoms it is possible for more such regimes at intermediate interatomic distances to arise.

An ensemble of many atoms within the volume given by the blockade radius with one collective excitation is called a *superatom* [176, 177]. The superatom behaves similar to a conventional Rydberg-dressed atom, although with modified properties such as an enhanced Rabi driving $\tilde{\Omega} = \sqrt{N}\Omega$ [178].

Soft-core potential

The soft-core interaction potential defines the interaction between Rydberg-dressed atoms also referred to as the *dressed interaction* [179–181]. The wave function of a system with N Rydberg-dressed atom can be written as

$$\left|\Psi_0^N\right\rangle = |\tilde{g}_1, \tilde{g}_2, ..., \tilde{g}_N\rangle \,. \tag{2.65}$$

For two atoms $N = 2$, the soft-core potential is directly given by lowest energy, which takes the shape given by

$$U(R) = \frac{U_0}{1 + (\frac{R}{R_c})^6} \tag{2.66}$$

with the potential height U_0 and the characteristic length $R_c = \left(\frac{C_6}{2|\Delta|}\right)^{\frac{1}{6}}$. Note, that the characteristic length is not identical to the blockade radius and merely helps to define the shape of the potential $U(R)$.
In the limit of large distance, the tail of the soft-core potential follows the previously defined rescaled van-der-Waals interaction strength $U(R \gg R_c) = \beta^4 C_6/R^6$ (see Fig. 2.11 (a)). The potential height U_0 can be obtained through the subspace of $|g,g\rangle$ and $|+\rangle$ in Eq. (2.60), since the long-range interaction isolates $|e,e\rangle$. The potential height is then given by

$$\begin{aligned} U_0 &= \frac{1}{2}(\Delta - \sqrt{\Delta^2 + 2\Omega^2} + \sqrt{\Delta^2 + \Omega^2}) \\ &\approx 2|\Delta|\beta^4 = \frac{\Omega^4}{(2|\Delta|)^3} \end{aligned} \tag{2.67}$$

and as expected we find the dressed interaction to be dependent on the admixture $\propto \beta^4$. Ultimately all properties of Rydberg-dressed atoms can be defined or tuned by the choice of the Rydberg level, the coupling scheme, the Rabi frequency and the detuning.

Note, that in this section we focused on the case of both atoms coupled to the same Rydberg level. While a two-atom excited state composed of two different Rydberg states, i.e. $|e,e'\rangle$, may exhibit similar physics, it is dependent on the addressed pair state. For example, it is possible that the two-body ground state is resonantly coupled to a molecular state if the distance R matches the molecular bond length (see Section 2.3.3).
Although in the two-atom system we obtain a transition between the unperturbed and the superatom regime, N-atom system exhibit additional features at intermediate distances. The four-atom system, arranged as a square with length R of the edges, possesses an additional regime inbetween both previously-discussed limits. Before transitioning into a superatom, it becomes energetically more favorable due to the long-range interaction to only have two excited atoms, while the other two atoms are in their ground state (see Fig. 2.11 (b)). Due to the indistinguishability of the atoms, the two Rydberg excitations in the intermediate regime are shared among the four atoms, similar to how a single excitation is shared among all atoms within the superatom regime. Further decreasing the distance leads to a superatom consisting of four atoms.

2.4.3 Rydberg ensembles

Although the few particle system has been well studied, albeit not completely understood, a large focus lies on Rydberg ensembles. One of the major experimental accomplishments in this field was the observation of crystalline structures in Rydberg gases [182, 183]. In an experiment involving a Rubidium ^{87}Rb gas trapped in a two-dimensional, square optical lattice it was possible to create a few Rydberg-excited atoms through the appropriate coupling scheme. The distribution of these excitations revealed the repulsive nature of the van-der-Waals interaction, as the excitations emerged in a ring-like constellation with equal distance to their neighbors (see Fig. 2.12). This experimental realization paved the

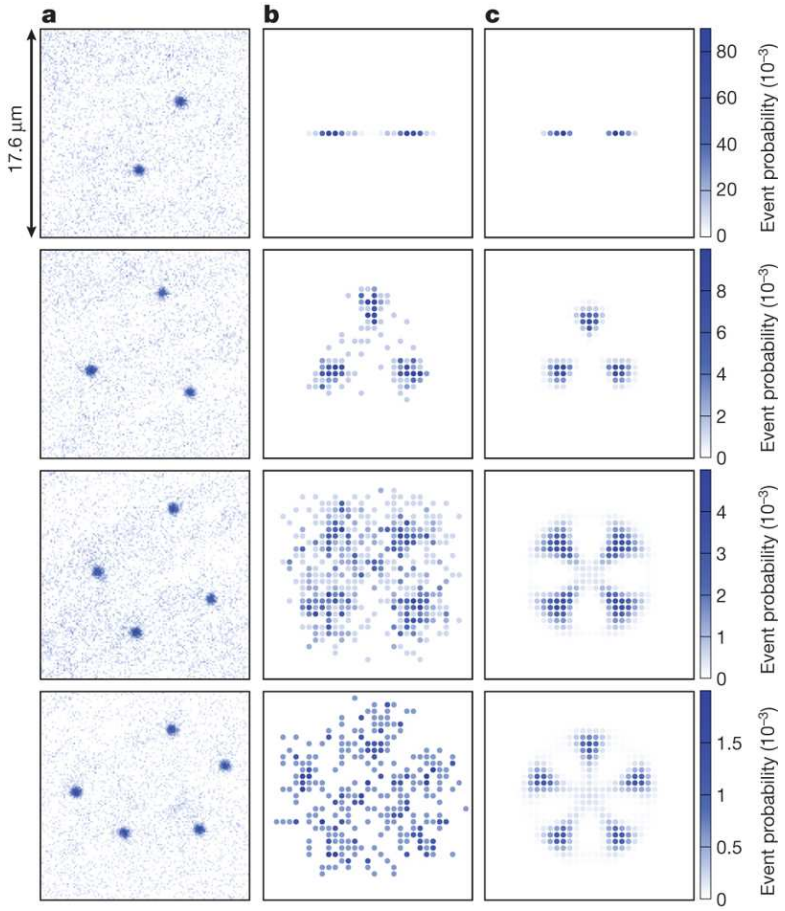

Figure 2.12: (a) Fluorescence image of trapped bosonic quantum gas with few excitations, e.g. $N_e \in [2, 5]$ (blue spots). (b) Histogram of fluorescence images with equal number of excited atoms. After centering and aligning of the images a clearer distribution of the excitations is revealed. (c) Theoretical predictions of excitation distribution obtained through the computation of the many-body ground state of Hamiltonian Eq. (2.57). Reprinted figure with permission from [182]. © 2012 by the American Physical Society.

way towards further studies on Rydberg crystals such as anisotropic crystals [145] and crystals in higher dimensions [184].
Another important research direction in the context of Rydberg-dressed quantum gases is the engineering of spin lattices with high tunability [112, 113, 183]. Since the theoretical study of spin systems are despite their simplicity at high computational cost, the simulation of such system through quantum systems gained significant importance. Although many potential candidates exist, the low energy scale of crucial mechanism, such as superexchange processes available in these candidates does not allow for intensive research of the hereby simulated spin systems [185]. However the van-der-Waals interaction between Rydberg atoms vastly surpasses the spin-spin interactions engineered by

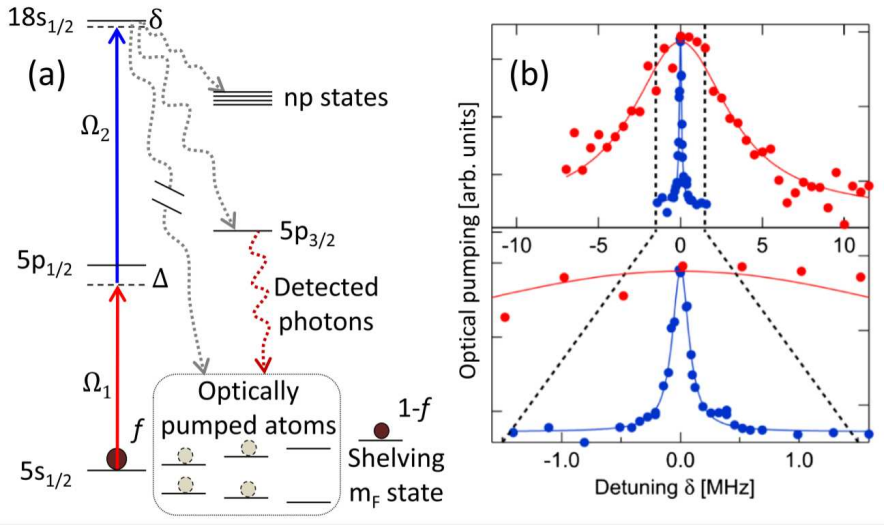

Figure 2.13: (a) Exemplary two-photon excitation scheme including possible transition to lower-lying and other Rydberg states. The atom can either decay radiatively to short-lived state, which ultimately decay back to a ground state or occupy an energetically close Rydberg state through blackbody transition. (b) Anomalous broadening of the excitation spectra versus the detuning δ to the excited state for a electronic ground state occupation fraction $f = 0.35$ and effective Rabi frequency $\Omega = 2\pi \times 3$ kHz (red markers) and $f = 0.7$ and $\Omega = 2\pi \times 140$ kHz (blue markers). In the single-atom limit the width of the Gaussian distribution hints at the linewidth of the coupling laser and therefore only near-resonant excitation ($|\delta| \approx 0$) leads to a vanishing occupation of the excited state. However for a large fraction of the atoms coupled through this scheme the excitation to the Rydberg state can also take place in the far off-resonant regime ($|\delta| \gg 0$) due to blackbody facilitated excitations. Reprinted figure with permission from [190]. © 2016 by the American Physical Society.

previous candidates, which makes Rydberg-dressed systems a promising platform for simulating spin Hamiltonians. To this end we map the electronic ground state and a single Rydberg-dressed state onto spin states and thus the physics of such quantum gases could be effectively described by a spin Hamiltonian. Following the first experimental realization, many theoretical and experimental studies on Rydberg-dressed spin lattices emerged for the study of various phenomena such as quantum magnets [186, 187] and Bloch oscillations [188]. Furthermore quantum information and computing by means of Rydberg atoms became an increasingly growing research field in recent years [114–117, 189]. Through previously discussed mechanism such as the Rydberg blockade and dipolar exchange processes, quantum gates for quantum information processing can be realized.

Despite all advantages and uses of Rydberg-dressed systems several, there exist limitations to their applicability. A major obstacle, and still in the focus of current research, is the

often observed rapid, chain-like loss of coherence and even of Rydberg-dressed atoms themselves referred to as *avalanche dephasing* [190–192]. The underlying cause of this phenomenon is the spontaneous decay of an atom in a Rydberg state to an energetically close Rydberg state, which is in this context often referred to as contaminant state (see Fig. 2.13). As discussed in Subsection 2.2.3 an atom, initially in its electronic ground state and subsequently excited to a Rydberg state, can decay either via radiative decay or blackbody radiation. While radiative decay leads to the population of low lying states with negligible lifetime, nearby Rydberg states can be accessed through the blackbody radiation mechanism. Since these states possess similar lifetimes compared to the initially adressed Rydberg state, it is able to interact with other atoms coupled to Rydberg states and even facilitate the excitation to undesirable Rydberg states. The initial contamination spreads through the system and leads to the population of many different Rydberg states not involved in the coupling scheme, which only includes the electronic ground and target Rydberg state. This leads to substantial decoherence in the system and potentially the loss of atoms, since in these Rydberg states the atom is not coupled to the trapped ground state anymore. The avalanche dephasing can already occur if only one blackbody transition populates a contaminant state, which implies a lifetime of the system linearly decreasing with the Rydberg fraction n_i^e in the ensemble, e.g. $\tau_c \propto \tau_{\mathrm{BBR}} / \sum_i n_i^e$. Thus results in a vastly decreased lifetime of the overall system compared to the lifetime of a single atom.
The avalanche dephasing mechanism is of key importance. Different approaches to overcome this obstacle have been proposed: By operating in cryogenic temperatures it is possible to keep the blackbody transition rate at a minimum. Lowering the average occupation of Rydberg state lengthens the typical lifetimes of the system as well [157, 193]. On the other hand it is also in principle possible to get rid of the contamination by either a second coupling scheme which couples the contaminant state to a lower-lying, short-lived state, hereby deexciting the atom to the electronic ground state before it is able to trigger the avalanche dephasing. Additionally tailored-trapping techniques can be used to expel any atoms not in the electronic ground or target Rydberg state from the system such that interactions between the contamination and other atoms do not take place [194–196]. Finally another way to limit the population of contaminant states has been proposed, which consists of using the spatial shape of the coupling laser [197]. In the bulk of a system the admixture of the Rydberg state is marginal due to the strong, repulsive van-der-Waals interaction, while the boundary is not as affected and thus possesses a overall larger Rydberg admixture. However since the profile of the coupling laser can be engineered to a certain degree, it is possible to also suppress the Rydberg admixture on the boundary, hereby reducing the rate with which contaminant states are populated.

Chapter 3

Numerical aspects and methods

In this chapter we review important theories, aspects and methods through which results obtained within the scope of this thesis have been computed. In Section 3.2 we introduce Gutzwiller theory, a mean-field theory allowing us to truncate the Hilbert space of the considered system and hereby greatly reducing computational cost of the numerical calculation. We then derive the different mean-fields obtained through the decoupling of the non-local operators. Through some exemplary phase diagram calculations we review the quality of the method with respect to the severity of the Hilbert space truncation. In Section 3.3 we derive the Lindblad master equation, a generalized master equation for open quantum systems that includes dissipative and decoherent processes. We start with the von-Neumann equation, introduce the Born-Markov approximation and finally obtain the Lindblad master equation. In the end we elaborate on quench-type and adiabatic time evolutions and briefly discuss the adiabatic criteria.

3.1 Introduction

The computation of many-body ground states and their properties is no easy feat. The most straightforward way to compute the ground state of an Hamiltonian is through the time-independent Schrödinger equation, which would only require exact diagonalization (ED) given an appropriate basis. However for many-body systems the Hilbert space of the problem is usually immense and thus the computation of the corresponding many-body ground states through ED too demanding. In order to reduce the computational effort and cost of solving the problem, while achieving high accuracy of the result, several methods established themselves in the context of quantum gases trapped in optical lattices over the years.
Among these popular methods are the Quantum Monte Carlo (QMC) methods, used to obtain phase transitions and simulate dynamical behavior of bosonic and fermionic systems [198–203], and the dynamical mean-field theory (DMFT) with its many extensions, with which band structures, distribution of local quantities and even nonequilibrium systems can be investigated [204–208].

Another significant method lies within Gutzwiller mean-field theory. Developed by Martin Gutzwiller around 1963 this theory was original intended to provide a variational wave function for strongly correlated electrons on a rigid lattice, which was later used to compute ground states of fermionic systems trapped in optical lattices [209–212]. The idea behind Gutzwiller mean-field theory for bosonic systems is simple: If the Hilbert space of the full system, of which we want to compute the many-body ground state, is too large, we divide the system into subsystems embedded in a mean-field given by the surrounding subsystems. The dimension of the corresponding Hilbert spaces are thus reduced and computation of the many-body ground state through becomes computationally feasible. As Gutzwiller theory appeared to be a promising method for computing properties of fermionic systems [213–215], a bosonic variant was developed [216, 217] and since then successfully applied on plain and extended Bose-Hubbard models [218–220]. The many-body ground states of mixtures of bosonic and fermionic atoms have also been hereby obtained [221].
In what follows we discuss Gutzwiller mean-field theory, its variational wave function and the mean-field decouplings necessary to adequately compute the ground state of a subsystem.

3.2 Gutzwiller mean-field theory

For a lattice system with N sites and at most $k \in \mathbb{N}$ bosons per site, the size of the Hilbert space $\mathcal{H}$ is given by $\dim(\mathcal{H}) = k^N$ and thus ED of the relevant Hamiltonian requires a high computational effort. Within Gutzwiller theory however, we can introduce a variational ansatz, also known as variational Gutzwiller approach or Gutzwiller ansatz, to the many-body wave function by which we reduce the dimensionality of the system. For bosons trapped in a periodic lattice, the lattice wave function thus factorizes as

$$|\Psi\rangle = \prod_{\mathcal{C}} |\Psi\rangle_{\mathcal{C}}\,, \tag{3.1}$$

where $|\Psi\rangle_{\mathcal{C}}$ is the wave function of a subsystem $\mathcal{C}$ of the lattice. Note that the Gutzwiller variational wave function was originally given by a product of wave functions on single sites and the generalization to non-trivial subsystems has been provided in a recent work [222]. The computational power required for numerical calculations within the subsystems is significantly smaller, as the dimension of the corresponding reduced Hilbert space for N' sites is $\dim(\mathcal{H}) = k^{N'}$ with $N \gg N'$. According to the variational ansatz Eq. (3.1), the many-body ground state of the whole system can then be retrieved through computation of the ground state wave function of each individual subsystem.
As each subsystem is treated individually within Gutzwiller theory, we need to derive their respective Hamiltonians through the original Hamiltonian of the full system. To this end, we decouple the Hamiltonian $\hat{H}$ as

$$\hat{H} = \sum_{\mathcal{C}} \hat{H}_{\mathcal{C}}, \tag{3.2}$$

with the subsystem Hamiltonians $\hat{H}_{\mathcal{C}}$. The local terms of the Hamiltonian $\hat{H}$ are already decoupled, since each subsystem possesses its own set of unique lattice sites. However, decoupling non-local processes proves to be more challenging, since these terms connect sites of different subsystems and therefore need to be dealt with in a different way. Note that Eq. (3.2) is an approximation, since it already assumes the existence of decoupled and hereby approximated non-local terms.
Gutzwiller theory however is a mean-field theory, through which we can view each subsystem embedded in a mean-field, which is determined by the wave function of the surrounding subsystems it was previously connected to. Each subsystem possesses its own mean-field and effectively reproduces its coupling to previously connected subsystems. In the following, we introduce the relevant *mean-field approximations*, through which we are able to decouple the corresponding Hamiltonian terms and obtain the subsystem Hamiltonians.

3.2.1 Mean-field decoupling and approximations

We expand an operator $\hat{O} \in \{\hat{b}, \hat{n}\}$ around its expectation value $\langle \hat{O} \rangle = \langle \Psi | \hat{O} | \Psi \rangle$ as

$$\hat{O} = \langle \hat{O} \rangle + \delta O \tag{3.3}$$

with the quantum fluctuation $\delta O = \hat{O} - \langle \hat{O} \rangle$, which is the deviation from the expectation value. Within the mean-field theory, we assume these quantum fluctuations to be small enough such that they are vanishing in second order. This is the mean-field approximation and reads

$$(\delta O)^n \approx 0 \quad \text{for} \quad n \geq 2. \tag{3.4}$$

Although the mean-field approximation can be applied to many different non-local terms we use the approximation to decouple the kinetic hopping term and the long-range interaction.
The hopping process connects two different sites i and j, in our case nearest neighbors. If these two sites are from different subsystems $\mathcal{C}$ and $\mathcal{C}'$, i.e. $i \in \{1, ..., N'\}_{\mathcal{C}}$ and j with $i \in \{1, ..., N'\}_{\mathcal{C}'}$, the corresponding hopping term can be expanded and approximated through Eq. (3.3) and Eq. (3.4) as

$$\begin{aligned} \hat{b}_i^\dagger \hat{b}_j &\overset{(3.3)}{=} \hat{b}_i^\dagger \langle \hat{b} \rangle_j + \hat{b}_j \langle \hat{b}^\dagger \rangle_i - \langle \hat{b} \rangle_i \langle \hat{b}^\dagger \rangle_j + \delta \hat{b}_j^\dagger \delta \hat{b}_i \\ &\overset{(3.4)}{\approx} \hat{b}_i^\dagger \langle \hat{b}_j \rangle + \hat{b}_j \langle \hat{b}^\dagger \rangle_i - \langle \hat{b} \rangle_i \langle \hat{b}^\dagger \rangle_j. \end{aligned} \tag{3.5}$$

Through the approximation we decouple terms coupling different sites and hereby obtain local terms. By taking into account the sum over i and j, we can reorganize the terms and simplify as

$$\begin{aligned} J \sum_{\langle i,j \rangle} \hat{b}_i^\dagger \hat{b}_j &= J \sum_{\langle i,j \rangle} (2 \hat{b}_i^\dagger \langle \hat{b}_j \rangle - \langle \hat{b} \rangle_i \langle \hat{b}^\dagger \rangle_j) \\ &= J \sum_i (\hat{b}_i^\dagger \sum_{j \in \{\mathrm{NN}(i) \cap \mathcal{C}'\}} \langle \hat{b}_j \rangle - \frac{1}{2} \langle \hat{b}_i^\dagger \rangle \sum_{j \in \{\mathrm{NN}(i) \cap \mathcal{C}'\}} \langle \hat{b}_j \rangle). \end{aligned} \tag{3.6}$$

Here we used the fact that the sum over the pair of sites i and j can be split as

$$\sum_{\langle i,j\rangle} = \frac{1}{2}\sum_{i}\sum_{j\in\{\mathrm{NN}(i)\cap\mathcal{C}'\}}, \tag{3.7}$$

where the prefactor takes into account double counting and $\mathrm{NN}(i)$ denotes the nearest neighboring sites of site i. At this step, we already see the influence of the surrounding subsystem through the sum of the observable $\langle\hat{b}_j\rangle$ of the neighboring site j, which acts as the mean-field for site i. We thus introduce the first mean-field parameter

$$\xi_i \equiv \sum_{j\in\{\mathrm{NN}(i)\cap\mathcal{C}'\}}\langle\hat{b}_j\rangle \tag{3.8}$$

and rewrite the complete kinetic energy term of the original Hamiltonian as

$$J\sum_{\langle i,j\rangle}(\hat{b}_i^\dagger\hat{b}_j+\hat{b}_j^\dagger\hat{b}_i) = J\sum_{i}(\hat{b}_i^\dagger\xi_i+\hat{b}_i\xi_i^*-E_i^{\mathrm{hop}}) \tag{3.9}$$

with the energy offset $E_i^{\mathrm{hop}} = -\frac{1}{2}(\langle\hat{b}_i^\dagger\rangle\xi_i+\langle\hat{b}_i\rangle\xi_i^*)$ resulting from the Gutzwiller approximation. We hereby obtain a local term effectively describing the hopping process at the boundary of the cluster. Within this picture, the hopping of bosons between two neighboring sites of different subsystems is described as the creation or annihilation of bosons, with a rate depending on the surrounding mean-field. Although the kinetic term has been hereby decoupled, the influence of neighboring sites appears within the mean-field parameter through the expectation value of local observables.

In comparison to the kinetic term, the coupling due to long-range interaction is not restricted to nearest or next-nearest neighboring sites. Although the distance between two coupled sites is potentially seemingly infinite, e.g. in the case of van-der-Waals interaction, we expand the long-range interaction term in a similar way

$$\begin{aligned}\hat{n}_i\hat{n}_j &\overset{(3.3)}{=} \hat{n}_i\langle\hat{n}\rangle_j+\hat{n}_j\langle\hat{n}\rangle_i-\langle\hat{n}\rangle_i\langle\hat{n}\rangle_j+\delta\hat{n}_j\delta\hat{n}_i\\ &\overset{(3.4)}{\approx} \hat{n}_i\langle\hat{n}_j\rangle+\hat{n}_j\langle\hat{n}\rangle_i-\langle\hat{n}\rangle_i\langle\hat{n}\rangle_j.\end{aligned} \tag{3.10}$$

This type of approximation is referred to as the *Hartree approximation*. It was first introduced in order to decouple complicated electron-electron interaction terms [223] and is used in order to simplify various interaction processes through the introduction of single-particle wave functions [224, 225]. Within this approximation, the sum of long-range interaction processes, which couple two sites $i\in\mathcal{C}$ and $j\in\mathcal{C}'$ from different subsystems can be written as

$$\sum_i\sum_{j\neq i}V_{ij}\hat{n}_i\hat{n}_j = \sum_i(2\hat{n}_i\sum_{j\in\mathcal{C}'}V_{ij}\langle\hat{n}_j\rangle-\langle\hat{n}_i\rangle\sum_{j\in\mathcal{C}'}V_{ij}\langle\hat{n}_j\rangle). \tag{3.11}$$

The long-range interaction now resembles an additional on-site potential, the depth of which is given by the mean-field parameter

$$\eta_i \equiv 2 \sum_{j \in \mathcal{C}'} V_{ij} \langle \hat{n}_j \rangle. \tag{3.12}$$

The long-range interaction is then ultimately rewritten as

$$\sum_i \sum_{j \neq i} = \sum_i (\eta_i \hat{n}_i - E_i^{\text{int}}) \tag{3.13}$$

with the energy offset $E_i^{\text{int}} = -\frac{1}{2}\eta_i \langle \hat{n}_i \rangle$ of the interaction. The overall energy offset $E_i^{\text{off}} = E_i^{\text{hop}} + E_i^{\text{int}}$ does not affect the many-body eigenstates, but becomes relevant again for the calculation of the many-body ground state energies. Note that for homogeneous and some inhomogeneous systems the observables on the previously coupled sites are identical. For a single-site cluster, the mean-field parameters can be simplified to $\xi_i = z\langle \hat{b}_i \rangle$ and $\eta_i = z_{\text{int}} \langle \hat{n}_i \rangle$ with the coordination numbers z, which describes the number of nearest neighbors, and z_{int}, which describes the number of sites coupled to site i through the long-range interaction. These coordination numbers essentially rescale the hopping amplitude J and the long-range interaction V_{ij}.

We hereby obtain decoupled terms for the processes initially coupling two different subsystems and can now find the equilibrium ground state of the whole system through numerical diagonalization of each subsystem. Through the mean-field parameters ξ_i and η_i, each subsystem depends on the set of local observables of the subsystems they are connected to and therefore, finding the equilibrium ground-state of one subsystem requires all other subsystem to be already in their ground state. This is commonly handled through a self-consistent method, in which an initial guess of the subsystem's states converges to the many-body ground state through an iterative procedure (see Appendix A.1). In case different initial guesses lead to different converged many-body ground states, we choose the true ground state through comparison of the corresponding ground state energies.

3.2.2 Single-site Gutzwiller versus Cluster Gutzwiller

One commonly differentiates between the single-site Gutzwiller approximation for a subsystem of one site ($|\mathcal{C}| = 1$) and the cluster Gutzwiller approximation for larger subsystems ($|\mathcal{C}| > 1$). With respect to computational effort required for computing the many-body ground states of large, inhomogeneous systems, the single-site Gutzwiller has the upper hand. The size of the corresponding Hamiltonians are solely given by the cutoff of the bosonic Fock space k on each site, which is typically a few particles, and therefore its initialization and diagonalization do not come at high computational cost. Suppose we want to find the many-body ground state of a system consisting of N sites and a cutoff k per site, the computational cost of ED through singular value decomposition would thus be $\mathcal{O}(k^{3N})$. By splitting the system into at most M unique subsystems of N' sites, such

that $M \cdot N' \leq N$, we are able to achieve a reduced complexity bound by $\mathcal{O}(Mk^{3N'})$. In the single-site Gutzwiller limit $N' \to 1$, the ratio $\mathcal{O}(\frac{N}{N'}k^{3(N'-N)})$ converges to its lowest value possible.
On the other hand, reduction of computational effort by decreasing the size of the individual subsystems leads to a loss of potentially important quantum fluctuations. We therefore elaborate in what follows the impact of the mean-field decoupling on the many-body ground state and its severity based on the cluster size.

Validity of the mean-field approximations

The drawback of reducing the sizes of the subsystems is the severity of the Gutzwiller approximations. While quantum fluctuations at borders of subsystems are assumed to be vanishing, they are still taken into account within the bulks. Therefore reducing the subsystem size increases the ratio between border and bulk, ultimately leading to bulkless subsystems when going to the single-site Gutzwiller. In order to determine the importance of these quantum fluctuations, we compute the phase diagram of the Bose-Hubbard model for various subsystem sizes (see Fig. 3.1). We observe that the MI regime extends as the subsystem size increases. The MI phases close to the phase transition benefit from the additional quantum fluctuations, as they reduce the ground state energy of the insulating phase and therefore shifts the MI-SF phase transition to higher hopping amplitudes. The shift ultimately converges towards a critical hopping amplitude, which was determined through QMC to be $(zJ/U)_c \approx 0.239$ [198]. Although the shift is substantial, we obtain a qualitatively correct phase diagram even with single-site and cluster Gutzwiller variational ansatz of small subsystems, which are in agreement with phase diagrams obtained by other methods, such as DMFT and QMC [198, 207, 208].

For checking the validity of the Hartree approximation, we determine the previously-discussed soft-core potential through computation with the Hamiltonian given by Eq. (2.57) after Hartree decoupling. For an atom i in the basis $\{|g\rangle, |e\rangle\}$ the decoupled Hamiltonian given by

$$\hat{H}_i^{\mathrm{Hrt}} = \begin{pmatrix} 0 & \Omega/2 \\ \Omega/2 & -\Delta + \eta_i \end{pmatrix} + E_i^{\mathrm{Hrt}} \tag{3.14}$$

with the mean-field parameter $\eta_i = C_6 \sum_j \langle \hat{n}_i^e \rangle / R_{ij}^6$ and the energy offset E_i^{int} obtained through the Hartree approximation. For $N = 2$, the mean-field parameter simplifies to $\eta_i = C_6 \langle \hat{n}_j^e \rangle / R^6$, where $\langle \hat{n}_j^e \rangle$ is the excited-state admixture of the other atom $j \neq i$ and R the interatomic distance between atoms i and j. We obtain the equilibrium ground state of the system self-consistently (see Appendix A.1).

We find that the soft-core potential $U^{\mathrm{ex}}(R)$ of the full Hamiltonian and the soft-core potential $U^{\mathrm{ap}}(R)$ calculated within the Hartree approximation match in shape, although they differ by their amplitude U_0 (see Fig. 3.2). While the ratio $U^{\mathrm{ex}}/U^{\mathrm{ap}}$ is relatively large for $\Delta/\Omega > 0$ and converges to one in the limit of large detunings, the mismatch becomes substantial for negative detunings $\Delta/\Omega < 0$. On the other hand the strength

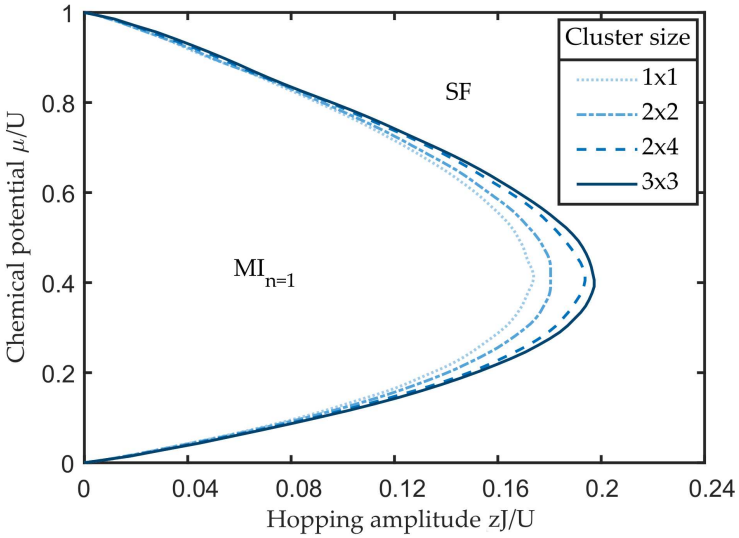

Figure 3.1: Phase transition between the $\mathrm{MI}_{n=1}$ and the SF regime computed for different cluster sizes. Larger clusters allow to incorporate more quantum fluctuations, which reduce the energy of the MI phase close to the phase transition and hereby shifts the boundary to larger hopping amplitudes. By further increasing the cluster size beyond the considered clusters the tip of the lobe converges to a finite value obtained through QMC calculations [198].

V/Ω of the long-range interaction does not influence the quality of the approximation, but merely affects the extent of the soft-core potential. This is in agreement with the analytic expression of the soft-core potential Eq. (2.66), as the long-range interaction only affects the characteristic range R_c of the potential. While the ratio becomes substantial for negative detunings, it is worth mentioning that the phases obtained for these values have weak excited-state admixture, since the detuning acts as a repulsive on-site potential for the excited state. Both soft-core potentials obtained might appear to be differing strongly through the ratio $U^{\mathrm{ex}}/U^{\mathrm{ap}}$, but their amplitudes U_0 are insignificantly small.

We further check the quality of the Hartree approximation for few atoms $N > 2$. As the basis increases rapidly with growing atom number, we omit the matrix representation and write the full Hamiltonian

$$\hat{H}_i^{\mathrm{Hrt}} = -\Delta \hat{n}_i^e + \frac{\Omega}{2}((\hat{b}_i^e)^\dagger \hat{b}_i^g + \mathrm{h.c.}) + \eta_i \hat{n}_i^e + E_i^{\mathrm{int}} \tag{3.15}$$

For $N = 3$ and $N = 4$ atoms, the geometry of the system starts to play a role. Since in periodic systems we expect distributions of equidistant atoms to be resulting in the equilibrium state with lowest energy, we consider a triangular constellation of three atoms and a square of four atoms with length R of the edges. We have the possibility to treat each atom individually, but since we have more atoms now, we can also split the system into subsystems containing more than one atom. The various combinations of subsystem

d or

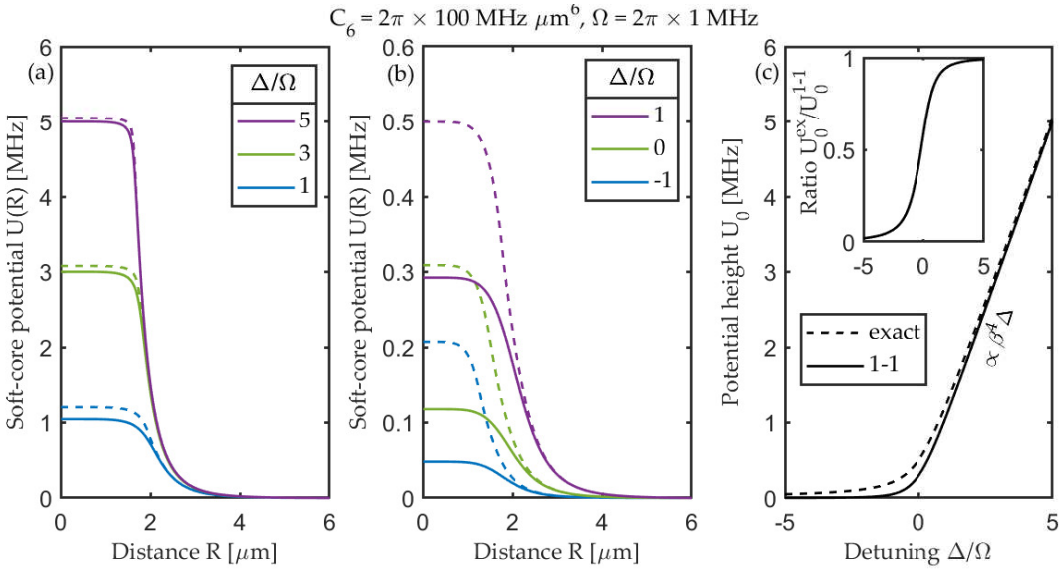

Figure 3.2: The exact soft-core potentials $U^{\mathrm{ex}}(R)$ (solid line) and soft-core potentials $U^{\mathrm{ap}}(R)$ obtained through the Hartree-approximation (dashed line) at (a) positive detunings and (b) negative detunings for two atoms. For positive detunings the approximated soft-core potential highly resembles the exact potential, although the difference becomes more substantial at zero or negative detunings. While the absolute difference of their height U_0 is not substantial for any detunings (c), the ratio shows the discrepancy at negative values (see inset).

sizes allows to investigate the influence of quantum fluctuations further. Note that the computed soft-core potentials for $N > 2$ are then the averaged soft-core potential between all atoms of different subsystems. The soft-core potential between two atoms of the same subsystem corresponds to the exact soft-core potential.
For both $N = 3$ and $N = 4$, we find an increasing match between the potentials of the exact Hamiltonian and within the Hartree approximation for any subsystem combination at higher detunings Δ/Ω (see Fig. 3.3 and 3.4). Similar to the results obtained for $N = 2$, the potentials begin to differ strongly as we go to negative detunings. Now that we can compare different subsystem combinations, we observe that larger subsystems improve the quality of the Hartree approximation. The ratio $U_0^{\mathrm{ex}}/U_0^{\mathrm{ap}}$ determined for single-atom subsystems does not seem to depend on the number of atoms.
We therefore conclude that the Hartree approximation gives adequate results for relevant detunings. Although negative detunings appear to greatly overestimate the correct soft-core potential height, the admixture of the excited state in this regime is vanishingly small and thus we expect the physics of the electronic ground state to dominate.

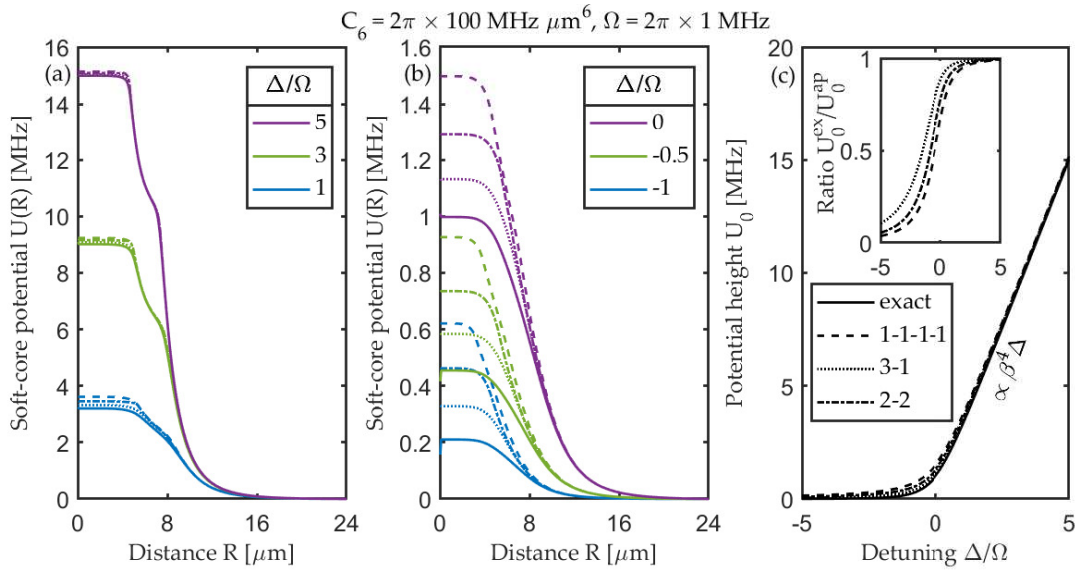

Figure 3.3: The exact soft-core potentials $U^{\mathrm{ex}}(R)$ (solid line) and soft-core potentials $U^{\mathrm{ap}}(R)$ obtained through the Hartree-approximation (dashed line) at (a) positive detunings and (b) negative detunings for three atoms, and (c) their height U_0 versus detuning. The system can be decoupled either in three subsystems of one atom or two subsystem with one and two atoms. The latter provides a better approximation for any detunings as it allows to incorporate more density fluctuations neglected in the three subsystem splitting.

In the end Gutzwiller mean-field theory provides qualitatively very good results and has been used since its formulation for the computation of many-body ground states of many different types of bosonic systems [218–220]. However it is important to acknowledge that actual phase transitions may differ from the ones obtained through the variational Gutzwiller ansatz and thus benchmark calculations can potentially become necessary in the vicinity of boundaries in the phase diagram.

3.3 Master equation in Lindblad form

Besides calculating equilibrium ground states of systems, an Hamiltonian can be used to determine dynamics as well. The parameters of each term within the Hamiltonian can not only be seen as energies tied to certain quantum mechanical and physical processes, but also as their amplitudes, with which they occur. Within the Schrödinger picture, in which the state is time-dependent, the Hamiltonian is the generator of time-evolution through the time-dependent Schrödinger equation

$$\hat{H}\,|\Psi(t)\rangle = i\hbar\frac{d}{dt}\,|\Psi(t)\rangle\,, \tag{3.16}$$

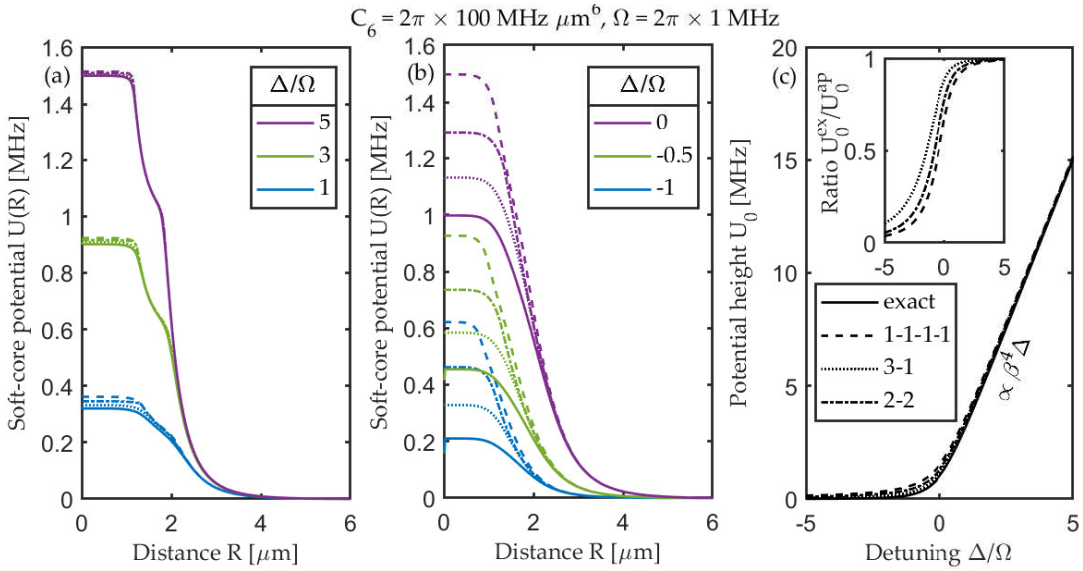

Figure 3.4: The exact soft-core potentials $U^{\mathrm{ex}}(R)$ (solid line) and soft-core potentials $U^{\mathrm{ap}}(R)$ obtained through the Hartree-approximation (dashed line) at (a) positive detunings and (b) negative detunings for four atoms, and (c) their height U_0 versus detuning. For four atoms there are more ways to decouple the system and the splitting into two subsystems with one and three atoms yields the best approximation.

where $|\Psi(t)\rangle$ is an arbitrary state at time t and $\hat{H}$ the Hamiltonian of the system. Its solution yields the unitary time-evolution of the given state, with which the state at a latter time t' can be determined. It reads

$$\left|\Psi(t')\right\rangle = U(t',t)\left|\Psi(t)\right\rangle = e^{-\frac{i\hat{H}(t'-t)}{\hbar}}\left|\Psi(t)\right\rangle \tag{3.17}$$

with the unitary time evolution operator $U(t',t')$. If the current state of a system is an eigenstate of the Hamiltonian, the time-dependent Schrödinger equation reveals the time-independent equation

$$\begin{aligned}\hat{H}\left|\Psi_{GS}(t)\right\rangle &= i\hbar\frac{d}{dt}\left|\Psi_{GS}(t)\right\rangle \\ &= i\hbar\frac{d}{dt}e^{-\frac{i\hat{H}t}{\hbar}}\left|\Psi_{GS}(0)\right\rangle \\ &= Ee^{-\frac{i\hat{H}t}{\hbar}}\left|\Psi_{GS}(0)\right\rangle \\ &= E\left|\Psi_{GS}(t)\right\rangle\end{aligned} \tag{3.18}$$

and the state $|\Psi_{GS}(t)\rangle = |\Psi_{GS}\rangle$ is thus considered stationary. Its time-evolution only yields a phase

$$\left\langle\Psi(t)\middle|\Psi(t')\right\rangle = \left\langle\Psi(t)\right|e^{-\frac{i\hat{H}(t'-t)}{\hbar}}\left|\Psi(t)\right\rangle = e^{-\frac{iE(t'-t)}{\hbar}}. \tag{3.19}$$

Another way to describe time-evolution given by an Hamiltonian is through the density matrix $\hat{\rho}$, which is also time-dependent within the Schrödinger picture through the time-dependent states and its most general form reads

$$\hat{\rho}(t) = \sum_l p_l \left|\Psi_l(t)\right\rangle \left\langle\Psi_l(t)\right| \tag{3.20}$$

where p_l is the probability of the pure state $|\Psi_l(t)\rangle$. The time-evolution of the density matrix can be derived through the unitary time evolution of a pure state Eq. (3.16) as

$$\begin{aligned}\frac{d}{dt}\rho(t) &= \frac{d}{dt}\sum_l p_l \left|\Psi_l(t)\right\rangle \left\langle\Psi_l(t)\right| = \sum_l p_l \frac{d}{dt}(\left|\Psi_l(t)\right\rangle \left\langle\Psi_l(t)\right|) \\ &= -\frac{i}{\hbar}\sum_l p_l(\hat{H}\left|\Psi_l(t)\right\rangle \left\langle\Psi_l(t)\right| - \left|\Psi_l(t)\right\rangle \left\langle\Psi_l(t)\right|\hat{H}) \\ &= -\frac{i}{\hbar}(\hat{H}\hat{\rho} - \hat{\rho}\hat{H}),\end{aligned} \tag{3.21}$$

which finally yields

$$\frac{d}{dt}\hat{\rho}(t) = -\frac{i}{\hbar}[\hat{H}, \hat{\rho}(t)]. \tag{3.22}$$

This formula is known as the von Neumann equation, the quantum mechanical analogue to Liouville's theorem. Analogous to the stationary state $|\Psi_{GS}\rangle$ a density matrix diagonal in the eigenbasis of the Hamiltonian does not evolve in time, since in this case the Hamiltonian and the density matrix commute, i.e. $[\hat{H}, \hat{\rho}_{GS}] = 0$.
Although the unitary time-evolution is especially useful for numerical simulations of quench dynamics, i.e. time-evolution of states, which are not eigenstates of the studied Hamiltonian, the application is limited to system with reversible processes. Since the Hamiltonian is hermitian by definition, non-unitary processes can not be included.

Master equation

A formalism commonly used in the context of time evolution of open quantum systems are the so-called master equations. Since it was developed to model the time-evolution of systems, with dynamics that can be described by a probabilistic, time-dependent superposition of states, it possesses a high applicability in quantum physics. For a time-dependent density matrix $\rho(t)$, the master equation in its most general form yields

$$\frac{d}{dt}\rho(t) = f(t, \hat{H}, \hat{\rho}(t)) \tag{3.23}$$

In order to derive the master equation of a system with non-unitary time evolution, it is important to understand its origin. To this end, we consider an isolated system composed of two subsystems S and B with the corresponding Hamiltonian

$$\hat{H} = \hat{H}_S + \hat{H}_B + \hat{H}_{SB} \tag{3.24}$$

with their most-general form of the coupling Hamiltonian

$$\hat{H}_C = \hbar \sum_\alpha \hat{S}_\alpha \otimes \hat{B}_\alpha, \tag{3.25}$$

where the operators $\hat{S}_\alpha$ and $\hat{B}_\alpha$ acts on subsystem S and B respectively. If both subsystems were not coupled, i.e. $\hat{H}_{SB} = 0$, they would exhibit unitary evolution in time. For finite coupling however the exchange can lead to the loss of energy, which is referred to as *quantum dissipation*, and the loss of coherence, which is coined as *quantum decoherence* [226]. Although these processes affect both subsystems individually, the dynamics of the whole system however remain unitary.
Based on this notion we derive the master equation in Lindblad form also referred to as Lindblad master equation. Non-unitary processes couple a subsystem S to the environment, which can be seen as a bath B. In order to derive the non-unitary description in S, we consider the isolated system given by $\hat{H}$ and trace out the bath B. While the idea sounds simple, it requires extensive derivations and heavily relies on the properties in the bath.
The Lindblad master equation can be derived in various ways, such as with quantum dynamical maps [227] or through the Born-Markov master equation [228], and offers different insight based on the derivation. The derivation presented in this work is a generalized version of [229] and yields despite the more generous approximations the desired master equation.

Interaction picture

We consider the system containing both the subsystem S and the bath B. For no coupling the subsystems are isolated and the systems eigenstates are given by the eigenstates of S and B. For the sake of simplicity throughout the derivation, we thus define the unperturbed Hamiltonian $\hat{H}_0 = \hat{H}_S + \hat{H}_B$. Since the coupling can be understood as a perturbative term, it is useful to introduce the interaction picture, which is defined as

$$\hat{O}^I(t) = e^{\frac{i}{\hbar}\hat{H}_0 t}\hat{O}(t)e^{-\frac{i}{\hbar}\hat{H}_0 t} \tag{3.26}$$

For a time-dependent density matrix $\hat{\rho}(t) = e^{-\frac{i}{\hbar}\hat{H}t}\hat{\rho}(0)e^{\frac{i}{\hbar}\hat{H}t}$ of the isolated system, the interaction picture yields

$$\begin{aligned}\hat{\rho}^I(t) &= e^{\frac{i}{\hbar}\hat{H}_0 t}\hat{\rho}(t)e^{-\frac{i}{\hbar}\hat{H}_0 t} \\ &= e^{\frac{i}{\hbar}\hat{H}_0 t}e^{-\frac{i}{\hbar}\hat{H}t}\hat{\rho}(0)e^{\frac{i}{\hbar}\hat{H}t}e^{-\frac{i}{\hbar}\hat{H}t}.\end{aligned} \tag{3.27}$$

Taking the time-derivative, we obtain

$$\begin{aligned}\frac{d}{dt}\hat{\rho}^I(t) &= \frac{i}{\hbar}[\hat{H}_0, \hat{\rho}^I(t)] + e^{\frac{i}{\hbar}\hat{H}_0 t}\Big(\frac{d}{dt}\hat{\rho}(t)\Big)e^{-\frac{i}{\hbar}\hat{H}_0 t} \\ &= \frac{i}{\hbar}[\hat{H}_0, \hat{\rho}^I(t)] - \frac{i}{\hbar}e^{\frac{i}{\hbar}\hat{H}_0 t}[\hat{H}, \hat{\rho}(t)]e^{-\frac{i}{\hbar}\hat{H}_0 t} \\ &= \frac{i}{\hbar}[\hat{H}_0, \hat{\rho}^I(t)] - \frac{i}{\hbar}e^{\frac{i}{\hbar}\hat{H}_0 t}[\hat{H}_0 + \hat{H}_C, \hat{\rho}(t)]e^{-\frac{i}{\hbar}\hat{H}_0 t} \\ &= \frac{i}{\hbar}([\hat{H}_0, \hat{\rho}^I(t)] - [\hat{H}_0, \hat{\rho}^I(t)] - [\hat{H}_C^I, \hat{\rho}^I(t)])\end{aligned} \tag{3.28}$$

from which we obtain the von-Neumann equation in the interaction picture

$$\frac{d}{dt}\hat{\rho}^I(t) = -\frac{i}{\hbar}[\hat{H}_C^I, \hat{\rho}^I(t)] \tag{3.29}$$

Subsequent integration over time renders the expression iterative

$$\hat{\rho}(t) = \hat{\rho}(0) - \frac{i}{\hbar}\int_0^t dt_1[\hat{H}_C^I(t_1), \hat{\rho}^I(t_1)], \tag{3.30}$$

which can be written as a series expansion

$$\hat{\rho}(t) = \hat{\rho}(0) + \sum_{n>0}^{\infty}(-\frac{i}{\hbar})^n \int_0^t dt_1 ... \int_0^{t_{n-1}} dt_n[\hat{H}_C^I(t_1), ..., [\hat{H}_C^I(t_n), \hat{\rho}^I(0)]] \tag{3.31}$$

While the expression is exact, a simplification is required for the sake of numerical computation.

Born approximation

The most intuitive approximation to be made is based on the assumption, that the perturbation, i.e. the coupling between subsystem and bath, is vanishing for terms higher than second order. We therefore only expand the series up to the second order

$$\begin{aligned}\hat{\rho}(t) \approx \hat{\rho}(0) &- \frac{i}{\hbar}\int_0^t dt_1[\hat{H}_C^I(t_1), \hat{\rho}^I(0)] \\ &- \frac{1}{\hbar^2}\int_0^t dt_1 \int_0^{t_1} dt_2[\hat{H}_C^I(t_1), [\hat{H}_C^I(t_2), \hat{\rho}^I(0)]]\end{aligned} \tag{3.32}$$

and introduce this formula into the von-Neumann equation Eq. (3.29) and perform the trace over B

$$\frac{d}{dt}\hat{\rho}_S(t) \equiv \mathrm{tr}\Big(\frac{d}{dt}\hat{\rho}(t)\Big) = -\frac{i}{\hbar}\mathrm{tr}([\hat{H}_C^I(t), \hat{\rho}^I(0)]) - \frac{1}{\hbar^2}\int_0^t dt_1 \mathrm{tr}\Big(\Big[\hat{H}_C^I(t), [\hat{H}_C^I(t_1), \hat{\rho}^I(t_1)]\Big]\Big). \tag{3.33}$$

In order to perform the trace, let us first consider that the subsystem and the bath are initially decoupled, i.e. $\hat{\rho}(t) = \hat{\rho}_S(t) \otimes \hat{\rho}_B(0)$. Since the bath merely exists to introduce

and describe non-unitary processes in the system as a coupling of to environment, we expect its initial state to be thermal

$$\rho_B(0) = \frac{e^{\frac{\hat{H}_B}{k_B T}}}{Z} \tag{3.34}$$

with the partition function $Z = \mathrm{tr}(e^{\frac{\hat{H}_B}{k_B T}})$. We now assume the bath to be large and the coupling weak enough, such that the initial state of the bath is not considerably changed with time, i.e. $\hat{\rho}_B(t) \approx \hat{\rho}_B(0) \equiv \hat{\rho}_B$. This yields the *Born approximation*, which reads

$$\hat{\rho}(t) = \hat{\rho}_S(t) \otimes \hat{\rho}_B \tag{3.35}$$

and states that the subsystem and the bath are at no point in time entangled and allows us to simplify the series expansion. We thus calculate the first commutator on the right hand side of the equation with the general definition of the coupling Hamiltonian

$$\mathrm{tr}([\hat{H}_C^I(t), \hat{\rho}^I(0)]) = \sum_\alpha (\hat{S}_\alpha(t)\hat{\rho}_S(0)\mathrm{tr}_B(\hat{B}_\alpha(t)\hat{\rho}_B(0)) - \hat{\rho}_S(0)\hat{S}_\alpha(t)\mathrm{tr}_B(\hat{B}_\alpha(t)\hat{\rho}_B(0))) \tag{3.36}$$

Here it is safe to set the expectation value $\langle \hat{B}_\alpha(t) \rangle = \mathrm{tr}_B(\hat{B}_\alpha(t)\hat{\rho}_B(0)) = 0$, as it does not change the underlying physics. However if we assume the expectation value to be finite, we can simply reformulate the original coupling Hamiltonian H_C and find, that the finite expectation values of the bath operators simply shift the energies of the associated system operators by a constant value. We thus rewrite

$$\frac{d}{dt}\hat{\rho}_S^I(t) = -\frac{1}{\hbar^2}\int_0^t dt_1 \mathrm{tr}_B\Big(\Big[\hat{H}_C^I(t), [\hat{H}_C^I(t_1), \hat{\rho}_S(t_1) \otimes \hat{\rho}_B]\Big]\Big) \tag{3.37}$$

The time-evolution of the subsystem S now can be obtained from the integro-differential equation, which is reduced in complexity but still requires computation over the Hilbert space of the whole system and also expects the knowledge about the density matrix at all previous times.

Markov approximation

Through substituting the integration variable $t_1 \to t - t_1$ and extending the upper limit we obtain the so-called *Redfield equation* given by

$$\frac{d}{dt}\hat{\rho}_S^I(t) = \frac{1}{\hbar^2}\int_0^\infty dt_1 \mathrm{tr}_B\Big(\Big[\hat{H}_C^I(t), [\hat{H}_C^I(t-t_1), \hat{\rho}_S(t-t_1) \otimes \hat{\rho}_B]\Big]\Big). \tag{3.38}$$

The reformulation allows us to understand the meaning of the integral better: The integration adds the weighted contributions of past density matrices to determine the current matrix and thus, it is possible to rewrite the formula as a *Nakajima-Zwanzig equation*

$$\frac{d}{dt}\hat{\rho}_S^I(t) = \frac{1}{\hbar^2}\int_0^\infty dt_1 \gamma(t-t_1)\hat{\rho}_S(t-t_1). \tag{3.39}$$

Here, the memory kernel $\gamma(t-t_1)$ quantifies the memory of the system. For the sake of estimation, we explicitly rewrite the Redfield equation with the definition of the coupling Hamiltonian, which reads

$$\frac{d}{dt}\hat{\rho}_S^I(t) = \frac{1}{\hbar^2}\sum_{\alpha,\beta}\int_0^\infty dt_1(\hat{S}_\beta(t-t_1)\hat{\rho}_S(t-t_1)\hat{S}_\alpha(t) - \hat{S}_\alpha(t)\hat{S}_\beta(t-t_1)\hat{\rho}_S(t-t_1))\gamma'_{\alpha,\beta}(t,t_1). \tag{3.40}$$

The memory kernel $\gamma'_{\alpha,\beta}(t,t_1) \equiv \langle \hat{B}_\alpha(t)\hat{B}_\beta(t-t_1)\rangle = \mathrm{tr}_B(\hat{B}_\alpha(t)\hat{B}_\beta(t-t_1)\hat{\rho}_B)$ is a two-point correlation function and since we assumed the bath to be stationary, we can omit the time-dependency and only keep the relative time, i.e. $\gamma'_{\alpha,\beta}(t,t_1) \to \gamma'_{\alpha,\beta}(\tau)$. As a two-point correlation function, we expect its amplitude to decrease exponentially with time $|\gamma'_{\alpha,\beta}(\tau)| \sim \exp(-\tau/\tau_B)$ with the bath relaxation time τ_B. In accordance with the large bath and weak coupling assumption, we expect the relaxation time to be much smaller than the relevant timescales of the subsystem, which yields rapid decay of the two-point correlation $|\gamma'_{\alpha,\beta}(\tau)| \propto \delta(\tau)$. We therefore apply the *Markov approximation*, which implies that the time-evolution of the density matrix only depends on its current state. The Markovian Redfield equation is then rewritten as

$$\frac{d}{dt}\hat{\rho}_S^I(t) = -\frac{1}{\hbar^2}\int_0^\infty dt_1 \mathrm{tr}_B\Big(\Big[\hat{H}_C^I(t),[\hat{H}_C^I(t_1),\hat{\rho}_S(t)\otimes\hat{\rho}_B]\Big]\Big) \tag{3.41}$$

The hereby obtained master equation is known as the *Born-Markov equation* based on the necessary approximation.

Tracing out the bath

We now discuss the time-dependent operators $\hat{S}_\alpha(t)$ and $\hat{B}_\alpha(t)$ of the coupling Hamiltonian. In the Schrödinger picture of the subsystem we write $\hat{S}_\alpha(t) = e^{-i\hat{H}_S t/\hbar}\hat{S}_\alpha(0)e^{-i\hat{H}_S t/\hbar}$ and expand $\hat{S}_\alpha(0) = \sum_\omega \hat{S}_{\alpha,\omega}(0)$ in the basis spanned by the eigenstates with energies $\hbar\omega$ of the Hamiltonian $\hat{H}_S$. For the sake of simplicity, we denote the stationary operators simply as $\hat{S}_{\alpha,\omega}(0) \equiv \hat{S}_{\alpha,\omega}$ until mentioned otherwise. The coupling Hamiltonian becomes

$$\hat{H}_C = \sum_{\alpha,\omega} e^{-i\omega t} S_{\alpha,\omega}\otimes\hat{B}_\alpha(t). \tag{3.42}$$

We input the reformulated coupling Hamiltonian in Eq. (3.40) and evaluate the commutators

$$\frac{d}{dt}\hat{\rho}_S^I(t) = \sum_{\substack{\alpha,\beta\\ \omega,\omega'}}\Big(e^{i(\omega'-\omega)t}\Gamma^\omega_{\alpha,\beta}\Big[\hat{S}_{\alpha,\omega}\hat{\rho}_S(t),\hat{S}^\dagger_{\beta,\omega'}\Big] + e^{i(\omega-\omega')t}(\Gamma^{\omega'}_{\alpha,\beta})^*\Big[\hat{S}_{\alpha,\omega},\hat{\rho}_S(t)\hat{S}^\dagger_{\beta,\omega'}\Big]\Big) \tag{3.43}$$

with the prefactors containing the memory kernel

$$\Gamma^\omega_{\alpha,\beta} = \int_0^\infty \mathrm{d}\tau e^{i\omega\tau}\gamma_{\alpha,\beta}(\tau). \tag{3.44}$$

We now apply the rotating wave approximation on the exponentials $e^{i(\omega'-\omega)t}$. As we expect oscillation given by $\omega - \omega'$ to be way faster than the evolution of the subsystem itself, we discard the off-resonant contributions, which simplifies the sum

$$\frac{d}{dt}\hat{\rho}_S^I(t) = \sum_{\alpha,\beta,\omega} \left(\Gamma^{\omega}_{\alpha,\beta} \left[\hat{S}_{\alpha,\omega}\hat{\rho}_S(t), \hat{S}^{\dagger}_{\beta,\omega} \right] + (\Gamma^{\omega}_{\alpha,\beta})^* \left[\hat{S}_{\alpha,\omega}, \hat{\rho}_S(t)\hat{S}^{\dagger}_{\beta,\omega} \right] \right). \tag{3.45}$$

In order to determine the factors $\Gamma^{\omega}_{\alpha,\beta}$, we specify the properties of the bath even further. We consider the bath to be given by bosons as

$$\hat{H}_B = \hbar \sum_k \omega_k \hat{b}_k^{\dagger}\hat{b}_k \tag{3.46}$$

with the annihilation operator $\hat{b}_k$ of a boson in mode k with energy ω_k. The coupling operators $\hat{B}_\alpha$ can then be rewritten in terms of creation and annihilation of bosons in these modes

$$\hat{B}_\alpha = \sum_k (g_{\alpha,k}\hat{b}_k^{\alpha} + g^*_{\alpha,k}(\hat{b}_k^{\dagger})^{\alpha}), \tag{3.47}$$

and the corresponding time-dependent operator

$$\hat{B}_\alpha(t) = \sum_k (g_{\alpha,k}\hat{b}_k^{\alpha} e^{-i\omega_k \alpha t} + g^*_{\alpha,k}(\hat{b}_k^{\dagger})^{\alpha} e^{i\omega_k \alpha t}) \tag{3.48}$$

Assuming the bath in its initial state is in thermal equilibrium, we can define the system through a collection of bosons in the mode $k = 0$ as

$$\hat{\rho}_B = |00...\rangle \otimes \langle 00...| \tag{3.49}$$

The expectation value of an operator $\hat{O}$ given the density matrix reads

$$\begin{aligned} \mathrm{tr}_B(\hat{O}\hat{\rho}_B) &= \sum_l \langle \Psi_l | \hat{O} | 00...\rangle \langle 00... | \Psi_l \rangle \\ &= \langle 00... | \hat{O} | 00... \rangle \end{aligned} \tag{3.50}$$

With these properties of the bath, we calculate the memory kernel through performing the trace as mentioned above. After some non-trivial algebra the memory kernel yields

$$\gamma'_{\alpha,\beta}(\tau) = \sum_{\alpha,k} |\tilde{g}_{\alpha,k}|^2 e^{-i\omega_k \alpha \tau} \delta_{\alpha,\beta} \tag{3.51}$$

with the rescaled coefficient $g^*_{\alpha,k} = g_{\alpha,k}\sqrt{\alpha}$ and the delta-kronecker $\delta_{\alpha,\beta}$, which breaks down the sum in Eq. (3.45). The prefactors are thus further expressed through

$$\Gamma^{\omega}_{\alpha} = \sum_{\alpha,k} |\tilde{g}_{\alpha,k}|^2 \int_0^{\infty} \mathrm{d}\tau e^{-i(\omega-\omega_{\alpha,k})\tau} = \pi \sum_{\alpha,k} |\tilde{g}_{\alpha,k}|^2 \delta(\omega - \omega_{\alpha,k}), \tag{3.52}$$

which resembles the density of states $J_\alpha^\omega(\tilde{\omega}) = \sum_{\alpha,k} |\tilde{g}_{\alpha,k}|^2 \delta(\tilde{\omega} - (\omega - \omega_{\alpha,k}))$ of the bath bosons with eigenenergy $\omega_{\alpha,k}$ rescaled by the energy ω of subsystem S. We rewrite the factor and finally arrive at

$$\Gamma_\alpha^\omega = \int_0^\infty \mathrm{d}\tilde{\omega} J_\alpha^\omega(\tilde{\omega}) \delta(\tilde{\omega}). \tag{3.53}$$

By application of $\delta(\tilde{\omega})$ obtained through the derivation of Γ_α^ω and reversing the eigenvalue decomposition performed in the beginning, Eq. (3.45) yields

$$\frac{d}{dt}\hat{\rho}_S(t) = \sum_\alpha \Gamma_\alpha \Big[\hat{S}_\alpha(t) \hat{\rho}_S(t) \hat{S}^\dagger(t)_\alpha - \frac{1}{2} \{ \hat{S}_\alpha^\dagger(t) \hat{S}_\alpha(t), \hat{\rho}_S(t) \} \Big] \tag{3.54}$$

In this form, we see that Γ_α gives the amplitude of a process α, which is defined through the subsystem operators $\hat{S}_\alpha$. The bath is traced out and its effect on the subsystem is defined within Γ_α. We conclude the extensive derivation by entering the Schrödinger picture, which yields on the left hand side

$$\begin{aligned} \frac{d}{dt}\hat{\rho}_S^I(t) &= \frac{d}{dt}(e^{\frac{i}{\hbar}\hat{H}_0 t} \hat{\rho}_S(t) e^{-\frac{i}{\hbar}\hat{H}_0 t}) \\ &= e^{\frac{i}{\hbar}\hat{H}_0 t} \Big(\frac{d}{dt}\hat{\rho}_S(t) \Big) e^{-\frac{i}{\hbar}\hat{H}_0 t} + \frac{i}{\hbar} e^{\frac{i}{\hbar}\hat{H}_0 t} \Big[\hat{H}_0, \hat{\rho}_S(t) \Big] e^{-\frac{i}{\hbar}\hat{H}_0 t} \end{aligned} \tag{3.55}$$

and the right hand side

$$\begin{aligned} &\Gamma \Big[\hat{S}(t) \hat{\rho}_S^I(t) \hat{S}^\dagger(t) - \frac{1}{2} \{ \hat{S}^\dagger(t) \hat{S}(t), \hat{\rho}_S^I(t) \} \Big] \\ &\qquad = e^{\frac{i}{\hbar}\hat{H}_0 t} \Gamma \Big[\hat{S} \hat{\rho}_S(t) \hat{S}^\dagger - \frac{1}{2} \{ \hat{S}^\dagger \hat{S}, \hat{\rho}_S(t) \} \Big] e^{-\frac{i}{\hbar}\hat{H}_0 t} \end{aligned} \tag{3.56}$$

of the equation. Note that the Hamiltonian $\hat{H}_B$ commutes with the density matrix $\hat{\rho}_S(t)$, i.e. $[\hat{H}_B, \rho_S(t)] = 0$. Through the transformation the master equation in Lindblad form appears as

$$\frac{d}{dt}\hat{\rho}(t) = -\frac{i}{\hbar} \Big[\hat{H}, \hat{\rho}(t) \Big] + \sum_\alpha \Gamma_\alpha \Big[\hat{S}_\alpha \hat{\rho}(t) \hat{S}_\alpha^\dagger - \frac{1}{2} \{ \hat{S}_\alpha^\dagger \hat{S}_\alpha, \hat{\rho}(t) \} \Big] \tag{3.57}$$

with $\hat{\rho}_S(t) \equiv \hat{\rho}(t)$ and $\hat{H}_S \equiv \hat{H}$. Without dissipation and decoherence $\Gamma_\alpha = 0$, we retrieve the unitary time-evolution given by the von-Neumann equation. The Lindblad master equation allows for the description of dissipative and decoherent processes through the operators $\hat{S}_\alpha$, also referred to as *jump operators*. These operators can be chosen to fit the desired non-unitary process such as two-body losses or decoherence.
Given an initial state, it thus possible to simulate the time-evolution of a system through its density matrix. Numerical calculations with this first-order differential equation can be performed through the Euler or Runge-Kutta method among others. Although many procedures exist with which first-order differential equations can be solved it is not guaranteed that physically conserved quantities stay conserved throughout the time evolution. To this end we employ the simplistic fourth-order Runge-Kutta method, which ensures the conservation of physical quantities (see Appendix A.3).

Decoupled master equation

Within Gutzwiller mean-field theory, the density matrix factorizes into density matrices for each subsystem $\mathcal{C}$ as

$$\hat{\rho}(t) = \prod_{\mathcal{C}} \hat{\rho}_{\mathcal{C}}(t) \tag{3.58}$$

This allows us to formulate a decoupled version of the Lindblad master equation, which is compatible with the many-body ground state calculations, since both rely on the cluster Hamiltonians $\hat{H}_{\mathcal{C}}$. The cluster Lindblad master equation thus reads

$$\begin{aligned}\frac{d}{dt}\hat{\rho}_{\mathcal{C}}(t) = &-\frac{i}{\hbar}\left[\hat{H}_{\mathcal{C}}, \hat{\rho}_{\mathcal{C}}(t)\right] + \sum_m \Gamma_m \left[\hat{S}_m \hat{\rho}_{\mathcal{C}}(t) \hat{S}_m^\dagger - \frac{1}{2}\{\hat{S}_m^\dagger \hat{S}_m, \hat{\rho}_{\mathcal{C}}(t)\}\right] \\ &+ \sum_n \tilde{\Gamma}_n \left[\hat{R}_n \hat{\rho}_{\mathcal{C}}(t) \hat{R}_n^\dagger - \frac{1}{2}\{\hat{R}_n^\dagger \hat{R}_n, \hat{\rho}_{\mathcal{C}}(t)\}\right]\end{aligned} \tag{3.59}$$

Note that the first sum only describes processes within the cluster. For non-local, dissipative and decoherent processes such as two-body atom loss of atoms at a specific distance, a mean-field treatment becomes necessary at the boundary of the cluster and thus the additional sum arises with the decoupled operators $\hat{R}_n$ derived through the previously discussed approximations.

3.3.1 Quench dynamics vs. adiabatic time evolution

Although generally an initial density matrix can be freely chosen as desired, we use the combination between the many-body ground state computation and Lindblad master equation to simulate experimentally realistic time evolutions. To this end, we compute the initial state of the corresponding cluster Hamiltonian $\hat{H}_{\mathcal{C}}$ through the iterative Gutzwiller procedure for a given set of parameters. The resulting many-body ground state $|\Psi_0\rangle$ forms the initial state of the system at $t = 0$. We then define the density matrix $\hat{\rho}(t = 0) = |\Psi_0\rangle \langle\Psi_0|$. Since the many-body ground state is also a steady state if the Hamiltonian $\hat{H}_{\mathcal{C}}$ remains unchanged or no non-unitary processes are present, dynamics are induced in the system by changing parameters of the Hamiltonian $\hat{H}_{\mathcal{C}} \to \hat{H}_{\mathcal{C}}(t)$ or the rates Γ_m. Here, one commonly differentiates between *quench type time evolutions* [230–232] or *adiabatic time evolution* [233–235] based on the time scale τ_{var} within which the parameters are varied: A quench type time evolution implies a sudden change of a parameter in the Lindblad master equation, while adiabatic time evolution involves slowly changing parameters over time. The underlying non-trivial difference is given by the *adiabatic quantum theorem* [236, 237], which states that a system exhibits different time evolutions based on the speed of the changing conditions. For slow, gradual variation of the parameters the many-body system adapts to the change and thus stays in its ground state throughout the complete time evolution. These time-dependent processes are referred to as adiabatic passages. At the end of the parameter ramp at $t = \tau$ the many-body state $\left|\Psi_0^{t=0}\right\rangle$, which was initially the ground state of $\hat{H}_{\mathcal{C}}(t = 0)$, evolves into the ground state $\left|\Psi_0^{t=\tau_{\text{var}}}\right\rangle$ of $\hat{H}_{\mathcal{C}}(t = \tau_{\text{var}})$. On the other hand, the rapid variation of the parameters does not allow

the many-body state to evolve and thus the wave function after the quench is still in the ground state of the initial Hamiltonian, which is an excited state of the Hamiltonian $\hat{H}_{\mathcal{C}}(t = \tau_{\text{var}})$. The transfer of a many-body ground state to an excited state through a quench is called diabatic passage.
For non-dissipative, coherent unitary time evolutions, the adiabatic criteria can be formulated through

$$\tau \gg \frac{\hbar}{\Delta \hat{H}_{\mathcal{C}}} \tag{3.60}$$

with $\Delta \hat{H}_{\mathcal{C}} = \langle \hat{H}_{\mathcal{C}}^2 \rangle - \langle \hat{H}_{\mathcal{C}} \rangle^2$. Note that this equation takes the time-energy variant of the Heisenberg uncertainty principle. The formulation of the adiabatic criteria has been a milestone in experiments involving almost complete population transfer of one ground-state to another [238, 239]. However strong losses and decoherence have been observed to impede such transfer processes [240, 241], which lead to the formulation of a modified adiabatic criteria for open quantum systems [242].
In our work both the quench type as well as the adiabatic time evolutions have their relevance. For the investigation of the existence of steady or long-lived states, quench type time evolutions are reasonable as we expect the system to reorganize and converge towards these states. Quench type time evolutions are also suitable for some experimental setups, where a lattice parameter is suddenly changed [243]. On the other hand, the preparation of a desired quantum phase given an initial many-body ground state requires adiabatic time evolution, since population of a many-body excited states can potentially lead to various problems such as increased temperatures or enhanced losses in an experiment [244].

Chapter 4

Rydberg-dressed bosonic quantum gases in optical lattices

This chapter presents the main results of the thesis. Based on the knowledge gained in Chapter 1 and Chapter 2 we investigate the phase diagrams of two models describing Rydberg-dressed trapped bosonic quantum gases. Although both models rely on the properties of Rydberg states they rely on different coupling schemes and thus manifest different features. In Section 4.2 we study a extended Bose-Hubbard model with two coherently coupled species, in which one species corresponds to the electronic ground state and the other to the excited state. The long-range interaction between the excited atoms is given by a repulsive van-der-Waals interaction, which is either isotropic or anisotropic based on the adressed Rydberg state. Additionally to the geometry of the interaction, we also study the system on different lattice geometries and investigate their influence on the quantum phases. To complete the picture we also investigate the effect of dissipation and decoherence on the many-body ground state. We incorporate the finite lifetime given by the spontaneous emission and the dephasing due to blackbody radiation through time evolution simulation and discuss whether exotic phases as many-body ground states of the extended Bose-Hubbard model are long-lived despite the dissipation and decoherence. In Section 4.3 we investigate another trapped bosonic quantum gas dressed with Rydberg states. However the atoms are pairwise dressed with macrodimer states arising from the potential wells. Coupling atoms to such states induces an interaction only felt by atoms separated by a distance matching the molecular bond length. Compared to the previous section we focus much more on the experimental setup behind this system, and elaborate on how to overcome previous limitations through the macrodimer dressing. We derive the dressed interaction and analyze its strength in dependence on various aspects of the addressed macrodimer states. After establishing the range of achievable experimental parameters we analyze the many-body ground state of a macrodimer-dressed bosonic quantum gas through the appropriate extended Bose-Hubbard model. Based on the corresponding phase diagrams we establish a way to experimentally prepare macrodimer-dressed systems. We elaborate on how to experimentally access the SS regime through an adiabatic time evolution even in the presence of dissipation and decoherence.

4.1 Introduction

Trapped quantum gases coupled to Rydberg states have been in the focus of many different studies, either as the subject itself or as a tool to simulate and study phenomena otherwise inaccessible. However most of these study do not rely on the condensation of the system and thus work in the so-called frozen limit, which is achieved by working in very deep lattices [245–247]. The atoms are thus localized on each site and suitable for the investigation of spin physics or for the realization of quantum gates.
While it is known that crystalline structures can emerged in such frozen systems, it is important to investigate the physics that lay beyond the frozen limit and study the interplay between hopping processes and long-range interaction.

4.2 Rydberg-dressed atoms in two-dimensional lattices

The most general Hamiltonian, which describes a many-body system of atoms trapped in a lattice coupled to a Rydberg state, is given by

$$\begin{aligned}\hat{H} = &\sum_{\nu\in\{g,e\}} \Big(-\mu_\nu \sum_i \hat{n}_i^\nu - J_\nu \sum_{\langle ij\rangle} ((\hat{b}_i^\nu)^\dagger \hat{b}_j^\nu + (\hat{b}_j^\nu)^\dagger \hat{b}_i^\nu) + \frac{U_\nu}{2} \sum_i \hat{n}_i^\nu (\hat{n}_i^\nu - 1) \Big) \\ &- \Delta \sum_i \hat{n}_i^e + \frac{\Omega}{2} \sum_i ((\hat{b}_i^g)^\dagger \hat{b}_i^e + (\hat{b}_i^e)^\dagger \hat{b}_i^g) + \sum_i \sum_{j\neq i} C_6 \frac{\hat{n}_i^e \hat{n}_j^e}{R_{ij}^6}\end{aligned} \tag{4.1}$$

It consists of two Bose-Hubbard models (see Eq. (1.77)) for each species $\nu \in \{g, e\}$, i.e. the electronic ground and excited state, with their corresponding chemical potential μ_ν, the hopping amplitudes J_ν and the on-site interactions U_ν. Additionally it contains the coupling Hamiltonian (see Eq. (2.57)), which includes the inter-species coupling through the Rabi frequency Ω, the detuning of the excited state Δ and the van-der-Waals interaction C_6. The Hamiltonian is treated in the grand-canonical ensemble and thus we do not fix or physically limit the number of atoms in the system. Within the Cluster Gutzwiller approach with a cluster consisting of N sites and a truncation of the Fock space defined through the cut-offs s_g and s_e for the ground and excited state respectively, the dimension of the Hilbert space is given by $\dim(\mathcal{H}) = (s_g s_e)^N$. The rapid growth with increasing cluster size is problematic for the Hamiltonian, as we expect the van-der-Waals interaction to lead to crystalline structures with large superlattices. Since computation with clusters matching these superlattices is not feasible, we opt for the single-site Gutzwiller approach in this section. The corresponding single-site Hamiltonian derived through the mean-field approximations introduced in 3.2.1 reads

$$\begin{aligned}\hat{H}_i = &\sum_{\nu\in\{g,e\}} \Big(-\mu_\nu \hat{n}_i^\nu - J_\nu ((\hat{b}_i^\nu)^\dagger \xi_i^\nu + \hat{b}_i^\nu (\xi_i^\nu)^*) + \frac{U_\nu}{2} \hat{n}_i^\nu (\hat{n}_i^\nu - 1) \Big) \\ &- \Delta \hat{n}_i^e + \frac{\Omega}{2} ((\hat{b}_i^g)^\dagger \hat{b}_i^e + (\hat{b}_i^e)^\dagger \hat{b}_i^g) + \hat{n}_i^e \eta_i + E(\xi_i, \nu_i)\end{aligned} \tag{4.2}$$

with the energy off-set $E(\xi_i, \nu_i)$. The van-der-Waals interaction may lead to inhomogeneous phases and thus the computation of the ground state through an iterative procedure on a single site is not sufficient to provide the complete many-body ground state of the system. We therefore define a superlattice, iteratively compute the ground state of all sites and hereby determine the many-body ground state. Since the chosen superlattice might not be preferred for a given set of Hamiltonian parameters, we repeat this procedure with many, unique superlattice unit cells and select the true ground state through comparison of their many-body ground state energy (see Appendix A.2).
Although the amount of parameters may be overwhelming, some are set by the intrinsic properties of the coherent coupling and the Rydberg states themselves. We first assume the coupling to dictate the relevant timescales of the Rydberg state, and thus expect the Rydberg states to be essentially frozen in the system. This implies a vanishing hopping amplitude of the excited state, i.e. $J_e/\Omega = 0$. Additionally beyond the weak dressing regime, coupling to Rydberg states can lead to the formation of molecules composed of at least one Rydberg-excited atom due to its large scattering cross section. In an optical lattice these molecules emerge when the two involved atoms are on the same site. They are not trapped and would be immediately lost upon formation. According to the Quantum Zeno effect these strong losses are heavily impeded, the system exhibits a hard-core behavior between the atoms potentially involved in the molecular formation [248–251]. The hard-core constraint can be modeled either by appropriate truncation of the Fock space or through the limits $U_{ge}, U_e \to \infty$.

4.2.1 Many-body ground state phase diagrams

For the subsequent calculations we set the fixed parameters of the Hamiltonian to $U_g/\Omega = 0.1$, $U_{ge}/\Omega = 100$ and $U_e/\Omega = 1000$. The chemical potentials are merely a theoretical tool to control the filling of both species, which we set $\mu_g = \mu_e \equiv \mu$. For the sake of simplicity, we denote the ground state hopping amplitude as $J_g \equiv J$. We consider isotropic long-range interaction obtained through coupling the electronic ground state to a Rydberg state $|e\rangle = |nS_{1/2}\rangle$ until mentioned otherwise. The corresponding C_6-coefficient is then independent of any angle and can be set to a constant. Here we choose $C_6/\Omega = 100$ unless mentioned otherwise.
In order to obtain the following phase diagrams we computed spatially averaged order parameters and the underlying superlattice unit cell area of the many-body ground states resulting from the Hamiltonian Eq. (4.1). While in this chapter only the phase boundaries are shown complementary phase diagrams of these quantities are displayed and discussed in Appendix B.

Comparison to the Bose-Hubbard model

We first compute the many-body ground states of the Hamiltonian within the range $\mu/U_g \in [-1, 3]$ and the hopping amplitude $zJ/U_g \in [0, 0.1]$ at fixed detuning $\Delta/\Omega = 2$. The resulting phase diagram exhibits features with striking similarity to the ones of the plain Bose-Hubbard model, although all regimes are replaced by their broken lattice

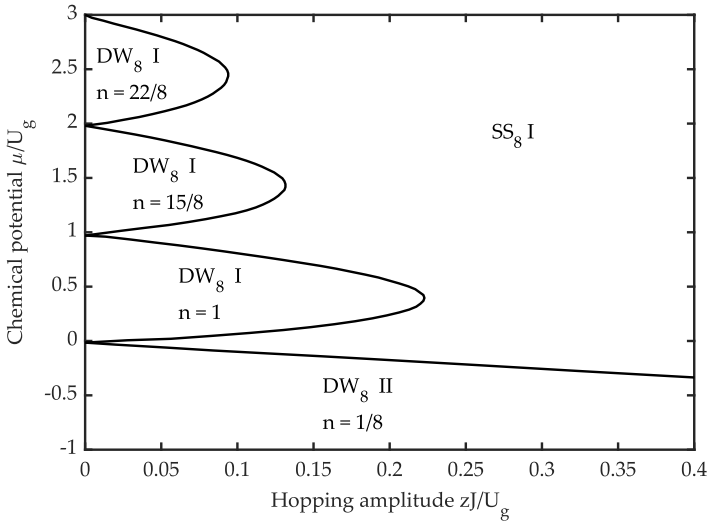

Figure 4.1: $J-\mu$ phase diagram and exemplary quantum phases for isotropic van-der-Waals interaction on a two-dimensional square lattice at $J_e/\Omega = 0$, $U_g/\Omega = 0.1$, $U_{ge}/\Omega = 100$, $U_e/\Omega = 1000$, $\Delta/\Omega = 2$ and $C_6/\Omega = 100$. The shape of the phase boundary resembles the one obtained for the Bose-Hubbard model (see Fig. 1.10). However the MI lobes, the vacuum regime and SF regime are replaced by DW II lobes, a DW I regime and a SS regime respectively. The indices denote the superlattice unit cell area A_{SL}. The crystalline structure of these phases does not vary throughout the phase diagram, which is a consequence of fixed detuning and long-range interaction strength.

translational symmetry counterparts (see Fig. 4.1). The lobe-shaped phase transitions are present, although the MI phases and the vacuum are exchanged with DW phases and the SF regime becomes a SS regime. Through the local admixture of both the electronic ground and the excited state of the DW phases, we find several interesting aspects: First, all phases possess the same crystalline structure, which is caused by the fixed detuning and the long-range interaction strength. Since neither the average filling of the excited state nor the van-der-Waals interaction are varied, the system exhibits only one crystalline structure (see Fig. 4.2). Although this is true within the parameter space considered, it is possible that larger hopping amplitudes or chemical potential lead to a larger Rydberg admixture due to the coherent coupling and thus force the system to change its crystalline structure. Additionally, the DW phases exhibit two type of spatial distributions of the electronic ground and Rydberg state admixtures. In phases of the first type (denoted by II) the maximum value of both admixtures are found on the same sites, while the other sites have weak admixtures and generally have a lower occupation. For a positive detuning $\Delta > 0$, these phases are found in the negative chemical potential regime $\mu < 0$. Positive detunings lead to a finite average filling of the excited state, which then induces a finite occupation of the electronic ground state due to the coherent coupling despite the negative

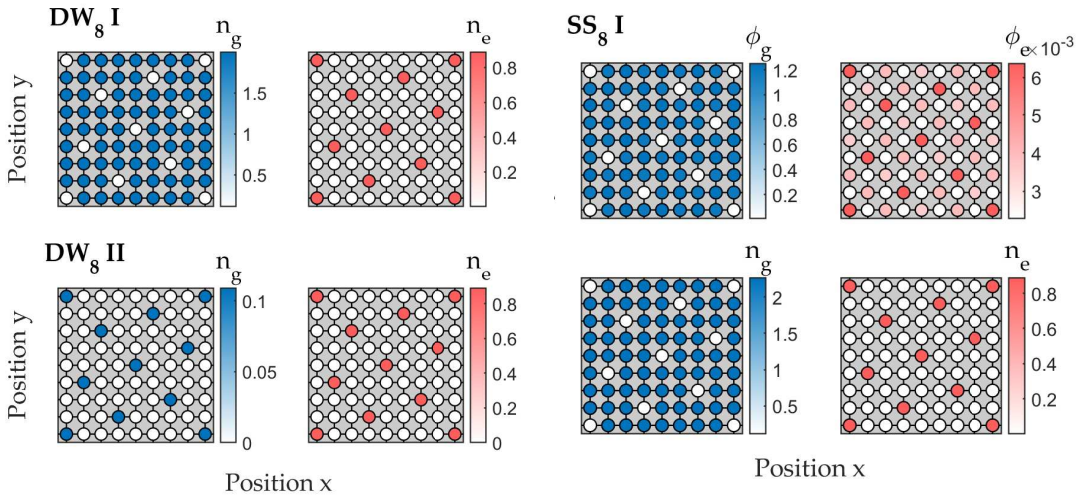

Figure 4.2: Exemplary DW and SS phases of the regimes found in the phase diagram displayed in figure 4.1. Due to the fixed detuning and long-range interaction we observe only one crystalline structure best described by a superlattice unit cell area $A_{\mathrm{SL}} = 8$. We find two types of the spatial modulation of the electronic ground and Rydberg state admixture, referred to as type I and type II.

chemical potential. On the other hand for positive chemical potentials $\mu > 0$ phases of the second type (denoted by I) arise, which have complementary distribution of the average filling. This means that the sites with large admixture of one species usually possess a small admixture of the other species. Usually the sites involved in the formation of the crystalline structure have larger excited state admixture, while the sites inbetween are filled with atoms in their ground state.
For finite hopping amplitudes both the DW I and II phases melt into a SS II regime with identical crystalline structure. Similar to the Bose-Hubbard model the phase transition between the insulating and condensed regime is of second-order [252].

We now compute the phase diagram obtained through variation of experimentally directly tunable parameters. Since we expect the competition between the hopping process and the long-range interaction to give rise to interesting quantum phases, we vary the hopping amplitude J of the electronic ground state and the detuning Δ, computate the respective many-body ground state and determine the corresponding ground state phase diagrams. Although it appears to be more intuitive to vary the long-range interaction strength through the C_6-coefficient, we choose to vary the detuning because it is an experimentally very well tunable parameter. Furthermore, the detuning appears in the Hamiltonian as an additional chemical potential of the excited state, and we can thus control the interaction strength through the average filling of the excited state. However it is always possible to choose the magnitude of the C_6-coefficient (see Section 2.3).

Frozen limit

We first consider the frozen limit ($J = 0$). We set the chemical potential to $\mu/\Omega = -0.25$. Within the frozen limit and due to the large on-site interactions a large filling is generally prohibited and the system opts for a unit filling of the lattice. Given that at most one atom occupies every site the only relevant parameters for the system are the chemical potential μ, the detuning Δ, the Rabi frequency Ω and the C_6-coefficient. However due to negative chemical potential and the large repulsive, long-range interaction substantial occupation of the system is energetically unfavorable. The detuning and the chemical potential thus become the decisive parameters and it is possible to define a critical detuning Δ_c/Ω for which the system is either occupied or in a vacuum state. Its value can be obtained analytically by considering the energy of a single atom within the above-mentioned condition. Through the corresponding Hamiltonian we obtain the energy

$$\epsilon_+ = -\mu - \frac{\Delta + \sqrt{\Delta^2 + \Omega^2}}{2} \tag{4.3}$$

The transition between an occupied and vacuum state is then given by a vanishing energy shift, i.e. when the adding or removing of an atom is associated to no energy cost. For ϵ_+ we can define the critical detuning as

$$\Delta_c/\Omega = \frac{1 - 4(\mu/\Omega)^2}{4(\mu/\Omega)} \tag{4.4}$$

For the given chemical potential $\mu/\Omega = -0.25$ we obtain the critical detuning $\Delta_c/\Omega = -0.75$. Now it is possible to define a range of relevant detunings for which we determine the many-body ground states and so we choose $(\Delta - \Delta_c)/\Omega \in [0, 10]$.

We obtain a manifold of crystalline DW II phases, that we characterize through their superlattice unit cell area A_{SL} and the average filling $\bar{n}_\nu$ of either species ν. These DW phases consist of sparsely distributed atoms forming the crystalline structure with either large or small excited state admixture. The sites inbetween these atoms are empty. The superlattice unit cell area, which essentially quantifies how sparsely the atoms are packed, increases as the detuning goes towards the transition to the vacuum state (see Fig. 4.3 (a)). Its scaling with the detuning can be analytically derived from the energy shift caused by the van-der-Waals interaction. If we assume isotropic long-range interaction to lead to equidistant atoms, we can define the average interatomic distance in a d-dimensional system as $R_a^d \sim A_{\mathrm{SL}}$. Through the definition of the average order parameters, we can relate the average filling to the distance $R_a^d \sim \bar{n}^{-1}$. Due to the characteristic decay of the van-der-Waals interaction with the distance, the energy gain of having an atom in the system is then given by

$$\epsilon_{\mathrm{vdW}} \sim \bar{n} \int_\infty^{R_a} \mathrm{d}R \frac{R^{d-1}}{R^6} \propto \bar{n} R_a^{d-6} \sim \bar{n}^{6/d} \tag{4.5}$$

Since this energy has to match the energy gain of adding the atom through the detuning, i.e. $\epsilon_+ \approx \epsilon_{\mathrm{vdW}}$, we obtain the scaling of the superlattice unit cell area with the detuning

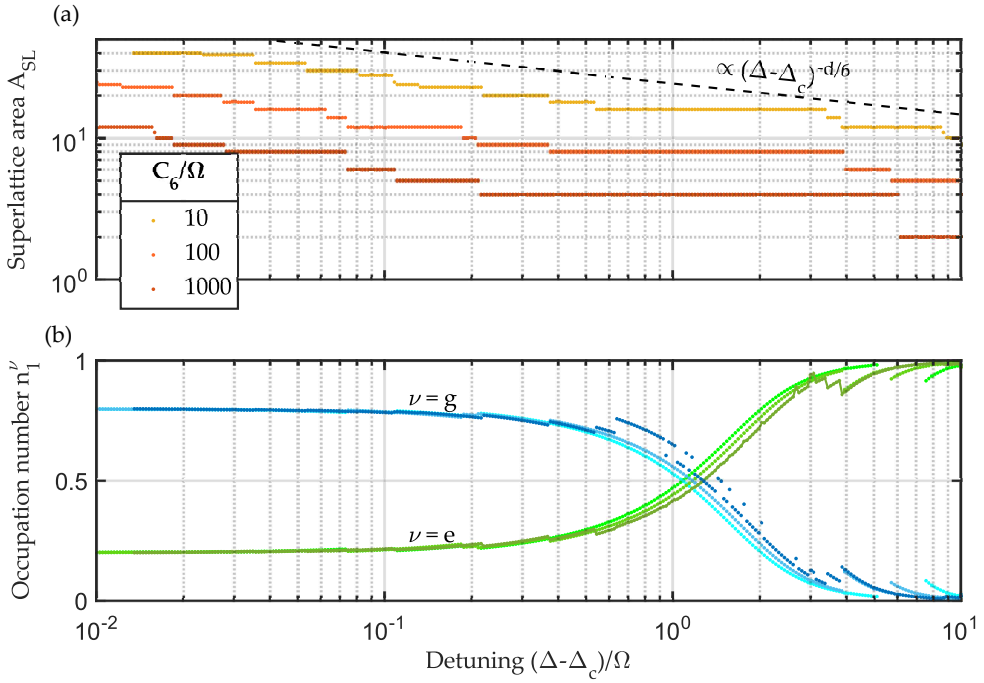

Figure 4.3: (a) Devil's staircase of DW II phases and (b) electronic ground state (blue markers) and excited state admixtures (green markers) of the atoms involved in the formation of the crystalline structure determined versus the detuning Δ/Ω at $J/\Omega = 0$, $J_e/\Omega = 0$, $U_g/\Omega = 0.1$, $U_{ge}/\Omega = 100$, $U_e/\Omega = 1000$, $\mu/\Omega = -0.25$ and $C_6/\Omega \in [10, 100, 1000]$. The devil's staircase exhibits larger superlattice unit cells as the detuning grows closer to its critical value Δ_c. The superlattice unit cell area also increases with stronger long-range interactions. On the other hand, the admixtures of both electronic states do not depend on the long-range interaction strength. At large, positive detunings the atoms are mostly in the excited state, i.e. $n_e = 1$, while for decreasing detunings the excited state admixture diminishes and converges towards a finite value.

$A_{\mathrm{SL}} \propto (\Delta - \Delta_c)^{-d/6}$. We confirm the scaling in our two-dimensional system $d = 2$ through an appropriate fit of the results.
Apart from increasing the interatomic distance, the system can also reduce its average Rydberg admixture by decreasing the Rydberg admixture of each atom individually. We plot the electronic ground state n_g and Rydberg state admixture n_e of the atoms involved in the crystalline structure (see Fig. 4.3 (b)). In the regime of very large detunings the atoms are all preferably in the excited state, i.e. $n_e = 1$ for $\Delta/\Omega \to \infty$. The long-range interaction is energetically costly, but the large detuning compensates it. As anticipated, the ratio between electronic ground and excited state grows as the detuning decreases, however after an initial decrease the Rydberg admixture converges towards a constant. This is caused by the coherent coupling, which prohibits a vanishing Rydberg admixture

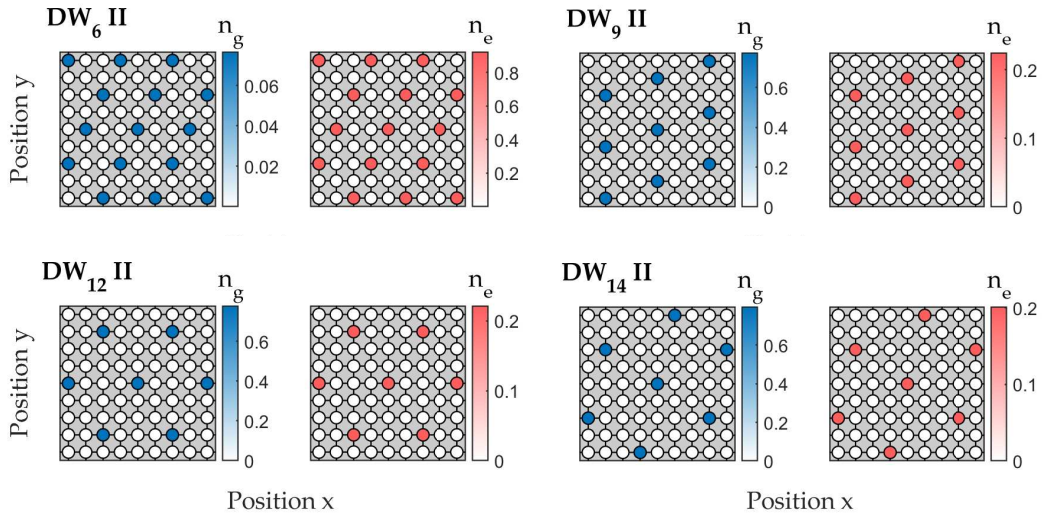

Figure 4.4: Exemplary DW phases, which form the devil's staircase displayed in figure 4.1 for $C_6/\Omega = 100$. Decreasing the detuning Δ/Ω leads to a smaller overall admixture of the Rydberg state to the system. As the detuning tends to its critical value Δ_0 the crystalline structures appearing become more sparse, while the Rydberg admixture of the occupied site converges to a finite value. Reprinted figure adapted with permission from [253]. © 2022 by the American Physical Society.

in the system.

These results are in very good agreement with previous studies on crystalline phases of Rydberg-dressed systems [182]. In these works the sequence of DW phases with monotonously decreasing superlattice unit cell area were coined as *devil's staircases* [254–256].

Beyond the frozen limit

We now investigate the many-body ground states beyond the frozen limit and compute the corresponding phase diagram. We therefore vary the hopping amplitude $zJ/\Omega \in [0, 0.2]$ additionally to the detuning $\Delta/\Omega \in [-2, 10]$. The phase diagram exhibits four regimes, namely a DW, a SS, a SF and a vacuum regime (see Fig. 4.5). The analytic description of the phase boundary between the SF and vacuum regimes can be obtained in a similar fashion as in Eq. (4.3). The energy shift of adding a delocalized atom to the system is given by the hopping amplitude J_g, the chemical potential μ, the detuning Δ and the Rabi frequency Ω, and within the mean-field approximation the critical value of the hopping amplitude for the vacuum phase transition reads

$$zJ_c = \frac{\Delta^2 + \Omega^2 - (2\mu + \Delta)^2}{4(\mu + \Delta)} \tag{4.6}$$

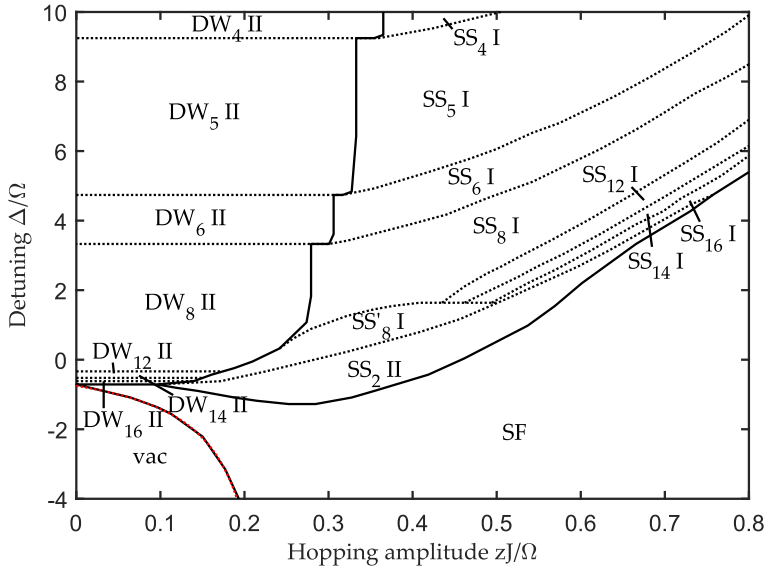

Figure 4.5: $zJ - \Delta$ phase diagram and exemplary quantum phases for isotropic van-der-Waals interaction on a two-dimensional square lattice at $J_e/\Omega = 0$, $U_g/\Omega = 0.1$, $U_{ge}/\Omega = 100$, $U_e/\Omega = 1000$, $\mu/\Omega = -0.25$ and $C_6/\Omega = 100$. We obtain a DW and a SS regime consisting of different phases with unique superlattice unit cells. Furthermore we find a SF and a vacuum regime. The red line represents the analytically obtained SF-vac phase boundary given by Eq. (4.6). The subscript denotes the superlattice unit cell area A_{SL}. Note that we find two SS phases with unit cell area $A_{\mathrm{SL}} = 8$. Reprinted figure adapted with permission from [257]. © 2019 by the American Physical Society.

with the coordination number z. In our two-dimensional square lattice, i.e. for $z = 4$, the numerically obtained phase transition is remarkably close to the derived analytic formula.

The devil's staircase of DW II phases does not immediately vanish beyond the frozen limit and extends to a finite hopping amplitude. The transition of sparse DW phases with weak Rydberg admixture to a condensed phase is obtained at lower hopping amplitudes, while denser crystalline structures in the regime of high detunings require larger hopping amplitudes. Beyond the critical value the DW II phases condense but keep their crystalline structure, giving rise to a SS regime with similar structure. Similar to the distribution of DW phases within the devil's staircase, reducing the detuning towards a critical value within the SS regime leads to a manifold of SS II phases with growing superlattice unit cell area. However close to the phase transition to the SF regime a SS I phase emerges. Additionally its superlattice unit cell area is the smallest possible and the phase exhibits a checkerboard-type spatial modulation. Although the chemical potential is negative, the moderate hopping amplitudes allow for a substantial admixture of the electronic ground state. For large enough hopping amplitudes the homogeneous SF phase becomes

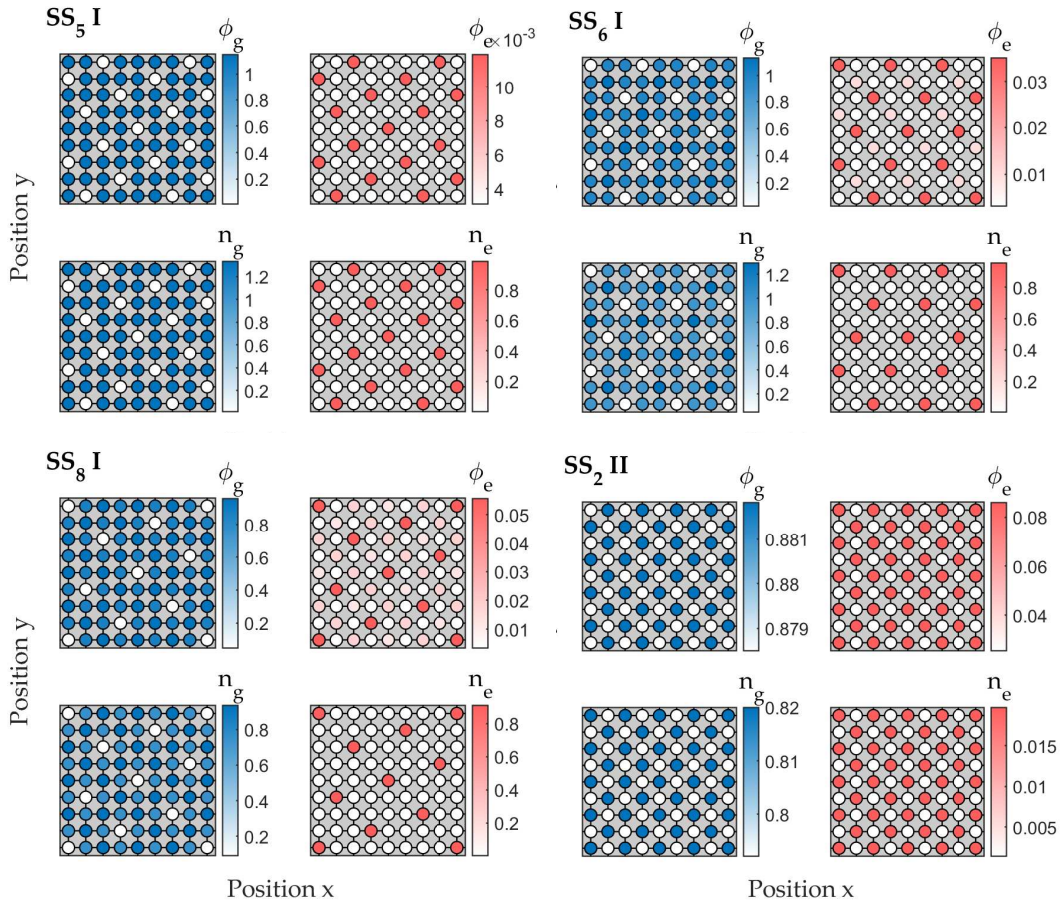

Figure 4.6: Exemplary phases of the SS regime found in the phase diagram displayed in figure 4.5. Decreasing the detuning Δ/Ω from the far off-resonant regime leads to SS I phases with increasing superlattice unit cell areas. Reprinted figure adapted with permission from [253]. © 2022 by the American Physical Society.

energetically more favorable and thus the SS I phase vanishes. The phase boundary between the SS and the SF regime shifts to higher detunings with increasing hopping amplitude due to the competition between hopping and long-range interaction.

Previous theoretical studies on weakly Rydberg-dressed systems beyond the frozen limit have predicted a so-called *two-stage melting* of the DW phases through increase of the hopping [258–260]. In these works the van-der-Waals interaction was simplified to nearest-neighbor interaction, which is a reasonable approximation for weak dressing and therefore weak long-range interaction. Thus the only crystalline structure that can potentially arise from the interaction is checkerboard-ordered. By increasing the hopping amplitude the checkerboard DW phase would melt into a checkerboard SS phase, i.e. start to exhibit finite

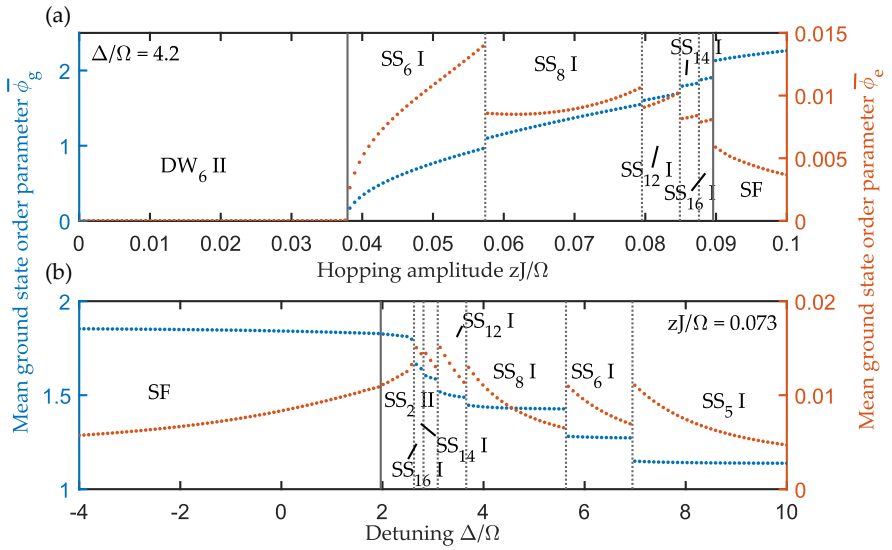

Figure 4.7: Average condensate order parameter of the electronic ground state (blue line) and excited state (red line) at fixed hopping amplitude $J/\Omega = 0.13$ (upper diagram) and fixed detuning $\Delta/\Omega = 2.5$ (lower diagram) at $J - \Delta$ phase diagram obtained for $J_e/\Omega = 0$, $U_g/\Omega = 0.1$, $U_{ge}/\Omega = 100$, $U_e/\Omega = 1000$, $\mu/\Omega = -0.25$ and $C_6/\Omega = 100$. We identify first order phase transitions through discontinuities (solid vertical line) and second order phase transitions through kinks (dashed vertical line) of the order parameters.

condensation but retain its crystalline structure. Further increasing the hopping amplitude then leads to the second melting from the SS phase into the homogeneous SF phase. In our case, we find a modification to the two-stage melting due to our full implementation of the van-der-Waals interaction: Given an initial DW phase within the frozen limit, the system undergoes a transition to the corresponding SS phase with identical crystalline structure, which represents the first melting. However before the second melting to a SF phase, the system undergoes several phase transitions to SS phases with larger superlattice unit cell area (see Fig. 4.7). The distribution of the atoms with larger excited state admixture becomes more and more sparse, while the admixture itself becomes weaker, until the system finally transitions into a SF phase. The phase transitions obtained are both first- and second-order. Similar to the previously obtained results, we find a second-order phase transition between the DW and the SS as only finite condensation distinguishes both phases at the boundary. However all SS phases within the regime are separated by first-order phase transitions. This is due to the discrete values of the superlattice unit cell areas. Since the system reorders at the phase transitions, we observe discontinuities of the average order parameters. In the end the transition from the last SS phase to the SF phase is again of second-order. Upon increasing the hopping amplitude the spatial distribution of the both admixtures vanishes and the observables on all site converge to the same values. Furthermore the admixture of the excited state becomes marginal such

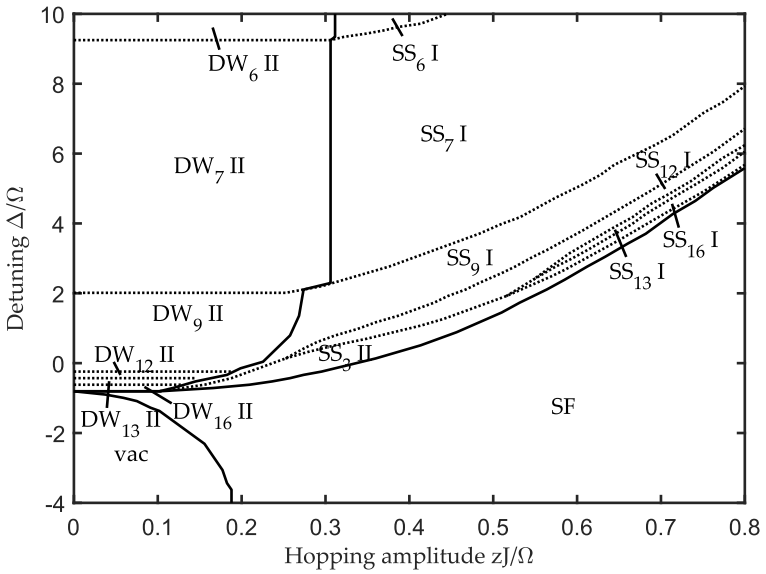

Figure 4.8: $zJ - \Delta$ phase diagram and exemplary quantum phases for isotropic van-der-Waals interaction on a two-dimensional triangular lattice at $J_e/\Omega = 0$, $U_g/\Omega = 0.1$, $U_{ge}/\Omega = 100$, $U_e/\Omega = 1000$, $\mu/\Omega = -0.25$ and $C_6/\Omega = 100$. The phase diagram strongly resembles the one obtained for a square lattice (see Fig. 4.5), although the phase boundary between the SS and the SF regime is shifted towards positive detunings at intermediate hopping amplitudes. Reprinted figure adapted with permission from [261]. © 2019 by the American Physical Society.

that the long-range interaction is not substantial enough for the emergence of a crystalline structure.

We conclude that Rydberg-dressed quantum systems trapped in a two-dimensional square optical lattice with isotropic van-der-Waals interaction exhibit various phase regimes and interesting non-trivial phenomenon within the considered parameter space. In order to obtain further understanding of the competition of the various processes in the system, we investigate in the following the role of the lattice geometry by performing calculations on a two-dimensional triangular lattice. Furthermore, we compute the phase diagram on the square lattice but with anisotropic van-der-Waals interaction.

Importance of the lattice geometry

Computation of the phase diagram on the triangular lattice reveals similar features to its square lattice counterpart (see Fig. 4.8). The DW regime exhibits various DW II phases with distinct crystalline structures with corresponding SS II phase beyond a critical hopping amplitude. At large amplitudes the slope of the phase boundary between SS and SF regime

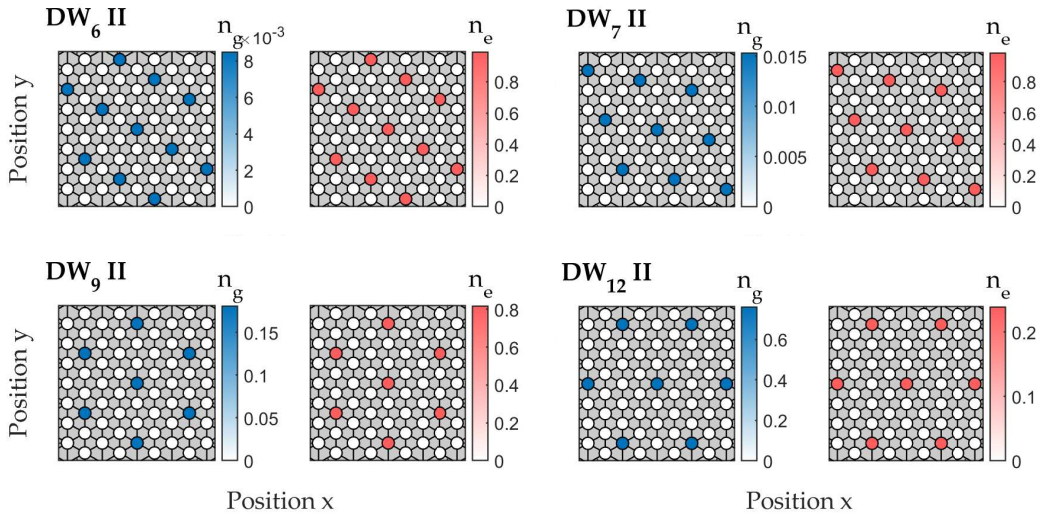

Figure 4.9: Exemplary phases of the DW regime found in the phase diagram displayed in figure 4.8. Similar to the phase diagram computed on a square lattice the DW phases on the triangular lattice are composed of equidistant atoms and the interatomic distance becomes larger as the detuning decreases Δ/Ω.

is very similar to the one in the phase diagram for the square lattice. However the main, albeit small, difference is found within the SS I phase at intermediate hopping amplitudes. Within the corresponding parameter regime the system with isotropic interaction usually exhibits its smallest, non-trivial crystalline structure of equidistant atoms with interatomic distance $d/a_{\text{lat}} = 2$. On the square lattice this corresponds to the checkerboard-type ordering with $A_{\text{SL}}^{\text{min}} = 2$, while on the triangular lattice the smallest, non-trivial crystalline structure possesses the superlattice unit cell area $A_{\text{SL}}^{\text{min}} = 3$. Reducing the detuning in the SS I phase diminishes the excited state admixture and thus the system favors crystalline structures with smaller superlattice unit cell area. Therefore we find the checkerboard-type SS I phase at detunings, where on the triangular lattice the system prefers to be a SF.

This was to be expected, since deep within the DW and SS regime at large, positive detunings the large admixture of the excited state leads to interatomic distances far bigger than the optical lattice constant, i.e. $d \gg a_{\text{lat}}$, while close to the SF phase transition at intermediate hoppings the interatomic distance becomes comparable, i.e. $d \sim a_{\text{lat}}$. At larger hopping amplitudes the SS phases close to the SS transition possess big superlattice unit cells and thus the phase transition obtained on the square lattice is recovered.

We conclude that the geometry of the triangular lattice only plays a role at intermediate hopping amplitudes, where the lattice symmetry becomes important due to the smaller interatomic distances. We furthermore gather that the phase transition at large detunings and hopping amplitudes is solely given by the geometry of the interaction. The latter

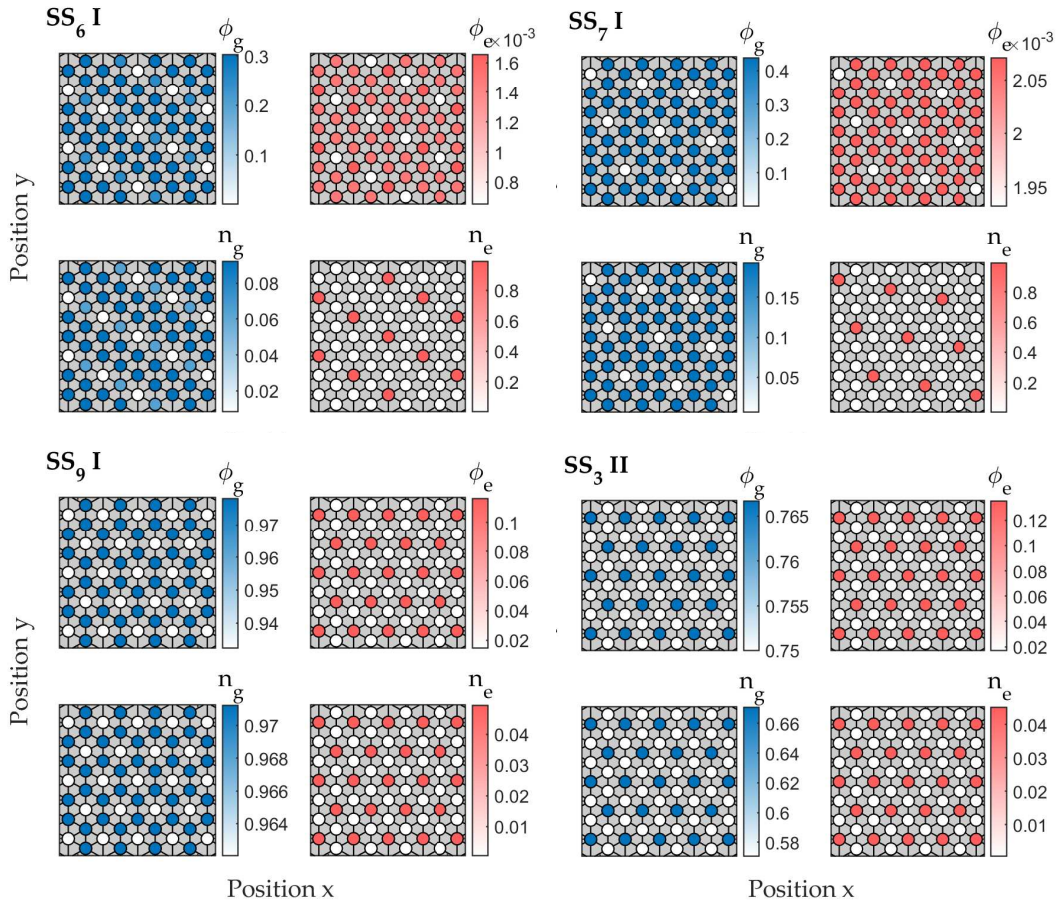

Figure 4.10: Exemplary phases of the SS regime found in the phase diagram displayed in figure 4.8. While most phases within this regime are of type I, we find a small region in which the system prefers a densely packed SS II phase with superlattice unit cell area $A_{\mathrm{SL}} = 3$, which represents the smallest possible inhomogeneous density modulation.

point is further established in the following, where we investigate the phase diagrams obatined with anistropic interaction.

Importance of the interaction geometry

Through coherent coupling to an excited state $|e\rangle = |nP_{1/2}\rangle$ the $C_6^p(\vartheta, \vartheta')$-coefficient becomes angular dependent and the Rydberg-dressing yields anisotropic long-range interaction. However since atoms with $\ell \neq 0$ possess a non-trivial angular wave function, an orientation can be attributed to them. The van-der-Waals interaction between two atoms then depends on the relative angle between the distance vector and both orientation axes. In principle, it would be possible to use then orientation of the atoms as an additional degree of freedom, through which the energy of the many-body ground state

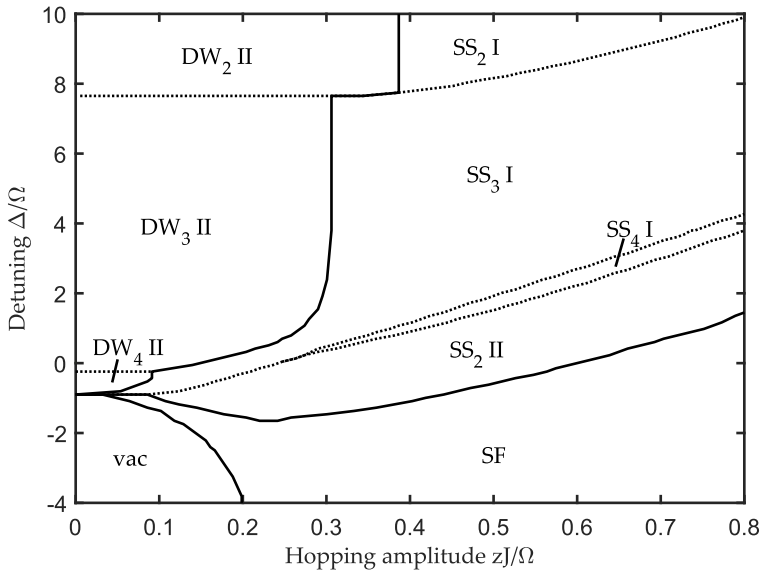

Figure 4.11: $J - \Delta$ phase diagram and exemplary quantum phases for anisotropic van-der-Waals interaction on a two-dimensional square lattice at $\vartheta_0 = 0$, $J_e/\Omega = 0$, $U_g/\Omega = 0.1$, $U_{ge}/\Omega = 100$, $U_e/\Omega = 1000$, $\mu/\Omega = -0.25$ and $C_6/\Omega = 100$. The crystalline structures of the DW and SS phases are striped and differ from one another through the distance between the stripes. The phase boundary between the SS and the SF at large hopping amplitudes is different from the one obtained for isotropic interaction. Reprinted figure adapted with permission from [253]. © 2022 by the American Physical Society.

can be further lowered. But this is unnecessary, since it vastly increases the necessary computational power required for the numerical procedure and also is experimentally irrelevant, since the orientation of all atoms can be easily controlled through an external magnetic field [262–264]. The two atoms the orient themselves along the field, which reduces the degrees of freedom to only one relative angle. We thus write the corresponding $C_6^P(\vartheta)$-coefficient as $C_6^P(\vartheta) = C_6^0 \sin^4(\vartheta) + C_6^1$, where $C_6^1 \ll C_6^0$ is the strength of the small residual, isotropic interaction. Note that although there is an additional angle φ, we can omit it since we perform our calculations on the two-dimensional lattice.

If we assume the magnetic field $\boldsymbol{B} = B \cdot \hat{\boldsymbol{e}}_B$ to be in plane, we can further define the orientation of the magnetic field through $\hat{\boldsymbol{e}}_B \cdot \hat{\boldsymbol{e}}_x = (\cos(\vartheta_0), \sin(\vartheta_0))$ with the relative angle ϑ_0 to the x-axis. We therefore gain an additional tunable parameter, through which we redefine the angle between both atoms as $\vartheta \to \vartheta - \vartheta_0$ (see Section 2.3). Due to the angular dependence of the van-der-Waals interaction, we expect crystalline structures of stripes parallel to the magnetic field to arise. The rotational symmetry of the optical lattice allows us to restrict the relative angle $\vartheta_0 \in [0, \pi/2)$ of the magnetic field.

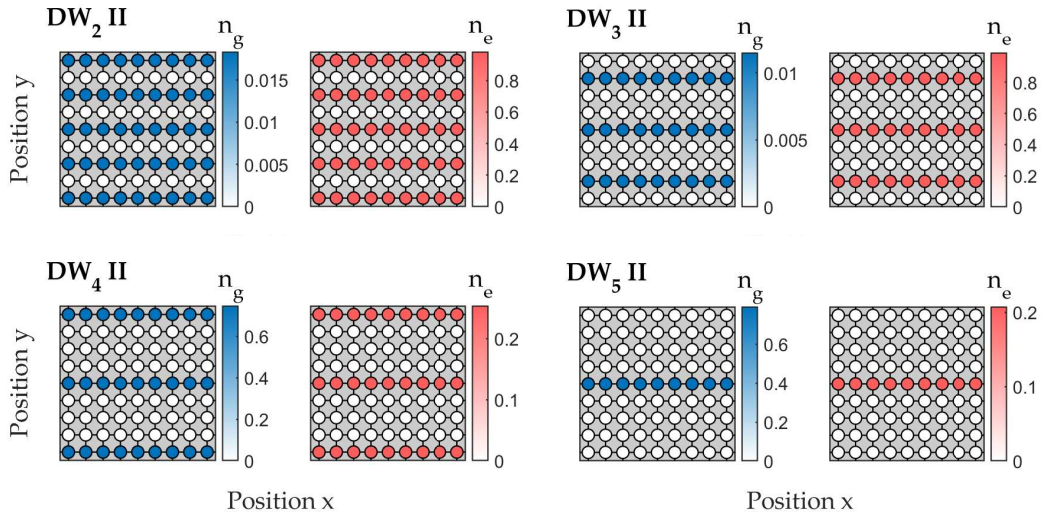

Figure 4.12: Exemplary phases of the DW regime found in the phase diagram displayed in figure 4.11. The crystalline structures are defined by stripes of atoms, which distance is given by the detuning Δ/Ω, due to the anisotropic long-range interaction.Reprinted figure adapted with permission from [253]. © 2022 by the American Physical Society.

In the subsequent calculations we keep the parameters $U_g/\Omega = 0.1$, $U_{ge}/\Omega = 100$, $U_e/\Omega = 1000$, $\mu/\Omega = -0.25$ and use the van-der-Waals interaction strengths $C_6^0/\Omega = 100$ and $C_6^1/\Omega = 1$. We for now set the relative angle $\vartheta_0 = 0$ obtained through application of a magnetic field along the x-axis. We compute the many-body ground states within the parameter space spanned by $J/\Omega \in [0, 0.2]$ and $\Delta/\Omega \in [-2, 10]$. The resulting phase diagram consisting of various striped phases is very similar to the one obtained for isotropic interaction, albeit less phases with distinct crystalline structure appear (see Fig. 4.11). This is purely a geometric effect caused by the anisotropy of the van-der-Waals interaction. As previously found isotropic long-range interaction leads to crystalline structures composed of equidistant atoms with interatomic distances $d/a_{\text{lat}} = \{1, \sqrt{2}, 2, \sqrt{5}, \sqrt{8}, ...\}$. On the other hand, striped crystalline structures emerging due to anisotropic interaction are only described by the stripe distances $d_\perp/a_{\text{lat}} = \{1, 2, ...\}$, while the distance between the atoms within the stripe is typically $d_\parallel/a_{\text{lat}} = 1$. The distance $d_\parallel$ however can become larger in the frozen limit close to the transition to the vacuum regime. Within the devil's staircase for a positive, vanishing $(\Delta - \Delta_0) \gtrsim 0$ the residual isotropic interaction given by C_6^1 becomes visible and gives rise to crystalline structures with $d_\parallel/a_{\text{lat}} > 1$, although $d_\perp \gg d_\parallel$. Such crystalline phases are not visible beyond the frozen limit as phases close to the vacuum transition in the frozen limit are highly susceptible and immediately condense at a finite hopping amplitude.

Despite the obvious similarities, such as the appearance of the two-stage melting with

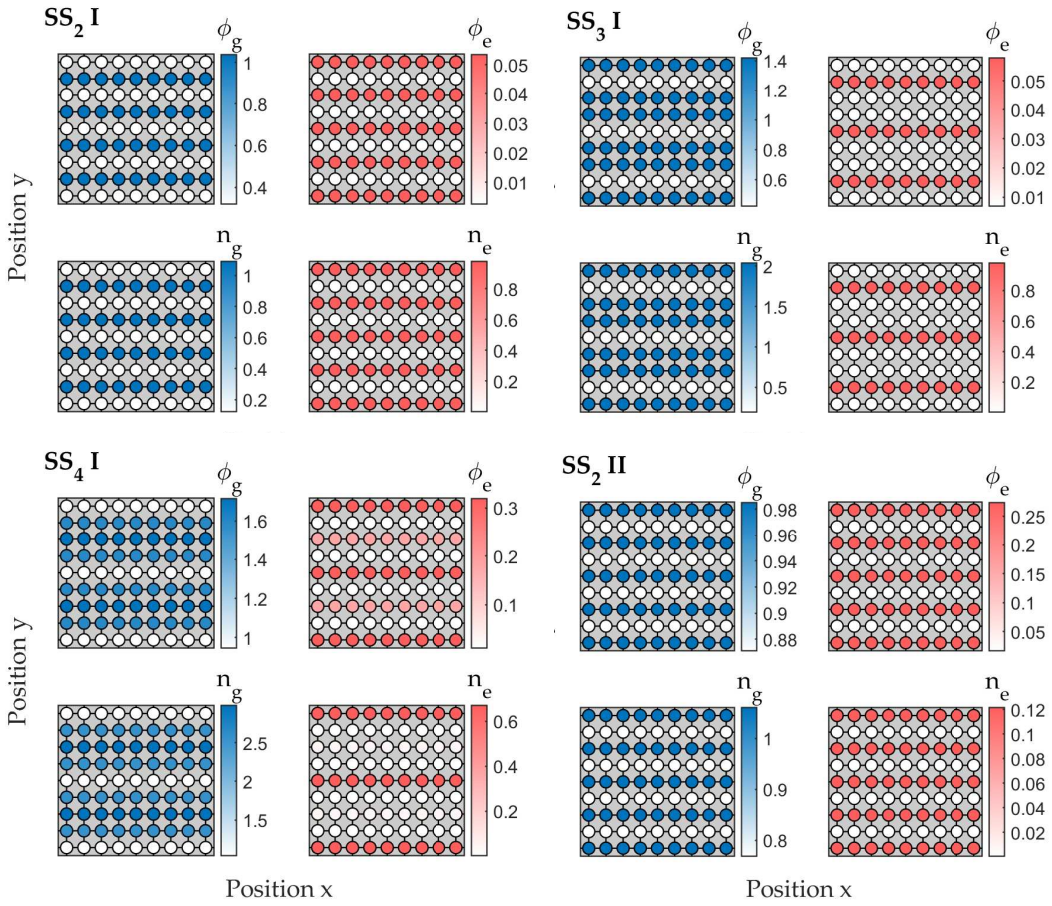

Figure 4.13: Exemplary phases of the SS regime found in the phase diagram displayed in figure 4.11. We obtain two SS phases of different types with identical crystalline structure, separated by SS I phases with larger superlattice unit cell area. Reprinted figure adapted with permission from [253]. © 2022 by the American Physical Society.

intermediate first-order transitions inbetween both melting points and the increasing superlattice unit cell area for decreasing detuning, an important difference appears in the SS regime. The phase boundary between the SS and the SF regime extends to larger hopping amplitudes compared to the boundary obtained for isotropic long-range interaction. Furthermore, the SS I phase does not vanish beyond a certain hopping amplitude, which we attribute to the striped crystalline structure of the SS regime. Isotropic long-range interaction, which favors crystallization of the system, is in direct competition to the delocalizing hopping process. This is especially apparent in the checkerboard-order SS I phase, where the nearest-neighbor hopping is impeded due to the dense crystalline structure and thus at large enough hopping amplitudes it becomes energetically more favorable to discard the crystalline structure of the system and completely condense, hence the phase

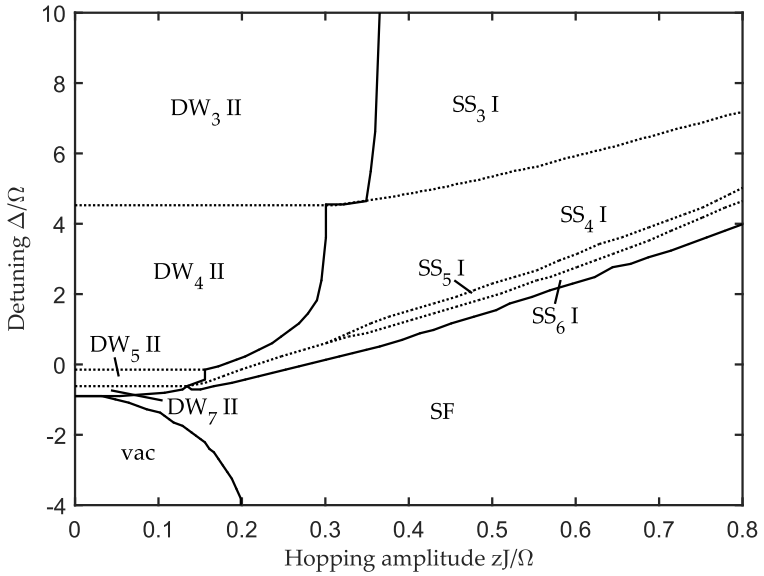

Figure 4.14: $zJ - \Delta$ phase diagram and exemplary quantum phases for tilted anisotropic van-der-Waals interaction on a two-dimensional square lattice at $\vartheta_0 = \pi/4$, $J_e/\Omega = 0$, $U_g/\Omega = 0.1$, $U_{ge}/\Omega = 100$, $U_e/\Omega = 1000$, $\mu/\Omega = -0.25$ and $C_6/\Omega = 100$. Due to the tilted anisotropic interaction the inhomogeneous phases exhibit diagonal stripes. Compared to all previous phase diagrams, the characteristic SS I phase at the phase boundary to the SF regime at intermediate hopping amplitudes is missing. Reprinted figure adapted with permission from [253]. © 2022 by the American Physical Society.

transition from the SS I phase to the SF regime. The anisotropic case, however, possesses a highly non-trivial property beneficial for the coexistence between condensation and spatial modulation: The direct competition between long-range interaction and hopping depends on the relative angle of the atoms. Since the interaction is minimal along the orientiation axis of the magnetic field, the atoms form striped structures and the hopping process between the stripes is quasi unimpaired. The only present damping appears through the atoms occupying the stripes, which are usually frozen due to their larger excited state admixture. Although the atoms inbetween the stripes are mostly in their electronic ground state the coherent coupling leads to a small, but finite admixture of the excited state through which the long-range interaction impedes the coherent flow of atoms to a certain extent. Since the system chooses its many-body ground states such that the long-range interaction and hopping process are not in direct competition, we observe the extended SS regime.

For a magnetic field oriented along $\theta_0 = \pi/4$, the anisotropic interaction is tilted and it is energetically more favorable to form stripes of atoms with large excited state admixture along the diagonals of the system. While the corresponding phase diagram is not too

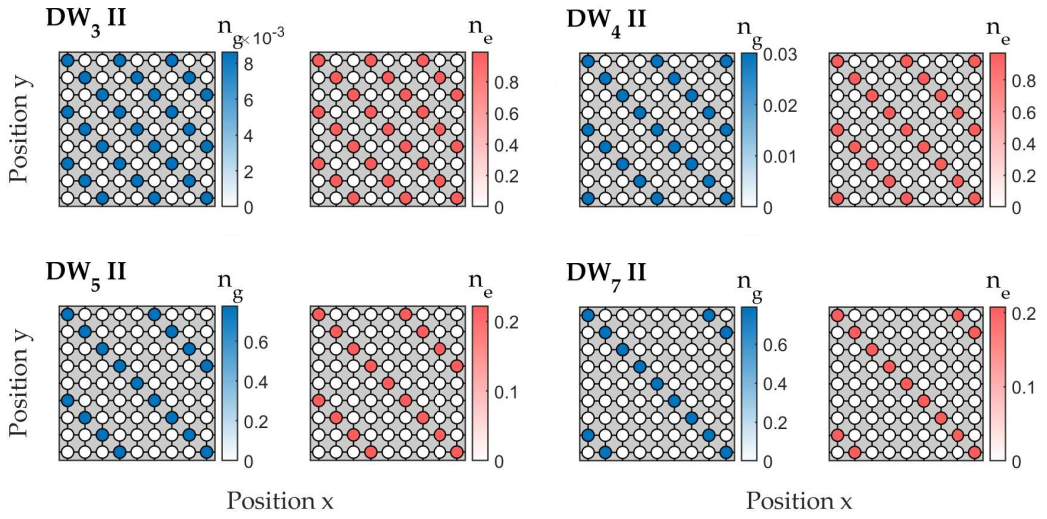

Figure 4.15: Exemplary phases of the DW regime found in the phase diagram displayed in figure 4.11. Due to the tilt of the anisotropic long-range interaction DW phases with crystalline structures composed of diagonal stripes becomes energetically more favorable. Reprinted figure adapted with permission from [253]. © 2022 by the American Physical Society.

different from the previously discussed again, the main difference is found within the SS regime (see Fig. 4.14). Interestingly the SS I phase is missing in this regime and the phase transition between the SS and SF regime is identical to the one for $\theta_0 = 0$ if we omit the SS I phase there. The lack of SS I phase is due to the increased interatomic distances $d_{\parallel}/\mathrm{lat} = \sqrt{2}$ within the stripes and the hopping process, which is only nearest neighbor. It is therefore energetically unfavorable to have a SS I phase for the tilted anisotropic interaction, especially since at smaller and negative detunings the crystalline structures of the previously obtained SS I phases tend to have a dense distribution of the atoms with larger excited-state admixture.

From comparison of all phase diagrams we see that the slope of the SS-SF phase boundary only depends on the type of interaction (see Fig. 4.17). Furthermore in the case of isotropic interaction the phase boundary between the homogeneous and inhomogeneous regimes interaction at vanishing hopping amplitudes ($zJ/\Omega \approx 0$) and large hopping amplitudes ($zJ/\Omega \gg 1$) appears to be independent on the lattice geometry. In these limits the system tends to exhibit sparse distribution of Rydberg-dressed atoms, which make up the crystalline structure of the many-body ground state, and thus the interatomic distances are typically much larger than the optical lattice constant. The geometry of the lattice hereby becomes irrelevant and the phase boundaries overlap.
Additionally we find that the DW-SS phase boundary only slightly depends on the interaction and lattice geometry. The boundaries become more alike as the detuning tends to

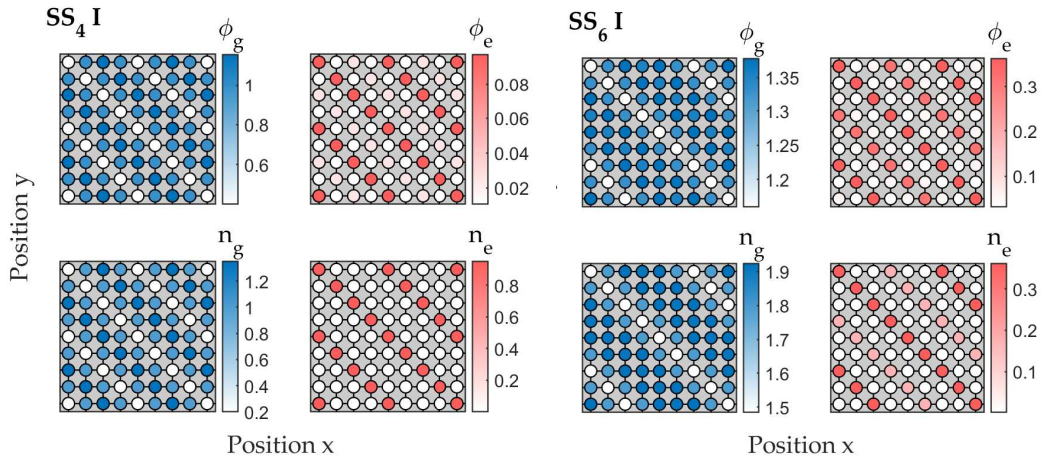

Figure 4.16: Exemplary phases of the SS regime found in the phase diagram displayed in figure 4.11. All obtained SS phases are of type I and no type II SS phase borders the SF regime. Reprinted figure adapted with permission from [253]. © 2022 by the American Physical Society.

its critical value.

4.2.2 Time evolution simulation

We now analyze the role of dissipation and decoherence on phases with finite excited state admixture, more specifically the DW and SS phases. Since their crystalline structure arises through the repulsive long-range interaction between Rydberg atoms with finite lifetime, it is possible that the experimentally relevant time scales for the observation of density modulated states is thus strongly inhibited. We therefore include the finite lifetime and blackbody radiation induced dephasing [265] in our system, which we incorporate in its description through the Lindblad master equation (see Section 3.3). The transition from the excited state to the electronic ground state is given by the Lindblad operator $\hat{L}_{\text{sp}} = \sum_i \sqrt{\Gamma}(\hat{b}_i^g)^\dagger \hat{b}_i^e$ with the decay rate Γ. The operator corresponding to the dephasing reads $\hat{L}_{dep} = \sum_i \sqrt{\kappa}\hat{n}_i^e$, since it is induced through additional interactions between the excited state and energetically close Rydberg states. Thus κ quantifies the speed with which these Rydberg states are populated. Since both these processes lead to dissipation and decoherence, the goal of this section is to estimate their magnitude in dependence on the Γ and κ. Note that we do not consider collective mechanism such as the avalanche dephasing in the subsequent calculations.
We expect the non-unitary processes to affect the system in two ways: First the dissipation leads to an overall decreasing excited state admixture and therefore potentially the loss of a crystalline structure. Additionally the decoherence induces a depletion of the condensate order parameter, since condensation occurs when atoms are phase coherent.

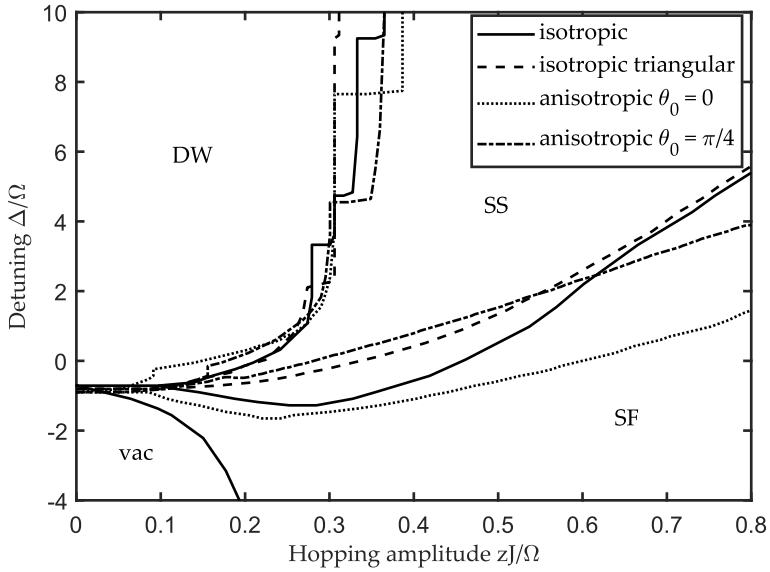

Figure 4.17: The phase boundaries of all previously determined $J - \Delta$ phase diagrams at $\vartheta_0 = \pi/4$, $J_e/\Omega = 0$, $U_g/\Omega = 0.1$, $U_{ge}/\Omega = 100$, $U_e/\Omega = 1000$, $\mu/\Omega = -0.25$ and $C_6/\Omega = 100$. The average position of the phase boundary between the DW and SS regime does not seem to depend on the lattice or interaction geometry, however we find a more substantial difference between all results with respect to the SS-SF transition. Non-tilted anisotropic interaction yields the largest SS regime. Reprinted figure adapted with permission from [253]. © 2022 by the American Physical Society.

The simplest way to assess the influence of dissipation and decoherence on the system is through quench-type time evolution (see Section 3.3.1). Using a many-body ground state of the Hamiltonian Eq. (4.1) as an initial state, we suddenly switch on the dissipative processes at a time $t = 0$ and simulate the time evolution, during which the local order parameters are computed. For the sake of simplicity we limit the time evolution simulation to an initial DW_8 I and SS_8 II obtained for isotropic interaction a square lattice. The parameters of the Hamiltonians in these calculations are the ones used to obtain the phase diagram in Fig. 4.5. We define the ranges of the decay rate as $\Gamma/\Omega \in [0.01, 20]$ and of the dephasing rate as $\kappa/\Omega \in [0.01, 20]$, and perform time evolutions until a time $\Omega t_{\max} = 40$. By investigating the time evolution of an initial DW phase it is possible to determine the magnitude of the dissipation caused by both processes considered here. As the condensate order parameter of either electronic state is vanishing in the DW regime and particle conservation holds throughout the time evolution, i.e. $\sum_{i,\nu} n_i^\nu(t) = N \ \forall t$, the we can reduce complexity of the problem to the analysis of the total excited state occupation number $n_e = \sum_{i \in \mathrm{SL}} n_e^i$ in the superlattice. For a DW phase this essentially represents the excited state occupation number on the occupied sites of the system.

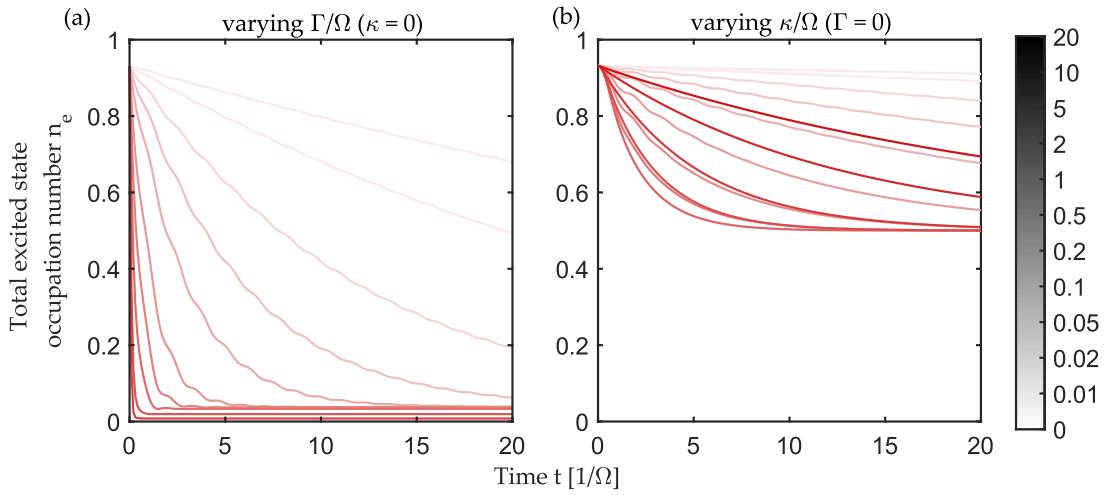

Figure 4.18: Total excited state occupation number n_e of an initial DW_8 II phase for varying decay rate Γ (a) and dephasing rate κ (b). The opacity of the line represents the strength of the active non-unitary process. The spontaneous emission leads to the almost complete loss of admixture of the Rydberg state, while the excited state occupation number converges towards a finite value through the dephasing independently on its rate.

The DW phase is obtained for a detuning $\Delta/\Omega = 2.5$ in the frozen limit. At a vanishing dephasing rate we see that a finite decay rate induces a decay of the excited state occupation number (see Fig. 4.18 (a)). Although the system reaches a steady state with finite n_i^e, its value converges towards zero as the decay rate increases. Additionally an underlying oscillation with period $T \approx \Omega/2$ emerges, which disappears once the steady state is reached. We therefore believe that the steady state and its associated finite excited state occupation number is defined through the competition between spontaneous emission and coherent coupling. On the other hand if we subject the system only to dephasing processes we do not observe such a substantial reduction of the excited state admixture (see Fig. 4.18 (b)). Since the dephasing is caused by additional interactions as mentioned before it acts as an additional chemical potential for the excited state and thus causes the depletion. The dephasing rate defines how fast the excited state occupation number decreases, however we find that the steady state is always defined by $n_e = 0.5$. The time until the steady state is reached decreases as the dephasing rate becomes larger and surprisingly increases again beyond a certain value. The slowing down of the dynamics due to substantial enough dephasing rates is consistent to the Quantum-Zeno effect [248–251].
We now compute the time evolution of an initial SS phase obtained for a detuning $\Delta/\Omega = 2.5$ and hopping amplitude $zJ/\Omega = 0.2$. Additionally to the total excited state occupation number we plot the total ground state condensate order parameter $\phi_g = \sum_{i\in \mathrm{SL}} \phi_i^g$. For only spontaneous emission we observe a declining ground state order parameter although not vanishing within the chosen time limit (see Fig.4.19 (a)). The excited state occupation number exhibits a similar behavior compared to the ones obtained for an

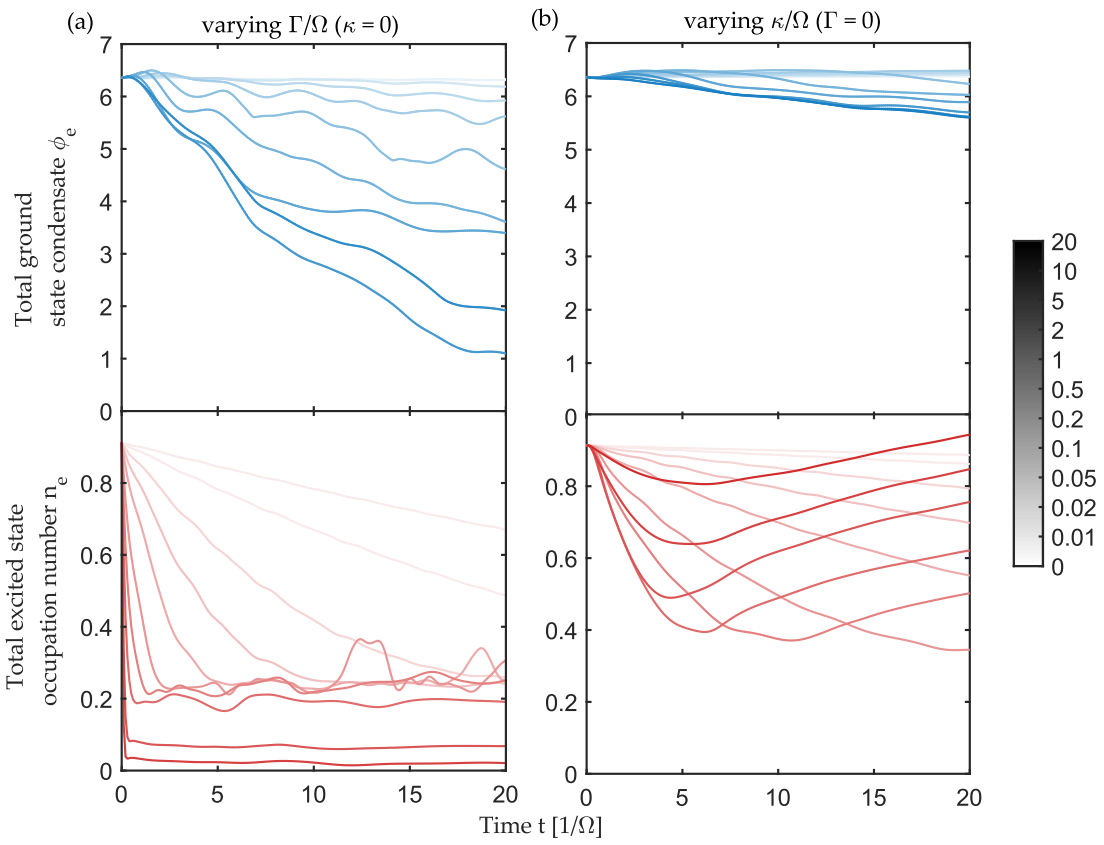

Figure 4.19: Total ground state condensate order parameter ϕ_g and total excited state occupation number n_e of an initial SS_8 I phase for varying decay rate Γ (a) and dephasing rate κ (b). The opacity of the line represents the strength of the active non-unitary process.

initial DW phase(see Fig.4.19 (c)). For intermediate and large decay rates however the system exhibits fast dynamics followed by a time evolution in which the total excited state occupation number fluctuates but does not decrease. The value around which n_e fluctuates is larger than the value of the steady states corresponding to the initial DW phase and the strength of the fluctuation decreases with larger decay rates.

In order to understand how the finite condensate order parameter contributes to this phenomenon we depict the local ground and excited state occupation numbers throughout the time evolution for $\Gamma/\Omega = 2$ and $\kappa/\Omega = 0$ (see Fig. 4.20). Due to the finite hopping amplitude the atoms are able to redistribute within the lattice. In combination with the decreasing excited state admixture the atoms exhibit highly non-trivial dynamics in the short time scales following the quench and finally converge towards an energetically more favorable distribution. The fluctuations observed in the total excited state number only affect the local order parameters individually and does not modify the density

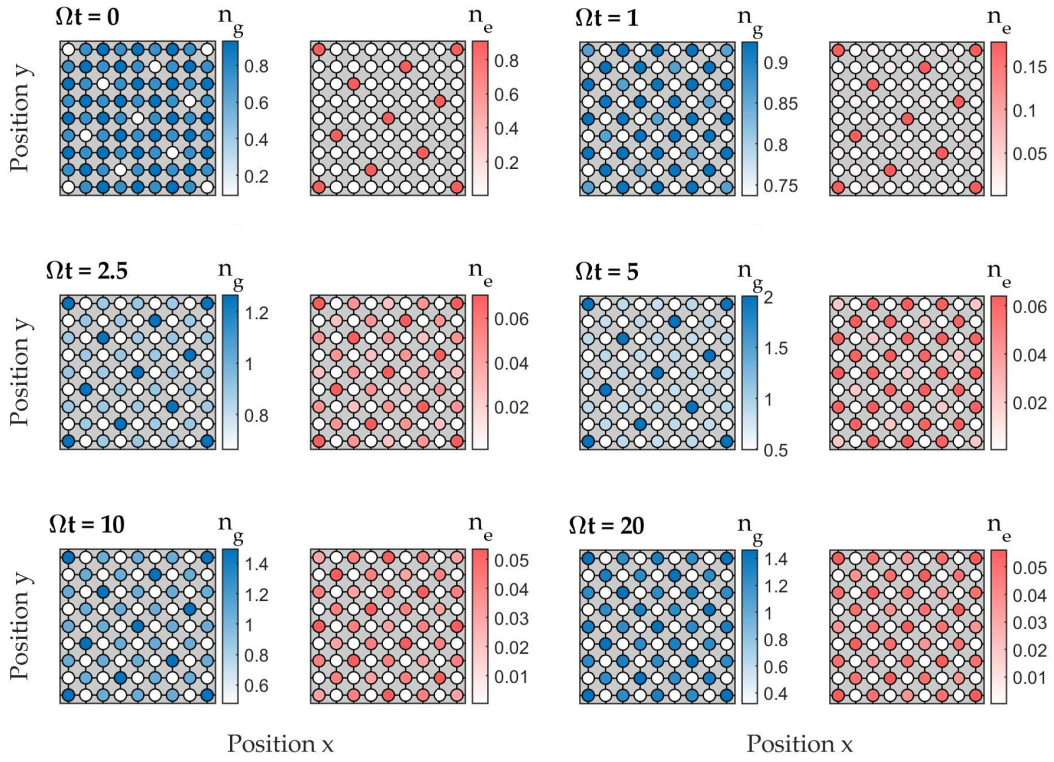

Figure 4.20: Depiction of the local order parameters of an initial SS_8 I phase induced through spontaneous emission at different times $\Omega t = [0, 1, 2.5, 5, 10, 20]$. The system quickly loses a substantial amount of excited state admixture, although through redistribution of the atoms transitions into a long-lived SS_2 II phase.

modulation in the system. Interestingly not only does the crystalline structure change but also the type of the SS phase. More specifically, the initial SS_8 I phase transitioned into a SS_2 II phase. This is in agreement with the previously discussed phase diagrams obtained in the many-body ground state calculation, through which we found that SS phases associated with small excited state admixture were generally of type II. While in these calculations the small admixture is caused by a detuning close to its critical value, it is induced in the time evolution simulation through the spontaneous emission. Thus the system loses a substantial amount of its excited state admixture and therefore redistributes. Although this SS_2 II phase appears to be metastable its total condensate order parameter decreases constantly until the state becomes insulating. Thus the SS_2 II phase appears to be a long-lived intermediate state before the system ultimately converges towards its steady state, the DW_2 II phase. It is worth mentioning that for the initial SS_8 I phase and spontaneous emission we obtain the SS_2 II phase as an intermediate state in the time evolution simulation as long as the decay rate is not large enough to lead to a vanishing excited state order parameter.

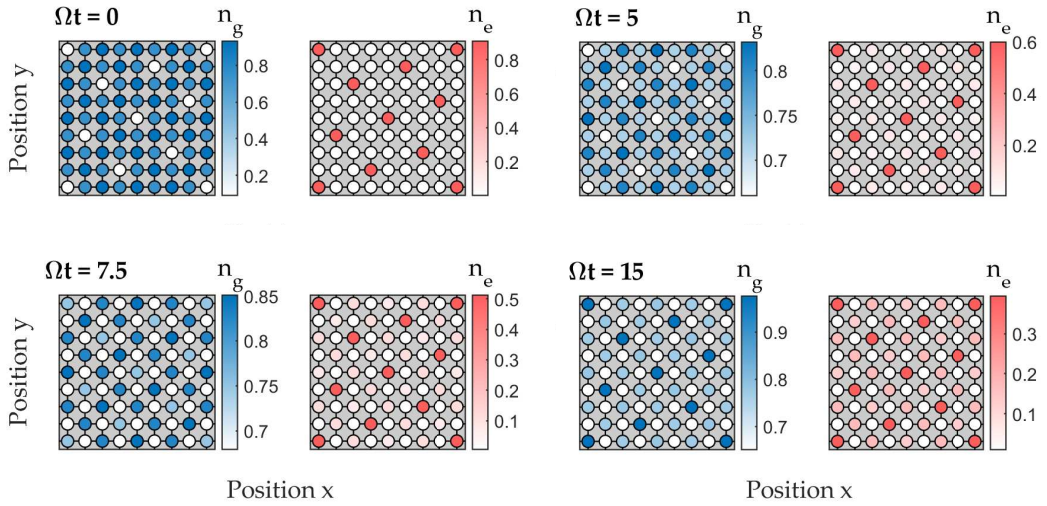

Figure 4.21: Depiction of the local order parameters of an initial SS_8 I phase induced through dephasing at different times $\Omega t = [0, 5, 7.5, 15]$. The atoms reorganize in such a way, that the total excited state occupation number of the system is distributed on more sites compared to the initial state, which allows the system to withstand the effect of the dephasing.

In contrast to the spontaneous emission the dephasing process does not yield a substantial loss of condensate (see Fig. 4.19 (b)). Additionally we find the initial dynamics of the excited state occupation number to be comparable to the ones obtained for the initial DW phase, albeit a large dephasing rate leads to non-monotonous behavior. Similar to the case of only spontaneous emission the initial drop leads to a redistribution of the local order parameters and the SS phase becomes of type II (see Fig. 4.21). Compared to the previous density modulation this new configuration is characterized by atoms with excited state admixture on more sites, although all sites possess a lower excited state occupation number. The contribution of the long-range interaction to the system's energy is weaker than before the redistribution and thus subsequently the system allows for a larger excited state admixture.
We thus conclude that the spontaneous emission is the dominant contribution in the dynamics of a dissipative and decoherent Rydberg-dressed system. We furthermore establish that the many-body ground state beyond the frozen limit benefits from the ability of the atoms to reorganize. Experimentally the SS_2 phase appears to be promising as it is long-lived despite large decay and dephasing rates. The limiting factor however is the condensate, which depletes considerably for large decay rates. Luckily typical lifetimes of the Rydberg state given by the spontaneous emission and blackbody radiation are on the order of μs^{-1} (see Fig. 2.4) [128, 129, 132–134] and experimentally relevant Rabi frequencies on the order of several hundred kHz [182, 266], which yields marginal decay

and dephasing rates, i.e. $\Omega \gg \Gamma, \kappa$. On these relevant time scales the loss of condensation would not be crucial and the intermediate long-lived SS_2 phase in principle experimentally observable.

The many-body ground state computation and time evolution simulation deliver a tremendous insight on what quantum phases are expected for Rydberg-dressed bosonic quantum gases trapped in two-dimensional optical lattices. Due to the extended SS regime in the phase diagram we conclude that non-tilted, anisotropic van-der-Waals interaction is the best candidate for the experimental realization of SS phases. Another experimental aspect in favor of the anisotropic van-der-Waals interaction is the required coupling scheme for dressing atoms with Rydberg p-states. Since due to selection rules it is possible to dress through only one coupling laser, the achievable interaction strengths become larger and the effective lifetime is enhanced thanks to the lack of an intermediate state within the coupling scheme.
Unfortunately the experimentally accessible parameter space is usually strongly limited. The hopping amplitudes of trapped bosons are usually capped by $J \approx 2\pi \times 150$ Hz, which is considerably smaller than the typical Rabi frequencies in the order of MHz. Based on the phase diagrams it appears to be beneficial to work close to resonance $\Delta \approx 0$, but the previously discussed AC Stark shift and avalanche dephasing mechanism (see Section 2.4) are particularly dominant in this regime, which strongly inhibits coherent hopping processes and the overall lifetime of the system. Thus the experimental observation of interesting quantum phases such as the checkerboard-ordered SS_2 II phase becomes a challenging task.
While several approaches to overcome the avalanche dephasing have been proposed, it is possible to bypass the effect of the AC Stark shift to a certain degree. Larger hopping amplitudes can be achieved by choosing a lighter chemical element than the usual candidate Rubidium ^{87}Rb [267]. Through this notion it recently became possible to experimentally access and study the finite hopping regime of Rydberg-dressed fermionic atoms [268]. These results may give cause for optimism regarding the realization of the discussed Rydberg-dressed systems, but it does not seem to be an easy task. Since we believe in the potential of coupling atoms to Rydberg-excited states, we establish another dressing scheme based on the pair state potential of the Rydberg levels. In the following, we illustrate the advantages of that dressing scheme with respect to the above-mentioned challenges, compute the phase diagrams of the corresponding model and propose a way to experimentally realize SS phases.

4.3 Macrodimer-dressed atoms in two-dimensional lattices

In the previous section the dressed interaction between two atoms was induced through the coupling to pair states of excited states, which interact through the van-der-Waals interaction. However interaction can also emerge in systems dressed with molecular bound states (see Section 2.3.3). A recent theoretical work suggested that coupling the ground state atoms to the potential wells of the pair potential landscape can lead to

distance-specific dressed interaction with tunable strength and the improved ratio between interaction strength and decoherence [269]. Additionally a recent experimental study has observed the formation of macrodimer states in an optical lattice through coupling to the corresponding potential well [107]. Within the experiment two atoms with interatomic distance matching the bond length of the molecular bound state were excited to the macrodimer state and lost upon formation, since they are not trapped by the lattice.
Motivated by the theoretical proposal and the experiment we establish a macrodimer-dressing scheme. Through weak dressing the atoms coupled to the macrodimer state are not lost, but benefit from a dressed interaction. Although similar to the dressing scheme in [269], our proposed macrodimer-dressing completes the description of the potential well dressing by including the properties of macrodimers such as vibrational modes and modified lifetimes.
The model corresponding to macrodimer-dressed atoms in an optical lattice is an extended Bose-Hubbard model and reads

$$\hat{H} = -\mu \sum_i \hat{n}_i - J \sum_{\langle ij \rangle} (\hat{b}_i^\dagger \hat{b}_j + \hat{b}_j^\dagger \hat{b}_i) + \frac{U}{2} \sum_i \hat{n}_i (\hat{n}_i - 1) + \sum_{ij} V_{ij} \hat{n}_i \hat{n}_j. \tag{4.7}$$

Contrary to the Hamiltonian Eq. (4.1) investigated in the first section of this chapter we assume the atoms to be only weakly dressed and thus study an effective single-species system. The creation and annihilation operators therefore do not create or annihilate atoms in their electronic ground or excited state, but instead atoms in the macrodimer-dressed ground state. The long-range interaction strength V_{ij} depends on the adressed macrodimer state and the corresponding bond length R_e.
The goal of this section is to determine the advantages of the macrodimer-dressing scheme, investigate the properties of the dressed interaction with respect to strength and bond length, and determine the phase diagram of the Hamiltonian. We furthermore analyze and illustrate the possibility of experimentally preparing inhomogeneous phases in a realistic manner while taking the finite lifetime of the macrodimers into account.

4.3.1 Coupling to macrodimer states

As discussed in Section 2.3.3 macrodimer states arise through the avoided crossing of various pair state energies. Similar to any molecular state the macrodimer states are more specifically attributed a vibrational mode ν. We write the macrodimer state as a superposition of all involved pair states

$$|\Psi_{\mathrm{Mol}}^{\nu}\rangle = \sum_{ij} c_{ij}(R) \left|e_i e_j\right\rangle, \tag{4.8}$$

with the admixture coefficient c_{ij} of pair state $\left|e_i e_j\right\rangle = |n\ell, n'\ell'\rangle$. Note that the wave function of the molecular state is normalized, i.e. $\sum_{ij} |c_{ij}|^2 = 1$ In the two-atom picture coupling the ground state $|gg\rangle$ to a macrodimer state $|\Psi_{\mathrm{Mol}}\rangle$ requires a two-photon transition with an intermediate state (see Fig. 4.22 (a)). The intermediate state is not uniquely defined, since each pair state $\left|e_i e_j\right\rangle$ relevant in the avoided crossing possesses their own set of

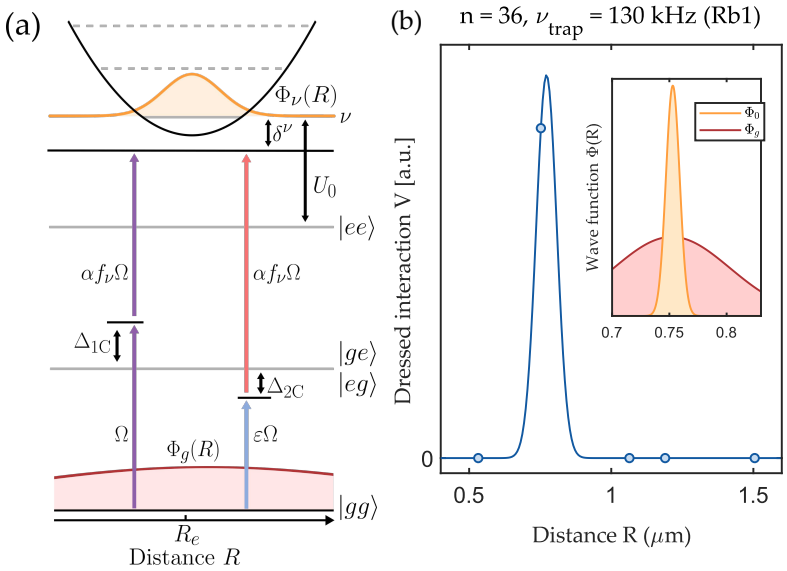

Figure 4.22: (a) Dressing scheme in the two-atom basis involving a ground state $|gg\rangle$, an intermediate state $|ge\rangle$ or $|eg\rangle$ and the excited state $|ee\rangle$. Left coupling shows the single-color scheme, where both transitions are driven by the same laser with Rabi frequency Ω. Right coupling represents the two-color scheme, for which the first laser has a reduced Rabi frequency $\varepsilon\Omega$ with $\varepsilon \ll 1$ compared to the second laser. The addressed potential well is described by the potential well minimum R_e, which corresponds to the bond length of the molecular state and a potential shift U_0 with respect to the asymptotic pair state $|ee\rangle$. (b) Schematic dressed interaction V versus distance R induced through the macrodimer-dressing. The distance-specific interaction results from the distance-dependent coupling of the two-atom ground state to the macrodimer state. The distance of the interaction can be changed by addressing a molecular bound state with different bond length R_e. Reprinted figure adapted with permission from [270]. © 2021 by the American Physical Society.

intermediate states $|i\rangle = |ge_i\rangle$ and $|j\rangle = |ge_j\rangle$. Going from the three level system to a two level system, we obtain the effective Rabi coupling of the ground state $|gg\rangle$ to the pair state $|e_i e_j\rangle$ defined by

$$\tilde{\Omega}_{ij} = \frac{\Omega_i \Omega_j}{2}\left(\frac{1}{\Delta_i} + \frac{1}{\Delta_j}\right) \tag{4.9}$$

with the single-photon transition Rabi frequencies $\Omega_i = \langle e_i | \hat{\boldsymbol{d}}\boldsymbol{E} | g\rangle$ and the detuning Δ_i of the intermediate state $|i\rangle$. The overall coupling to the vibrational mode ν of the molecular state is related to the superposition of all contributing pair states and thus reads

$$\tilde{\Omega}_\nu = \sum_{ij} \alpha_{ij} f_{ij}^\nu \tilde{\Omega}_{ij} \tag{4.10}$$

with the so-called *Franck-Condon factors* f_{ij}^{ν}. The prefactor $\alpha_{ij} \in [0,1]$ takes into account the difference between the single particle Rabi frequencies coupling the ground state to the intermediate states and the coupling of the intermediate to the macrodimer state [271]. The Franck-Condon factors further quantifies the coupling strength through the overlap of the initial relative ground state wave function $\Phi_g(R)$ and the vibrational wave function $\Phi_\nu(R)$ of the molecular state and reads

$$f_{ij}^{\nu} = \int \mathrm{d}R \Phi_\nu^*(R) c_{ij}(R) \Phi_g(R) \tag{4.11}$$

with the full Franck-Condon factor given by $f_\nu = \sum_{ij} f_{ij}^{\nu}$. The Rabi frequency of the coupling to the molecular state can be simplified in several ways without much loss of generality. First it can be assumed that the coefficients do not vary strongly within the region of the avoided crossing and can thus be seen as spatially independent, i.e. $c_{ij}(R) \to c_{ij}$. This allows to use the pair state independent, more general Franck-Condon factor, which only depends on the overlap as

$$f_\nu = \int \mathrm{d}R \Phi_\nu^*(R) \Phi_g(R). \tag{4.12}$$

Furthermore through close detuning to a single intermediate state it is possible to couple strongly off-resonant to all other intermediate states, which leads to vanishing effective Rabi frequencies $\tilde{\Omega}_{ij} = 0$. We hereby greatly simplify the effective Rabi frequency of the molecular coupling to

$$\tilde{\Omega}_\nu \approx \alpha f_\nu \frac{\Omega_1 \Omega_2}{2\Delta} \tag{4.13}$$

with the Rabi frequencies Ω_1 and Ω_2 of both relevant single-photon transitions and the detuning Δ. Similar to the calculation of the soft-core potential, the dressed interaction can be determined in the two-level picture composed of the ground state $|gg\rangle$ and the molecular state $|\Psi_{\mathrm{mol}}\rangle$ and yields

$$V = \sum_\nu V_\nu = \sum_\nu \alpha^2 f_\nu^2 \frac{\Omega_1^2 \Omega_2^2}{4\Delta^2 \delta} \tag{4.14}$$

with the detuning δ_ν to the vibrational mode ν of the molecular state. By working near-resonantly to the lowest vibrational mode $\nu = 0$ we expect the overall dressed interaction V to be predominantly given by V_0.

Even in its approximated form we see that the dressed interaction is dependent on many tunable parameters. Since a large enough dressed interaction strength is crucial for the emergence of inhomogeneous phases in trapped bosonic quantum system, it is important to grasp the accessible interaction strengths. While the experimentally tunable parameters are only restricted by the achievable range specific to the apparatus, the Franck-Condon factors could potential become a limiting factor. Since the vibrational wave function $\Phi_\nu(R)$ is substantially more narrow than the ground state wave function $\Phi_g(R)$, it is possible that their overlap and thus the Franck-Condon factors become vanishingly small (see Fig.

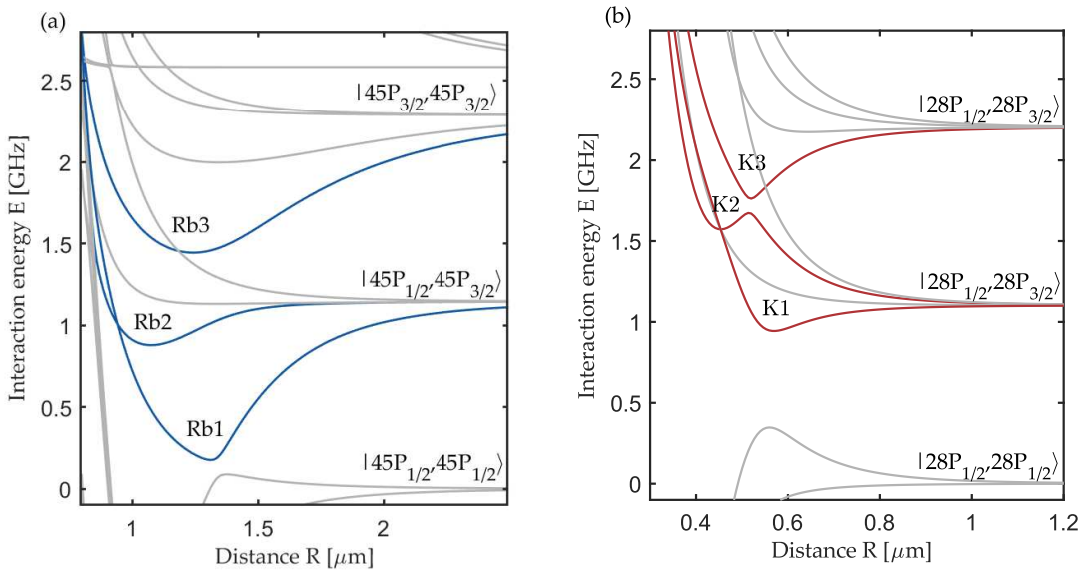

Figure 4.23: The three potential wells for (a) Rubidium ^{87}Rb and (b) Potassium ^{39}K arising from avoided crossing energetically located within the fine splitting of the pair states $|nP_{1/2}nP_{1/2}\rangle$, $|nP_{1/2}nP_{3/2}\rangle$ and $|nP_{3/2}nP_{3/2}\rangle$. We investigate the properties of these potential wells and the corresponding molecular bound states for $n \in [25, 75]$. Calculations for these results were performed with the help of the package `Pair Interaction` [146]. Reprinted figure adapted with permission from [270]. © 2021 by the American Physical Society.

4.22 (b)). However via the trapping frequency ν_{trap} of the optical lattice the width of the ground state wave function can be varied. Furthermore the vibrational wave function strongly depends on the addressed macrodimer state, since in a pair potential landscape many avoided crossings give rise to unique potential wells. The shape of each of these potential wells changes through variation of the principal quantum numbers n and n' of the relevant pair state. It is therefore important to understand the scaling behavior of these potential wells and their vibrational modes before discussing the possible values of the Franck-Condon factor.

Scaling properties of the potential wells

We analyze the properties of three potential wells appearing for Rubidium ^{87}Rb and Potassium ^{39}K (see Fig. 4.23). The potential wells are energetically located between the fine structure split states composed of $|e\rangle \equiv |nP_{1/2}\rangle$ and $|e\rangle' \equiv |nP_{3/2}\rangle$, since these were found to be very prominent, deep enough wells. For a given effective principal quantum number n^* we compute the pair state potential and characterize the potential wells through the position of its minimum R_e, i.e. the bond length of the macrodimer, the

depth D_e and the spacing Δ_ν of the vibrational levels. While the first two properties are determined by simply evaluating the pair state potentials, the calculation of the spacing requires to fit a quantum harmonic oscillator in the well and subsequent calculations of the levels. These three properties are determined for varied effective principal quantum number $n^* \in [25, 75]$ in order to obtain the scaling behaviour. Note, that variation of the effective principal quantum number n^* is identical to variation of the principal quantum number n, since the quantum defect $\delta_{n,\ell=1}$ is constant for these large values of n.
By fitting a power law, we find the position of the minimum to increase with the effective principal quantum number as $R_e \propto (n^*)^{8/3}$ and the depth to decrease with $D_e \propto (n^*)^{-3} + \epsilon(n^*)^{-4}$ with $\epsilon \ll 1$ (see Fig. 4.24). The decreasing depth can be easily understood in the context of high lying Rydberg levels: As the principal quantum number increases, the Rydberg levels become more densely packed. This also holds in the pair state basis, since for infinite distances between both atoms the energy of the pair state is given by the sum of the individual energies. As discussed in Section 2.2.1 the difference between two energy levels decreases as $(n^*)^{-3}$, which leads to more shallow depths with similar scaling behaviour. We obtain a scaling behavoir of the spacing $\Delta_\nu \propto (n^*)^{-3}$, which is related to the decreasing depth of the potential well. The quantum harmonic oscillator fitted becomes more wide and results in energetically closer vibrational modes.

Franck-Condon factors and dressed interaction

As mentioned before, the vibrational wave functions are determined within a quantum harmonic oscillator fit of the potential well. Thus the vibrational wave functions are given by the Hermite functions

$$\Phi_\nu(R) = \frac{1}{\sqrt{2^\nu \nu!}} \left(\frac{m\omega_{\text{well}}}{\pi\hbar}\right)^{1/4} e^{-\frac{m\omega_{\text{well}}R^2}{2\hbar}} H_\nu\left(\sqrt{\frac{m\omega_{\text{well}}}{\hbar}}R\right) \tag{4.15}$$

with the Hermite polynomials $H_\nu\left(\sqrt{\frac{m\omega_{\text{well}}}{\hbar}}R\right)$. The angular frequency ω_{well} is obtained through the harmonic fit of the potential well. Since we expect the lowest vibrational mode $\nu = 0$ to contribute the most to the overall dressed interaction, we focus for now on the Franck-Condon factor f_0 (see Appendix B). Therefore we first determine the vibrational wave function $\Phi_0(R)$ of the lowest mode given an effective principal quantum number n^* and the ground state wave function $\Phi_g(R)$, which consists of two Wannier functions, separated by distance R obtained within the deep lattice approximation for a given trapping frequency ν_{trap} (see Section 1.4.3). Through the overlap integral Eq. (4.12) we calculate the Franck-Condon factor f_0. We then either vary n^* or ν_{trap} in order to identify the scaling behavior of f_0.
For a fixed trapping frequency $\nu_{\text{trap}} = 40$ kHz, we find the Franck-Condon factor to be linearly proportional to the effective principal quantum number as $f_0 \propto n^*$ (see Fig. 4.25 (a)). The increasing Franck-Condon factor is in accordance with the potential depth D_e, which becomes shallower and thus yields wider vibrational wave functions. The Franck-Condon factor grows due to a larger overlap between both wave functions. Although

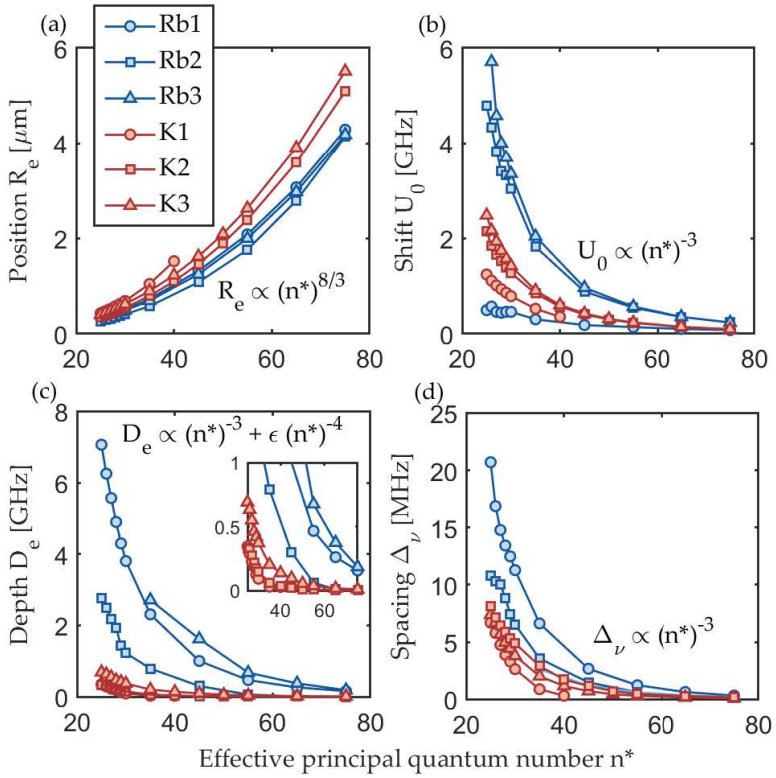

Figure 4.24: (a) Position of the potential minimum R_e, (b) shift U_0, (c) potential depth D_e and (d) spacing Δ_ν versus effective principal quantum number n^*. The scaling properties of the shift, the depth and the spacing are related to the dependence of the energy difference between neighboring Rydberg levels on n^* (see Section 2.2.1). Reprinted figure adapted with permission from [270]. © 2021 by the American Physical Society.

not reached within the range of studied effective principal quantum numbers, the Franck-Condon factor can reach the optimum $f_0 = 1$ for larger n^*, which lead to a vibrational wave function with a width comparable to the ground state wave function.

On the other hand, variation of the trapping frequency for a fixed effective principal quantum number $n^* = 35$ leads to a scaling of $f_0 \propto \nu_{\mathrm{trap}}^{1/4}$ (see Fig. 4.25 (b)-(c)), the origin of which can be found in the scaling behavior of the width of the Wannier function. Higher trapping frequencies lead to a more narrow Wannier function and for the studied potential wells, it is possible to reach the optimum value $f_0 = 1$ for very deep lattices. Within the calculations at a larger effective principal quantum number $n^* = 65$, the Franck-Condon factor reaches the optimum at lower trapping frequencies compared to the previous case. Furthermore, the Franck-Condon factor decreases beyond the optimum as $f_0 \propto \nu_{\mathrm{trap}}^{-1/4}$. In this case increasing the trapping frequency further leads to a Wannier function, which is even more narrow than the vibrational wave function and thus decreases the overlap.

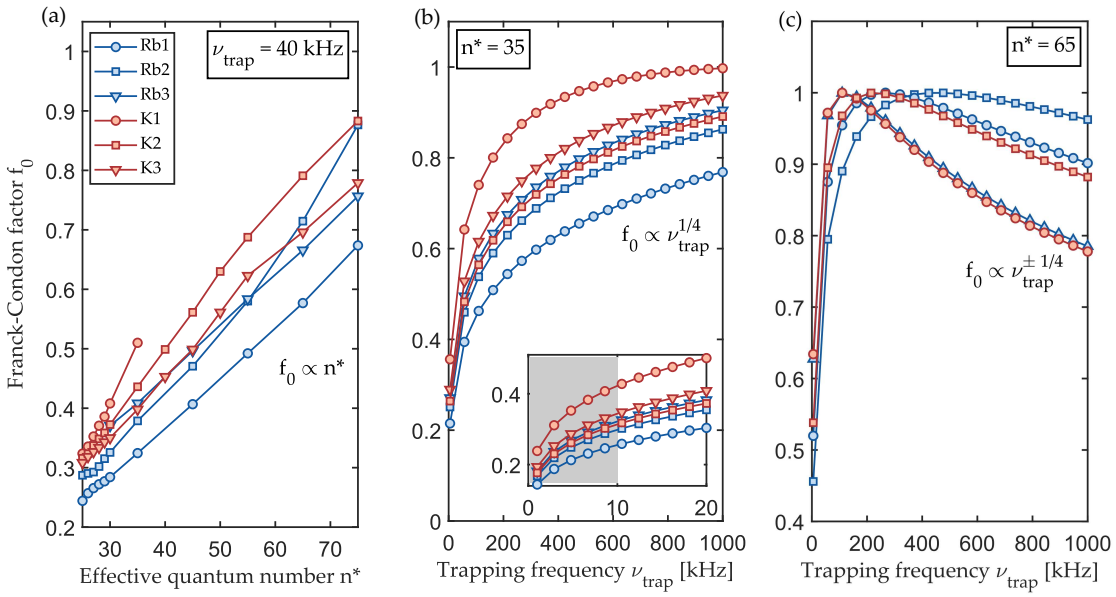

Figure 4.25: (a) Franck-Condon factor f_0 versus effective principal quantum number n^* for a fixed trapping frequency $\nu_{\text{trap}} = 40$ kHz. The Franck-Condon factor increases linearly with n^* independently of the chosen potential well. (b-c) Franck-Condon factor f_0 versus trapping frequency ν_{trap} for fixed effective principal quantum number (b) $n^* = 35$ and (c) $n^* = 65$. The scaling law can be derived from the Wannier function of the ground state $\Phi_g(R)$ as its width possesses the same scaling with ν_{trap}. For large n^* the Franck-Condon factor reaches its maximum value, i.e. $f_0 = 1$, within the considered range of ν_{trap}. Reprinted figure adapted with permission from [270]. © 2021 by the American Physical Society.

Although it thus appears to be more beneficial for the dressed interaction V_0 to work with larger effective principal quantum numbers, the scaling of the other parameters has to be taken into account. While the single-photon Rabi frequencies Ω_1 and Ω_2 appear to be only limited by the maximum power of the laser coupling, they additionally scale with the effective principal quantum number as $\Omega \propto (n^*)^{-3/2}$. The overall scaling of the dressed interaction becomes $V_0 \propto (n^*)^{-4}$ and it is therefore more convenient to work in the regime of smaller n^*.

Tunability and lifetimes

Before discussing the tunability of the system and the lifetime of the dressed ground state, we first elaborate the concepts of single-color and two-color dressing schemes. The single-color dressing scheme implies that the laser coupling the ground and intermediate state is also used for coupling the intermediate to the molecular state, i.e. $\Omega_1 = \Omega_2 = \Omega$.

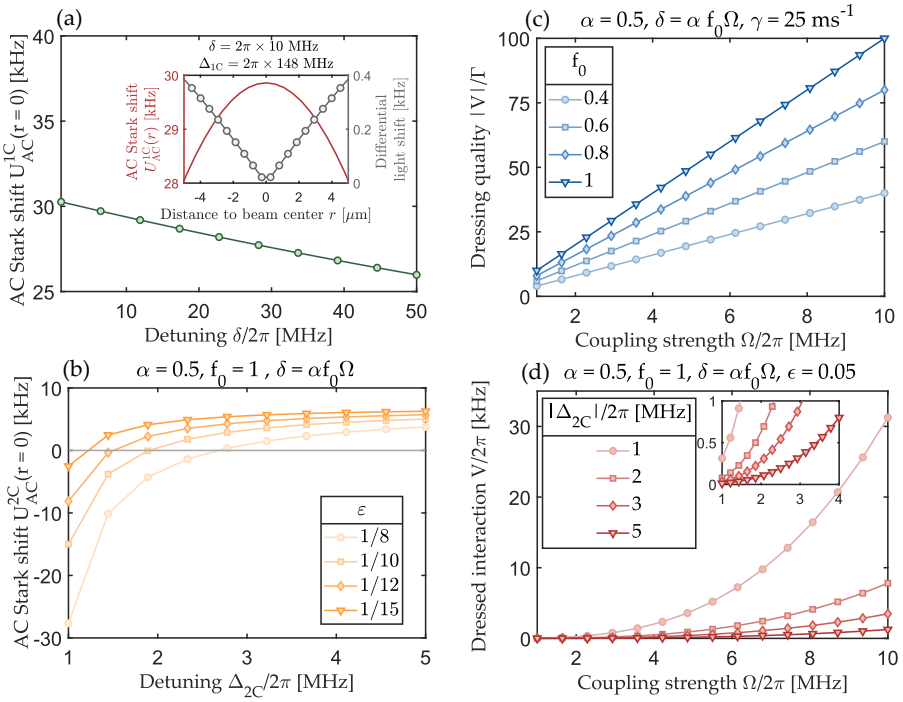

Figure 4.26: (a) AC Stark shift U_{AC}^{1C} obtained at the center of the laser beam for the single-color dressing scheme versus the detuning δ. Inset: The Gaussian profile of the laser causes an inhomogeneous AC Stark shift, which shifts neighboring sites out of resonance given by the differential light shift. (b) AC Stark shift U_{AC}^{2C} obtained at the center of the laser beam for the two-color dressing scheme versus the intermediate state detuning Δ_{2C}. The additional tunability allows to cancel out the AC Stark shift of both lasers. (c) The dressing quality $|V|/\Gamma$ versus the Rabi frequency Ω. At the optimum δ_{opt} the quality increases linearly with the frequency. (d) Dressed interaction strength V versus the Rabi frequency Ω. The dressed interaction becomes substantial for large frequencies. Reprinted figure adapted with permission from [270]. © 2021 by the American Physical Society.

We denote in this case the intermediate state detuning as Δ_{1C}. Within the single-color scheme it is not possible to choose the intermediate state detuning and the detuning of the lowest vibrational mode freely and their relation is given by $2\Delta_{1C} = U_0 + \delta$. On the other hand, within the two-color dressing scheme the two transitions are handled by two different lasers, i.e. $\Omega_2 = \Omega$ and $\Omega_1 = \varepsilon\Omega$ with $\varepsilon < 1$. This allows for the variation of the corresponding intermediate state detuning Δ_{2C}.
One major benefit of the two-color dressing scheme is the AC-Stark shift resulting from the coupling laser. As discussed in Section 2.4 each laser generates an AC Stark shift and due to the beam profile of the laser the shift is inhomogeneous. This is problematic since the inhomogeneous beam shifts neighboring sites out of resonance and can thus lead to the suppression of coherent hopping processes. The AC Stark shift in the single-color

dressing scheme reads

$$U_{\mathrm{AC}}^{1\mathrm{C}}(r) = \frac{\Omega^2(r)}{4\Delta_{1\mathrm{C}}} = \frac{\Omega^2(r)}{2(U_0+\delta)} \tag{4.16}$$

with the distance r to the beam center. The intensity profile of the laser beam with beam waist w is defined by $\Omega(r) = \Omega_0 e^{-r^2/w^2}$. Since the detuning δ is much smaller than the shift U_0, the AC Stark shift is not tunable and instead given by the adressed potential well and effective principal quantum number. The resulting AC Stark shift allows then only a handful of lattice sites at the center of the beam to be in resonance, while the differential light shift becomes to substantial already a couple of sites away from the beam center (see Fig. 4.26 (a)). Within the two-color dressing scheme however, it is possible to address this problem through the variation of the coupling laser Rabi frequency $\varepsilon\Omega$ and the tunable intermediate state detuning $\Delta_{2\mathrm{C}}$. The corresponding AC Stark shift is then given by the AC Stark shift of both coupling lasers

$$U_{\mathrm{AC}}^{2\mathrm{C}}(r) = \frac{\Omega^2(r)}{4}\Big(\frac{\varepsilon^2}{\Delta_{2\mathrm{C}}} + \frac{1}{U_0+\delta-\Delta_{2\mathrm{C}}}\Big) \tag{4.17}$$

For a fixed value of ε it is possible to achieve a vanishing AC Stark shift through variation of the intermediate state detuning $\Delta_{2\mathrm{C}}$ (see Fig 4.26 (b)). This allows to keep neighboring sites in resonance throughout the whole lattice and thus enables coherent hopping to occur.
The lifetimes of the macrodimer state are also of great importance for the experimental realization of macrodimer-dressed systems. In general, the overall decoherence rate of the dressed ground state due to the finite macrodimer lifetime is given by the intermediate state decoherence rate Γ_{Ryd} and the molecular decoherence rate Γ_{Mol} as

$$\Gamma = \Gamma_{\mathrm{Ryd}} + \Gamma_{\mathrm{Mol}} = P_{\mathrm{Ryd}}\gamma + P_{\mathrm{Mol}}\gamma_{\mathrm{Mol}} \tag{4.18}$$

with the squared admixtures P_{Ryd} and P_{Mol}, and the scattering rates γ and γ_{Mol} of the bare Rydberg state and the molecular state respectively. The molecular scattering rate is also given by the admixture of all possible pair states as $\gamma_{\mathrm{Mol}} = \sum_{ij} |c_{ij}|^2(\gamma_i + \gamma_j)$ with the scattering rate of the bare Rydberg state involved in the intermediate states $|i\rangle$ and $|j\rangle$. However within the previously established approximations, it is fine to simplify the molecular scattering rate as twice the scattering rate of the bare Rydberg state, i.e. $\gamma_{\mathrm{Mol}} = 2\gamma$. The squared admixtures P_{Ryd} and P_{Mol} are given by Eq. (2.53) with their respective detuning and Rabi frequency. For both dressing schemes, the decoherence rate of the dressed state reads

$$\Gamma = \Big(\frac{\Omega_1^2}{4\Delta^2} + \alpha^2 f_0^2 \frac{\Omega_1^2\Omega_2^2}{2\Delta^2\delta^2}\Big)\gamma \tag{4.19}$$

We see that the decoherence can be controlled through the choice of the single-photon Rabi frequencies, the detuning to the intermediate state and the detuning to the lowest vibrational mode. Unfortunately the dressed interaction possesses a similar scaling and tuning the parameters to reduce the decoherence rate would limit the dressed interaction strength. Additionally the lifetime increases with the effective principal quantum number

(see Section 2.2.3). The dressed interaction however decreases with the effective principal quantum number n^* as defined through the previously obtained scaling. In order to investigate the optimal parameter regimes we introduce the so-called *dressing quality* as

$$\frac{|V|}{\Gamma} = \Big[\Big(\frac{\delta}{\alpha^2 f_0^2 \Omega_2^2} + \frac{2}{\delta}\Big)\gamma\Big]^{-1} \tag{4.20}$$

Interestingly the dressing quality does not depend on the intermediate state and thus can be optimized through the coupling to the molecular state. The largest values of the dressing quality are obtained through the optimum detuning $\delta_{\text{opt}} = \alpha f_0 \Omega_2$. The dressing quality hereby simplifies to $|V|/\Gamma = \alpha f_0 \Omega_2/(2\gamma)$ and we see that the quality can be increased by going to larger Rabi frequencies Ω_2 (see Fig. 4.26 (c)). Note, that even though the dressing quality does not depend on the intermediate state, both admixtures are identical at the optimum detuning δ_{opt}, i.e. $P_{\text{mol}} = \tilde{\Omega}_0^2/(4\delta^2) \overset{\delta_{\text{opt}}}{=} \Omega_1^2/(4\Delta^2) = P_{\text{Ryd}}$. The overall scaling of the dressing quality with the effective principal quantum number depends on the dominant contribution to the bare Rydberg scattering rate. For large n^* the blackbody induced transitions lead to a decoherence rate $\Gamma_{\text{BBR}} \propto (n^*)^{-2}$, while in the regime of smaller n^* the spontaneous decay dominates $\Gamma_0 \propto (n^*)^{-3}$. The dressing quality therefore decreases as $|V|/\Gamma \propto (n^*)^{-2}$ or $|V|/\Gamma \propto (n^*)^{-3}$ with increasing principal quantum number in dependence on the dominant transitions, and working in the regime of smaller effective principal quantum numbers is thus more favorable for the observation of long-range interacting many-body ground states.
Since the two-color dressing scheme is more beneficial with respect to the AC Stark shift, we finally compute the dressed interaction within the optimum detuning for realistic parameters (see Fig. 4.26 (d)). For large, but experimentally achievable, Rabi frequencies the dressed interaction is of the order of several kHz. Even smaller Rabi frequencies yield reasonably significant dressed interactions of about several hundred Hz. These values are comparable to the typical on-site interaction strengths and hopping amplitudes and we therefore conclude that the dressed interaction induced by dressing atoms with macrodimer states may possibly lead to quantum phases with spontaneously broken lattice translational symmetry.

4.3.2 Many-body ground state phase diagram

We now study the phase diagram of the Hamiltonian Eq. (4.7) with the newly aquired knowledge on the macrodimer-dressing. Since two atoms are only coupled to the molecular state if their distance matches the corresponding bond length R_e, the dressed interaction results in

$$V_{ij} = V\delta(R_{ij} - R_e) \tag{4.21}$$

with the interatomic distance R_{ij}. Since the bond lengths of all studied potential wells are very similar, we can select the bond length solely by choice of the effective principal quantum number. For $n^* = 30$ the bond length matches the typical lattice constant $R_e \approx a_{\text{lat}} = 532$ nm and the resulting dressed interaction emerges between nearest

neighboring (NN) lattice sites. On the other hand $n^* = 36$ yields next-nearest neighbor (NNN) interaction, since the bond length is approximately given by $R_e \approx \sqrt{2}a_{\text{lat}}$. Although it is possible to obtain interactions on longer spatial scales by going to higher effective principal quantum numbers, the corresponding dressing quality is weaker and thus we limit our choice to the two above-introduced values of n^*.
For the sake of experimental relevance, we investigate the phase diagram with fixed filling $\bar{n} \in [0.5, 1]$. Since the filling is rather small, we can limit the Fock states to a small subspace and thus calculate the ground states within Cluster Gutzwiller theory. The single-cluster Hamiltonian of the system reads

$$\begin{aligned}\hat{H}_{\mathcal{C}} = &-\mu \sum_{i\in\mathcal{C}} \hat{n}_i - J \sum_{\langle ij\rangle\in\mathcal{C}} (\hat{b}_i^\dagger \hat{b}_j + \hat{b}_j^\dagger \hat{b}_i) + \frac{U}{2} \sum_{i\in\mathcal{C}} \hat{n}_i(\hat{n}_i - 1) + V \sum_{ij\in\mathcal{C}} \hat{n}_i \hat{n}_j \delta(R_{ij} - R_e) \\ &- J \sum_{i\in\partial\mathcal{C}} (\hat{b}_i^\dagger \varphi_i + \hat{b}_i \varphi_i^*) + V \sum_{i\in\partial\mathcal{C}} \hat{n}_i \eta_i + E(\varphi, \eta)\end{aligned} \tag{4.22}$$

with the mean-fields ϕ_i, η_i and the energy offset $E(\phi, \eta)$.
For the calculation of the phase diagrams, we set the on-site interaction $U = 2\pi \times 0.5$ kHz, the range of the hopping rate to $J/2\pi \in [0, 100]$ Hz and the range of the dressed interaction strength $V/2\pi \in [0, 250]$ Hz, all of which are experimentally accessible. Note that since we only possess one species in the dressed picture, we omit the type I and II notation previously used to specify inhomogeneous phases. For a fixed filling $\bar{n} = 0.5$, we investigate and compare the phase diagrams obtained with NN and NNN interaction (see Fig. 4.27 (a)). In both cases we find a DW and a SF regime seperated by a SS regime. Although both diagrams exhibit a similar shape, the SS regime is much larger for NNN interaction compared to its NN counterpart. The difference originates from the type of inhomogeneous phases arising from the interaction. As discussed in Section 1.6 NN interaction yields a checkerboard-type structure of the DW and SS phases. Since the hopping and the dressed interaction couple the same pair of sites, the direct competition pushes the boundary between the DW and the SS to larger hopping amplitudes. On the other hand NNN interaction yields striped phases, which exhibit a weakened competition between the hopping and the dressed interaction. Within the SS regime, the atoms can coherently tunnel within along the stripe with only little friction provided by the atoms in the neighboring stripes through the interaction. Therefore it is possible to have coexisting spatial modulation of the density and condensation in the system for a broader range of the tunable parameters. We thus conclude that the NNN interaction is more favorable with respect to the experimental realization of SS phases.

We now consider NNN interaction with varying filling $\bar{n} \in [0.5, 1]$, since the filling is also experimentally adjustable (see Fig. 4.27 (b)). The boundary between the SS and the SF regime changes significantly with increasing filling. While the boundary in the lower hopping amplitude range shifts to larger dressed interaction strength, we observe a shift to lower dressed interactions for higher hopping amplitudes. For unit filling $\bar{n} = 1$, the phase transition can be analytically computed. Since the competition between hopping and interaction is of second-order, we can determine the phase transition through perturbation

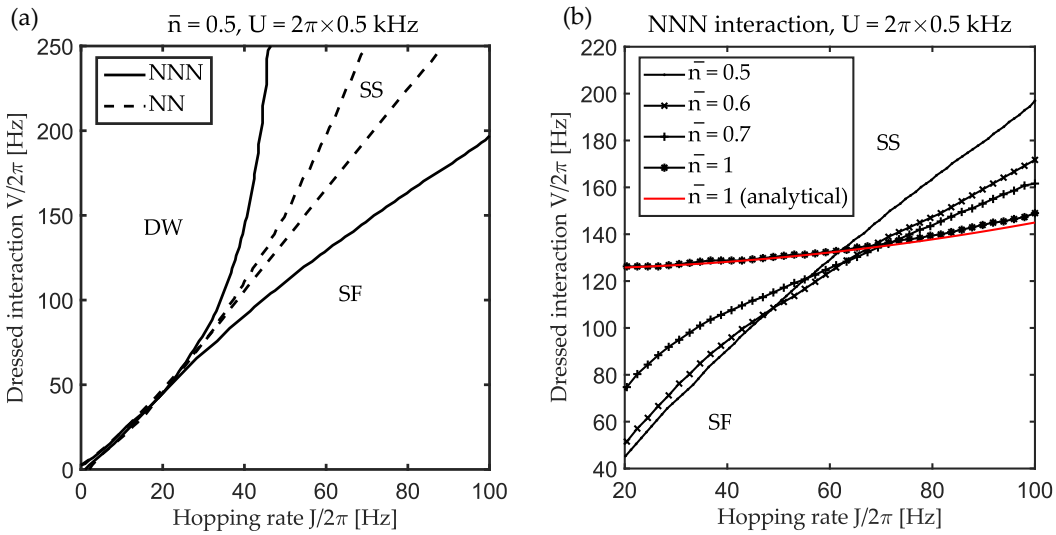

Figure 4.27: (a) $J - V$ phase diagram for fixed filling $\bar{n} = 0.5$ and $U = 2\pi \times 500$ Hz for NN and NNN interaction. SS regime is extended for NNN interaction due to the advantages of thus induced striped phases with respect to coexisting spatial modulation of the wave function and finite condensation. (b) $J - V$ phase diagram for various fillings $\bar{n} \in [0.5, 1]$. Larger filling shifts the boundary between the SS and the SF regime to stronger dressed interactions for lower hopping amplitudes, while at larger amplitudes the boundary is shifted to weaker interactions. Reprinted figure adapted with permission from [270]. © 2021 by the American Physical Society.

theory [272]. The resulting phase transition is given by the relation $V_c = U/4 + J^2/U$ and is in very good agreement with the numerically computed transition. This can be understood through the proportionalities in the Hamiltonian Eq. (4.7). While the dressed interaction term grows with the occupation number as $\propto \hat{n}^2$, the hopping term only scales linearly $\propto \hat{n}$. The simultaneous occupation of two neighboring sites becomes thus less energetically favorable for higher densities and therefore extends the range of inhomogeneous phases to larger hopping amplitudes and weaker dressed interactions. In the end the choice of the filling depends on the hopping amplitude and has to be chosen appropriately.

4.3.3 Preparation of macrodimer-dressed systems

Although the Hamiltonian yields SS phases as ground states of the system, their preparation is a non-trivial task. Driving an initially homogeneous system to a phase with spontaneously broken lattice translational symmetry requires an adiabatic parameter protocol. Furthermore, the losses of bare Rydberg-excited atoms and of macrodimers from the optical lattice limit the time scale during which SS phases can be observed. In order to investigate possible preparations of SS phases through the macrodimer-

dressing, we perform dissipative time-evolution simulations with realistic decoherence rates. Given an initially homogeneous system in a SF phase we increase the coupling to the macrodimer state, which translates to an adiabatic, linear ramp-up of the dressed interaction $V(t) = t/t_{\mathrm{ramp}} V_{\mathrm{max}}$ given with the ramping time t_{ramp} and the final dressed interaction V_{max} for $t \in [0, t_{\mathrm{ramp}}]$. During the time-evolution we include dissipative processes through the Lindblad master equation Eq. (3.59). We take into account single-body losses through the Lindblad operator $\hat{L}_{\mathrm{Ryd}} = \sum_i \sqrt{\Gamma_{\mathrm{Ryd}}} \hat{b}_i$ and macrodimer losses as $\hat{L}_{\mathrm{Mol}} = \sum_{ij} \sqrt{\Gamma_{\mathrm{Mol}}} \hat{b}_i \hat{b}_j \delta(R_{ij} - R_e)$. Note, that the macrodimer loss affects two atoms, whose distance matches the bond length. Although the scattering rates of these losses increase as the coupling is ramped up, we take their full value already in the beginning of the time-evolution. Furthermore, a numerical problem of the simulation is the absence of density fluctuations through which spontaneous symmetry breaking can be facilitated. Since phases with crystalline structure are degenerate with respect to translation and rotation, a perfectly homogeneous SF phase does not favor any of these phases and thus the breaking of the translational lattice symmetry is impeded until numerical fluctuations allow for the a phase transition. Therefore in order to lift the degeneracy, we impose an external, anisotropic harmonic confinement. Through the spatial choice of its minimum it is possible to isolate only one phase with broken lattice translational symmetry and thus enable the possibility of time evolution.
For the realization of the SS phases through NNN interaction it is more favorable to work with higher hopping amplitudes as they speed up the dynamics and allow for faster preparation. According to the above-obtained knowledge, we therefore perform the simulations with an average filling $\bar{n} = 1$. We keep the on-site interaction $U = 2\pi \times 0.5$ kHz, and limit the range of the hopping amplitude to $J/2\pi \in [50, 100]$ Hz and the range of the maximum dressed interaction strength to $V_{\mathrm{max}} \in [50, 200]$ Hz. For an effective principal quantum number $n^* = 30$, we obtain the bare Rydberg scattering rate $\Gamma_{\mathrm{Ryd}} = 4\,\mathrm{s}^{-1}$ and the molecular scattering rate $\Gamma_{\mathrm{Mol}} = 8\,\mathrm{s}^{-1}$. Note, that these rates have been determined for atoms at room temperature $T = 300K$ and since the atoms in the experiments are vastly cooler, these scattering rates present an upper bound of the experimentally relevant rates. We perform time evolution simulations up to $t_{\mathrm{max}} = 500$ ms for different values of the ramping time $t_{\mathrm{ramp}} = [100, 400]$ ms given a set of Hamiltonian parameters. According to the quantum adiabatic theorem, the adiabaticity of the time evolution is given for a ramping time of t_{ramp} for any of the dressed interactions considered during these calculations (see Section 3.3.1).

In order to determine whether the lattice translational symmetry has been broken during a time evolution simulation, we introduce the imbalance $\mathcal{I} = |\bar{n}_{\mathrm{odd}} - \bar{n}_{\mathrm{even}}|/N$ with the number of sites N as a staggered order parameter. Since numerical fluctuations during the time evolution could yield a finite imbalance even if the system stays in a SF phase, we use a threshold value $\mathcal{I}_{\mathrm{th}}$ to distinguish between time evolution with or without breaking of the translational lattice symmetry.
We find that the critical dressed interaction V_c, which is the minimum dressed interaction strength in order to have finite imbalance $\mathcal{I} > \mathcal{I}_{\mathrm{th}}$ during the time evolution, increases

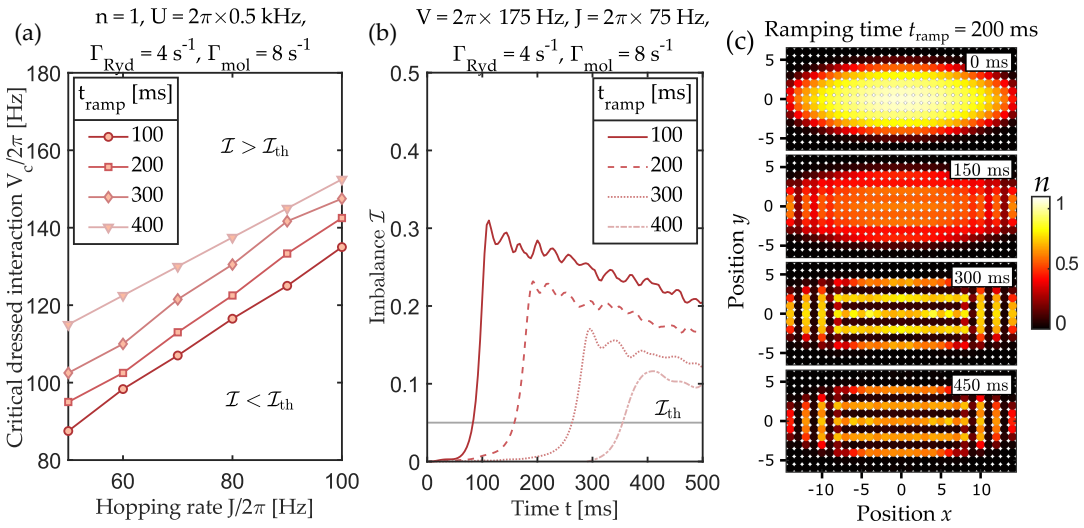

Figure 4.28: (a) Parameter regime of spontaneously broken lattice translational symmetry time evolution ($\mathcal{I} > \mathcal{I}_{\text{th}}$) and homogeneous time evolution ($\mathcal{I} < \mathcal{I}_{\text{th}}$) given by the critical dressed interaction V_c versus the hopping rate J for different values of the ramping times with $\mathcal{I}_{\text{th}} = 0.05$. Longer ramping times require larger dressed interaction for the imbalance $\mathcal{I}$ to become finite within the evolution times considered here. (b) Imbalance $\mathcal{I}$ versus time t for an initial SF state for fixed parameters of the extended Bose-Hubbard model $U = 2\pi \times 0.5$ kHz, $J = 2\pi \times 75$ Hz, $V = 2\pi \times 175$ Hz, a bare Rydberg scattering rate $\Gamma_{\text{Ryd}} = 4\,\text{s}^{-1}$ and a molecular scattering rate $\Gamma_{\text{mol}} = 8\,\text{s}^{-1}$ for different values of the ramping times $t_{\text{ramp}} \in [100, 400]$ ms. We find a finite imbalance emerging after ramping up the coupling to the macrodimer state. The later onset of a finite imbalance occurs for longer ramping times and its value decays due to the single particle and macrodimer losses. (c) Exemplary depiction of the time evolution of (b) with ramping time $t_{\text{ramp}} = 200$ ms at times $t \in [0, 150, 300, 450]$ ms where the occupation number n at each site is shown. The average filling $\bar{n} = 1$ is determined at the center of the trap. Reprinted figure adapted with permission from [270]. © 2021 by the American Physical Society.

with larger hopping amplitudes (see Fig. 4.28 (a)). For dressed interaction strengths below the critical value V_c the time-evolution is not able to break the lattice translational symmetry and the system stays SF. On the other hand, a large enough dressed interaction allows for the system to transition to a SS phase. The critical dressed interaction V_c shifts to larger values if we increase the ramping time t_{ramp}. Although the difference in ramping times is quite substantial, the boundary only shifts a dozen Hz and stays in the range of experimentally accessible dressed interactions. Note that variation of the numerical threshold $\mathcal{I}_{\text{th}}$ shifts all boundaries, although not beyond the range of achievable dressed interaction (see Appendix B).

For further understanding of the time evolution, we analyze the dynamically changing imbalance for the different ramping times (see Fig. 4.28 (b)). In all cases the imbalance grows fast and after reaching its maximum value it decays slowly. The maximum imbal-

ance is achieved around the ramping time t_{ramp}. We also depict the spatially modulated density for one of the ramping times to observe the spontaneous breaking of the lattice translational symmetry (see Fig. 4.28 (c)). The initially homogeneously system loses atoms as the coupling to the lossy Rydberg and macrodimer state is ramped up. Due to the rapid growth of the imbalance, the system transitions to the SS phase in a fast manner and depletes only slowly. Note, that the SS phase is not a perfectly striped phase but rather exhibits domains with perpendicular stripes. These domains arise due to the symmetry breaking occuring at different times in different places of the lattice due to the external, anisotropic harmonic confinement. At the more narrow borders of the trap the potential is steeper, which facilitates stripes perpendicular to the gradiant at earlier times.
Ultimately the experimental observation of SS phases in macrodimer-dressed systems appears to be possible based on the results obtained within the time evolution calculations. Even with the relatively large scattering rates considered in the computations, the system was able to transition into a SS phase before substantial depletion of the particles. The dressed interaction strengths necessary to access phases with spontaneously broken lattice translational symmetry are well within the realm of the achievable dressed interactions.

Chapter 5

Summary and outlook

We studied bosonic quantum gases trapped in an optical lattice coupled to Rydberg states. The associated model is described a two-component system consisting of atoms in the electronic ground state and in the Rydberg state. The model also includes a coupling term between the two components and the van der Waals interaction between the Rydberg atoms. To gain as much insight into this model as possible, we determined the many-body ground states for both isotropic and anisotropic van-der-Waals interactions. The calculations are performed for square optical lattices as well as for triangular optical lattices. Regardless of the geometry of the long-range interaction and the optical lattice, we found phase diagrams consisting of DW, SF and SS phases, with their parameter ranges depending on the geometries. The crystalline structures appearing in the DW and SS phases exhibited a wide variety of interatomic distances between Rydberg atoms. We found that anisotropic interaction leads to striped density modulations, which is particularly beneficial for the coexistence of crystalline structure and finite condensation. The difference between a square and a triangular optical lattice was only relevant for parameters through which the system exhibited dense density modulation and whose length scale is comparable to the lattice constant. For parameters however, through which phases consisting of Rydberg atoms with large interatomic distances appeared, the difference between the lattice geometries is hardly noticeable in the phase diagram. Since these results are promising for experimental realization, we completed the study by quantifying the influence of dissipation and decoherence, which arose from the spontaneous emission and blackbody radiation present for excited states. It was suspected that the finite lifetime of the Rydberg states and dephasing processes are so detrimental to the characteristic properties of SS phases, which would render SS phase of Rydberg-dressed quantum gases experimentally undetectable. Using the Lindblad master equation, we checked the strength of dissipation and decoherence in the context of time evolutions. We took as initial states both a DW and a SS phase obtained in the scope of the previous calculations and let these states evolve in time in the presence of the two mentioned processes. We found that indeed dissipation and decoherence increase with increasing rates of spontaneous emission and dephasing. Moreover, we observed that the SS phase benefits from the associated finite hopping amplitude, since redistribution of atoms in

the system allowed the system to be less affected by dissipation and decoherence. The long-lived state after reorganization of the atoms possessed a finite condensate decreasing with time, but for typical lifetimes and dephasing rates, this condensate did not disappear completely within the time ranges considered, which is promising for the experimental observation of such phases. We therefore conclude that bosonic quantum gases trapped in optical lattices and coupled to Rydberg states is a promising candidate for the realization of SS phases.
However, since collective phenomena and other experimental hurdles, such as the maximum realizable tunnel amplitude and coupling strength, could potentially pose difficulties, we proposed another system, through which SS phases could be realized. In contrast to the previous Rydberg-dressed bosonic quantum gas, the atoms in the electronic ground state are now weakly coupled pairwise to macrodimer states. As a result, the atoms in the ground state acquire an effective long-range interaction, however only if the distance between the two atoms matches the molecular bond length. We presented the single-color and two-color coupling schemes associated to the macrodimer dressing and discussed their differences with regards to the effective dressed interaction, the total AC Stark shift of the coupling lasers and the lifetime of such macrodimer states. For the calculation of the dressed interaction we computed three potential landscapes of two chemical elements and determined the coupling strength to the macrodimer states emerging from the avoided crossings in these potentials. We found that the coupling strength generally increases with larger principal quantum number or higher trapping frequencies. For trapping frequencies relevant in systems with finite hopping amplitude the coupling strength did not reach its optimal value, however the resulting dressed interaction becomes comparable to the values typically used for the on-site interaction and hopping amplitude. Furthermore we discovered that the magnitude of the dressed interaction did not depend on the type of coupling scheme, while the total AC Stark shift can be tuned out for a two-color coupling scheme. The vanishing differential light shift would then allow for coherent hopping processes. We calculated and shown that the dressing quality, i.e. the ratio between dressed interaction and decoherence, obtained through the macrodimer dressing is significantly larger than the dressing quality associated with the usual Rydberg dressing. Due to these promising aspects of the proposed system, we studied the phase diagram of the corresponding extended Bose-Hubbard model. Since the distance-dependency of the interaction can be changed based on the selection of the addressed macrodimer state, we compared the phase diagram for both NN as well as NNN interaction. Within the range of the determined dressed interaction strengths, the phase diagrams consisted DW, SF and SS regimes. We found that NNN interactions lead to striped crystalline structures, which is advantageous for SS phases. We furthermore varied the average filling of the lattice and investigate the necessary dressed interaction strengths. Interestingly we computed a lower necessary dressed interaction for lower fillings in the regime of small hopping amplitudes, while larger amplitudes profit from a higher filling. Since these results were particularly promising, we concluded the section with a proposal on how SS phases can be adiabatically prepared in macrodimer-dressed systems. To this end we simulated the slow ramp up of the coupling to the macrodimer states, while including the finite lifetime

of these states throughout the time evolution. We determined critical dressed interaction above which an initial SF phase exhibits spontaneously broken lattice translational symmetry. Since the admixture of the macrodimer state in the system decreases with time due to their finite lifetime, we discovered that longer ramping times require a larger dressed interaction. However even for long ramping times the necessary dressed interaction was well within the range of calculated dressed interactions and we are thus confident, that macrodimer-dressed systems could lead to the experimental realization and observation of SS phases.

On a personal note, as these results have been in the making for a while it was interesting to experience the ups and downs along the years as new insight about Rydberg ensembles continuously emerged. On one hand the phase diagrams of Rydberg-dressed gases displayed in the first part of Chapter 4 received ambiguous reactions as the concept behind such systems seemed simple yet promising, however limiting phenomena such as differential light shifts of the coupling laser impeding coherent hopping or lifetime inhibiting avalanche dephasing processes were only recently observed at that time and not fully understood yet. On the other hand through advances in technology and engineering of innovative methods tremendous insight about these obstacles was gained, which even allowed to overcome some of the previously limiting factors. A few years ago for example it thus became possible to realize a Rydberg-dressed fermionic quantum gas, in which dynamics given by the interplay of hopping and long-range interaction were experimentally observed [268]. Due to the amount of effort invested in the field of Rydberg ensembles, we are thus hopeful that in the future SS phases will be experimentally observed in trapped Rydberg-dressed and macrodimer-dressed quantum bosonic systems.

Appendix A

Numerical details

Between the application of the Gutzwiller mean-field approximations discussed in Section 3.2 and obtaining the different phase diagrams and time evolution simulation discussed in Sections 1.6, 4.2 and 4.3, we require a non-trivial self-consistent procedure and additional numerical methods.
In Section A.1 we elaborate on the core self-consistency procedure involved in the computation of the many-body ground states within Gutzwiller theory and briefly discuss the computational effort of the procedure based on the number and size of the clusters introduced through the mean-field decoupling. We then explain in Section A.2 how to construct and utilize superlattices in order to compute phase diagrams, in which the spatial modulation varies from one regime to another. Finally in Section A.3 we review the Runge-Kutta method, a method used to numerically solve the differential equation given by the Lindblad master equation.

A.1 Gutzwiller self-consistency procedure

In the core of the Gutzwiller self-consistency procedure are the local order parameters ϕ_i^ν and n_i^ν on site i of species ν (see figure A.1) given a fixed set of system parameters. After an initial guess of these parameters their values are updated each iterative loop until convergence is reached. Each of these loops consists of the calculation of the mean-fields ξ_i^ν and η_i in a cluster $\mathcal{C}$ with N sites, through which the Hamiltonian $\hat{H}_\mathcal{C}$ is created. The eigenvector $|\Psi_0\rangle$ corresponding to the lowest eigenvalue E_0 is obtained through ED and are subsequently used to determine the updated local order parameters $\tilde{\phi}_i^\nu$ and $\tilde{n}_i^\nu$ through $O = \langle\Psi_0|\,\hat{O}\,|\Psi_0\rangle$ with $\hat{O} \in \{\hat{b}_i^\nu, \hat{n}_i^\nu\}$. In order to check whether convergence is reached, we check the difference between the non-updated and updated order parameters. If the difference is below a numerical threshold ε, the calculation are treated as converged and the eigenvector $|\Psi_0\rangle$ and eigenvalue E_0 stored as the many-body ground state and its energy.
While the procedure might seem simple, its complexity becomes apparent when considering a system split into M unique clusters with N sites, since all clusters are connected through their respective mean fields. When performing the self-consistency procedure

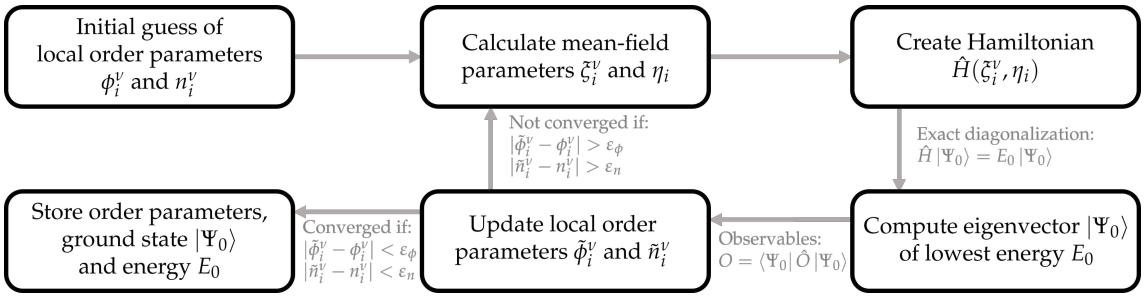

Figure A.1: Schematic representation of the self-consistency procedure in the core of the numerical many-body ground state computation within Gutzwiller mean-field theory. The local order parameters ϕ_i^ν and n_i^ν serve as the convergence criteria of the procedure. Their values are updated in a loop involving the computation of the mean-fields, of the matrix representation of the Hamiltonian, of the eigenvectors and eigenvalues through ED and finally of the new local order parameters $\tilde{\phi}_i^\nu$ and $\tilde{n}_i^\nu$. The convergence criteria is more specifically defined by numerical thresholds ε_ϕ and ε_n, which indicate whether the update of the order parameters lead to a significant difference or not.

with several, interconnected clusters we randomly select which cluster to update through the iterative loop. This allows all clusters to reach a converged state evenly and thus reveals the correct many-body ground state of the whole system. Generally speaking the number of sites N in a cluster defines the numerical complexity of a single loop, since the Hilbert space of the Hamiltonian $\hat{H}_C$ scales exponentially with N. On the other hand the number of iterative loops within the procedure necessary for convergence scales approximately linearly with M. It is thus, from a computational point of view, more convenient to work with a larger number of unique clusters with less sites, although important quantum fluctuations are thereby lost (see Section 3.2).

A.2 Computing with superlattices

In this work we compute the many-body ground state of a finite system with periodic boundary conditions (PBC) unless mentioned otherwise. This is especially important in the context of ground states, which can potentially exhibit spontaneously broken lattice translational symmetry, as the numerically determined density modulation is strongly restricted by the geometry of the considered system. For the sake of clarity, let us focus on an infinite system $\mathcal{S}$ in a two-dimensional optical lattice. For the computation of the ground state we select a *superlattice unit cell* $\mathcal{S}' \in \mathcal{S}$, smaller system representative of the whole system $\mathcal{S}$ due to the imposed PBC. This superlattice unit cell is defined through the two spanning vectors $\boldsymbol{a}_1, \boldsymbol{a}_2 \in \mathbb{Z}^2$ in units of lattice constant a_{lat} and an area $A_{\text{SL}} = \boldsymbol{a}_1 \times \boldsymbol{a}_2$ (see figure A.2 (a)). As an example we consider a Hamiltonian, which for a given set of its parameters we know that the many-body ground state is checkerboard-ordered.

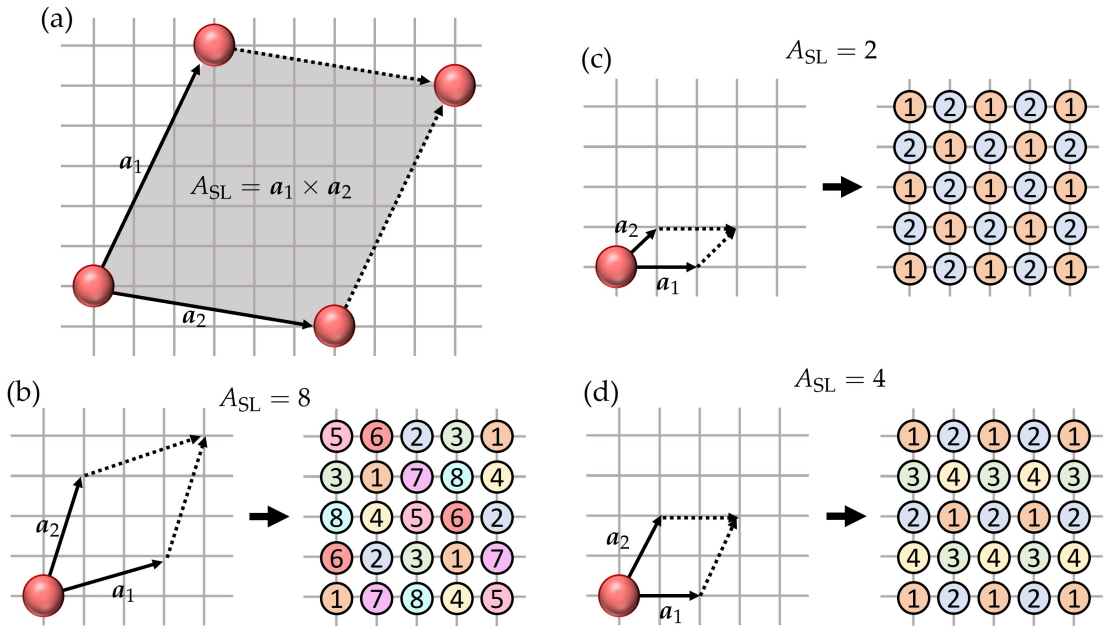

Figure A.2: (a) Schematic definition of a superlattice unit cell on an optical lattice defined through the spanning vectors $\boldsymbol{a}_1$ and $\boldsymbol{a}_2$ and the corresponding superlattice unit cell area $A_{SL} = \boldsymbol{a}_1 \times \boldsymbol{a}_2$. (b)-(d) Arbitrary superlattice unit cells with unique sets of spanning vectors, which allow to obtain different kinds of density modulation during the numerical computation of the many-body ground state. For the self-consistency procedure we furthermore characterize each superlattice unit cell by the sites it includes and their positions.

While it is possible to obtain checkerboard-ordered phases in a system with spanning vectors $\boldsymbol{a}_1 = (1,1)$ and $\boldsymbol{a}_2 = (0,2)$ (see figure A.2 (c)), other set of spanning vectors such as $\boldsymbol{a}_1 = (2,1)$ and $\boldsymbol{a}_2 = (0,2)$ geometrically prohibit this type of density modulation (see figure A.2 (d)). Although the numerical computation of the many-body ground state for these parameters might converge, the obtained many-body ground state differs from the correct one. Luckily it is possible to determine the true ground state as the energy of the geometrically frustrated many-body ground state is always larger and thus the comparison reveals the preferred density modulation of the system.

The extended, single-species Bose-Hubbard models considered in this thesis possess NN and NNN interaction terms and we can therefore conclude on the possible crystalline structures of the many-body ground states. However in the case of the van-der-Waals interaction appearing in the extended, two-species models the crystalline structure for a given set of Hamiltonian parameters is unknown. As using an arbitrarily chosen superlattice unit cell would potentially force the system into an energetically unfavorable ground state, it is crucial to perform the computation with many, different unit cell

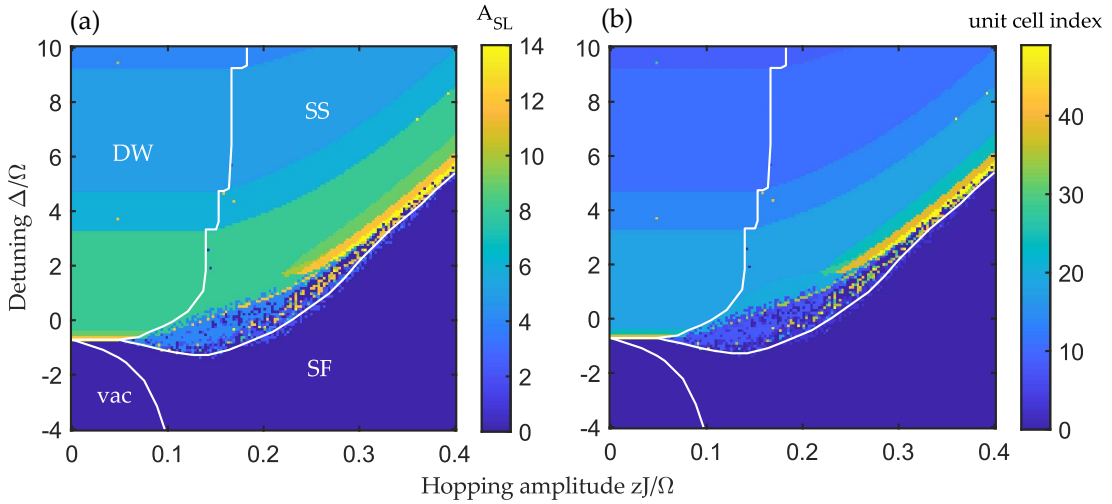

Figure A.3: (a) Superlattice unit cell area A_{SL} and (b) unit cell index of the preferred unit cell of the many-body ground state corresponding to the phase diagram in Fig. 4.5. While not all phase boundaries between the different regimes can be obtained by mapping these values, we are able to obtain the phase boundaries within the different regimes as the crystalline structure of the many-body ground state varies within the DW and SS regime.

uniquely characterized by their spanning vectors. We hereby obtain various many-body ground states and determine the true many-body ground state through comparison of their energies. In the end we store the properties of the superlattice unit cell of the many-body ground state, as in combination with the local observables within the unit cell allows to reconstruct the density modulation. Especially the superlattice unit cell area A_{SL} yields valuable information about the many-body ground state, as it hints at the distribution of the atoms with larger excited state admixture.
The superlattice unit cell area can furthermore be used to determine phase boundaries (see figure A.3). While the phase boundaries between insulating and condensed regimes does not become visible through the unit cell area if the underlying density modulation remains the same upon the phase transition, it allows us to detect boundaries within the regimes. Note that mapping the superlattice unit cell area is not sufficient in certain cases, as two neighboring regimes may possess unique crystalline structures but with equal superlattice unit cell area (see figure A.3 (right)). Thus indexing all unit cells used in the numerical computation allows us to better distinguish between different, unique density modulations. In combination with the mapping of average order parameters (see Appendix B.1) the superlattice unit cell area provides important information through which the different regimes in the phase diagram are recognized.

In the numerical computation used for calculating the phase diagrams displayed in Section 4.2 we selected a set of 50 different superlattice unit cells. The constraint was

given through the maximum superlattice unit cell area $A_{\mathrm{SL}}^{\max} = 16$. The effect of including larger superlattice unit cells would become visible if we zoom in at the DW-vacuum phase transition and at the SS-SF phase transition for large hopping amplitudes. Note that for the isotropic interaction the superlattice unit cell area in the SS_2 II regime is not homogeneous, but rather full of different values. This is because many superlattice unit cells are able to reproduce the checkerboard-order observed in the phases within this regime. Thus in the numerical computation all superlattice unit cell yield the same energy with the same ordering and the energy comparison becomes prone to numerical fluctuations.
The computational effort linked to the self-consistency procedure of a single superlattice unit cell depends on its area, as a bigger superlattice unit cell contains larger amount of lattice sites. More specifically through Pick's theorem the number of sites in a unit cell is given by the area itself, e.g. $A_{\mathrm{SL}} = N_{\mathcal{S}'}$. Understandably prone to confusion, the superlattice unit cell and the clusters used in the description within Gutzwiller theory are not identical. Although it is possible to use the complete superlattice unit cell as the cluster for the self-consistency procedure, it is often necessary to split the system into M clusters of size N as the superlattice unit cell can become too big to be handled by a single cluster. Under the condition $N_{\mathcal{S}'} = M \cdot N$ the unit cell can be split in any way as desired.

A.3 Solving ordinary differential equations

The various time evolutions computed in the scope of the thesis arise from the Lindblad master equation given by Eq. (3.57) discussed in Section 3.3. As an *ordinary differential equation* (ODE) of high complexity, it does not possess an exact solution and thus numerical methods become necessary. Here specifically these methods are used to compute the evolution of the time-dependent density matrix ρ_t of a system given an initial condition $\rho_{t=0} = \rho_0$. The temporal discretization of the ODE allows us to track the change of ρ_t and thus the time evolution of the whole system by computing local observables at every time step through $O = \mathrm{tr}(\rho\hat{O})$ with $\hat{O} \in \{\hat{b}_i^\nu, \hat{n}_i^\nu\}$.
Many methods, such as the Euler method [273, 274], the Backward analysis [275, 276] and the Richardson extrapolation [277–279], have been established to solve ODEs with initial value problems. Among those exists a widely popular method called the *Runge-Kutta method*, a multistep variation and thus generalization of the Euler method [280, 281]. In this thesis all time evolution simulations are performed by means of a symplectic, fourth-order Runge-Kutta method, which we discuss in the following.

Runge-Kutta methods

Runge-Kutta methods describe a class of s-step iterative methods, which expressed through the relevant variables in this work read

$$\rho_{t+\Delta t} = \rho_t + \Delta t \sum_{i=1}^{s} b_i k_i. \tag{A.1}$$

Here Δt describes the time step, and thus defines the temporal discretization, and $b_i \in [0,1]$ denotes the weight of the slope

$$k_i = f(t + c_i \Delta t, \rho_t + \Delta t \sum_{j=1}^{s} a_{ij} k_j), \tag{A.2}$$

where $c_i \in [0,1]$ are known as the nodes and $f(\cdot)$ stands for the RHS of the Lindblad master equation. a_{ij} form the Runge-Kutta matrix and are linked to the nodes $c_i = \sum_j a_{ij}$. They are often visualized in the so-called *Butcher tableau*, which generally reads

$$\begin{array}{c|cccc} c_1 & a_{11} & a_{12} & \dots & a_{1s} \\ c_2 & a_{21} & a_{22} & \dots & a_{2s} \\ \vdots & \vdots & \vdots & \ddots & \vdots \\ c_s & a_{s1} & a_{s2} & \dots & a_{ss} \\ \hline & b_1 & b_2 & \dots & b_s \end{array}$$

with $\sum_i b_i = 1$. Each Runge-Kutta method is thus uniquely defined by the number of steps s and Runge-Kutta matrix elements, the weights and the nodes as long as the above-mentioned equations are fulfilled. The trivial choice $s = 1$ gives back the Euler method. The fourth-order Runge-Kutta method ($s = 4$) is usually chosen as it yields marginal errors in the order of $\mathcal{O}((\Delta t)^5)$ for low computational cost. The values in the Butcher tableau of the commonly used fourth-order Runge-Kutta method read tableau is

$$\begin{array}{c|cccc} 0 & 0 & 0 & 0 & 0 \\ \frac{1}{2} & \frac{1}{2} & 0 & 0 & 0 \\ \frac{1}{2} & 0 & \frac{1}{2} & 0 & 0 \\ 1 & 0 & 0 & 1 & 0 \\ \hline & \frac{1}{6} & \frac{1}{3} & \frac{1}{3} & \frac{1}{6} \end{array}$$

While this choice is valid for most applications of the Runge-Kutta method, it has been discovered that its application to physical systems can potentially lead to fluctuation and variation of otherwise conserved quantities [282]. Although in Section 4.3 we consider particle loss, the non-unitary processes considered in the calculation in Section 4.2 does not affect the average filling of the system and thus should be conversed throughout the whole time evolution.
To this end a symplectic variation of the Runge-Kutta method has been developed [283–285]. For this purpose the Butcher tableau has to be set such that the method preserves the quadratic first integral due to its link to the symplectic nature of the method [286, 287]. Ultimately this leads to the symplectic condition given by

$$0 = (b_i b_j - b_i a_{ij} - b_j a_{ji}). \tag{A.3}$$

This condition ensures that physically conserved quantities stay conserved and other observables do not experience drastic changes due to numerical artifacts.

Appendix B

Supplementary figures

In the following we provide additional phase diagrams and plots through which the computed results of this thesis can be further understood. Section B.1 comprises complementary phase diagrams through the depiction of the mean observables. These figures complement the phase diagrams determined through the plain Bose-Hubbard model and the extended Bose-Hubbard model in Section 1.6.5 as well as the phase diagrams of the extended, two-species Bose-Hubbard model discussed in Section 4.2. In Section B.2 we display additional plots accompanying the results obtained for the macrodimer-dressing studied in Section 4.3.

B.1 Order parameters in the phase diagrams

As discussed in Section we distinguish between different types of phases through computation of order parameters with their respective many-body ground state. When discussing the phase diagram of the plain Bose-Hubbard model it is common to depict the two relevant order parameters within the chosen parameter space, namely the local condensate order parameter ϕ and the local occupation number n (see figure B.1). The vacuum regime and the Mott lobes are identified through a vanishing condensate order parameter $\phi = 0$, while it is finite valued $\phi \in \mathbb{R}$ in the SF regime. Additionally we observe an increasing condensate order parameter as the hopping amplitude and the chemical potential become larger. With respect to the hopping amplitude this is not too surprising, since the hopping amplitude gives a measure of how delocalized the atoms are. On the other hand the chemical potential dictates the filling of the system. A larger average occupation of the system implies more atoms which can condense and subsequently leads to an increased condensate order parameter. The occupation number n lets us distinguish between the vacuum regime $n = 0$ and the different Mott lobes $n \in \mathbb{N}$, while its value in the SF regime indicates the average filling $n \in \mathbb{R}$ of each site. For non-condensed phases the occupation number is integer-valued, as all atoms are highly localized, and each atom can be attributed to a single site. Since there is no term within the Hamiltonian yielding spontaneously broken lattice translational symmetry, the system is homogeneous and

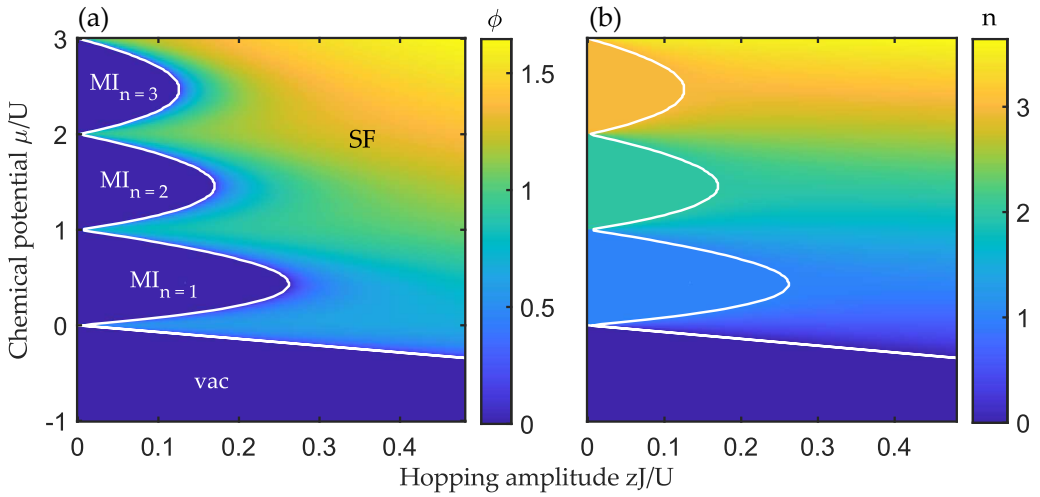

Figure B.1: $zJ - \mu$ phase diagrams obtained through the local condensate order parameter ϕ (a) and the occupation number n (b) corresponding to Fig. 1.10.

therefore well-described by these local order parameters.

The extended Bose-Hubbard model requires additional order parameters through which homogeneous and inhomogeneous phases can be uniquely characterized. As the extended Bose-Hubbard model discussed in this thesis possesses repulsive nearest neighbor interaction, we expect checkerboard-ordered phases as possible many-body ground states. We thus compute the staggered condensate order parameter $\phi^{\text{ch}}_{\text{stag}}$ and the staggered occupation number $n^{\text{ch}}_{\text{stag}}$ as defined in Section 1.6. For inhomogeneous phases it is not sufficient to compute the local order parameters ϕ_i and n_i only on one site i, which requires the spatially averaged observables $\bar{\phi}$ and $\bar{n}$.
For the extended Bose-Hubbard model at $zV/U = 1$ the spatially averaged condensate order parameter and occupation number yield phase diagrams comparable to the ones computed for the plain Bose-Hubbard model (see figure B.2). However the addition of the staggered order parameters allow to differentiate between MI and DW phases in the insulating regime $\bar{\phi} = 0$, and SF and SS regimes in the condensed regime $\bar{\phi} \in \mathbb{R}$. Through the staggered occupation number $n^{\text{ch}}_{\text{stag}} \in \mathbb{R}$ we identify two lobes of inhomogeneous phases, each comprised of an insulating and condensed regime. The staggered condensate order parameter more clearly exhibits the features of SS phases. Although these additional order parameters are crucial for characterizing the various regimes of the phase diagrams, the DW regimes can be potentially identified solely through the spatially averaged condensate order parameter and occupation number. Since some of the insulating regimes exhibit non-integer $\bar{n} \in \mathbb{Q}$, we can assume non-homogeneous distribution of the atoms within the lattice and thus identify the DW lobes.

Similarly for a larger repulsive nearest neighbor interaction $zV/U = 1.5$ we identify the

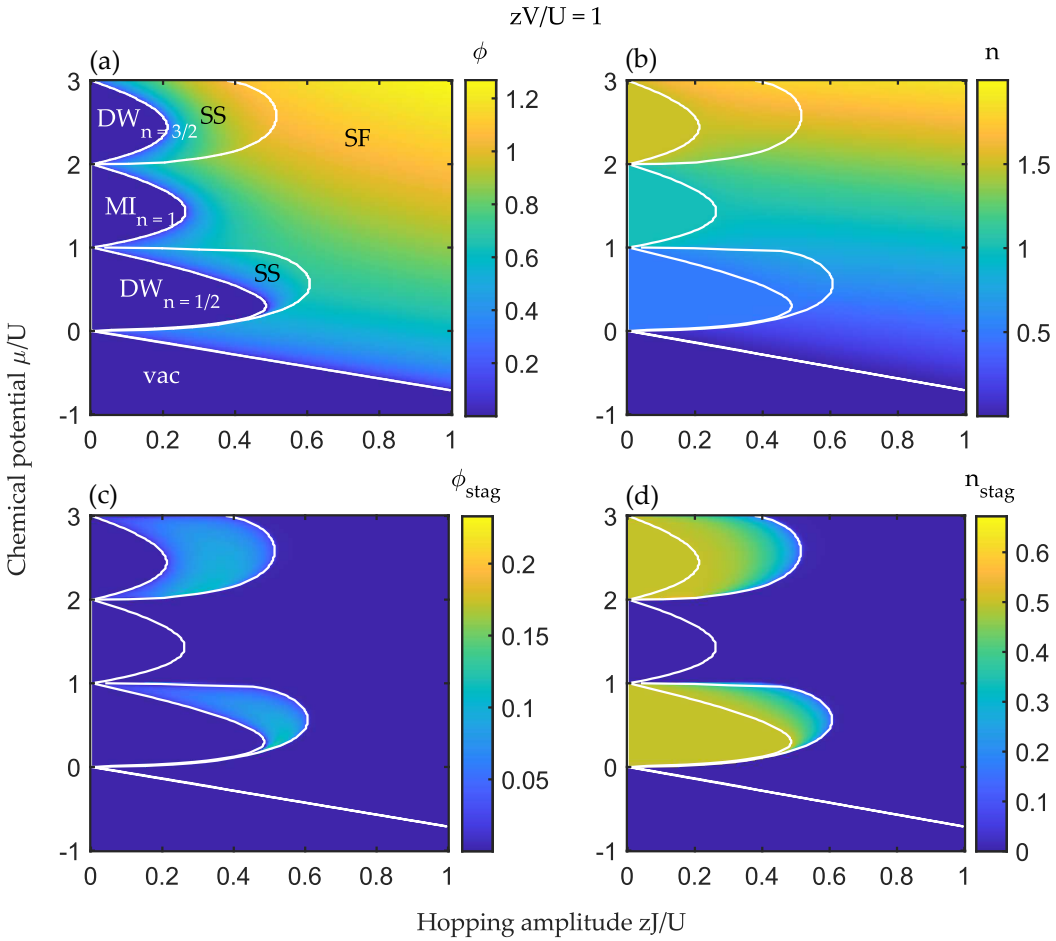

Figure B.2: $zJ - \mu$ phase diagrams obtained through the computation of the spatially averaged condensate order parameter $\bar{\phi}$ (a) and the occupation number n (b) as well as the staggered condensate order parameter $\phi^{\text{ch}}_{\text{stag}}$ (c) and the staggered occupation number $n^{\text{ch}}_{\text{stag}}$ (d) at $zV/U = 1$ corresponding to Fig. 1.12(a).

insulating, condensed, homogeneous and inhomogeneous phases through the spatially averaged and staggered order parameters (see figure B.3). However compared to the previous phase diagram it is not possibly to distinguish between the MI and DW lobes solely through the spatially averaged occupation number $\bar{n}$. Within the phase diagram we find a DW lobe with integer filling, which possesses identical spatially averaged order parameters to its MI counterpart. This emphasizes the importance of staggered ordered parameters for identifying the various regimes within the phase diagram.

A similar approach is used to determine the phase boundaries in the diagrams depicted

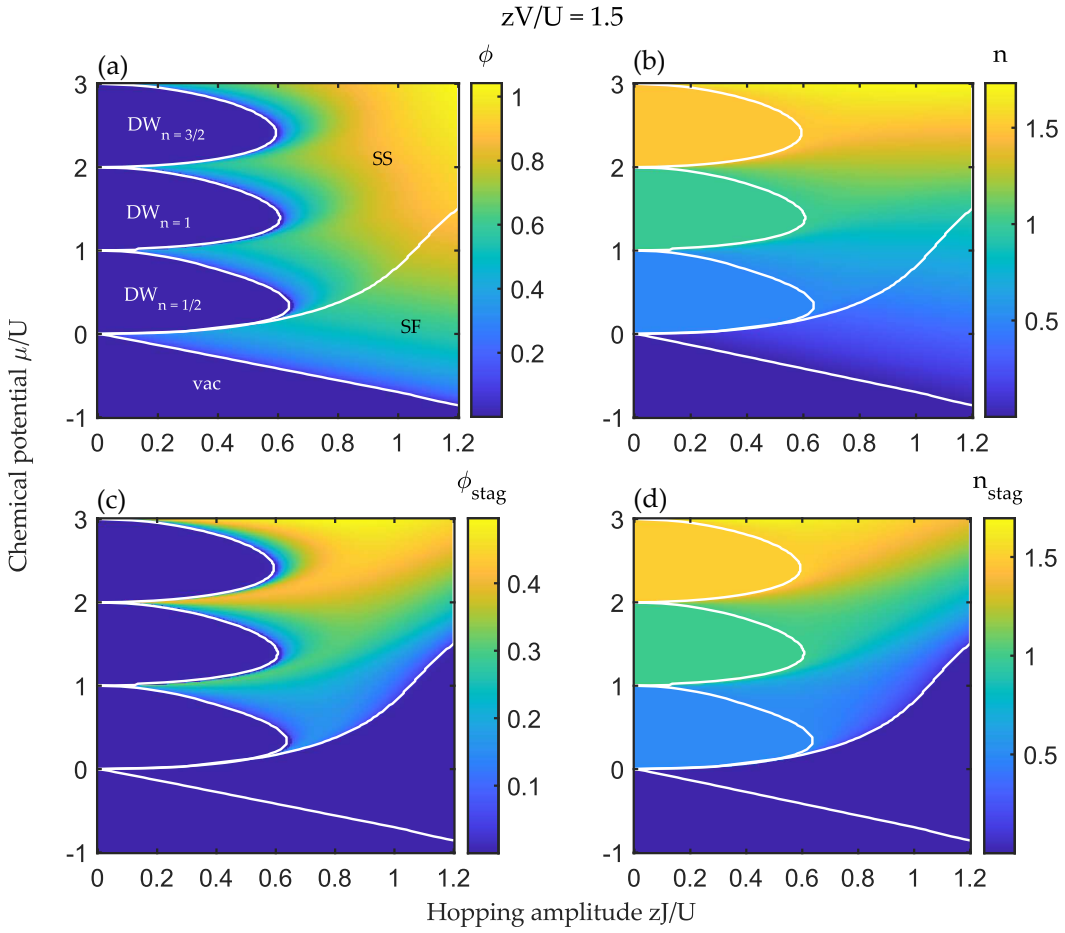

Figure B.3: $zJ - \mu$ phase diagrams obtained through the spatially averaged condensate order parameter $\bar{\phi}$ (a) and the occupation number $\bar{n}$ (b) as well as the staggered condensate order parameter $\phi^{\mathrm{ch}}_{\mathrm{stag}}$ (c) and the staggered occupation number $n^{\mathrm{ch}}_{\mathrm{stag}}$ (d) at $zV/U = 1.5$ corresponding to Fig. 1.12(b).

and discussed in Section 4.3. Additionally to checkerboard-ordered many-body ground states the extended Bose-Hubbard model relevant in that section yields striped phases if the repulsive interaction occurs between next-nearest neighboring sites. Identification of theses phases requires its own set of staggered order parameters as defined in Section 1.6. Subsequent determination of the regimes follows the above-explained reasoning.
The model studied in Section 4.2 describes a system consisting of two species, an electronic ground $|g\rangle$ and excited state $|e\rangle$, and thus it is necessary to compute species-specific order parameters in order to gain more information about the many-body ground states. However here the computation of spatially averaged and staggered order parameters for

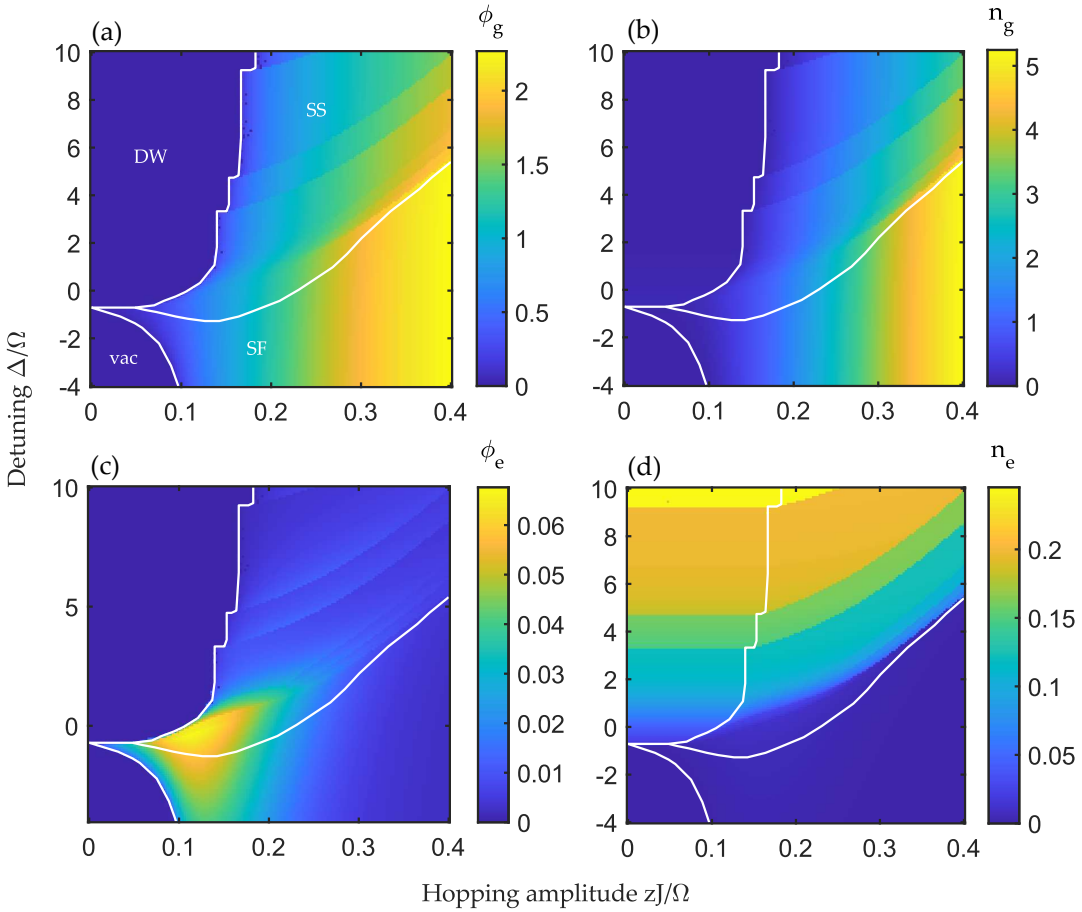

Figure B.4: $zJ - \Delta$ phase diagram obtained through the spatially averaged ground state condensate order parameter $\bar{\phi}_g$ (a) and the occupation number $\bar{n}_g$ (b) as well as the excited state condensate order parameter $\bar{\phi}_e$ (c) and the staggered occupation number $\bar{n}_e$ (d) corresponding to Fig. 4.5. Reprinted figure adapted with permission from [257]. © 2019 by the American Physical Society.

the sake of identifying the various regimes is not favorable, as the long-range interaction does not geometrically favor one type of ordering. In principal it would require us to define staggered order parameters for any possible spatial modulation and even then, it is likely that a many-body ground state with one type of ordering yields staggered order parameters of different ordering finite. We therefore compute the many-body ground state energy of many, unique orderings defined and determine the true many-body ground state through comparison of their energies (see Appendix A.2). Additionally we compute the spatially averaged order parameters in order to further understand the effect of hopping

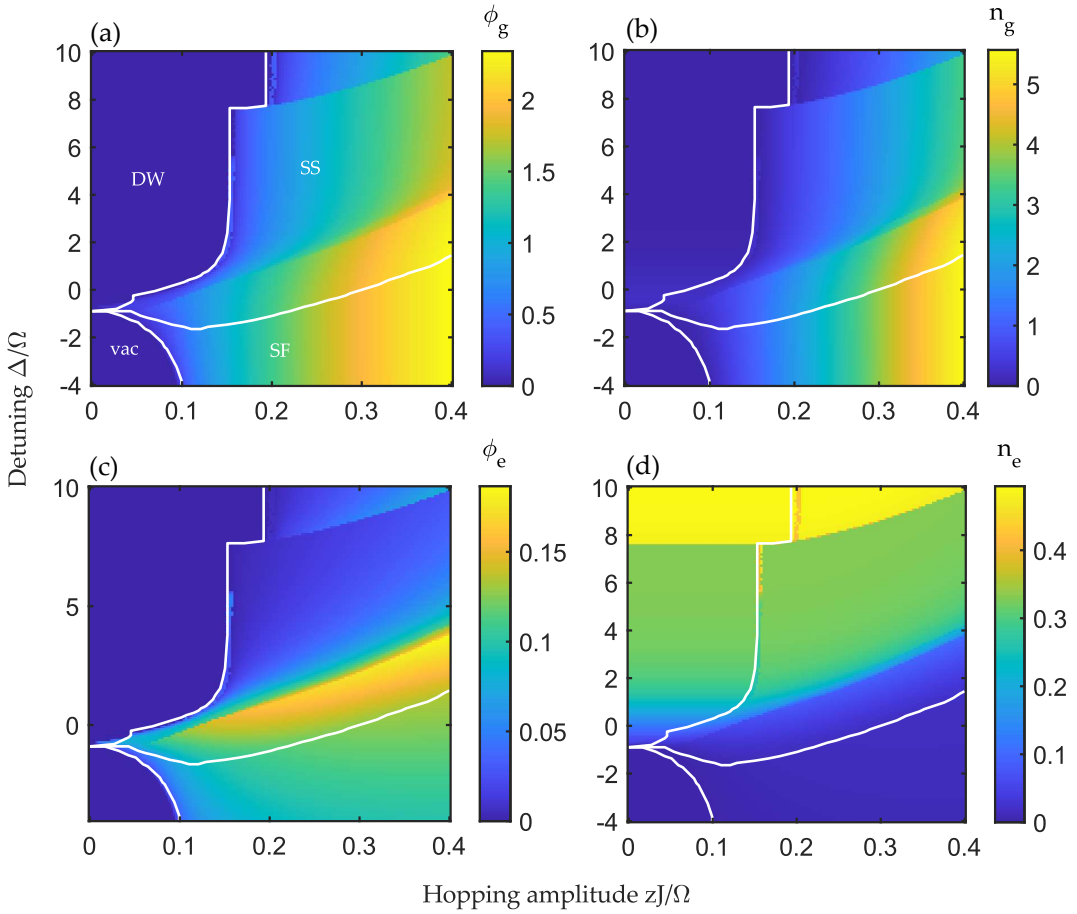

Figure B.5: $zJ - \Delta$ phase diagram obtained through the spatially averaged ground state condensate order parameter $\bar{\phi}_g$ (a) and the occupation number $\bar{n}_g$ (b) as well as the excited state condensate order parameter $\bar{\phi}_e$ (c) and the staggered occupation number $\bar{n}_e$ (d) corresponding to Fig. 4.11.

amplitude and detuning.
For isotropic interaction the spatially averaged ground state condensate order parameter $\bar{\phi}_g$ and occupation number $\bar{n}_g$ increase as the hopping amplitude becomes larger, which is in agreement with the previously obtained diagrams of the plain Bose-Hubbard model (see figure B.4). Furthermore the detuning controls not only the spatially averaged excited state occupation number $\bar{n}_e$, but also slightly its ground state counterpart. Similar to the devil's staircase a detuning decreasing towards its critical value, which denotes the phase transition between the homogeneous and inhomogeneous regimes, generally leads to larger $\bar{n}_g$ and smaller $\bar{n}_e$. Surprisingly the spatially averaged excited state condensate

order parameter $\bar{\phi}_e$ does not show monotonic behavior as it peaks around the region, where the system favors a checkerboard-ordered SS_2 I phase. The initial growth of $\bar{\phi}_e$ can be linked to the coherent coupling between the ground and excited state. Although the excited atoms are considered frozen condensation can occur through their coupling to the ground state, which become delocalized due to a finite hopping amplitude. $\bar{\phi}_e$ thus increases with the hopping amplitude around $\Delta \approx 0$ and decreases beyond a certain hopping amplitude, as the system then prefers a completely homogeneous, delocalized SF state. around At its maximum value increasing the detuning leads to larger $\bar{n}_e$ and therefore more repulsive interaction, which yields stronger localization of the excited state and thus a decreasing $\bar{\phi}_e$. On the other hand decreasing the detuning simply yields a smaller admixing of the excited state and therefore a vanishing $\bar{\phi}_e$.
The phase boundaries between the insulating and condensed regimes are extracted from these diagrams. Furthermore it is possible to identify the first-order phase transitions within the DW and SS regime as the spatially averaged excited state occupation number displays pronounced discontinuities upon variation of either the hopping amplitude or the detuning. Unfortunately the phase transition between the SF and SS regimes is not clearly visible, because it is of second-order (see figure 4.7). To this end investigating the phase diagram of the preferred superlattice unit cell reveals the phase boundary.
Although these results are computed on the square lattice we find highly similar phase diagrams for the triangular lattice.
For anisotropic interaction the phase diagrams possess comparable features. However a major difference is the region in which the spatially averaged excited state condensate order parameter takes its largest values (see figure B.5). Instead of a global maximum we find $\bar{\phi}_e$ to take large values in the SS_2 I phase regime. Due to the indirect competition between the delocalized ground state and repulsively interacting excited state it is possible to have a finite $\bar{\phi}_e$ even for large hopping amplitudes. Although no SS phase of type I exists for tilted anisotropic interaction its phase diagrams also exhibit this feature. We thus further confirm that the type of interaction has a larger impact on the many-body ground state compared to the lattice geometry.

B.2 Additional plots to the macrodimer-dressing proposal

During the discussion of the Franck-Condon factors, the dressed interaction and the dressing quality in Section 4.3, we focused on the Franck-Condon factor f_0 of the lowest vibrational mode of the studied potential wells. Although the coupling to a single higher lying vibrational mode is weaker due to the larger detuning and the smaller overlap of the corresponding wave function with the electronic ground state wave function, the accumulated contribution of all higher lying modes can become important. As an example we analyze the correction to dressed interaction computed solely with the Franck-Condon factor f_0 through inclusion of Franck-Condon factors f_ν of higher lying modes with vibrational quantum number ν.
For the potential well Rb1 (see figure 4.23) at a principal quantum number $n = 35$ and trapping frequency $\nu_{\text{trap}} = 40$ kHz, we see that the Franck-Condon factor f_ν decays as the

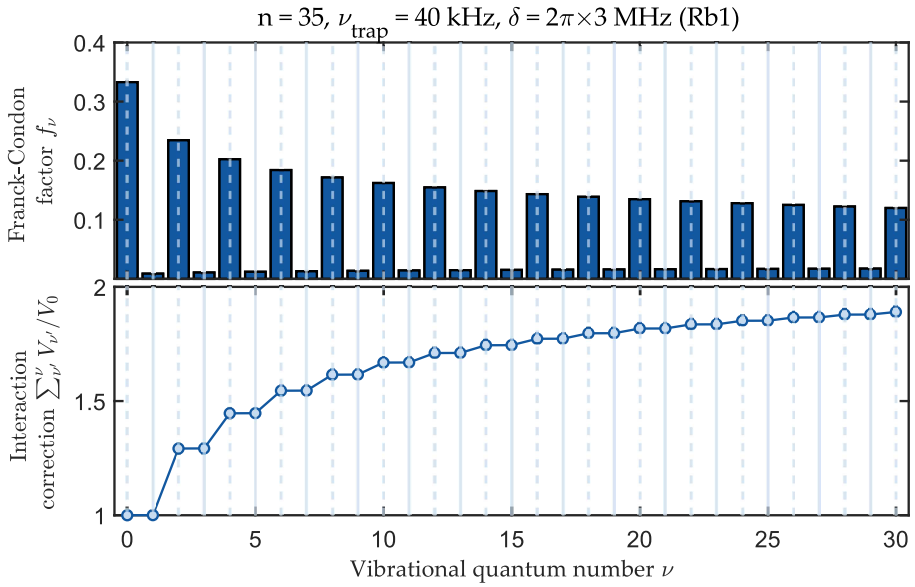

Figure B.6: Franck-Condon factors f_ν (upper) and correction $\sum_{\nu'=0}^{\nu} V_{\nu'}/V_0$ to the dressed interaction V_0 versus vibrational quantum number ν for the potential well Rb1 at $n = 35$, $\nu_{\text{trap}} = 40$ kHz and $\delta = 2\pi \times 3$ MHz. Reprinted figure adapted with permission from [270]. © 2021 by the American Physical Society.

vibrational quantum number ν increases (see figure B.6). Since the Wannier function of the elecronic ground state is symmetric and the wave functions of the vibrational modes, which are given by the Hermite functions (see Eq. (4.15)), are symmetric for even and antisymmetric for odd values of ν, we obtain nearly vanishing Franck-Condon factors f_ν for odd vibrational quantum numbers. The macrodimer bond length corresponding to the Rb1 potential at $n = 35$ does not exactly match the distance between nearest neighbor sites in an optical lattice with lattice constant $a_{\text{lat}} = 532$ nm and thus the center of the Wannier function and the Hermite functions are shifted to one another, yielding the nearly zero but finite Franck-Condon factor f_ν for odd values of ν. As discussed in section 4.3 the weight distribution of the Franck-Condon factor f_0 can be changed through variation of the principal quantum number or the trapping frequency. Although not shown here the Franck-Condon factors f_ν of higher lying vibrational modes behave opposite to f_0. This means that a larger value of f_0 brings along small values of f_ν and vice versa.
Through the Franck-Condon factors f_ν we can determine the full dressed interaction $V = \sum_\nu V_\nu$ with the contribution $V_\nu = \hbar\tilde{\Omega}_\nu^2/4\delta_\nu$ to the interaction through the coupling to the vibrational mode ν. The detuning δ_ν is given by the detuning to the lowest vibrational mode and the spacing between different vibrational modes as $\delta_\nu = \delta + \Delta_\nu$ (see figure 4.24). We compute the correction $\sum_{\nu'=0}^{\nu} V_{\nu'}/V_0$ to the dressed interaction computed only with the lowest vibrational mode up to a vibrational mode given by ν (see figure B.6).

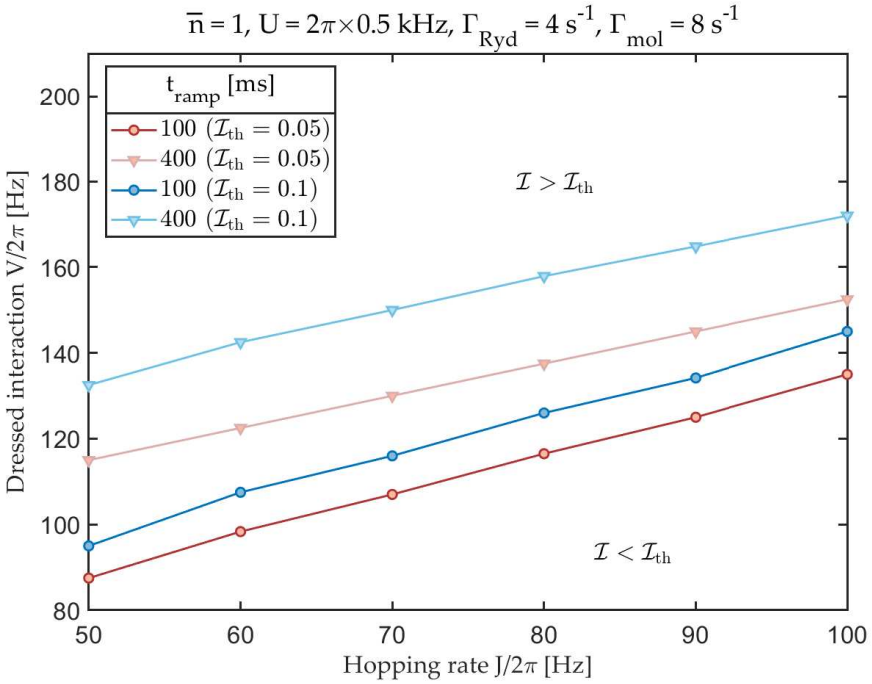

Figure B.7: Phase boundary between time evolution simulation leading to homogeneous ($\mathcal{I} < \mathcal{I}_{th}$) and sponatenously broken lattice translational symmetry ($\mathcal{I} < \mathcal{I}_{th}$) phases for two different values of the threshold $\mathcal{I}_{th} \in [0.05, 0.1]$. Reprinted figure adapted with permission from [270]. © 2021 by the American Physical Society.

While the correction appears to converge for the considered vibrational quantum numbers we obtain overall a factor two as the correction. This means that the dressed interaction displayed in Fig. 4.26 underestimates the correct dressed interaction achievable through the proposed macrodimer coupling, which is favorable for our results.
In Section 4.3 we discuss the dynamical preparation of SS phases and make use of a threshold $\mathcal{I}_{th}$ of the imbalance for the sake of distinguishing whether the system exhibits pronounced features of inhomogeneous, spatial modulation of the many-body state. This threshold value however is purely numerical and the phase boundaries displayed in figure 4.28 is susceptible to this threshold value. In order to understand its impact we determine the phase boundaries between homogeneous and sponatenously broken lattice translational symmetry time evolution for a larger threshold (see figure B.7). As expected the phase boundary between both regimes is shifted towards larger dressed interaction strengths as we increase the threshold, since many-body states that exhibit weak, inhomogeneous features fall under the threshold and thus the system requires larger dressed interactions to give rise to more distinct features. However this shift is only about a dozen Hz and thus not substantial. We therefore believe that phases with

spontaneously broken lattice translational symmetry are achievable for reasonable values of the dressed interaction.

Bibliography

[1] S. N. Bose, "Plancks Gesetz und Lichtquantenhypothese," 1924.

[2] A. Einstein, "Quantentheorie des einatomigen idealen Gases: zweite Abhandlung," *Albert Einstein: Akademie-Vorträge: Sitzungsberichte der Preußischen Akademie der Wissenschaften 1914–1932*, pp. 245–257, 2005.

[3] M. H. Anderson, J. R. Ensher, M. R. Matthews, C. E. Wieman, and E. A. Cornell, "Observation of Bose-Einstein Condensation in a Dilute Atomic Vapor," *Science*, vol. 269, no. 5221, pp. 198–201, 1995.

[4] S. Jochim, M. Bartenstein, A. Altmeyer, G. Hendl, S. Riedl, C. Chin, J. Hecker Denschlag, and R. Grimm, "Bose-einstein condensation of molecules," *Science*, vol. 302, no. 5653, pp. 2101–2103, 2003.

[5] J. Klaers, J. Schmitt, F. Vewinger, and M. Weitz, "Bose–einstein condensation of photons in an optical microcavity," *Nature*, vol. 468, no. 7323, pp. 545–548, 2010.

[6] B. P. Anderson and M. A. Kasevich, "Macroscopic quantum interference from atomic tunnel arrays," *Science*, vol. 282, no. 5394, pp. 1686–1689, 1998.

[7] Y. B. Ovchinnikov, J. Müller, M. Doery, E. Vredenbregt, K. Helmerson, S. Rolston, and W. Phillips, "Diffraction of a released bose-einstein condensate by a pulsed standing light wave," *Physical review letters*, vol. 83, no. 2, p. 284, 1999.

[8] J. Stenger, S. Inouye, A. P. Chikkatur, D. Stamper-Kurn, D. Pritchard, and W. Ketterle, "Bragg spectroscopy of a bose-einstein condensate," *Physical Review Letters*, vol. 82, no. 23, p. 4569, 1999.

[9] L. Deng, E. W. Hagley, J. Denschlag, J. Simsarian, M. Edwards, C. W. Clark, K. Helmerson, S. Rolston, and W. D. Phillips, "Temporal, matter-wave-dispersion talbot effect," *Physical Review Letters*, vol. 83, no. 26, p. 5407, 1999.

[10] J. Simon, W. S. Bakr, R. Ma, M. E. Tai, P. M. Preiss, and M. Greiner, "Quantum simulation of antiferromagnetic spin chains in an optical lattice," *Nature*, vol. 472, no. 7343, pp. 307–312, 2011.

[11] C. Navarrete-Benlloch, I. de Vega, D. Porras, and J. I. Cirac, "Simulating quantum-optical phenomena with cold atoms in optical lattices," *New Journal of Physics*, vol. 13, no. 2, p. 023024, 2011.

[12] J. Struck, C. Ölschläger, R. Le Targat, P. Soltan-Panahi, A. Eckardt, M. Lewenstein, P. Windpassinger, and K. Sengstock, "Quantum simulation of frustrated classical magnetism in triangular optical lattices," *Science*, vol. 333, no. 6045, pp. 996–999, 2011.

[13] F. Schäfer, T. Fukuhara, S. Sugawa, Y. Takasu, and Y. Takahashi, "Tools for quantum simulation with ultracold atoms in optical lattices," *Nature Reviews Physics*, vol. 2, no. 8, pp. 411–425, 2020.

[14] J. K. Pachos and P. L. Knight, "Quantum computation with a one-dimensional optical lattice," *Physical review letters*, vol. 91, no. 10, p. 107902, 2003.

[15] A. Kay and J. K. Pachos, "Quantum computation in optical lattices via global laser addressing," *New Journal of Physics*, vol. 6, no. 1, p. 126, 2004.

[16] T. Hänsch and A. Schawlow, "Cooling of gases by laser radiation," *Optics Communications*, vol. 13, no. 1, pp. 68–69, 1975.

[17] H. Metcalf and P. van der Straten, "Laser cooling and trapping," *Journal of the Optical Society of America B*, vol. 20, 05 2003.

[18] P. O. Schmidt, S. Hensler, J. Werner, T. Binhammer, A. Görlitz, and T. Pfau, "Doppler cooling of an optically dense cloud of magnetically trapped atoms," *J. Opt. Soc. Am. B*, vol. 20, pp. 960–967, May 2003.

[19] D. J. Wineland, J. Dalibard, and C. Cohen-Tannoudji, "Sisyphus cooling of a bound atom," *J. Opt. Soc. Am. B*, vol. 9, pp. 32–42, Jan 1992.

[20] Y. Castin, K. Berg-So/rensen, J. Dalibard, and K. Mo/lmer, "Two-dimensional sisyphus cooling," *Phys. Rev. A*, vol. 50, pp. 5092–5115, Dec 1994.

[21] P. Hamilton, G. Kim, T. Joshi, B. Mukherjee, D. Tiarks, and H. Müller, "Sisyphus cooling of lithium," *Phys. Rev. A*, vol. 89, p. 023409, Feb 2014.

[22] N. R. Newbury, C. J. Myatt, E. A. Cornell, and C. E. Wieman, "Gravitational sisyphus cooling of ^{87}Rb in a magnetic trap," *Phys. Rev. Lett.*, vol. 74, pp. 2196–2199, Mar 1995.

[23] V. V. Ivanov and S. Gupta, "Laser-driven sisyphus cooling in an optical dipole trap," *Phys. Rev. A*, vol. 84, p. 063417, Dec 2011.

[24] W. Ketterle and N. V. Druten, "Evaporative cooling of trapped atoms," vol. 37 of *Advances In Atomic, Molecular, and Optical Physics*, pp. 181–236, Academic Press, 1996.

[25] K. B. Davis, M.-O. Mewes, M. A. Joffe, M. R. Andrews, and W. Ketterle, "Evaporative cooling of sodium atoms," *Phys. Rev. Lett.*, vol. 74, pp. 5202–5205, Jun 1995.

[26] O. J. Luiten, M. W. Reynolds, and J. T. M. Walraven, "Kinetic theory of the evaporative cooling of a trapped gas," *Phys. Rev. A*, vol. 53, pp. 381–389, Jan 1996.

[27] T. Lahaye, Z. Wang, G. Reinaudi, S. P. Rath, J. Dalibard, and D. Guéry-Odelin, "Evaporative cooling of a guided rubidium atomic beam," *Phys. Rev. A*, vol. 72, p. 033411, Sep 2005.

[28] N. Lorenz, L. Festa, L.-M. Steinert, and C. Gross, "Raman sideband cooling in optical tweezer arrays for rydberg dressing," *SciPost Physics*, vol. 10, no. 3, p. 052, 2021.

[29] V. Vuletić, C. Chin, A. J. Kerman, and S. Chu, "Degenerate raman sideband cooling of trapped cesium atoms at very high atomic densities," *Physical Review Letters*, vol. 81, no. 26, p. 5768, 1998.

[30] V. Vuletić, C. Chin, A. J. Kerman, and S. Chu, "Degenerate raman sideband cooling of trapped cesium atoms at very high atomic densities," *Phys. Rev. Lett.*, vol. 81, pp. 5768–5771, Dec 1998.

[31] M. Gröbner, P. Weinmann, E. Kirilov, and H.-C. Nägerl, "Degenerate raman sideband cooling of ^{39}K," *Phys. Rev. A*, vol. 95, p. 033412, Mar 2017.

[32] G. E. Marti, R. Olf, E. Vogt, A. Öttl, and D. M. Stamper-Kurn, "Two-element zeeman slower for rubidium and lithium," *Phys. Rev. A*, vol. 81, p. 043424, Apr 2010.

[33] A. M. Steane and C. J. Foot, "Laser cooling below the doppler limit in a magneto-optical trap," *Europhysics Letters (EPL)*, vol. 14, pp. 231–236, feb 1991.

[34] V. Finkelstein, P. R. Berman, and J. Guo, "One-dimensional laser cooling below the doppler limit," *Phys. Rev. A*, vol. 45, pp. 1829–1842, Feb 1992.

[35] Y. Castin, H. Wallis, and J. Dalibard, "Limit of doppler cooling," *JOSA B*, vol. 6, no. 11, pp. 2046–2057, 1989.

[36] G. E. Marti, R. Olf, E. Vogt, A. Öttl, and D. M. Stamper-Kurn, "Two-element zeeman slower for rubidium and lithium," *Phys. Rev. A*, vol. 81, p. 043424, Apr 2010.

[37] S. Chu, L. Hollberg, J. E. Bjorkholm, A. Cable, and A. Ashkin, "Three-dimensional viscous confinement and cooling of atoms by resonance radiation pressure," *Phys. Rev. Lett.*, vol. 55, pp. 48–51, Jul 1985.

[38] D. Sesko, C. Fan, and C. E. Wieman, "Production of a cold atomic vapor using diode-laser cooling," *JOSA B*, vol. 5, no. 6, pp. 1225–1227, 1988.

[39] J. Dalibard and C. Cohen-Tannoudji, "Laser cooling below the doppler limit by polarization gradients: simple theoretical models," *JOSA B*, vol. 6, no. 11, pp. 2023–2045, 1989.

[40] X. Fang, K. F. MacDonald, E. Plum, and N. I. Zheludev, "Coherent control of light-matter interactions in polarization standing waves," *Scientific reports*, vol. 6, no. 1, pp. 1–7, 2016.

[41] M. T. DePue, C. McCormick, S. L. Winoto, S. Oliver, and D. S. Weiss, "Unity occupation of sites in a 3d optical lattice," *Phys. Rev. Lett.*, vol. 82, pp. 2262–2265, Mar 1999.

[42] N. B. Delone and V. P. Krainov, "Ac stark shift of atomic energy levels," *Physics-Uspekhi*, vol. 42, no. 7, p. 669, 1999.

[43] J. N. Bardsley and M. J. Comella, "ac stark effect for short-range potentials with intense electromagnetic fields," *Phys. Rev. A*, vol. 39, pp. 2252–2255, Feb 1989.

[44] R. Grimm, M. Weidemüller, and Y. B. Ovchinnikov, "Optical dipole traps for neutral atoms," *Advances in atomic, molecular, and optical physics*, vol. 42, pp. 95–170, 2000.

[45] J. D. Jackson, "Classical electrodynamics," 1999.

[46] T. C. Li, H. Kelkar, D. Medellin, and M. G. Raizen, "Real-time control of the periodicity of a standing wave: an optical accordion," *Opt. Express*, vol. 16, pp. 5465–5470, Apr 2008.

[47] L. Fallani, C. Fort, J. E. Lye, and M. Inguscio, "Bose-einstein condensate in an optical lattice with tunable spacing: transport and static properties," *Opt. Express*, vol. 13, pp. 4303–4313, May 2005.

[48] I. Bloch, J. Dalibard, and W. Zwerger, "Many-body physics with ultracold gases," *Reviews of modern physics*, vol. 80, no. 3, p. 885, 2008.

[49] S. Diehl, E. Rico, M. A. Baranov, and P. Zoller, "Topology by dissipation in atomic quantum wires," *Nature Physics*, vol. 7, no. 12, pp. 971–977, 2011.

[50] M. V. Katkov and C. Piermarocchi, "Coherent control of lattice deformations in quantum wires by optical self-trapping," *Phys. Rev. B*, vol. 73, p. 033305, Jan 2006.

[51] F. Meinert, M. Knap, E. Kirilov, K. Jag-Lauber, M. B. Zvonarev, E. Demler, and H.-C. Nägerl, "Bloch oscillations in the absence of a lattice," *Science*, vol. 356, no. 6341, pp. 945–948, 2017.

[52] G.-B. Jo, J. Guzman, C. K. Thomas, P. Hosur, A. Vishwanath, and D. M. Stamper-Kurn, "Ultracold atoms in a tunable optical kagome lattice," *Phys. Rev. Lett.*, vol. 108, p. 045305, Jan 2012.

[53] L. Santos, M. A. Baranov, J. I. Cirac, H.-U. Everts, H. Fehrmann, and M. Lewenstein, "Atomic quantum gases in kagomé lattices," *Phys. Rev. Lett.*, vol. 93, p. 030601, Jul 2004.

[54] B. Damski, H. Fehrmann, H.-U. Everts, M. Baranov, L. Santos, and M. Lewenstein, "Quantum gases in trimerized kagomé lattices," *Phys. Rev. A*, vol. 72, p. 053612, Nov 2005.

[55] C. Lee, T. J. Alexander, and Y. S. Kivshar, "Melting of discrete vortices via quantum fluctuations," *Phys. Rev. Lett.*, vol. 97, p. 180408, Nov 2006.

[56] A. M. Rey, G. Pupillo, C. W. Clark, and C. J. Williams, "Ultracold atoms confined in an optical lattice plus parabolic potential: A closed-form approach," *Physical Review A*, vol. 72, no. 3, p. 033616, 2005.

[57] H. P. Büchler, G. Blatter, and W. Zwerger, "Commensurate-incommensurate transition of cold atoms in an optical lattice," *Phys. Rev. Lett.*, vol. 90, p. 130401, Apr 2003.

[58] T. Müller-Seydlitz, M. Hartl, B. Brezger, H. Hänsel, C. Keller, A. Schnetz, R. J. C. Spreeuw, T. Pfau, and J. Mlynek, "Atoms in the lowest motional band of a three-dimensional optical lattice," *Phys. Rev. Lett.*, vol. 78, pp. 1038–1041, Feb 1997.

[59] H. A. Gersch and G. C. Knollman, "Quantum cell model for bosons," *Phys. Rev.*, vol. 129, pp. 959–967, Jan 1963.

[60] M. Lkacki, D. Delande, and J. Zakrzewski, "Dynamics of cold bosons in optical lattices: effects of higher bloch bands," *New Journal of Physics*, vol. 15, p. 013062, jan 2013.

[61] W. Xu, M. Olshanii, and M. Rigol, "Multiband effects and the bose-hubbard model in one-dimensional lattices," *Physical Review A*, vol. 94, no. 3, p. 031601, 2016.

[62] J. Larson, A. Collin, and J.-P. Martikainen, "Multiband bosons in optical lattices," *Physical Review A*, vol. 79, no. 3, p. 033603, 2009.

[63] P. Courteille, R. Freeland, D. J. Heinzen, F. Van Abeelen, and B. Verhaar, "Observation of a feshbach resonance in cold atom scattering," *Physical Review Letters*, vol. 81, no. 1, p. 69, 1998.

[64] D. Dickerscheid, U. Al Khawaja, D. Van Oosten, and H. Stoof, "Feshbach resonances in an optical lattice," *Physical Review A*, vol. 71, no. 4, p. 043604, 2005.

[65] K. Sengupta and N. Dupuis, "Mott insulator to superfluid transition of ultracold bosons in an optical lattice near a feshbach resonance," *EPL (Europhysics Letters)*, vol. 70, no. 5, p. 586, 2005.

[66] E. Fradkin, *Field theories of condensed matter physics*. Cambridge University Press, 2013.

[67] C. J. Pethick and H. Smith, *Bose–Einstein condensation in dilute gases*. Cambridge university press, 2008.

[68] L. Landau, "Theory of the superfluidity of helium ii," *Phys. Rev.*, vol. 60, pp. 356–358, Aug 1941.

[69] I. M. Khalatnikov, *An introduction to the theory of superfluidity*. CRC Press, 2018.

[70] G. Baym and C. J. Pethick, "Landau critical velocity in weakly interacting bose gases," *Phys. Rev. A*, vol. 86, p. 023602, Aug 2012.

[71] F. London, "On the bose-einstein condensation," *Phys. Rev.*, vol. 54, pp. 947–954, Dec 1938.

[72] G. E. Astrakharchik and L. P. Pitaevskii, "Motion of a heavy impurity through a bose-einstein condensate," *Phys. Rev. A*, vol. 70, p. 013608, Jul 2004.

[73] C. Raman, M. Köhl, R. Onofrio, D. S. Durfee, C. E. Kuklewicz, Z. Hadzibabic, and W. Ketterle, "Evidence for a critical velocity in a bose-einstein condensed gas," *Phys. Rev. Lett.*, vol. 83, pp. 2502–2505, Sep 1999.

[74] T. Ohgoe, T. Suzuki, and N. Kawashima, "Ground-state phase diagram of the two-dimensional extended bose-hubbard model," *Physical Review B*, vol. 86, no. 5, p. 054520, 2012.

[75] M. Iskin, "Route to supersolidity for the extended bose-hubbard model," *Phys. Rev. A*, vol. 83, p. 051606, May 2011.

[76] W. Neil, M. ASHCROFT, and N. David, *SOLID STATE PHYSICS*. CENGAGE LEARNING CUSTOM P, 2020.

[77] D. Sherrington, "Long range order in solids," *Nature*, vol. 284, no. 5754, pp. 382–382, 1980.

[78] G. V. Chester, "Speculations on bose-einstein condensation and quantum crystals," *Phys. Rev. A*, vol. 2, pp. 256–258, Jul 1970.

[79] H. Matsuda and T. Tsuneto, "Off-diagonal long-range order in solids," *Progress of Theoretical Physics Supplement*, vol. 46, pp. 411–436, 1970.

[80] A. Andreev and I. Lifshits, "Quantum theory of defects in crystals," *Zhur Eksper Teoret Fiziki*, vol. 56, no. 6, pp. 2057–2068, 1969.

[81] A. J. Leggett, "Can a solid be" superfluid"?," *Physical Review Letters*, vol. 25, no. 22, p. 1543, 1970.

[82] J. Léonard, A. Morales, P. Zupancic, T. Esslinger, and T. Donner, "Supersolid formation in a quantum gas breaking a continuous translational symmetry," *Nature*, vol. 543, no. 7643, pp. 87–90, 2017.

[83] K. Baumann, C. Guerlin, F. Brennecke, and T. Esslinger, "Dicke quantum phase transition with a superfluid gas in an optical cavity," *nature*, vol. 464, no. 7293, pp. 1301–1306, 2010.

[84] R. Mottl, F. Brennecke, K. Baumann, R. Landig, T. Donner, and T. Esslinger, "Roton-type mode softening in a quantum gas with cavity-mediated long-range interactions," *Science*, vol. 336, no. 6088, pp. 1570–1573, 2012.

[85] L. Chomaz, D. Petter, P. Ilzhöfer, G. Natale, A. Trautmann, C. Politi, G. Durastante, R. M. W. van Bijnen, A. Patscheider, M. Sohmen, M. J. Mark, and F. Ferlaino, "Long-lived and transient supersolid behaviors in dipolar quantum gases," *Phys. Rev. X*, vol. 9, p. 021012, Apr 2019.

[86] L. Tanzi, E. Lucioni, F. Famà, J. Catani, A. Fioretti, C. Gabbanini, R. N. Bisset, L. Santos, and G. Modugno, "Observation of a dipolar quantum gas with metastable supersolid properties," *Phys. Rev. Lett.*, vol. 122, p. 130405, Apr 2019.

[87] F. Böttcher, J.-N. Schmidt, M. Wenzel, J. Hertkorn, M. Guo, T. Langen, and T. Pfau, "Transient supersolid properties in an array of dipolar quantum droplets," *Phys. Rev. X*, vol. 9, p. 011051, Mar 2019.

[88] A. Gallemí, S. M. Roccuzzo, S. Stringari, and A. Recati, "Quantized vortices in dipolar supersolid bose-einstein-condensed gases," *Phys. Rev. A*, vol. 102, p. 023322, Aug 2020.

[89] M. Guo, F. Böttcher, J. Hertkorn, J.-N. Schmidt, M. Wenzel, H. P. Büchler, T. Langen, and T. Pfau, "The low-energy goldstone mode in a trapped dipolar supersolid," *Nature*, vol. 574, no. 7778, pp. 386–389, 2019.

[90] L. Tanzi, S. Roccuzzo, E. Lucioni, F. Famà, A. Fioretti, C. Gabbanini, G. Modugno, A. Recati, and S. Stringari, "Supersolid symmetry breaking from compressional oscillations in a dipolar quantum gas," *Nature*, vol. 574, no. 7778, pp. 382–385, 2019.

[91] A. Sen, P. Dutt, K. Damle, and R. Moessner, "Variational wave-function study of the triangular lattice supersolid," *Physical review letters*, vol. 100, no. 14, p. 147204, 2008.

[92] V. Kashurnikov, N. Prokof'ev, and B. Svistunov, "Revealing the superfluid–mott-insulator transition in an optical lattice," *Physical Review A*, vol. 66, no. 3, p. 031601, 2002.

[93] F. Gerbier, S. Trotzky, S. Fölling, U. Schnorrberger, J. Thompson, A. Widera, I. Bloch, L. Pollet, M. Troyer, B. Capogrosso-Sansone, *et al.*, "Expansion of a quantum gas released from an optical lattice," *Physical review letters*, vol. 101, no. 15, p. 155303, 2008.

[94] W. S. Bakr, J. I. Gillen, A. Peng, S. Fölling, and M. Greiner, "A quantum gas microscope for detecting single atoms in a hubbard-regime optical lattice," *Nature*, vol. 462, no. 7269, pp. 74–77, 2009.

[95] E. Haller, J. Hudson, A. Kelly, D. A. Cotta, B. Peaudecerf, G. D. Bruce, and S. Kuhr, "Single-atom imaging of fermions in a quantum-gas microscope," *Nature Physics*, vol. 11, no. 9, pp. 738–742, 2015.

[96] L. W. Cheuk, M. A. Nichols, M. Okan, T. Gersdorf, V. V. Ramasesh, W. S. Bakr, T. Lompe, and M. W. Zwierlein, "Quantum-gas microscope for fermionic atoms," *Physical review letters*, vol. 114, no. 19, p. 193001, 2015.

[97] R. Courant and D. Hilber, *The Calculus of Variations*, ch. 4, pp. 164–274. John Wiley & Sons, Ltd, 1989.

[98] M. Greiner, O. Mandel, T. Esslinger, T. Haensch, and I. Bloch, "Quantum phase transition from a superfluid to a mott insulator in a gas of ultracold atoms," *Nature*, vol. 415, pp. 39–44, 02 2002.

[99] J. N. Kupferschmidt and E. J. Mueller, "Role of interactions in time-of-flight expansion of atomic clouds from optical lattices," *Physical Review A*, vol. 82, no. 2, p. 023618, 2010.

[100] M. Karski, L. Förster, J. M. Choi, W. Alt, A. Widera, and D. Meschede, "Nearest-neighbor detection of atoms in a 1d optical lattice by fluorescence imaging," *Phys. Rev. Lett.*, vol. 102, p. 053001, Feb 2009.

[101] Y. Miroshnychenko, D. Schrader, S. Kuhr, W. Alt, I. Dotsenko, M. Khudaverdyan, A. Rauschenbeutel, and D. Meschede, "Continued imaging of the transport of a single neutral atom," *Opt. Express*, vol. 11, pp. 3498–3502, Dec 2003.

[102] K. D. Nelson, X. Li, and D. S. Weiss, "Imaging single atoms in a three-dimensional array," *Nature Physics*, vol. 3, no. 8, pp. 556–560, 2007.

[103] M. Pyzh, S. Krönke, C. Weitenberg, and P. Schmelcher, "Quantum point spread function for imaging trapped few-body systems with a quantum gas microscope," *New Journal of Physics*, vol. 21, no. 5, p. 053013, 2019.

[104] O. Elíasson, J. S. Laustsen, R. Heck, R. Müller, J. J. Arlt, C. A. Weidner, and J. F. Sherson, "Spatial tomography of individual atoms in a quantum gas microscope," *Phys. Rev. A*, vol. 102, p. 053311, Nov 2020.

[105] J. F. Sherson, C. Weitenberg, M. Endres, M. Cheneau, I. Bloch, and S. Kuhr, "Single-atom-resolved fluorescence imaging of an atomic mott insulator," *Nature*, vol. 467, no. 7311, pp. 68–72, 2010.

[106] M. Miranda, R. Inoue, N. Tambo, and M. Kozuma, "Site-resolved imaging of a bosonic mott insulator using ytterbium atoms," *Physical Review A*, vol. 96, no. 4, p. 043626, 2017.

[107] S. Hollerith, J. Zeiher, J. Rui, A. Rubio-Abadal, V. Walther, T. Pohl, D. M. Stamper-Kurn, I. Bloch, and C. Gross, "Quantum gas microscopy of rydberg macrodimers," *Science*, vol. 364, no. 6441, pp. 664–667, 2019.

[108] J. Simon, W. S. Bakr, R. Ma, M. E. Tai, P. M. Preiss, and M. Greiner, "Quantum simulation of antiferromagnetic spin chains in an optical lattice," *Nature*, vol. 472, no. 7343, pp. 307–312, 2011.

[109] A. Omran, M. Boll, T. A. Hilker, K. Kleinlein, G. Salomon, I. Bloch, and C. Gross, "Microscopic observation of pauli blocking in degenerate fermionic lattice gases," *Phys. Rev. Lett.*, vol. 115, p. 263001, Dec 2015.

[110] H. Weimer, M. Müller, I. Lesanovsky, P. Zoller, and H. P. Büchler, "A rydberg quantum simulator," *Nature Physics*, vol. 6, no. 5, pp. 382–388, 2010.

[111] T. L. Nguyen, J.-M. Raimond, C. Sayrin, R. Cortinas, T. Cantat-Moltrecht, F. Assemat, I. Dotsenko, S. Gleyzes, S. Haroche, G. Roux, *et al.*, "Towards quantum simulation with circular rydberg atoms," *Physical Review X*, vol. 8, no. 1, p. 011032, 2018.

[112] J. Zeiher, R. Bijnen, P. Schauß, S. Hild, J.-y. Choi, T. Pohl, I. Bloch, and C. Gross, "Many-body interferometry of a rydberg-dressed spin lattice," *Nature Physics*, vol. 12, 02 2016.

[113] D. Barredo, H. Labuhn, S. Ravets, T. Lahaye, A. Browaeys, and C. S. Adams, "Coherent excitation transfer in a spin chain of three rydberg atoms," *Phys. Rev. Lett.*, vol. 114, p. 113002, Mar 2015.

[114] M. Saffman, T. G. Walker, and K. Mølmer, "Quantum information with rydberg atoms," *Reviews of modern physics*, vol. 82, no. 3, p. 2313, 2010.

[115] D. Paredes-Barato and C. Adams, "All-optical quantum information processing using rydberg gates," *Physical review letters*, vol. 112, no. 4, p. 040501, 2014.

[116] I. I. Ryabtsev, I. I. Beterov, D. B. Tretyakov, V. M. Entin, and E. A. Yakshina, "Spectroscopy of cold rubidium rydberg atoms for applications in quantum information," *Physics-Uspekhi*, vol. 59, no. 2, p. 196, 2016.

[117] M. Reetz-Lamour, T. Amthor, J. Deiglmayr, S. Westermann, K. Singer, A. L. de Oliveira, L. G. Marcassa, and M. Weidemüller, "Prospects of ultracold rydberg gases for quantum information processing," *Fortschritte der Physik: Progress of Physics*, vol. 54, no. 8-10, pp. 776–787, 2006.

[118] C. J. Foot *et al.*, *Atomic physics*, vol. 7. Oxford University Press, 2005.

[119] M. J. Seaton, "Quantum defect theory," *Reports on Progress in Physics*, vol. 46, pp. 167–257, feb 1983.

[120] M. Mack, F. Karlewski, H. Hattermann, S. Höckh, F. Jessen, D. Cano, and J. Fortágh, "Measurement of absolute transition frequencies of ^{87}Rb to *nS* and *nD* rydberg states by means of electromagnetically induced transparency," *Phys. Rev. A*, vol. 83, p. 052515, May 2011.

[121] N. Šibalić, J. Pritchard, C. Adams, and K. Weatherill, "Arc: An open-source library for calculating properties of alkali rydberg atoms," *Computer Physics Communications*, vol. 220, pp. 319–331, 2017.

[122] J. Murray-Krezan, "The classical dynamics of rydberg stark atoms in momentum space," *American Journal of Physics*, vol. 76, no. 11, pp. 1007–1011, 2008.

[123] T. Fließbach, *Elektrodynamik: Lehrbuch zur Theoretischen Physik II*, vol. 2. Springer-Verlag, 2012.

[124] W. Demtröder, *Experimentalphysik 3: Atome, Moleküle und Festkörper*. Springer-Verlag, 2016.

[125] T. F. Gallagher, *Rydberg Atoms*. Cambridge Monographs on Atomic, Molecular and Chemical Physics, Cambridge University Press, 1994.

[126] W. P. Spencer, A. G. Vaidyanathan, D. Kleppner, and T. W. Ducas, "Measurements of lifetimes of sodium rydberg states in a cooled environment," *Physical Review A*, vol. 24, no. 5, p. 2513, 1981.

[127] X. He, A. Chen, C. Zhang, and B. Li, "Model-potential calculation of lifetimes of Rydberg states of alkali atoms," *Journal of Physics B Atomic Molecular Physics*, vol. 23, pp. 661–678, Feb. 1990.

[128] T. Gallagher and W. Cooke, "Interactions of blackbody radiation with atoms," *Physical Review Letters*, vol. 42, no. 13, p. 835, 1979.

[129] W. Cooke and T. Gallagher, "Effects of blackbody radiation on highly excited atoms," *Physical Review A*, vol. 21, no. 2, p. 588, 1980.

[130] J. W. Farley and W. H. Wing, "Accurate calculation of dynamic stark shifts and depopulation rates of rydberg energy levels induced by blackbody radiation. hydrogen, helium, and alkali-metal atoms," *Phys. Rev. A*, vol. 23, pp. 2397–2424, May 1981.

[131] C. E. Theodosiou, "Lifetimes of alkali-metal—atom rydberg states," *Phys. Rev. A*, vol. 30, pp. 2881–2909, Dec 1984.

[132] C. Seiler, J. A. Agner, P. Pillet, and F. Merkt, "Radiative and collisional processes in translationally cold samples of hydrogen rydberg atoms studied in an electrostatic trap," *Journal of Physics B: Atomic, Molecular and Optical Physics*, vol. 49, no. 9, p. 094006, 2016.

[133] I. Beterov, I. Ryabtsev, D. Tretyakov, and V. Entin, "Quasiclassical calculations of blackbody-radiation-induced depopulation rates and effective lifetimes of rydberg ns, np, and nd alkali-metal atoms with $n \leq 80$," *Physical review A*, vol. 79, no. 5, p. 052504, 2009.

[134] T. Gallagher, S. Edelstein, and R. Hill, "Radiative lifetimes of the s and d rydberg levels of na," *Physical Review A*, vol. 11, no. 5, p. 1504, 1975.

[135] A. Reinhard, T. C. Liebisch, B. Knuffman, and G. Raithel, "Level shifts of rubidium rydberg states due to binary interactions," *Phys. Rev. A*, vol. 75, p. 032712, Mar 2007.

[136] C. S. E. van Ditzhuijzen, A. F. Koenderink, J. V. Hernández, F. Robicheaux, L. D. Noordam, and H. B. v. L. van den Heuvell, "Spatially resolved observation of dipole-dipole interaction between rydberg atoms," *Phys. Rev. Lett.*, vol. 100, p. 243201, Jun 2008.

[137] T. J. Carroll, K. Claringbould, A. Goodsell, M. J. Lim, and M. W. Noel, "Angular dependence of the dipole-dipole interaction in a nearly one-dimensional sample of rydberg atoms," *Phys. Rev. Lett.*, vol. 93, p. 153001, Oct 2004.

[138] S. Ravets, H. Labuhn, D. Barredo, T. Lahaye, and A. Browaeys, "Measurement of the angular dependence of the dipole-dipole interaction between two individual rydberg atoms at a förster resonance," *Phys. Rev. A*, vol. 92, p. 020701, Aug 2015.

[139] A. P. n. Orioli, A. Signoles, H. Wildhagen, G. Günter, J. Berges, S. Whitlock, and M. Weidemüller, "Relaxation of an isolated dipolar-interacting rydberg quantum spin system," *Phys. Rev. Lett.*, vol. 120, p. 063601, Feb 2018.

[140] S. de Léséleuc, V. Lienhard, P. Scholl, D. Barredo, S. Weber, N. Lang, H. P. Büchler, T. Lahaye, and A. Browaeys, "Observation of a symmetry-protected topological phase of interacting bosons with rydberg atoms," *Science*, vol. 365, no. 6455, pp. 775–780, 2019.

[141] H. Schempp, G. Günter, S. Wüster, M. Weidemüller, and S. Whitlock, "Correlated exciton transport in rydberg-dressed-atom spin chains," *Phys. Rev. Lett.*, vol. 115, p. 093002, Aug 2015.

[142] V. Lienhard, P. Scholl, S. Weber, D. Barredo, S. de Léséleuc, R. Bai, N. Lang, M. Fleischhauer, H. P. Büchler, T. Lahaye, and A. Browaeys, "Realization of a density-dependent peierls phase in a synthetic, spin-orbit coupled rydberg system," *Phys. Rev. X*, vol. 10, p. 021031, May 2020.

[143] S. de Léséleuc, D. Barredo, V. Lienhard, A. Browaeys, and T. Lahaye, "Optical control of the resonant dipole-dipole interaction between rydberg atoms," *Phys. Rev. Lett.*, vol. 119, p. 053202, Aug 2017.

[144] A. W. Glaetzle, M. Dalmonte, R. Nath, I. Rousochatzakis, R. Moessner, and P. Zoller, "Quantum spin-ice and dimer models with rydberg atoms," *Phys. Rev. X*, vol. 4, p. 041037, Nov 2014.

[145] B. Vermersch, M. Punk, A. W. Glaetzle, C. Gross, and P. Zoller, "Dynamical preparation of laser-excited anisotropic rydberg crystals in 2d optical lattices," *New Journal of Physics*, vol. 17, p. 013008, jan 2015.

[146] S. Weber, C. Tresp, H. Menke, A. Urvoy, O. Firstenberg, H. P. Büchler, and S. Hofferberth, "Calculation of rydberg interaction potentials," *Journal of Physics B: Atomic, Molecular and Optical Physics*, vol. 50, p. 133001, jun 2017.

[147] H. Saßmannshausen and J. Deiglmayr, "Observation of rydberg-atom macrodimers: Micrometer-sized diatomic molecules," *Phys. Rev. Lett.*, vol. 117, p. 083401, Aug 2016.

[148] A. Schwettmann, J. Crawford, K. R. Overstreet, and J. P. Shaffer, "Cold cs rydberg-gas interactions," *Phys. Rev. A*, vol. 74, p. 020701, Aug 2006.

[149] J. Deiglmayr, H. Saßmannshausen, P. Pillet, and F. Merkt, "Observation of dipole-quadrupole interaction in an ultracold gas of rydberg atoms," *Phys. Rev. Lett.*, vol. 113, p. 193001, Nov 2014.

[150] C. Tresp, P. Bienias, S. Weber, H. Gorniaczyk, I. Mirgorodskiy, H. P. Büchler, and S. Hofferberth, "Dipolar dephasing of rydberg *d*-state polaritons," *Phys. Rev. Lett.*, vol. 115, p. 083602, Aug 2015.

[151] N. Samboy and R. Côté, "Rubidium rydberg macrodimers," *Journal of Physics B: Atomic, Molecular and Optical Physics*, vol. 44, p. 184006, sep 2011.

[152] N. Samboy, J. Stanojevic, and R. Côté, "Formation and properties of rydberg macrodimers," *Phys. Rev. A*, vol. 83, p. 050501, May 2011.

[153] A. Schwettmann, K. R. Overstreet, J. Tallant, and J. P. Shaffer, "Analysis of long-range cs rydberg potential wells," *Journal of Modern Optics*, vol. 54, no. 16-17, pp. 2551–2562, 2007.

[154] K. R. Overstreet, A. Schwettmann, J. Tallant, D. Booth, and J. P. Shaffer, "Observation of electric-field-induced cs rydberg atom macrodimers," *Nature Physics*, vol. 5, no. 8, pp. 581–585, 2009.

[155] J. Shaffer, S. Rittenhouse, and H. Sadeghpour, "Ultracold rydberg molecules," *Nature communications*, vol. 9, no. 1, pp. 1–12, 2018.

[156] H. Saßmannshausen and J. Deiglmayr, "Observation of rydberg-atom macrodimers: Micrometer-sized diatomic molecules," *Phys. Rev. Lett.*, vol. 117, p. 083401, Aug 2016.

[157] T. Boulier, E. Magnan, C. Bracamontes, J. Maslek, E. A. Goldschmidt, J. T. Young, A. V. Gorshkov, S. L. Rolston, and J. V. Porto, "Spontaneous avalanche dephasing in large rydberg ensembles," *Phys. Rev. A*, vol. 96, p. 053409, Nov 2017.

[158] J. Honer, H. Weimer, T. Pfau, and H. P. Büchler, "Collective many-body interaction in rydberg dressed atoms," *Phys. Rev. Lett.*, vol. 105, p. 160404, Oct 2010.

[159] C. Gaul, B. J. DeSalvo, J. A. Aman, F. B. Dunning, T. C. Killian, and T. Pohl, "Resonant rydberg dressing of alkaline-earth atoms via electromagnetically induced transparency," *Phys. Rev. Lett.*, vol. 116, p. 243001, Jun 2016.

[160] T. Macrì and T. Pohl, "Rydberg dressing of atoms in optical lattices," *Phys. Rev. A*, vol. 89, p. 011402, Jan 2014.

[161] T.-L. Chen, S.-Y. Chang, Y.-J. Huang, K. Shukla, Y.-C. Huang, T.-H. Suen, T.-Y. Kuan, J.-T. Shy, and Y.-W. Liu, "Inverted-ladder-type optical excitation of potassium rydberg states with hot and cold ensembles," *Phys. Rev. A*, vol. 101, p. 052507, May 2020.

[162] E. Brion, L. H. Pedersen, and K. Mølmer, "Adiabatic elimination in a lambda system," *Journal of Physics A: Mathematical and Theoretical*, vol. 40, pp. 1033–1043, jan 2007.

[163] R. Löw, H. Weimer, J. Nipper, J. B. Balewski, B. Butscher, H. P. Büchler, and T. Pfau, "An experimental and theoretical guide to strongly interacting rydberg gases," *Journal of Physics B: Atomic, Molecular and Optical Physics*, vol. 45, no. 11, p. 113001, 2012.

[164] N. Henkel, R. Nath, and T. Pohl, "Three-dimensional roton excitations and supersolid formation in rydberg-excited bose-einstein condensates," *Physical review letters*, vol. 104, no. 19, p. 195302, 2010.

[165] V. Paulisch, R. Han, H. K. Ng, and B.-G. Englert, "Beyond adiabatic elimination: A hierarchy of approximations for multi-photon processes," *The European Physical Journal Plus*, vol. 129, 09 2012.

[166] R. Han, H. K. Ng, and B.-G. Englert, "Raman transitions without adiabatic elimination: a simple and accurate treatment," *Journal of Modern Optics*, vol. 60, no. 4, pp. 255–265, 2013.

[167] M. Sanz, E. Solano, and Í. L. Egusquiza, "Beyond adiabatic elimination: Effective hamiltonians and singular perturbation," in *Applications + Practical Conceptualization + Mathematics = fruitful Innovation* (R. S. Anderssen, P. Broadbridge, Y. Fukumoto, K. Kajiwara, T. Takagi, E. Verbitskiy, and M. Wakayama, eds.), (Tokyo), pp. 127–142, Springer Japan, 2016.

[168] A. M. Hankin, Y.-Y. Jau, L. P. Parazzoli, C. W. Chou, D. J. Armstrong, A. J. Landahl, and G. W. Biedermann, "Two-atom rydberg blockade using direct 6s to np excitation," *Phys. Rev. A*, vol. 89, p. 033416, Mar 2014.

[169] D. Petrosyan, "Dynamics and equilibration of rydberg excitations in dissipative atomic ensembles," *Journal of Physics B: Atomic, Molecular and Optical Physics*, vol. 46, p. 141001, jun 2013.

[170] I. Lesanovsky and J. P. Garrahan, "Kinetic constraints, hierarchical relaxation, and onset of glassiness in strongly interacting and dissipative rydberg gases," *Phys. Rev. Lett.*, vol. 111, p. 215305, Nov 2013.

[171] M. Höning, D. Muth, D. Petrosyan, and M. Fleischhauer, "Steady-state crystallization of rydberg excitations in an optically driven lattice gas," *Phys. Rev. A*, vol. 87, p. 023401, Feb 2013.

[172] E. Urban, T. Johnson, T. Henage, L. Isenhower, D. Yavuz, T. Walker, and M. Saffman, "Observation of rydberg blockade between two atoms," *Nature Physics*, vol. 5, 05 2008.

[173] M. Ebert, M. Kwon, T. G. Walker, and M. Saffman, "Coherence and rydberg blockade of atomic ensemble qubits," *Phys. Rev. Lett.*, vol. 115, p. 093601, Aug 2015.

[174] I. I. Beterov and M. Saffman, "Rydberg blockade, förster resonances, and quantum state measurements with different atomic species," *Phys. Rev. A*, vol. 92, p. 042710, Oct 2015.

[175] X. L. Zhang, L. Isenhower, A. T. Gill, T. G. Walker, and M. Saffman, "Deterministic entanglement of two neutral atoms via rydberg blockade," *Phys. Rev. A*, vol. 82, p. 030306, Sep 2010.

[176] N. Stiesdal, H. Busche, J. Kumlin, K. Kleinbeck, H. P. Büchler, and S. Hofferberth, "Observation of collective decay dynamics of a single rydberg superatom," *Phys. Rev. Research*, vol. 2, p. 043339, Dec 2020.

[177] T. Weber, M. Höning, T. Niederprüm, T. Manthey, O. Thomas, V. Guarrera, M. Fleischhauer, G. Barontini, and H. Ott, "Mesoscopic rydberg-blockaded ensembles in the superatom regime and beyond," *Nature Physics*, vol. 11, 01 2015.

[178] J. Zeiher, P. Schauß, S. Hild, T. Macrì, I. Bloch, and C. Gross, "Microscopic characterization of scalable coherent rydberg superatoms," *Phys. Rev. X*, vol. 5, p. 031015, Aug 2015.

[179] G. McCormack, R. Nath, and W. Li, "Dynamical excitation of maxon and roton modes in a rydberg-dressed bose-einstein condensate," *Phys. Rev. A*, vol. 102, p. 023319, Aug 2020.

[180] W. Li, L. Hamadeh, and I. Lesanovsky, "Probing the interaction between rydberg-dressed atoms through interference," *Phys. Rev. A*, vol. 85, p. 053615, May 2012.

[181] S. Helmrich, A. Arias, N. Pehoviak, and S. Whitlock, "Two-body interactions and decay of three-level rydberg-dressed atoms," *Journal of Physics B: Atomic, Molecular and Optical Physics*, vol. 49, p. 03LT02, jan 2016.

[182] P. Schauß, M. Cheneau, M. Endres, T. Fukuhara, S. Hild, A. Omran, T. Pohl, C. Gross, S. Kuhr, and I. Bloch, "Observation of spatially ordered structures in a two-dimensional rydberg gas," *Nature*, vol. 491, no. 7422, pp. 87–91, 2012.

[183] P. Schauß, J. Zeiher, T. Fukuhara, S. Hild, M. Cheneau, T. Macrì, T. Pohl, I. Bloch, and C. Gross, "Crystallization in ising quantum magnets," *Science*, vol. 347, no. 6229, pp. 1455–1458, 2015.

[184] R. Bijnen, S. Smit, K. Leeuwen, E. Vredenbregt, and S. Kokkelmans, "Adiabatic formation of rydberg crystals with chirped laser pulses," *Journal of Physics B-atomic Molecular and Optical Physics - J PHYS-B-AT MOL OPT PHYS*, vol. 44, 03 2011.

[185] S. Trotzky, P. Cheinet, S. Folling, M. Feld, U. Schnorrberger, A. M. Rey, A. Polkovnikov, E. A. Demler, M. D. Lukin, and I. Bloch, "Time-resolved observation and control of superexchange interactions with ultracold atoms in optical lattices," *Science*, vol. 319, no. 5861, pp. 295–299, 2008.

[186] A. W. Glaetzle, M. Dalmonte, R. Nath, C. Gross, I. Bloch, and P. Zoller, "Designing frustrated quantum magnets with laser-dressed rydberg atoms," *Phys. Rev. Lett.*, vol. 114, p. 173002, Apr 2015.

[187] H. Labuhn, D. Barredo, S. Ravets, S. De Léséleuc, T. Macrì, T. Lahaye, and A. Browaeys, "Tunable two-dimensional arrays of single rydberg atoms for realizing quantum ising models," *Nature*, vol. 534, no. 7609, pp. 667–670, 2016.

[188] M. Magoni, P. P. Mazza, and I. Lesanovsky, "Emergent bloch oscillations in a kinetically constrained rydberg spin lattice," *Phys. Rev. Lett.*, vol. 126, p. 103002, Mar 2021.

[189] A. Mokhberi, M. Hennrich, and F. Schmidt-Kaler, "Chapter four - trapped rydberg ions: A new platform for quantum information processing," vol. 69 of *Advances In Atomic, Molecular, and Optical Physics*, pp. 233–306, Academic Press, 2020.

[190] E. A. Goldschmidt, T. Boulier, R. C. Brown, S. B. Koller, J. T. Young, A. V. Gorshkov, S. L. Rolston, and J. V. Porto, "Anomalous broadening in driven dissipative rydberg systems," *Phys. Rev. Lett.*, vol. 116, p. 113001, Mar 2016.

[191] J. B. Balewski, A. T. Krupp, A. Gaj, S. Hofferberth, R. Löw, and T. Pfau, "Rydberg dressing: understanding of collective many-body effects and implications for experiments," *New Journal of Physics*, vol. 16, p. 063012, jun 2014.

[192] J. A. Aman, B. J. DeSalvo, F. B. Dunning, T. C. Killian, S. Yoshida, and J. Burgdörfer, "Trap losses induced by near-resonant rydberg dressing of cold atomic gases," *Phys. Rev. A*, vol. 93, p. 043425, Apr 2016.

[193] C. Gaul, B. J. DeSalvo, J. A. Aman, F. B. Dunning, T. C. Killian, and T. Pohl, "Resonant rydberg dressing of alkaline-earth atoms via electromagnetically induced transparency," *Phys. Rev. Lett.*, vol. 116, p. 243001, Jun 2016.

[194] L. Festa, N. Lorenz, L.-M. Steinert, Z. Chen, P. Osterholz, R. Eberhard, and C. Gross, "Blackbody-radiation-induced facilitated excitation of rydberg atoms in optical tweezers," *Physical Review A*, vol. 105, no. 1, p. 013109, 2022.

[195] M. Saffman and T. G. Walker, "Analysis of a quantum logic device based on dipole-dipole interactions of optically trapped rydberg atoms," *Phys. Rev. A*, vol. 72, p. 022347, Aug 2005.

[196] L. Li, Y. Dudin, and A. Kuzmich, "Entanglement between light and an optical atomic excitation," *Nature*, vol. 498, no. 7455, pp. 466–469, 2013.

[197] A. Geißler, U. Bissbort, and W. Hofstetter, "Quasiparticle spectra of supersolid lattice gases at near-resonant rydberg dressing," *Phys. Rev. A*, vol. 98, p. 063635, Dec 2018.

[198] B. Capogrosso-Sansone, i. m. c. G. m. c. Söyler, N. Prokof'ev, and B. Svistunov, "Monte carlo study of the two-dimensional bose-hubbard model," *Phys. Rev. A*, vol. 77, p. 015602, Jan 2008.

[199] L. Pollet, "Recent developments in quantum monte carlo simulations with applications for cold gases," *Reports on progress in physics*, vol. 75, no. 9, p. 094501, 2012.

[200] F. Gerbier, S. Trotzky, S. Fölling, U. Schnorrberger, J. D. Thompson, A. Widera, I. Bloch, L. Pollet, M. Troyer, B. Capogrosso-Sansone, N. V. Prokof'ev, and B. V. Svistunov, "Expansion of a quantum gas released from an optical lattice," *Phys. Rev. Lett.*, vol. 101, p. 155303, Oct 2008.

[201] S. Wessel, F. Alet, M. Troyer, and G. G. Batrouni, "Quantum monte carlo simulations of confined bosonic atoms in optical lattices," *Phys. Rev. A*, vol. 70, p. 053615, Nov 2004.

[202] J. F. Corney and P. D. Drummond, "Gaussian quantum monte carlo methods for fermions and bosons," *Phys. Rev. Lett.*, vol. 93, p. 260401, Dec 2004.

[203] A. Isacsson, M.-C. Cha, K. Sengupta, and S. M. Girvin, "Superfluid-insulator transitions of two-species bosons in an optical lattice," *Phys. Rev. B*, vol. 72, p. 184507, Nov 2005.

[204] A. Georges, G. Kotliar, W. Krauth, and M. J. Rozenberg, "Dynamical mean-field theory of strongly correlated fermion systems and the limit of infinite dimensions," *Reviews of Modern Physics*, vol. 68, no. 1, p. 13, 1996.

[205] H. Aoki, N. Tsuji, M. Eckstein, M. Kollar, T. Oka, and P. Werner, "Nonequilibrium dynamical mean-field theory and its applications," *Reviews of Modern Physics*, vol. 86, no. 2, p. 779, 2014.

[206] J. Freericks, V. Turkowski, and V. Zlatić, "Nonequilibrium dynamical mean-field theory," *Physical review letters*, vol. 97, no. 26, p. 266408, 2006.

[207] H. U. R. Strand, M. Eckstein, and P. Werner, "Nonequilibrium dynamical mean-field theory for bosonic lattice models," *Phys. Rev. X*, vol. 5, p. 011038, Mar 2015.

[208] W.-J. Hu and N.-H. Tong, "Dynamical mean-field theory for the bose-hubbard model," *Phys. Rev. B*, vol. 80, p. 245110, Dec 2009.

[209] M. C. Gutzwiller, "Effect of correlation on the ferromagnetism of transition metals," *Physical Review Letters*, vol. 10, no. 5, p. 159, 1963.

[210] M. C. Gutzwiller, "Correlation of electrons in a narrow s band," *Physical Review*, vol. 137, no. 6A, p. A1726, 1965.

[211] J. Kanamori, "Electron correlation and ferromagnetism of transition metals," *Progress of Theoretical Physics*, vol. 30, no. 3, pp. 275–289, 1963.

[212] J. Hubbard, "Electron correlations in narrow energy bands," *Proceedings of the Royal Society of London. Series A. Mathematical and Physical Sciences*, vol. 276, no. 1365, pp. 238–257, 1963.

[213] T. Rice and K. Ueda, "Gutzwiller variational approximation to the heavy-fermion ground state of the periodic anderson model," *Physical review letters*, vol. 55, no. 9, p. 995, 1985.

[214] A. Reynolds, D. Edwards, and A. Hewson, "The gutzwiller approach to magnetic instabilities in heavy-fermion systems," *Journal of Physics: Condensed Matter*, vol. 4, no. 37, p. 7589, 1992.

[215] W. Metzner and D. Vollhardt, "Ground-state properties of correlated fermions: Exact analytic results for the gutzwiller wave function," *Physical review letters*, vol. 59, no. 1, p. 121, 1987.

[216] D. S. Rokhsar and B. G. Kotliar, "Gutzwiller projection for bosons," *Phys. Rev. B*, vol. 44, pp. 10328–10332, Nov 1991.

[217] K. Sheshadri, H. Krishnamurthy, R. Pandit, and T. Ramakrishnan, "Superfluid and insulating phases in an interacting-boson model: Mean-field theory and the rpa," *EPL (Europhysics Letters)*, vol. 22, no. 4, p. 257, 1993.

[218] D. L. Kovrizhin, G. V. Pai, and S. Sinha, "Density wave and supersolid phases of correlated bosons in an optical lattice," *Europhysics Letters (EPL)*, vol. 72, pp. 162–168, oct 2005.

[219] T. Kimura, S. Tsuchiya, and S. Kurihara, "Possibility of a first-order superfluid–mott-insulator transition of spinor bosons in an optical lattice," *Phys. Rev. Lett.*, vol. 94, p. 110403, Mar 2005.

[220] P. Buonsante, F. Massel, V. Penna, and A. Vezzani, "Gutzwiller approach to the bose-hubbard model with random local impurities," *Phys. Rev. A*, vol. 79, p. 013623, Jan 2009.

[221] A. Albus, F. Illuminati, and J. Eisert, "Mixtures of bosonic and fermionic atoms in optical lattices," *Physical Review A*, vol. 68, no. 2, p. 023606, 2003.

[222] D.-S. Lühmann, "Cluster gutzwiller method for bosonic lattice systems," *Phys. Rev. A*, vol. 87, p. 043619, Apr 2013.

[223] D. R. Hartree, "The wave mechanics of an atom with a non-coulomb central field. part i. theory and methods," *Mathematical Proceedings of the Cambridge Philosophical Society*, vol. 24, no. 1, p. 89–110, 1928.

[224] J. C. Slater, "The self consistent field and the structure of atoms," *Phys. Rev.*, vol. 32, pp. 339–348, Sep 1928.

[225] J. A. Gaunt, "A theory of hartree's atomic fields," *Mathematical Proceedings of the Cambridge Philosophical Society*, vol. 24, no. 2, p. 328–342, 1928.

[226] H.-P. Breuer, F. Petruccione, *et al.*, *The theory of open quantum systems*. Oxford University Press on Demand, 2002.

[227] G. Lindblad, "On the generators of quantum dynamical semigroups," *Communications in Mathematical Physics*, vol. 48, no. 2, pp. 119–130, 1976.

[228] H.-P. Breuer, F. Petruccione, *et al.*, *The theory of open quantum systems*. Oxford University Press on Demand, 2002.

[229] C. A. Brasil, F. F. Fanchini, and R. d. J. Napolitano, "A simple derivation of the lindblad equation," *Revista Brasileira de Ensino de Física*, vol. 35, pp. 01–09, 2013.

[230] A. Daley, H. Pichler, J. Schachenmayer, and P. Zoller, "Measuring entanglement growth in quench dynamics of bosons in an optical lattice," *Physical review letters*, vol. 109, no. 2, p. 020505, 2012.

[231] E. Guardado-Sanchez, P. T. Brown, D. Mitra, T. Devakul, D. A. Huse, P. Schauß, and W. S. Bakr, "Probing the quench dynamics of antiferromagnetic correlations in a 2d quantum ising spin system," *Physical Review X*, vol. 8, no. 2, p. 021069, 2018.

[232] S. R. Manmana, S. Wessel, R. M. Noack, and A. Muramatsu, "Strongly correlated fermions after a quantum quench," *Physical review letters*, vol. 98, no. 21, p. 210405, 2007.

[233] T. Gericke, F. Gerbier, A. Widera, S. Fölling, O. Mandel, and I. Bloch, "Adiabatic loading of a bose–einstein condensate in a 3d optical lattice," *Journal of Modern Optics*, vol. 54, no. 5, pp. 735–743, 2007.

[234] A. S. Sørensen, E. Altman, M. Gullans, J. Porto, M. D. Lukin, and E. Demler, "Adiabatic preparation of many-body states in optical lattices," *Physical Review A*, vol. 81, no. 6, p. 061603, 2010.

[235] V. Murg and J. I. Cirac, "Adiabatic time evolution in spin systems," *Physical Review A*, vol. 69, no. 4, p. 042320, 2004.

[236] T. Kato, "On the adiabatic theorem of quantum mechanics," *Journal of the Physical Society of Japan*, vol. 5, no. 6, pp. 435–439, 1950.

[237] G. Nenciu, "On the adiabatic theorem of quantum mechanics," *Journal of Physics A: Mathematical and General*, vol. 13, pp. L15–L18, feb 1980.

[238] R. Unanyan, M. Fleischhauer, B. Shore, and K. Bergmann, "Robust creation and phase-sensitive probing of superposition states via stimulated raman adiabatic passage (stirap) with degenerate dark states," *Optics Communications*, vol. 155, no. 1, pp. 144–154, 1998.

[239] V. S. Malinovsky and D. J. Tannor, "Simple and robust extension of the stimulated raman adiabatic passage technique to n-level systems," *Physical Review A*, vol. 56, no. 6, p. 4929, 1997.

[240] P. A. Ivanov, N. V. Vitanov, and K. Bergmann, "Effect of dephasing on stimulated raman adiabatic passage," *Phys. Rev. A*, vol. 70, p. 063409, Dec 2004.

[241] N. Vitanov and S. Stenholm, "Population transfer via a decaying state," *Physical Review A*, vol. 56, no. 2, p. 1463, 1997.

[242] M. Sarandy and D. Lidar, "Adiabatic approximation in open quantum systems," *Physical Review A*, vol. 71, no. 1, p. 012331, 2005.

[243] D. Chen, M. White, C. Borries, and B. DeMarco, "Quantum quench of an atomic mott insulator," *Physical Review Letters*, vol. 106, no. 23, p. 235304, 2011.

[244] D. Chen, M. White, C. Borries, and B. DeMarco, "Quantum quench of an atomic mott insulator," *Phys. Rev. Lett.*, vol. 106, p. 235304, Jun 2011.

[245] I. Mourachko, D. Comparat, F. de Tomasi, A. Fioretti, P. Nosbaum, V. M. Akulin, and P. Pillet, "Many-body effects in a frozen rydberg gas," *Phys. Rev. Lett.*, vol. 80, pp. 253–256, Jan 1998.

[246] W. Anderson, J. Veale, and T. F. Gallagher, "Resonant dipole-dipole energy transfer in a nearly frozen rydberg gas," *Physical review letters*, vol. 80, no. 2, p. 249, 1998.

[247] R. Löw, H. Weimer, U. Krohn, R. Heidemann, V. Bendkowsky, B. Butscher, H. P. Büchler, and T. Pfau, "Universal scaling in a strongly interacting rydberg gas," *Physical Review A*, vol. 80, no. 3, p. 033422, 2009.

[248] Y. S. Patil, S. Chakram, and M. Vengalattore, "Measurement-induced localization of an ultracold lattice gas," *Phys. Rev. Lett.*, vol. 115, p. 140402, Oct 2015.

[249] Y. Cao, Y.-H. Li, Z. Cao, J. Yin, Y.-A. Chen, H.-L. Yin, T.-Y. Chen, X. Ma, C.-Z. Peng, and J.-W. Pan, "Direct counterfactual communication via quantum zeno effect," *Proceedings of the National Academy of Sciences*, vol. 114, no. 19, pp. 4920–4924, 2017.

[250] J. J. García-Ripoll, S. Dürr, N. Syassen, D. M. Bauer, M. Lettner, G. Rempe, and J. I. Cirac, "Dissipation-induced hard-core boson gas in an optical lattice," *New Journal of Physics*, vol. 11, p. 013053, jan 2009.

[251] I. Vidanović, D. Cocks, and W. Hofstetter, "Dissipation through localized loss in bosonic systems with long-range interactions," *Phys. Rev. A*, vol. 89, p. 053614, May 2014.

[252] J. Mun, P. Medley, G. K. Campbell, L. G. Marcassa, D. E. Pritchard, and W. Ketterle, "Phase diagram for a bose-einstein condensate moving in an optical lattice," *Phys. Rev. Lett.*, vol. 99, p. 150604, Oct 2007.

[253] M. Barbier, H. Lütjeharms, and W. Hofstetter, "Supersolid phases of ultracold bosons trapped in optical lattices dressed with rydberg *p* states," *Phys. Rev. A*, vol. 105, p. 013326, Jan 2022.

[254] Z. Lan, J. Minář, E. Levi, W. Li, and I. Lesanovsky, "Emergent devil's staircase without particle-hole symmetry in rydberg quantum gases with competing attractive and repulsive interactions," *Physical review letters*, vol. 115, no. 20, p. 203001, 2015.

[255] J. Cui, R. van Bijnen, T. Pohl, S. Montangero, and T. Calarco, "Optimal control of rydberg lattice gases," *Quantum Science and Technology*, vol. 2, no. 3, p. 035006, 2017.

[256] M. Rader and A. M. Läuchli, "Floating phases in one-dimensional rydberg ising chains," *arXiv preprint arXiv:1908.02068*, 2019.

[257] M. Barbier, A. Geißler, and W. Hofstetter, "Decay-dephasing-induced steady states in bosonic rydberg-excited quantum gases in an optical lattice," *Phys. Rev. A*, vol. 99, p. 033602, Mar 2019.

[258] A. Lauer, D. Muth, and M. Fleischhauer, "Transport-induced melting of crystals of rydberg dressed atoms in a one-dimensional lattice," *New Journal of Physics*, vol. 14, p. 095009, sep 2012.

[259] H. Weimer and H. P. Büchler, "Two-stage melting in systems of strongly interacting rydberg atoms," *Phys. Rev. Lett.*, vol. 105, p. 230403, Nov 2010.

[260] Z. Lan, W. Li, and I. Lesanovsky, "Quantum melting of two-component rydberg crystals," *Phys. Rev. A*, vol. 94, p. 051603, Nov 2016.

[261] J. Panas, M. Barbier, A. Geißler, and W. Hofstetter, "Supersolid phases of rydberg-excited bosons on a triangular lattice," *Phys. Rev. A*, vol. 99, p. 063625, Jun 2019.

[262] J. Wang, J. Bai, J. He, and J. Wang, "Single-photon cesium rydberg excitation spectroscopy using 318.6-nm uv laser and room-temperature vapor cell," *Opt. Express*, vol. 25, pp. 22510–22518, Sep 2017.

[263] D. Barredo, S. Ravets, H. Labuhn, L. Béguin, A. Vernier, F. Nogrette, T. Lahaye, and A. Browaeys, "Demonstration of a strong rydberg blockade in three-atom systems with anisotropic interactions," *Phys. Rev. Lett.*, vol. 112, p. 183002, May 2014.

[264] V. Lienhard, P. Scholl, S. Weber, D. Barredo, S. de Léséleuc, R. Bai, N. Lang, M. Fleischhauer, H. P. Büchler, T. Lahaye, and A. Browaeys, "Realization of a density-dependent peierls phase in a synthetic, spin-orbit coupled rydberg system," *Phys. Rev. X*, vol. 10, p. 021031, May 2020.

[265] U. Raitzsch, R. Heidemann, H. Weimer, B. Butscher, P. Kollmann, R. Löw, H. Büchler, and T. Pfau, "Investigation of dephasing rates in an interacting rydberg gas," *New Journal of Physics*, vol. 11, no. 5, p. 055014, 2009.

[266] J. Zeiher, P. Schauß, S. Hild, T. Macrì, I. Bloch, and C. Gross, "Microscopic characterization of scalable coherent rydberg superatoms," *Phys. Rev. X*, vol. 5, p. 031015, Aug 2015.

[267] H. Hara, H. Konishi, S. Nakajima, Y. Takasu, and Y. Takahashi, "A three-dimensional optical lattice of ytterbium and lithium atomic gas mixture," *Journal of the Physical Society of Japan*, vol. 83, no. 1, p. 014003, 2014.

[268] E. Guardado-Sanchez, B. Spar, P. Schauss, R. Belyansky, J. T. Young, P. Bienias, A. V. Gorshkov, T. Iadecola, and W. S. Bakr, "Quench dynamics of a fermi gas with strong long-range interactions," *Energy*, vol. 10, no. 5, p. 1, 2020.

[269] R. Van Bijnen and T. Pohl, "Quantum magnetism and topological ordering via rydberg dressing near förster resonances," *Physical review letters*, vol. 114, no. 24, p. 243002, 2015.

[270] M. Barbier, S. Hollerith, and W. Hofstetter, "Extended bose-hubbard models with rydberg macrodimer dressing," *Phys. Rev. A*, vol. 104, p. 053304, Nov 2021.

[271] S. Hollerith, J. Rui, A. Rubio-Abadal, K. Srakaew, D. Wei, J. Zeiher, C. Gross, and I. Bloch, "Microscopic electronic structure tomography of rydberg macrodimers," *Physical Review Research*, vol. 3, no. 1, p. 013252, 2021.

[272] M. Iskin and J. K. Freericks, "Strong-coupling perturbation theory for the extended bose-hubbard model," *Phys. Rev. A*, vol. 79, p. 053634, May 2009.

[273] G. Hahn, "A modified euler method for dynamic analyses," *International Journal for Numerical Methods in Engineering*, vol. 32, no. 5, pp. 943–955, 1991.

[274] D. Ravat, "Analysis of the euler method and its applicability in environmental magnetic investigations," *Journal of Environmental and Engineering Geophysics*, vol. 1, no. 3, pp. 229–238, 1996.

[275] S. Skelboe and P. U. Andersen, "Stability properties of backward euler multirate formulas," *SIAM journal on scientific and statistical computing*, vol. 10, no. 5, pp. 1000–1009, 1989.

[276] C. S. Peskin and T. Schlick, "Molecular dynamics by the backward-euler method," *Communications on pure and applied mathematics*, vol. 42, no. 7, pp. 1001–1031, 1989.

[277] I. Celik and O. Karatekin, "Numerical experiments on application of richardson extrapolation with nonuniform grids," 1997.

[278] S. A. Richards, "Completed richardson extrapolation in space and time," *Communications in numerical methods in engineering*, vol. 13, no. 7, pp. 573–582, 1997.

[279] W. F. Ford and A. Sidi, "An algorithm for a generalization of the richardson extrapolation process," *SIAM journal on Numerical Analysis*, vol. 24, no. 5, pp. 1212–1232, 1987.

[280] J. R. Dormand and P. J. Prince, "A family of embedded runge-kutta formulae," *Journal of computational and applied mathematics*, vol. 6, no. 1, pp. 19–26, 1980.

[281] J. C. Butcher, "A history of runge-kutta methods," *Applied numerical mathematics*, vol. 20, no. 3, pp. 247–260, 1996.

[282] M. Dixon and S. Reich, "Symplectic time-stepping for particle methods," *GAMM-Mitteilungen*, vol. 27, no. 1, pp. 9–24, 2004.

[283] M. Sofroniou and W. Oevel, "Symplectic runge-kutta schemes i: Order conditions," *SIAM Journal on Numerical Analysis*, vol. 34, no. 5, pp. 2063–2086, 1997.

[284] S. Gan, Z. Shang, and G. Sun, "A class of symplectic partitioned runge–kutta methods," *Applied Mathematics Letters*, vol. 26, no. 9, pp. 968–973, 2013.

[285] J. Sanz-Serna, "Symplectic runge-kutta and related methods: recent results," *Physica D: Nonlinear Phenomena*, vol. 60, no. 1-4, pp. 293–302, 1992.

[286] B. Moore and S. Reich, "Backward error analysis for multi-symplectic integration methods," *Numerische Mathematik*, vol. 95, no. 4, pp. 625–652, 2003.

[287] T. Schlick, *Molecular modeling and simulation: an interdisciplinary guide*, vol. 2. Springer, 2010.

List of Figures

Abbreviations

BEC	Bose-Einstein condensate
MOT	Magneto-optical trap
ODLRO	Off diagonal long-range order
LRO	Long-range order
MI	Mott insulator
SF	Superfluid
DW	Density wave
SS	Supersolid
vac	vacuum
NN	Nearest neighbor
NNN	Next-nearest neighbor
TOF	Time-of-flight
RF	Rotating frame
RWA	Rotating wave approximation
vdW	van-der-Waals
ED	exact diagonalization
QMC	Quantum Monte Carlo
DMFT	Dynamical mean-field theory

Data, Software, and Permissions

Data and codes are archived at the Institute for Theoretical Physics of the Goethe University Frankfurt in Frankfurt am Main, Germany. Data and codes can be accessed by the Hofstetter group.
The results of this work were computed with codes written in Matlab and C++.
The author owns permissions from the journals of the peer-reviewed publications to reproduce figures 1.1, 1.2, 1.3, 1.4, 1.5, 1.15, 1.16, 2.9, 2.12, 2.13, 4.4, 4.5, 4.6, 4.8, 4.11, 4.12, 4.13 4.14, 4.15, 4.16, 4.17, 4.22, 4.24, 4.25, 4.26, 4.27, 4.28, B.4, B.6 and B.7.
Journal title abbreviations correspond to the ones of the Caltech library at:
www.library.caltech.edu/journal-title-abbreviations, December 2021

Acknowledgement

In the past I have never concerned myself with writing acknowledgments as it always appeared to me as a futile exercise in recognizing all individuals deserving of appreciation. During the writing of this thesis and the studies in general I cannot fathom how strenuous life would have been without my friends and family. As all these people already know how deeply I care for them it would be nonsensical to list and thank them all. Thus I dedicate this introductory paragraph to my family, namely my sister **Léa**, my father **Régis** and my mother **Souad**, who I am beyond thankful to have in my life.

There are however a few individuals that I want to acknowledge by name as they have deeply imprinted on my mind and had significant impact on my life as a researcher. As for all people from different walks of life, the ceaseless influx of challenges feeds self-doubt and insecurities sapping one's energy. More specifically, being in a field surrounded by brilliant minds and in an institute with passionately devoted researchers, it is difficult not to question one's place time and time again. Luckily I was fortunate enough to meet extraordinary people, who shared their feelings and struggles with me, which helped me persist through difficult times. It is an oxymoron, as I wish these people all the best on whatever way they choose, but it is comforting to know that everyone, even these diligent and outstandingly smart people, fight their own fights.
The first person I would like to acknowledge is **Martina Jung**, former bachelor student of mine and passionate novel writer. I had the privilege to work on a research project with her, which turned out to be an invaluable time for me. We tackled various challenges, discussed scientific problems and through her one-of-a-kind attentive and reflective presence I grew greatly. Her unwavering dedication will lead her to great places, of this I am certain, and I am waiting with anticipation for what to come.
As my former master student, **Henrik Lütjeharms** proved me that relentless effort is always rewarded. Between the beginning and the end of my supervision I do not remember a single period in which Henrik appeared neglectful of the work at hand and showed perpetual interest not only about his research topic but also towards branching fields in general. Through regular communication, even during his year abroad, I was able to see him progress steadily and hereby learned about the value of persistence.
Another person I had the immense pleasure to meet is **Niklas Heinsdorf**, an individual I not only greatly respect as a friend but also as a researcher. Although we (thankfully) did not work on a project together, I learned from his attitude towards research that in order to be a great scientist you should not take everything too seriously. The many challenges he has faced until now could have been too much of a burden for many, yet he withstood everything and, even though he would not admit it, overcame these past hurdles with shining success.
Finally I would like to acknowledge **Dr. Kira Riedl**, which during the full extend of my doctorate was a guiding star and shining beacon in the gloom. Fortunate as I was I got to know Kira right at the beginning of my studies, while she was wrapping up her own doctorate. I recall all the discussions we had about the difficulty and hardships of research,

about which I am thankful now. During times in which it seemed like insurmountable obstacles were piling up because I should not have been in research in the first place, it soothed me to remember that an utterly brilliant, studious and competent researcher such as Kira also felt similarly. If I were to become only half the researcher she is, I could not be happier.

Last but definitely not least my doctoral supervisor **Walter Hofstetter** merits the greatest acknowledgement I have to give. I have known Walter for roughly ten years now, as a lecturer and supervisor for many theses. I was often asked why I did not leave in between studies to experience different groups with different topics, but the immersion into the research provided already during my bachelor studies kept me anticipated for what to come in the field. Already at the beginning of my time in the group eight years ago I was encouraged to go to conferences, workshops and summer schools, develop a network of researchers and acquire knowledge through questions and discussions. I was proposed to work on current topics in the field and allowed to pursuit my own projects. I therefore firmly believe that there could have been no better introduction into the working world of a researcher. I am glad to have had a supervisor I hold in high esteem such as Walter and proud to have learned from what I consider to be one of the smartest people I know.

And finally to any struggling scientist reading this thesis, hang in there and keep your head up high. Because if I am certain of anything, it is that this thesis itself is a singular proof of many of the proverb *where there is a will, there is a way*.